The redshift evolution of galactic-scale magnetic fields

Dissertation

zur

Erlangung des Doktorgrades (*Dr. rer. nat.*)

der

Mathematisch-Naturwissenschaftlichen Fakultät

der

Rheinischen Friedrich–Wilhelms–Universität Bonn

vorgelegt von

Tímea Kovács

aus

Budapest, Ungarn

Bonn 2024

Angefertigt mit Genehmigung der Mathematisch-Naturwissenschaftlichen Fakultät
der Rheinischen Friedrich–Wilhelms–Universität Bonn

1. Referent: Prof. Dr. Michael Kramer
2. Referent: Prof. Dr. Pavel Kroupa
Tag der Promotion: 26. 04. 2024
Erscheinungsjahr: 2024

RHEINISCHE FRIEDRICH–WILHELMS–UNIVERSITÄT BONN

Abstract

by Timea Kovacs

for the degree of

Doctor rerum naturalium

Magnetic fields play an important role in galaxy evolution, from processes such as gas dynamics and star formation to galactic outflows. However, the redshift evolution of galactic-scale magnetic fields is not well constrained, with only a handful of direct magnetic field strength measurements in distant galaxies. In my thesis, I investigate this evolution using both radio polarimetric observations and synthetic observations made with the IllustrisTNG50 simulation.

Chapter 1 of this thesis summarizes the importance of magnetic fields in galaxies and the currently available measurements of magnetic fields in distant galaxies. The techniques used in radio polarimetry, and the calculations carried out on the simulation data are described in Chapter 2.

In the first half of my thesis (Chapters 3 and 4) I present the analysis of broadband (1 – 8 GHz) spectro-polarimetric Very Large Array observations of two lensing systems (B1600+434 and B0218+357), and the derived magnetic field strength of the lensing galaxies at $z = 0.414$ and $z = 0.685$ (corresponding to galaxies 4.4 and 6.3 Gyr ago). We expanded on a recently demonstrated new method, which was only used on one lensing system (at $z = 0.439$) before this thesis. While one of our systems probe to higher redshift than before, our other system allows us to measure the magnetic field of the galaxy's halo - which has not been measured in distant galaxies before. We derived the magnetic field strengths by applying Rotation Measure (RM) synthesis and Stokes QU fitting to the data to obtain the polarization properties and assuming different magnetic field geometry models to calculate the field strength. In Chapter 3, we find a halo field of 1.2 – 1.8 μG in the lensing galaxy of the system B1600+434, which is the highest redshift measurement of a magnetic field in a galaxy's halo to date. In Chapter 4, we possibly find an axisymmetric disk field of 2 – 20 μG in the lensing galaxy of the system B0218+357, which would be the highest redshift measurement of a regular disk magnetic field to date. Our results are in agreement with the magnetic field strength and structure of nearby galaxies, and the e-folding time of the large-scale dynamo we derived also falls into the range of values derived from the dynamo theory ($\tau_{\rm dynamo} = 2 \cdot 10^8$ yr), thus our results are compatible with the dynamo theory. We find that the dynamo has likely already built up a regular field in galaxies at $z \sim 0.7$.

In the second half of my thesis (Chapters 5 and 6) I compute how the ob-

servables of magnetic fields evolve over redshift using 16 500 galaxies at redshifts of $0 \leq z \leq 2$, with stellar masses in the range $9 \leq \log(M_*/\mathrm{M}_\odot) \leq 12$, from the state-of-the-art cosmological magneto-hydrodynamic simulation IllustrisTNG50. This is the first time such a large number of galaxies is used from IllustrisTNG50 simulation to create a large database of rotation measure and dispersion measure contribution of galaxies. We explore two methods used to obtain cosmic magnetic field strengths: deriving the magnetic field strength of intervening galaxies in front of polarized background quasars and deriving the magnetic field strength of the IGM by utilizing FRBs. In both cases, we exploit the effect of Faraday rotation: the observed RM of a polarized quasar or an FRB will contain contributions of all magneto-ionic medium along the line-of-sight. Thus, if we can isolate the RM of one component, we can derive its magnetic field strength, with constraints on the electron density. In Chapter 5, we estimate the RM contribution of FRB host galaxies and how it changes with redshift, galaxy type, the stellar mass of the galaxies, galaxy inclination, and on an FRB's offset from the center of the galaxy. With these predictions we can isolate the RM of the IGM and derive its magnetic field strength. To constrain an $\sigma_{\mathrm{RM,IGM}}$ of 2 rad m^{-2} with 95% confidence level we need to observe 95 000 FRBs at $z = 0.5$, while at $z = 2$ this number is significantly lower: 9 500 FRBs. In Chapter 6, I present the calculated RM of the intervening galaxies and how it changes with redshift. The derived probability density functions can be compared to those of observed samples, in order to calculate the magnetic field strength of the intervening galaxies, and indicate if the intervening galaxies are more likely to have a large-scale regular field or a random field.

The findings of the thesis are summarized in Chapter 7, where I also describe the future prospects in the field of galactic magnetism that will occur in the near future with the aid of future polarization surveys and new radio telescopes. Once the Square Kilometer Array starts operating in 2029, we expect the number of both lensing systems and quasars with intervening galaxies to dramatically increase (by 100 000 and 50 000 new systems respectively). Our results and way of analysis of the lensing systems demonstrate how this method can be applied to different galaxies. The number of observed polarized FRBs is also steadily increasing, and based on the results of this thesis, we would expect to measure the magnetic field strength of the IGM with a 2 rad m^{-2} precision in under 10 years.

"The story so far: In the beginning the Universe was created. This has made a lot of people very angry and been widely regarded as a bad move."

Douglas Adams, The Restaurant at the End of the Universe

Acknowledgements

I would like to thank everyone, who helped me during my PhD, as it is finally coming to an end.

I would like to thank my advisor Dr. Sui Ann Mao, for providing me with the interesting projects to work on, and for her help and expertise on polarization and magnetism.

I would like to thank my supervisor Prof. Dr. Michael Kramer for allowing me to work in the Fundamental Physics in Astronomy group, and for his comments and suggestions on my work.

I would also like to thank the members of my thesis advisory committee: Prof. Dr. Pavel Kroupa, for his suggestions, and Dr. Rainer Beck for his insights in magnetism and his suggestions and comments, and discussions about my work.

I would like to thank Prof. Dr. Jochen Dingfelder and Prof. Dr. Heiko Röglin for being part of my PhD comission.

I would like to thank Dr. Aritra Basu for his insights on magnetism and techniques in polarimetry, and help with my projects, especially with the project presented in Chapter 6. My thanks also goes to him for welcoming me in Tautenburg, along with the other staff and students in Tautenburg who welcomed me in my short but very pleasant stay.

I would like to thank my other collaborators on our project about FRB host galaxies, presented in Chapter 5: Dr. Laura Spitler, Dr. Ruediger Pakmor, and Dr. Charlie Walker for our meetings, and their inputs into the work and their help and comments on the paper draft.

My thanks also goes to past and present members of the magnetism group at the institute for our discussions on magnetism and polarization, Dr. Maja Kierdorf, Dr. Yik Ki (Jackie) Ma, Dr. Sarrvesh Sridhar, Jaswanth Subramanyam, Shilpa Ranchod, and Dr. Ancor Damas. I was especially happy when Jaswanth and Shilpa joined, so I was not the only PhD student in the magnetism group and we could share our experiences. I also enjoyed occasionally catching up with Maja at C'est la Vie. I also want to thank Jackie for his support in countless things, such as our hikes and trips, helping when I was very sick, listening to me venting. Although I was sad to see you leave, as Bonn was never the same since then.

I would like to thank my office mate, Shalini, even though we only shared an office in person for a relatively short while, it was nice to chat and vent about things, and I missed you since you left the institute. I would like to thank Weiwei for our chats when we would occasionally bump into each other. I would also like to thank Jonah for occasionally popping into my office, even when I was very wrapped up in work. And I would like to say thanks for our chats with Tasha, Tim, Joscha, Miquel, Jompoj, Madhuri, and also all the other students and members of the Fundi group. My thanks also goes to Dr. David Champion for giving me advice and helping me with postdoc applications. Also thanks again for Shilpa, Jaswanth and Ancor for hyping me up

before my interview.

I would like to thank Kira Kühn, Tuyet-Le Tran, and Silvia Schaenzler for helping with administrative issues. Special thanks to Tuyet-Le Tran and Silvia Schaenzler for quickly sorting out issues at the end of my PhD, and again for Prof. Dr. Michael Kramer for accommodating my stay for a bit longer, and helping me at the final stages of my thesis submission, and also for Dr. Ann Mao for helping me out when I struggled to sort this out.

I would like to thank my parents, József Kovács and Gyöngyi Molnár, and my brother, Róbert Kovács. It was always nice to have our weekly call, and also to play games online with my brother. I was looking forward to going home every time and spending time with all of you, sometimes wishing I could stay longer. While at home, my cat, Cili, always comforted me, up until her last moment, but I never stopped missing you.

I would like to thank my friends in Hungary, István, Zoli, and Máté, with who we still managed to keep an almost weekly online movie night since the pandemic. It was also helpful to talk and vent to Zoli about the process of going through a PhD. And my thanks also goes to my hungarian friends in astronomy, who reached out to me even though I disappeared for a while, and catching up when I was back at home.

Contents

List of Figures

List of Tables

Nomenclature

Frequently Used Symbols

B	Magnetic field strength
$B_{\parallel}$	Magnetic field strength along line of sight
$B_{\perp}$	Magnetic field strength perpendicular to line of sight
b_{offset}	FRB's projected distance from the center of host galaxy
f_{ion}	ionization fraction
h	vertical distance from the midplane of the galaxy
i	inclination
λ	Wavelength
M_*	stellar mass
n_e	electron density
N_e	electron column density
N_{H}	hydrogen column density
ν	Frequency
r	radial distance from center of galaxy
$r_{\mathrm{SF},99}$	Radius containing 99% of the star-forming gas of a galaxy
σ_{RM}	Faraday dispersion
S/N	Signal-to-noise ratio
τ_{dynamo}	Amplification time-scale of mean-field dynamo (e-folding time)
z	Redshift

Physical and Astrophysical Constants

Jansky	$1\,\mathrm{Jy}$	$=$	$10^{-23}\,\mathrm{erg\,s^{-1}\,cm^{-2}\,Hz^{-1}}$
Parsec	$1\,\mathrm{pc}$	$=$	$3.08568 \times 10^{18}\,\mathrm{cm}$

Frequently Used Acronyms

AGN	Active galactic nucleus
BIC	Bayesian information criterion
CASA	Common Astronomy Software Applications
CGM	Circumgalactic medium
CHIME	Canadian Hydrogen Intensity Mapping Experiment
DM	Dispersion measure
FRB	Fast radio burst
HST	Hubble Space Telescope
IGM	Intergalactic medium
IGMF	Intergalactic magnetic field
ISM	Interstellar medium
JWST	James Webb Space Telescope
ΛCDM	Lambda cold dark matter
MHD	Magneto-hydrodynamic
MOND	Modified Newtonian dynamics
MW	Milky Way
PA	Polarisation position angle
PI	Polarised intensity
PF	Polarization fraction
PDF	Probability density function
QSO	Quasi-stellar object - quasar
RFI	Radio frequency interference
RM	Rotation measure
RMS	root mean square
SAM	Semi-analytic model
SKA	Square Kilometre Array
SFR	Star formation rate
VLA	Very Large Array

Chapter 1

Introduction

In my thesis, I derive the magnetic field strength and structure of distant galaxies using polarimetric measurements and predict how its observables change with redshift[1] using a state-of-the-art cosmological magneto-hydrodynamic simulation. In this Section, I give an overview of magnetic fields in galaxies. First, I describe why magnetic fields in galaxies are important and all the processes they affect, then the theory explaining the mechanism responsible for generating and maintaining the magnetic fields in galaxies and what we know about them from the observations of nearby galaxies. As we cannot use the methods applied to nearby galaxies in distant galaxies, the current number of magnetic field strength measurements is limited. Thus, we need more observational constraints at high redshift for the theory. I introduce the methods we can use to measure magnetic fields in distant galaxies, which are also utilized in this thesis in Chapters 3 and 4. I also present different simulations of galaxies with magnetic fields, including the one used in the thesis in Chapters 5 and 6. Lastly, I describe why the magnetic field of the intergalactic medium is important and how it can be measured, which I further explore in Chapter 5.

Contents

[1] The light of distant galaxies is red shifted because they are seemingly moving away from us due to the expansion of the Universe - this effect is similar to the Doppler effect. Higher redshift means a galaxy is further away from us in space and time. If we explore how something changes with redshift, we in fact are looking at its evolution with time.

1.1 Why are magnetic fields in galaxies important?

There is evidence that many processes in galaxies, including gas dynamics (e.g. of molecular clouds, Planck Collaboration et al. 2016a), galactic outflows (Hanasz et al. 2013), the propagation of cosmic rays (Wiener et al. 2013), the star formation rate (SFR, Birnboim et al. 2015; Tabatabaei et al. 2017; Krumholz & Federrath 2019) and the initial mass function (IMF, Rees 1987; Sharda et al. 2020) are all affected by the magnetic field of galaxies (Beck 2015a). However, we still know little of its origin and evolution, even though the magnetic field (B) of galaxies can affect the evolution of galaxies (Beck et al. 2019).

We can see that galactic magnetic fields are dynamically important, if we compare their properties to other constituents of the interstellar matter in galaxies. It was found that the typical magnetic field energy density in galaxies ($\sim 10^{-11}$ erg cm^{-3}) is comparable to the energy densities of the other components of the interstellar matter: cosmic rays and the kinetic energy density of the turbulent neutral and warm ionized gas (see e.g. Heiles & Haverkorn 2012; Beck 2015a). This means that all these components are important and closely linked in the interstellar medium. Magnetic fields can act on charged particles through the Lorentz-force, but this can be passed on to the neutral phase of gas through ion-neutral collisions (Spitzer 1958; Ferrière 2001). Most of the interstellar medium is ionized highly enough (at least 0.01%, see Kulkarni & Heiles 1987) so that the neutral and ionized phase are coupled together, and to the magnetic field.

On large scales (e.g. galaxy-scales) magnetic fields can help in keeping the hydrostatic equilibrium of the interstellar matter (i.e. supports matter against gravitational potential, see Boulares & Cox 1990), and confine cosmic rays to the disk of the galaxies. Through the Parker instability (Parker 1966, a mechanism for forming dense clouds from an initially uniform medium), magnetic fields can also aid the development of new molecular clouds (Elmegreen 1982), which results in an increase in star formation in the galaxy. On small scales ($\lesssim 100$ pc) the magnetic fields can directly affect the turbulent motion of gas, for example in supernova remnants and their bubbles (Slavin & Cox 1992).

Galactic properties are linked to the magnetic field properties of galaxies. For example, galaxies with higher star formation rates show higher magnetic field strengths (e.g. M82 - Greaves et al. 2000). However, galaxies with violent star formation/very high star formation activity have weaker regular magnetic fields (see e.g. Tabatabaei et al. 2008 in M33, and Drzazga et al. 2011 in interacting galaxies), as it is disturbed by the increased turbulence. The magnetic field of galaxies is also connected to the magnetic field of the intergalactic medium (IGM), as galactic outflows can magnetize the IGM (Bertone et al. 2006), and the origin of the magnetic field of the IGM (IGMF) is still an open question.

1.2 Magnetic fields in nearby galaxies and the Milky Way

1.2.1 Observational methods

First we need to define the different magnetic field components (Beck et al. 2019). The magnetic field can be separated into regular (also called coherent) and turbulent field. While regular fields have a well defined direction in the telescope beam resulting in a finite average over the beam, turbulent fields have spatial reversals and their average over the beam vanishes. Furthermore, turbulent fields can be either isotropic (i.e. random, have the same spatial dispersion in all directions) or anisotropic (have a preferred a orientation, but reverse their direction in the telescope beam). By observing the synchrotron intensity of galaxies we can measure the total magnetic field strength (including all above components), and by measuring the polarized synchrotron emission we can derive the plane-of-the-sky component of the ordered field, which is the combination of regular and anisotropic turbulent field. We show an illustration of the regular, ordered, and random field in Fig. 1.1.

1.2.1.1 Synchrotron emission

An ordered large-scale magnetic field was first discovered by Beck (1982) in M31, and the polarized synchrotron emission and thus the magnetic field of many (~ 100) galaxies have been observed since then (e.g. Krause et al. 1989; Fletcher et al. 2004, 2011, and a list of galaxies with measured magnetic field strength can be found in Beck 2013 - with an updated version published in 2021 on `arXiv.org`). The Faraday rotation of the diffuse synchrotron radiation in external galaxies can also be used to estimate the line of sight component of the magnetic field (Zweibel & Heiles 1997), as the Faraday rotation effect causes the polarization angle of polarized light to change as a function of frequency, when the light passes through a magneto-ionic medium. This can be described as the line-of-sight integral of the electron density (n_e) and line-of-sight magnetic field ($B_{||}$), called the rotation measure (RM). Recently, the development of broadband radio polarimetric observations have improved on the earlier measurements of narrow band observations, and the new methods of RM synthesis and Stokes QU fitting was applied to derive their magnetic field strength and structure (see e.g. Mao et al. 2015, Kierdorf et al. 2020). Faraday rotation also causes another effect: internal Faraday dispersion, which occurs because emission from the turbulent cells within the beam suffer different amount of Faraday rotation, causing different polarization angles which causes the polarization vectors to cancel out (Sokoloff et al. 1998), and can be used to measure the random magnetic field.

1.2.1.2 Faraday rotation and polarization of background sources

Investigating the Faraday rotation of pulsars and extragalactic polarized sources can be used to determine the line-of-sight magnetic field strengths and direction in the Milky Way and external galaxies. Additionally, in the case of the Milky Way, pulsars can also be used. The polarized light of background quasars undergoes Faraday

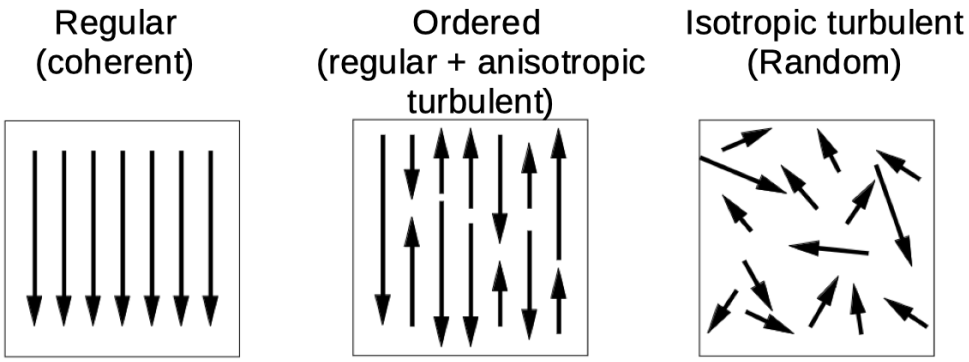

Figure 1.1: Illustration of the regular, ordered, and random field. The figure is based on a figure from Jaffe et al. (2010).

rotation as it passes through the magneto-ionic medium of the galaxies. If we have a large number of polarized background sources, we can investigate the structure and strength of the magnetic field in the intervening galaxy (see e.g. Mao et al. 2012b in the Large Magellanic Cloud with 300 sources). However, if the source number is low (e.g. $\sim$ 30) the magnetic field properties can not be derived (Gießübel et al. 2013 in M31).

1.2.1.3 Zeeman effect

The longitudinal Zeeman effect in optical spectrum lines and the HI absorption line in the radio (e.g. Verschuur 1968; Davies 2007 in the Milky Way) can be exploited to detect regular magnetic fields in the line-of-sight because due to the magnetic field, the line is splitted into two circularly polarized components. In the case of the transversal Zeeman effect, the magnetic field is perpendicular to the line-of-sight, and the original line and the components are all linearly polarized. Ogbodo et al. (2020) exploited the Zeeman effect in masers in the Milky Way to measure the Galactic magnetic field, and Li & Henning (2011) measured the magnetic field strength in molecular clouds in M31. However, this method can only measure strong magnetic fields in dense regions: $\sim$ 10 μG in the Milky Way, and mG strength in other galaxies (e.g. see Robishaw et al. (2008), who observed mega masers in five nearby ultraluminous galaxies).

1.2.1.4 Far-infrared polarized emission

The far-infrared thermal polarized emission of magnetically aligned dust grains can also be used to trace the ordered magnetic field in the plane of the sky (for a review, see Andersson et al. 2015). This method has been applied for dust clouds in the Milky Way (e.g. Tang et al. 2009) and in nearby galaxies using observations from the Stratospheric Observatory For Infrared Astronomy (SOFIA, Lopez-Rodriguez et al. (2022)). However, this method gives us the ordered magnetic field (i.e. the combination of regular and anisotropic turbulent field), which makes interpretation difficult. It is

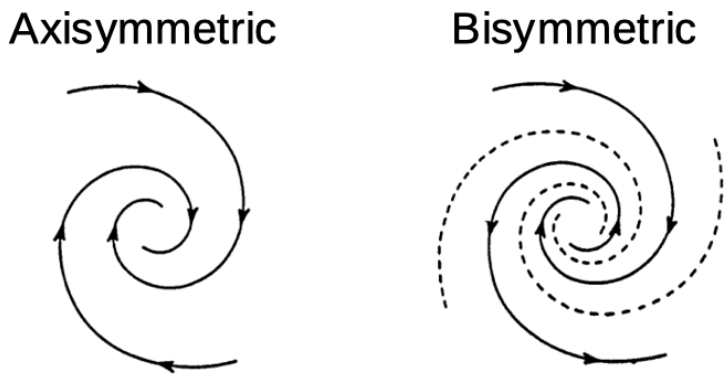

Figure 1.2: An illustration of an axisymmetric and a bisymmetric spiral structure (figure taken from Krause 1990).

also worth noting that the FIR might only trace the colder phases of the ISM, in contrast to the more general ISM traced by synchrotron emission (Borlaff et al. 2023).

1.2.2 Magnetic field properties of nearby galaxies

In nearby galaxies, we can see a regular large-scale magnetic field, with an additional spiral pattern in spiral galaxies that can follow the spiral arms, or the interarm regions (Beck & Wielebinski 2013; Beck 2015a). The average equipartition field strength (defined when the energy in magnetic fields and relativistic particles is equal) is 4 - 19 μG, and it increases towards the center of galaxies and in spiral arms (e.g. 20 - 30 μG in the case of M51 Fletcher et al. 2011).

Most galaxies have an axisymmetric field (e.g. M31, NGC 253, IC 342 - Fletcher et al. 2004; Heesen et al. 2009; Beck 2015b), and a few show a dominating bisymmetric field (e.g. M81 - Krause et al. 1989). Fig. 1.2 illustrates the two field structures.

Most observed galaxies have the same sign of magnetic field strength in the whole disk (i.e. either positive or negative). This can be seen separately for the different magnetic field components (azimuthal, radial, vertical). For example, M31 has a large-scale field in most of the galaxy, with a sign change only in its central 0.5 kpc region (Beck et al. 2020). If a galaxy has a large area with positive and another with negative magnetic field strength, it has a reversal in the large-scale magnetic field. Only a few galaxies show a reversal in the direction of the magnetic field in their disk, for example, the Milky Way (Brown et al. 2007) and NGC 4666 (Stein et al. 2019).

In edge-on galaxies, we can observe the halo magnetic field, which can have a quadrupole (i.e. even) symmetry with a vertical field with sign reversal above and below the disk (i.e. $B_{\rm vert}\ (-h) = -B_{\rm vert}\ (h)$, where h is the distance from the midplane, Beck et al. 2019), or odd symmetry with the same sign of vertical magnetic field ($B_{\rm vert}\ (-h) = B_{\rm vert}\ (h)$), showed in Fig. 1.3. Krause (2009) found that the halo field is "X-shaped" with a strong vertical component. Observations of edge-on galaxies in the CHANG-ES survey (Mora-Partiarroyo et al. 2019; Stein et al. 2019) reinforced this, which found

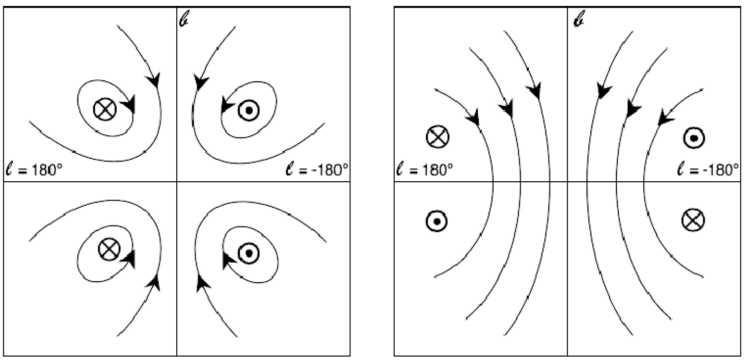

Figure 1.3: An illustration of a quadrupole (also called even or symmetric) and a dipole (also called odd or antisymmetric) halo magnetic field configuration (figure taken from Haverkorn & Heesen 2012). In this illustration, we look at the galaxy in edge-on view: the horizontal line shows the midplane of the disk, and the vertical line is perpendicular to the disk.

the halo field strength of NGC 4631 to be 4 μG.

1.3 The dynamo theory

The presence of large-scale magnetic fields in galaxies requires the existence of a seed field, an amplification process, and the ordering and sustaining of the large-scale field (Beck 2015a).

The origin of seed fields is either primordial, astrophysical or a combination of both. Primordial seed fields are generated in the early Universe before structure formation: in this case, the magnetic field of voids in the IGM would be the same as the original seed field (Durrer & Neronov 2013). An astrophysical origin would mean the seed field developed during or after structure formation. Some possibilities are the Weibel instability in colliding cosmological plasmas (Lazar et al. 2009, spontaneous magnetization of a plasma with a temperature anisotropy), by the Biermann mechanism in supernova explosions of the first stars (Hanayama et al. 2005, which results in magnetic fields in the shocked region between the bubble and ISM), and plasma instabilities in protogalaxies (Schlickeiser 2012).

After the development of a seed field, the magnetic field is amplified by turbulent gas motions from spiral shocks (Kim et al. 2006) and supernova explosions (Ferriere 1996) transforming kinetic energy into magnetic energy, called the small-scale dynamo. This can result in a turbulent field of μG strength in $< 10^8$ years (Beck et al. 2012).

The mean-field dynamo (Ruzmaikin et al. 1988; Shukurov 2005) is the mechanism that is most likely generating and sustaining the large-scale regular magnetic fields. After the amplification by the small-scale field, the turbulent field undergoes amplification and ordering on kpc scale by the α-Ω (mean-field) dynamo, which results in a regular field within a few 10^9 year (Arshakian et al. 2009). The turbulent motions

induced by supernova explosions cause the α effect, and the Ω effect is the differential rotation of the galaxy's disk. Galaxy disks can already form at a redshift of 2 - based on observations with high-resolution optical integral field spectroscopy of the ionized gas (Genzel et al. 2006).

From the dynamo theory, we expect different magnetic field configurations in spiral and elliptical galaxies, for example, only random and no large-scale magnetic field in the latter (as they do not have an overall rotation). Nevertheless, magnetic fields in elliptical galaxies have not been measured before (Arshakian et al. 2009; Beck et al. 2019), apart from in the CGM of large elliptical galaxies Shah & Seta (2021).

However, the predictions from the theory have limited observational evidence due to the low number of magnetic field measurements in distant galaxies. Thus, to truly constrain the amplification time scale and to see if it agrees with the theory (e.g. Arshakian et al. 2009), we need further observations of distant galaxies.

1.4 Magnetic fields in distant galaxies

1.4.1 Observations of magnetic fields in distant galaxies

It is crucial to obtain measurements of the magnetic field of distant galaxies, as with that, we can put constraints on the time scale of the mean-field dynamo theory (Shukurov 2005), which subsequently would have implications on galaxy evolution models. However, due to the capabilities of current radio facilities, the same methods we use for nearby galaxies cannot be applied to faint distant galaxies, as their synchrotron and FIR emission is weak, and the Zeeman-effect can only be used in high density regions with strong magnetic fields, so we must develop different techniques to measure the magnetic field strength in normal galaxies. Only a handful of measurements exist of high redshift galaxies: a few direct measurements (Mao et al. 2017; Kronberg et al. 1992; Wolfe et al. 2011), and some statistical detections (Kronberg et al. 2008; Bernet et al. 2008, 2013; Farnes et al. 2014, 2017). Many earlier studies only resulted in upper limits (e.g. using Zeeman splitting - Wolfe et al. 2011 or dust polarization - Geach et al. 2023). Most measurements exploit systems with intervening galaxies, but some could not precisely separate the RM due to the intervening galaxy from other contributors, which could also have contributions from the background source (Kronberg et al. 1992). Another method aimed at deriving the magnetic field of elliptical galaxies can only measure the magnetic field in the CGM (Seta et al. 2021), not in the inner parts of galaxies.

In the following subsections, I review two methods in detail (demonstrated by Bernet et al. 2008 and Mao et al. 2017), which both use intervening galaxies in front of polarized background quasars, and aim to isolate the RM due to the intervening galaxies, with no (or minimal) contribution from the background source, the IGM, and the Milky Way. We can use these methods to derive the regular field in the intervening galaxies, which can tell us about the time-scale of the mean-field dynamo. In the rest of this subsection, I review some of the previous measurements in more detail.

Kronberg et al. (1992) measured the magnetic field of an intervening galaxy at

$z = 0.395$ in front of an absorption line quasar by using the optical absorption spectrum of the system together with its Faraday rotation from radio polarimetric observations. They found the intervening galaxy's magnetic field to be bisymmetric (similar to M81), with a magnetic field strength of 1-4 μG. However, they could not completely rule out that the observed RM is (at least partly) from the background quasar. They argued that it is more likely to be associated with the intervening galaxy and not from the jet, the immediate environment, cluster, or a shell of gas surrounding the quasar host galaxy (e.g. there is no spectroscopic evidence of an absorber at the redshift of the quasar).

Wolfe et al. (2011) observed 3C 286 in radio, and found $B_{||} < 17$ μG in the intervening gas at $z = 0.692$ using the Zeeman-splitting technique. They could only give an upper limit, as even though they detect a small absorption feature in Stokes V, they note that it might be due to polarization leakage.

Elliptical galaxies lack a strong synchrotron emission, but Seta et al. (2021) proposed that these can be studied by exploiting the Laing-Garrington effect (asymmetry in the observed polarization fraction between radio galaxy jets) in the case of large elliptical galaxies with AGNs (i.e. radio galaxies). While the magnetic field in the CGM of the AGN's host galaxy can be measured, one drawback of this method is that the magnetic field in the inner parts of the host galaxy can not. Shah & Seta (2021) found in elliptical radio galaxies at redshifts from 0.01 to 0.46, that the small-scale field at scales smaller than 300 pc is between $0.1 - 2.75$ μG, which is a magnitude smaller compared to spiral galaxies.

Recently, Geach et al. (2023) observed the polarized FIR emission of a lensed galaxy at $z = 2.6$ with the Atacama Large Millimeter Array (ALMA) and measured an ordered magnetic field of < 500 μG of 5 kpc scale. The ordered field is a combination of the regular and anisotropic turbulent field; thus, it is challenging to evaluate if the magnetic field is due to the action of the mean-field dynamo. On the contrary, measuring the Faraday rotation of background quasars behind intervening and lensing galaxies can provide us with the regular magnetic field and a direct constraint on the e-folding time of the mean-field dynamo.

1.4.2 Background quasars with intervening galaxies method

One of the key studies that use a method with quasar absorption line systems, illustrated in Fig. 1.4, is Bernet et al. 2008, who found that galaxies at $z = 1.3$ already have magnetic fields with comparable strength to nearby galaxies: around 10 μG. They compared the Faraday rotation measure distributions of quasars with MgII absorption (which indicates intervening galaxies along the line of sight, called the target sample) to that of quasars with no absorption (called the control sample) in order to derive the magnetic field properties in the intervening galaxies statistically. Mg II absorption occurs when the light of the quasars passes through an intervening galaxy, and it can probe the ionized interstellar and circumgalactic matter of normal galaxies (with a wide range of luminosities) out to 100 kpc (Nielsen et al. 2013). Bernet et al. (2008) concluded that the difference in the distributions was significant (a Kolmogorov-

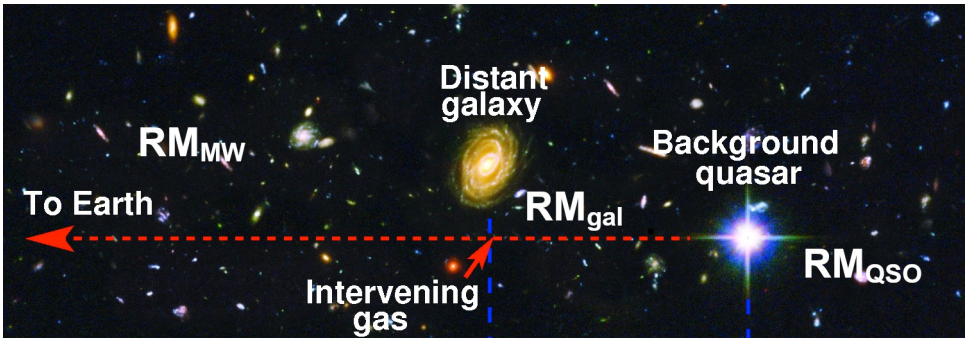

Figure 1.4: Illustration of the background quasar experiment: the light from the quasar (QSO) goes through an intervening galaxy, which shows up as absorption in its spectrum. The Rotation Measures (RM) of the QSO, the intervening galaxy, and the Milky Way (MW) add up. We need to use a large sample of such systems to derive the magnetic field of the intervening galaxy. The image was taken from (Pettini 2011)

Smirnov test rejected the possibility they come from the same distribution at 92.2%), and they observed a higher |RM| because of the intervening galaxies, not because of some intrinsic property of the quasars. Similarly, it has been found that the |RM| in systems with intervening galaxies is larger compared to systems without intervening galaxies in flat spectrum Mg II absorbers (Farnes et al. 2014) and Lyman limit systems (LLS, Farnes et al. 2017), suggesting the presence of a coherent magnetic field of 1.8 $\pm$ 0.4 μG, and $B \leq 2.4$ μG, respectively, which are consistent with each other, but lower than Bernet et al. (2008). Additionally, the |RM| of intervening galaxies was also found to change with impact parameter (Bernet et al. 2013), with larger |RM| for sightlines below an impact parameter of 50 kpc compared to ones above 50 kpc. A strong magnetic field of 10s of μG was found out to 50 kpc, suggesting the presence of magnetized winds associated with Mg II systems.

One main limitation of the studies using this method until now is that they did not consider that the RM of the background sources can change with redshift. Basu et al. (2018) found that quasars in the control sample need to be at a similar redshift as the target sample to isolate the RM of the intervening galaxies properly, and it is also better to compare RM instead of |RM| as the latter introduces a bias. This is because the increase in |RM| might be only due to increased dispersion in the RM of sightlines rather than because of larger RMs due large-scale field.

1.4.3 Lensing system method

Another method was demonstrated by Mao et al. (2017), who directly measured the magnetic field strength in the disk (4−17 μG) of a galaxy at $z = 0.439$ using broadband radio observations of a background quasar gravitationally lensed by a foreground galaxy, illustrated in Fig. 1.5. The method was first proposed by Narasimha & Chitre (2004), who suggested there is evidence of ~ 10 μG in galaxies between $z = 0.3$ and $z = 0.9$. However, they were using narrowband radio data to derive the RMs, which can

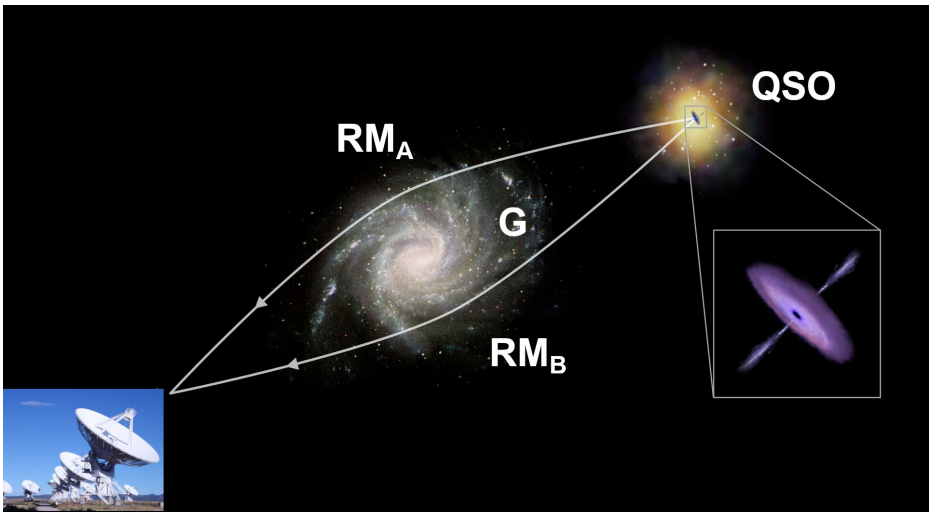

Figure 1.5: Illustration of the lensing system method: the light from the quasar (QSO) is gravitationally lensed into two or more images by the intervening (lensing) galaxy. The difference in the Rotation Measures (RM) of the two images (RM_A and RM_B) is caused by the magneto-ionic medium of the lensing galaxy, as the RM of the QSO, IGM, and the Milky Way are the same for both sightlines. This method provides direct measurement of the magnetic field in the lensing galaxy. Images were taken from ESA/ATG medialab and Shutterstock.

lead to incorrect RMs. Mao et al. (2017) investigated the differences between the two lensed images, which had impact parameters of a few kpc (2.6 and 6.5 kpc). Since lensing is achromatic and non-polarizing (Dyer & Shaver 1992), the intrinsic polarization properties of the quasar are the same in both images. The difference in Faraday rotation caused by the Milky Way in the two sightlines is negligible, as the image separation is only 1-2" or less, and the Milky Way RM foreground does not change significantly at such scales. Because of this, the RM differences can be attributed to the lensing galaxy's magneto-ionic medium. Mao et al. (2017) detected a coherent magnetic field with a strength of 4 - 17 μG, by assuming an axisymmetric or bisymmetric model for the magnetic field, and a typical electron density of a Milky Way-typed galaxy (with multiple assumptions, e.g. on ionization fraction). The small-scale magnetic field can be estimated from differential Faraday dispersion (i.e. the wavelength-dependent beam depolarization due to n_e and $B_{||}$ fluctuations in the beam), and the large-scale magnetic field from the differential Faraday rotation between the images. The structure of the magnetic field can be determined because we have multiple images that go through different parts of the galaxy.

1.4.4 Comparison of methods

Both of the methods described have their advantages and limitations. The method in Mao et al. (2017) is a direct estimation of the magnetic field, as we get information

about an individual galaxy, compared to the statistical method used by Bernet et al. (2008). On the other hand, there are not many systems we can use for the lensing method. To date, 200 systems with strong gravitational lensing by galaxies have been discovered, but for this method, they are required also to be bright and polarized. Additionally, we are only sensitive to high mass galaxies ($>10^{10}$ $M_{\odot}$) that can cause strong lensing with a high enough image separation for us to resolve the lensing images spatially. The method in Bernet et al. (2008) can be used for galaxies with lower mass, and at higher redshifts, there are more observable systems, and it probes larger impact parameters. The lensing method probes smaller impact parameters (<20 kpc), giving us information about the ISM in the lensing galaxy. The two different methods complement each other well.

1.5 Simulations of magnetic fields in galaxies

Apart from observations, simulations and models are often used to study the properties and evolution of galaxies. One of the simplest ones are simulations of isolated galaxies (see e.g Wang & Abel (2009); Pakmor & Springel (2013)). These simulations numerically solve the equations of ideal magneto-hydrodynamics (MHD, which couples Maxwell's equations with hydrodynamics) and follow the collapse of a protogalaxy and the formation and evolution of its disk. In Wang & Abel (2009), the side length of the simulation box is ∼200 kpc.

Nevertheless, we can study a larger number of galaxies and different galaxy types if we use simulations with cosmological models, which are done in significantly larger volumes (side length of ∼ 100 Mpc). Most of these models are based on the ΛCDM model, which consists of three main components: dark energy (Λ), cold dark matter, and ordinary matter. Dark matter and dark energy are essential parts of these simulations, as these make up 95% of the energy density, and baryons (e.g. stars and gas) only account for 5%. Even though we still do not know the true nature of dark matter and dark energy, and whether dark matter even exists, the models can make mostly adequate predictions (e.g. galaxy properties) based on their general characteristics (Vogelsberger et al. 2020). The shortcomings of this model, and alternatives are discussed in Subsection 1.5.2. More and more simulations also include magnetic fields, which was often left out in previous simulations (e.g. in Illustris - Vogelsberger et al. 2014), and is vital in helping us to understand the origin and evolution of magnetic fields in galaxies. While magneto-hydrodynamic (MHD) simulations are computationally expensive, dark matter only N-body simulations take less time to run. Thus semi-analytic models (SAM, Baugh 2006) use the combination of N-body simulations and analytic galaxy evolution models (e.g. gas accretion, gas cooling, star formation, and feedback processes) to calculate galaxy properties of a large sample of galaxies. The disadvantage of SAMs is that they are less self-consistent, and the gas component is not resolved (Vogelsberger et al. 2020).

In the rest of this subsection, I give details of three examples of recent, different types of simulations and models: cosmological MHD zoom-in simulations (Grand et al.

2017), SAM (Rodrigues et al. 2019), and a simulation of an isolated galaxy (Ntormousi et al. 2020). All these simulations contain many processes, including a dark matter halo, a gaseous disk, processes of star formation and supernova feedback, but Grand et al. (2017) and (Rodrigues et al. 2019) additionally also includes AGN feedback, galaxy mergers, and (Rodrigues et al. 2019) even contains photo-ionization feedback.

Individual galaxy simulations have the highest physical resolution (Ntormousi et al. 2020 with 20 pc), significantly better than cosmological zoom-in simulations (Grand et al. 2017 with $\sim$ 180 pc). However, the results from the SAM used by Rodrigues et al. (2019) are very different, and it only provides radial profiles of the strength of the radial and toroidal components of the coherent magnetic field instead.

All types of simulations and models reproduce the observed magnetic field strength or structure to some extent, but all have their limitations. Ntormousi et al. (2020) predicted a quadrupolar field in the disk and a dipolar field in the halo (same as the prediction from dynamo theory), but the magnetic field strength never reached equipartition. A typical magnetic field strength of $10 - 50\mu$G was reached at $z = 2 - 3$ in the Auriga galaxies, and the structure of the magnetic field is dominated by the azimuthal magnetic field (Pakmor et al. 2017, 2018). Rodrigues et al. (2019) found that both the B field strength and the density decline exponentially with the distance from the plane. A large fraction of their galaxy sample (60% with $\log(M_*/\mathrm{M}_\odot)$=9) has a very weak B field strength ($<$0.05 μG), much lower than what is seen in observations.

In summary, all types of simulations and models have their advantages. Still, zoom-ins of cosmological MHD simulations (or cosmological simulations with high physical resolutions) can provide relatively high-resolution results by considering many different physical processes. In my thesis I use the IllustrisTNG50 cosmological MHD simulation, which currently can provide us with the best magnetic field statistics on many galaxies compared to other simulations, due to its high physical resolution.

1.5.1 IllustrisTNG50

The IllustrisTNG is a state-of-the-art cosmological magnetohydrodynamical (MHD) simulation (Pillepich et al. 2018, Nelson et al. 2019a), which already has physical resolution comparable to zoom-in simulations. It consists of three simulation volumes: TNG300, TNG100, and TNG50, with side lengths of approximately 300, 100, and 50 Mpc, respectively. The smaller simulation volumes have larger physical resolutions, and the physical resolution also depends on the gas density, which results in higher resolutions and larger numbers of cells in high-density regions (e.g. galaxies), and lower resolutions and numbers of cells in the IGM. The average cell size of star-forming cells in the different simulation volumes is 715 pc in TNG300, 355 pc in TNG100, and 70 – 140 pc in TNG50 (Nelson et al. 2019a; Pillepich et al. 2019, Nelson et al. 2019b). While the simulation was run from $z = 12$ to $z = 0$, the magnetic field information in TNG50 was saved in 20 snapshots by the TNG team, restricting magnetic field studies to the redshifts associated with these snapshots. The simulation includes thousands of galaxies, also called 'subhalos': the friends-of-friends algorithm organizes the dark matter particles into halos, and the subfind algorithm separates the halos into subhalos.

The simulation has a wide variety of galaxies, such as normal spiral galaxies and giant ellipticals.

To study the magnetic field strength and structure of galaxies and calculate its observables, we require a simulation with the highest possible resolution, as based on observations of the Milky Way, both n_e and $B_{||}$ can change on small scales (a few 10s of pc) due to turbulence (Haverkorn et al. 2008). Currently, IllustrisTNG50 is the simulation containing the highest number of different galaxies with the highest physical resolution. This makes TNG50 uniquely capable of statistically studying the magnetic fields in a large sample of simulated galaxies, and it is better suited for this than other simulations. For example, even though the simulation of an isolated galaxy (e.g. see Ntormousi et al. 2020) has a physical resolution of 20 pc, which is better than TNG50, it does not account for galaxy interactions that also affect the magnetic field evolution of galaxies and for the diversity of galaxy properties in reality.

1.5.2 Simulations without dark matter

There has been evidence that some observations can not completely be explained by the standard model of cosmology (Kroupa 2015; Kroupa et al. 2023). One of these issues is the missing satellite problem. According to the dual dwarf galaxy theorem, there should be two populations of dwarf galaxies, primordial (dark matter only) and ones formed from tidal interactions. The former are distributed spherically. But compared to observations, the ΛCDM model predicts fewer satellite galaxies than we observe.

Recent results from the *James Webb Space Telescope* (see e.g. Ferreira et al. 2022 and Labbé et al. 2023) might challenge results from simulations based on the ΛCDM model, which predicts fewer massive galaxies beyond $z = 2$ due to hierarchical structure formation. On the contrary, the new observations show the presence of massive galaxies and a higher rate of galaxy disks at earlier cosmological times than expected from the ΛCDM model.

One alternative model to the ΛCDM model is Modified Newtonian dynamics (MOND), first proposed by Milgrom (1983). Instead of assuming the existence of invisible dark matter, this theory assumes that Newton's law of gravitation needs to be modified, motivated by the unexpectedly large rotational velocities at high radii in galaxies. The basis of MOND is that Newton's law has yet to be proved at extremely low accelerations (e.g. for stars in the outskirts of galaxies).

Recently, a modification of RAMSES (Teyssier 2002, an N-body and hydrodynamical code) to include MOND has been developed, the Phantom of RAMSES (Lüghausen et al. 2015; Nagesh et al. 2021). The first cosmological hydrodynamical simulation based on MOND was developed by Wittenburg et al. (2023). However, currently, there are no published cosmological MHD simulations (with magnetic fields) without dark matter. Thus I can only use the TNG50 simulation in my thesis, which assumes a ΛCDM model, to calculate the observables of magnetic fields in many galaxies. Still, in the future, it would be important to compare the results presented in this thesis to those derived in simulations without dark matter to see the differences in the predictions between the two models.

1.6 Magnetic field of the IGM

The magnetic field of the intergalactic medium (IGM) is affected by the magnetic field of galaxies through outflows (Bertone et al. 2006). However, the origin of the intergalactic magnetic field (IGMF) is still an open question in astrophysics (for a recent review, see Vazza et al. 2021). The two main possible scenarios are primordial and astrophysical. In the case of a primordial origin, magnetic fields developed due to processes that took place after the Big Bang. On the contrary, if the IGMF has an astrophysical origin, it is caused by processes due to galaxy evolution, such as feedback, AGNs, and star formation. In a primordial case, the IGMF would still be affected by the mentioned processes in filaments, but the magnetic fields in voids would be the same as the seed field of galaxies (Durrer & Neronov 2013).

There have been many measurements with different methods in the past (e.g. from CMB anisotropies - Planck Collaboration et al. 2016c, or measurements with the Low-Frequency Array, LOFAR - Carretti et al. 2023), however, most of these measure the magnetic field only in filaments. Thus, we have limited constraints on the low-density Universe. Nevertheless, a new technique using Fast radio bursts (FRBs) could provide better measurements of the IGMF.

FRBs are millisecond radio pulses of extragalactic origin (Lorimer et al. 2007; Petroff et al. 2022), and their emission can be polarized (Petroff et al. 2015). This makes a large sample of FRBs a good tool to measure the magnetic field of the IGM (Zheng et al. 2014; Akahori et al. 2016), illustrated in Fig. 1.6. The observed dispersion measure (DM, the integrated column density of free electrons between the FRB and the observer, manifesting in the dispersion of radio waves in time as a function of frequency) and RM of the FRBs consists of the contributions of its immediate environment, the host galaxy, the IGM, and the Milky Way. If we can isolate the contribution of the IGM from the other contributors, we can measure the magnetic field of the IGM. This technique would be better than other methods, as FRBs account for all the ionized baryons along the line of sight (Zheng et al. 2014; Akahori et al. 2016). This method is similar to using background quasars to measure the magnetic field of intervening galaxies, but we do not have a control sample in this case. The Milky Way RM contribution is well known from all-sky RM maps (Hutschenreuter et al. 2022), and models are available for the FRB's local environment. The host galaxy contribution also needs to be modeled, but as the host galaxies of FRBs can be very different from each other, we need to consider a wide range of models of galaxies with different properties. Alternatively, this method could also be used to probe the magnetic field of the host galaxies, if we assume the RM of the IGM based on different measurements.

1.7 Outline of thesis

In the first half of my thesis, I use the lensing system method to derive the magnetic field strength in two galaxies: the lensing systems of B1600+434 and B0218+357. In the second half of my thesis, I use the IllustrisTNG50 simulation to calculate the RM of galaxies in order to predict the observability of magnetic fields. I explore the

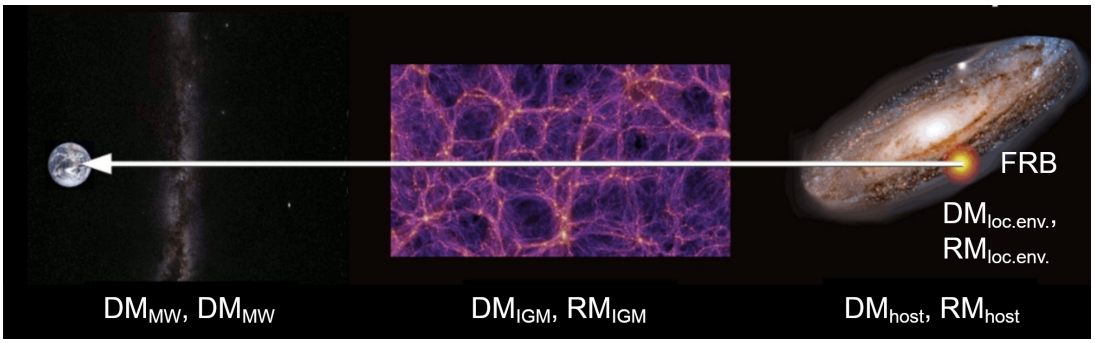

Figure 1.6: Illustration of using fast radio bursts (FRB) to measure the magnetic field of the IGM: the signal from the FRB experiences Faraday rotation from its immediate environment, its host galaxy, the IGM, and the Milky Way. Images were taken from the NASA Earth Polychromatic Imaging Camera Team, ESO/S. Brunier, the Millenium simulation (Springel et al. 2005) and Wikimedia Commons (David Dayag).

background quasar method by deriving the RM of the intervening galaxies, which will help us study the magnetic field of distant galaxies. Similarly, I calculate the RM of FRB host galaxies, which will help explore the magnetic field of the IGM.

Here follows a brief outline of the thesis:

- In Chapter 2, I give an overview of radio data calibration, imaging, methods in polarimetry, and an overview of using the simulation data of TNG50.
- In Chapter 3, I show the measurement of the magnetic field in the halo of a spiral galaxy at $z = 0.414$, which corresponds to a galaxy 4.4 Gyr ago.
- In Chapter 4, I show the measurement of the magnetic field in a galaxy at $z = 0.685$, which corresponds to a galaxy 6.3 Gyr ago.
- In Chapter 5, I show the RM and DM of FRB host galaxies from the IllustrisTNG50 simulation, and how these change with redshift and galaxy properties.
- In Chapter 6, I show the RM of intervening galaxies from the IllustrisTNG50 simulation, and how these change with redshift.
- In Chapter 7, I summarize the findings of the thesis.

Chapter 2

Methods

In this Chapter I describe the observational methods of radio polarimetry and how to work with the data of the IllustrisTNG simulation.

Contents

2.1 Radio polarimetric observations

In Chapters 3 and 4, I use polarimetric observations of lensing systems to derive the magnetic field in the lensing galaxies. In this section, I give an overview of the techniques of radio polarimetry that I used in those chapters, including radio data reduction, turning the radio data into radio imaging, and retrieving the polarization properties of the sources.

2.1.1 Radio synchrotron emission

Radio continuum emission consists of thermal and non-thermal emissions. Synchrotron emission is non-thermal and is emitted by relativistic electrons gyrating in a magnetic field due to the Lorentz Force, thus radio synchrotron emission can be used to study magnetic fields (the physics of synchrotron emission is discussed in detail in Rybicki & Lightman 1979; Govoni & Feretti 2004). An isotropic and homogeneous population of electrons has a power-law energy distribution, which can be written as

$$N(\varepsilon)\mathrm{d}\varepsilon \sim \varepsilon^{-\delta}\mathrm{d}\varepsilon, \tag{2.1}$$

where δ is the particle distribution index, and N (ε) is the energy number density of electrons with energies between ε and $\varepsilon + \mathrm{d}\varepsilon$.

The radio synchrotron emission spectrum is the sum of the emission spectra of separate electrons, and is also a power-law:

$$S_\nu = \nu^{-\alpha}, \tag{2.2}$$

where ν is the frequency, and α is the spectral index. The spectral index is 0.7 (Condon et al. 2002; Condon & Ransom 2016), and is connected to δ in the following way: $\alpha = \frac{\delta-1}{2}$.

However, the observed spectral index can depend on ν if the emission is not completely synchrotron radiation, and includes thermal radiation. In this case, it is defined as:

$$\alpha(\nu) = \frac{\partial \log S_\nu(\nu)}{\partial \log \nu}. \tag{2.3}$$

Synchrotron emission is linearly polarized, and the theoretical degree of intrinsic linear polarization is given by:

$$p_{\mathrm{int}} = \frac{3\delta + 3}{3\delta + 7}, \tag{2.4}$$

which, for typical values of α, is $\sim$ 78-80 %. In reality, the observed polarization fraction of most astrophysical sources is lower ($<$10 %) as their light becomes depolarized. This can be caused by a magnetic field that changes its direction either in the line-of-sight (causing Faraday depolarization, which is wavelength-dependent) or over the beam, leading to depolarization.

2.1.2 Radio interferometry

The wavelength range of radio astronomy can be defined by the atmospheric opacity on the short wavelength end (0.3 mm). The Earth's ionosphere reflects radio waves with wavelengths above 30 m, which can be considered the radio range's upper end. This is the radio window (in terms of frequencies, it is 10 MHz to 1THz) where it is possible to conduct observations on the ground.

Radio interferometry was developed because single telescopes have a limited angular resolution at radio wavelengths (0.3 mm - 30 m). The angular resolution (θ) of a telescope is given by

$$\theta \approx 1.22 \frac{\lambda}{D}, \tag{2.5}$$

where λ is the wavelength, and D is the diameter of the telescope. At present, the largest single-dish radio telescope is the five-hundred-meter aperture spherical radio telescope (FAST), which in reality corresponds to a 300-meter dish, as only part of the dish is "illuminated" by the receiver at a time. Even this telescope only has an angular resolution of 2.9 arcminutes at 21 cm. However, the angular resolution can be

increased by using an array of antennas called an interferometer. In this case, instead of the diameter of the antenna, the resolution is determined by the distance between the antennas, called the baseline (B), allowing us to reach angular resolution on the scale of arcseconds. For example, with the Very Large Array (VLA), we can achieve an angular resolution of 1.3" in its configuration of longest baselines at 15 – 30 cm (L-band, see Table 2.1 for other bands of the VLA).

The principles of radio astronomy are discussed in detail, for example, in Taylor et al. (1999); Thompson et al. (2017). Interferometers measure the interference pattern produced by multiple apertures (similar to the double slit experiment). In Fig. 2.1, we show a schematic illustration of a two-antenna interferometer. The signal from the astrophysical source reaches the antennas at different times; for example, in Fig. 2.1, it reaches Antenna A with a delay of τ compared to Antenna B. Correlators measure the spatial coherence function, also called the visibility function ($V(u,v)$), where u and v correspond to the coordinates in the antenna plane. Images of distant radio sources can be obtained from this, as the two-dimensional intensity distribution on the sky ($T(x,y)$, where x and y are the coordinates in the sky plane) can be derived by applying a two-dimensional Fourier transform to $V(u,v)$:

$$V(u,v) = \int\int T(x,y)e^{2\pi i(ux+vy)}\mathrm{d}x\mathrm{d}y \qquad \text{Fourier space,} \tag{2.6}$$

$$T(x,y) = \int\int V(u,v)e^{-2\pi i(ux+vy)}\mathrm{d}u\mathrm{d}v \qquad \text{Image space.} \tag{2.7}$$

If we have more antennas, we sample the $u-v$ plane better, resulting in a better image. This is described with the sampling function: $S(u,v)$, which is zero where no data has been taken. The largest baselines record information on small structures, and the smallest baselines record information on large-scale structures in the sky plane. Because of this, interferometers also have their limitations, as the smallest baseline determines the largest angular scale, making the array blind to emissions on scales larger than this scale.

In my thesis, I use data from the VLA. It has 28 25-meter dishes (of which 27 are operating at once), which can be moved into different configurations with different baselines and resolutions. All the data in this thesis was taken in A configuration, which has the highest angular resolution, and the telescopes are moved the furthest away from each other compared to the other configurations. In this case, the maximal baseline (B_{max}) is 36.4 km, and the minimal baseline (B_{min}) is 0.68 km.

2.1.3 Radio data reduction

In this section, I describe the procedure of flagging and calibrating radio interferometric data. Although the radio band is wide, I will concentrate on the 1 - 8 GHz frequency range (L-, S-, and C-bands), as the observations that I use in Chapters 3 and 4 were taken in these bands. During calibration, we derive a series of scaling factors and apply them to the data. When we proceed to the next calibration step, we must give the calibration tables derived from the previous steps. The Common Astronomy

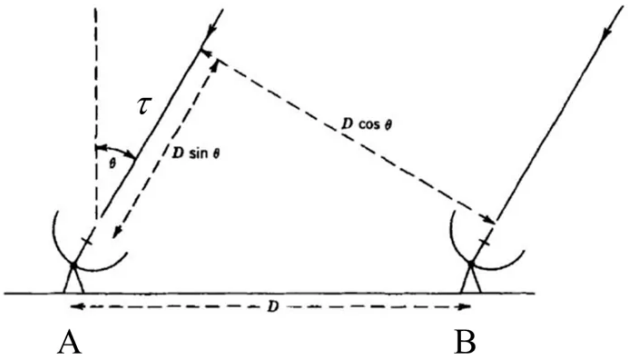

Figure 2.1: A schematic illustration of a two-antenna interferometer. Image credits: Thompson et al. (2017).

Table 2.1: Radio bands at 1-8 GHz (defined by the Institute of Electrical and Electronics Engineers - IEEE). The VLA's resolution and max angular scale in A configuration are also listed.

Band	Wavelength range (cm)	Frequency range (GHz)	Angular resolution (")	Max angular scale (")
L	15 - 30	1 - 2	1.3	36
S	7.5 - 15	2 - 4	0.65	18
C	3.7 - 7.5	4 - 8	0.33	8.9

Software Applications (CASA, McMullin et al. 2007; CASA Team et al. 2022) was used for the data calibration.

2.1.3.1 Flagging

Radio Frequency Interferences (RFI) can introduce bad data in our science observations, which can be intermittent or continuous. They have either an external or internal origin, and most external RFIs are caused by satellites. Some of the strongest RFIs in L-band are due to aircraft navigation and GPS. In S-band, strong RFIs are caused by the satellite downlinks and Sirius/XM Satellite radio. Some RFI sources in C-band are microwave links and satellite downlinks. Only a few frequency ranges at 1-8 GHz are protected for radio astronomy: 1400-1427 MHz, 1660.6-1670.0 MHz, 2690-2700 MHz, and 4990-5000 MHz.

In the procedure of flagging, we need to flag bad channels, antennas, time intervals, and baselines. The result of radio imaging is often worse if we use bad-quality data than if we use less data, which is why ensuring the flagging is done well is essential.

Usually, we have to flag the first and last few channels of each spectral window, as the edges of each spectral window have lower sensitivity. Theoretically, we could

correct this via bandpass calibration, but the low S/N data can cause wrong calibration solutions. We also flag the initial samples of each scan (i.e. quack flagging) because the array needs some time to settle down after the start of a scan.

We can also plot the amplitude as a function of frequency and time to inspect the data further and manually flag insufficient data. This is an important step, but it can be very time-consuming, and RFIs can affect many different times and baselines. To deal with this, multiple algorithms were designed to flag bad data automatically. We must be careful while using these methods to avoid accidentally flagging good data. First, we should manually flag the most prominent RFIs and then use one (or both) of the automatic flagging algorithms:

- The TFCrop (Time-Frequency Crop, first described in the NCRA Technical Report 202, Oct 2003) algorithm can detect outliers in the time-frequency plane in un-calibrated data, best for strong, narrowband RFI.

- The RFlag algorithm (first described in the Astronomical Image Processing System Cookbook[1] subsection E.5) can detect outliers by iterating through the data in chunks of time with a sliding window, and calculating the deviation of local root-mean-square noise (RMS) from the median RMS. This algorithm has to be run on calibrated data.

2.1.3.2 Calibration

The steps of calibrating visibilities using CASA:

- Antenna position correction: As the complex visibility ($V(u, v)$) depends on the separation of two antennas, it is important to know the positions of the antennas precisely. Incorrect antenna positions would cause errors in the projected baseline and, subsequently, in the image. For example, NRAO monitors the positions of the VLA antennas, and we can access this database from CASA using the task *gencal* Sometimes, the updated positions are added later than the observation was made, and the measurement files have the old positions, making it essential to check the database before calibration.

- Initial flux density scaling: First, we must set a flux density model for the amplitude calibrator. Some sources have periodically updated models (e. g., Perley and Butler 2013) and can also be accessed in CASA using the task *setjy*.

- Initial phase calibration: We average over the variations of phase with time in the bandpass using the task *gaincal*. Usually, only the central 10% of channels is used in this calibration step. A reference antenna has to be chosen from this step onward, which should be near the center of the array and should not have many problems and flagged data.

[1]Maintained by the National Radio Astronomy Observatory, http://www.aips.nrao.edu/cook.html

- Delay calibration: In this step, we remove the differences caused by the different path lengths to different antennas using task *gaincal* and solve for the relative delay of each antenna compared to the reference antenna. The delay is usually less than four nanoseconds.

- Bandpass calibration: We have to do bandpass calibration to compensate for changes in the gain as a function of frequency. The time variations of these changes are usually very small. We need a strong calibrator source with a flat spectrum over the frequency range, but it does not need to be a point source. The complex bandpass is B_i, and in CASA, we use the task *bandpass* and average over all times and scans.

- Gain calibration: We use the *gaincal* task to derive the complex antenna gains for the amplitude and the phase.

- Scaling amplitude gains: Finally, we transfer the flux scale we determined to the other calibrator sources using the task *fluxscale*.

After these steps, we arrive at visibilities that we can turn into total intensity radio images. We note that we need additional steps for polarimetry calibration, described in Section 2.1.5.2.

2.1.4 Imaging

The Fourier inversion of the visibilities results in the dirty image (I_D), which is the true intensity distribution (I) convolved with the synthesized beam (the Fourier transform of the sampling function). To reconstruct I, we need to do deconvolution. In CASA, this is done with the task *clean*, an algorithm first developed by Högbom (1974). The Hogbom deconvolver is optimal for fields of isolated point sources but unsuitable for extended emission. On the other hand, the Clark deconvolver is faster for large images but can have errors if there are bright sources spread over a wide field of view.

We often need to weigh the visibilities at different positions in the $u - v$ plane differently due to the non-uniformity of the sampling function, which usually results in oversampling of the inner regions of the $u - v$ plane (corresponding to antennas with short baselines). How we weigh the visibilities is important in the resulting image's angular resolution and sensitivity. There are three main methods:

- Natural weighting: The visibilities are not weighted before gridding, and scales with more baselines will dominate the image (e.g. short-baselines and large-scales). It provides better sensitivity (highest SNR) but the poorest angular resolution.

- Uniform weighting: Each scale in the image-plane will have the same weight. This provides better resolution but poorer sensitivity compared to natural weighting.

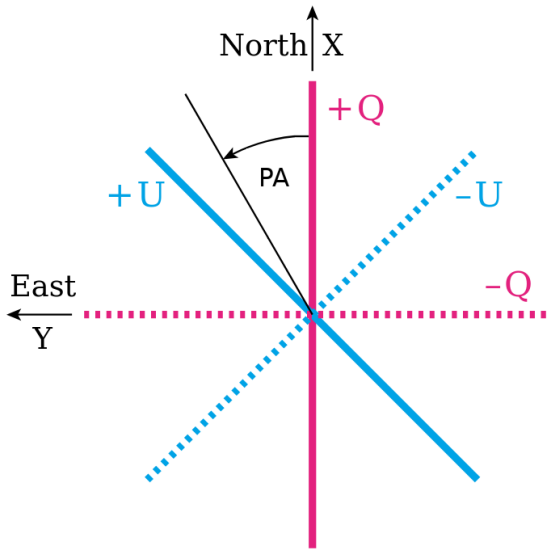

Figure 2.2: The Stokes Q and U parameters defined by the International Astronomical Union Contopoulos & Jappel (1974). Illustration taken from NASA/LAMBDA (https://lambda.gsfc.nasa.gov/product/about/pol_convention.html).

- Briggs weighting (Briggs 1995a): It is a compromise between the two weightings above and tries to have both good resolution and sensitivity. It is parametrized by the robust parameter (R), which has a range of [-2,2]. This allows us to manually pick a trade-off between resolution and sensitivity, which depends on the dataset. A few specific values of the robust parameter:

  $R = 0$ is a good trade-off between resolution and sensitivity,

  $R = -2$ corresponds to uniform weighting,

  $R = 2$ corresponds to natural weighting.

The radio images presented in Chapters 3 and 4 were produced with the Clark deconvolver, and Briggs weighting with a robust parameter of -2, to achieve high resolution to separate the lensed images.

2.1.5 Polarimetry

2.1.5.1 Polarization properties

The Stokes parameters (I, Q, U, V) were defined by Stokes (1851) and describe the polarization properties of electromagnetic radiation. The standard definition by the International Astronomical Union (Contopoulos & Jappel 1974, and also summarized in Hamaker & Bregman 1996) is shown in Fig. 2.2, with the local x-axis pointing North and the local y-axis pointing East, and the local z-axis pointing inwards to the observer. Stokes I is the total intensity (polarized and unpolarized), Stokes Q and U

give information about the strength and direction of linear polarization, and Stokes V of the circular polarization.

The Stokes parameters defined as on a linearly and a circularly polarized basis:

$$\begin{aligned} I &= E_X^2 + E_Y^2 & &= E_R^2 + E_L^2 \\ Q &= E_X^2 - E_Y^2 & &= 2E_R^2 E_L^2 \cos(\delta_{RL}) \\ U &= 2E_X^2 E_Y^2 \cos(\delta_{XY}) & &= 2E_R^2 E_L^2 \sin(\delta_{RL}) \\ V &= 2E_X^2 E_Y^2 \sin(\delta_{XY}) & &= E_R^2 - E_L^2 \end{aligned} \tag{2.8}$$

Some telescopes with linear feed types are MeerKAT, ASKAP, and ATCA, while VLA has a circular feed. The advantage of telescopes with circular feed is that calibration is easier for imaging, as they need a circularly unpolarized source for the calibration, and most continuum sources have close to 0% circular polarization.

If the radiation is fully polarized, $I^2 = Q^2 + U^2 + V^2$. but we rarely see astronomical sources with 100% polarization, apart from pulsars (Lorimer & Kramer 2004).

The polarized properties of radiation can be described with the Stokes parameters as listed below. The linear polarised intensity (PI) can be given as:

$$\mathrm{PI} = \sqrt{Q^2 + U^2}, \tag{2.9}$$

the fraction of linear polarisation (PF) is given by:

$$\mathrm{PF} = \frac{\mathrm{PI}}{I}, \tag{2.10}$$

and the polarisation angle (PA) is:

$$\mathrm{PA} = 0.5 \arctan \frac{U}{Q}. \tag{2.11}$$

Finally, the complex polarization (the linear polarization described as complex vector) is:

$$P = Q + iU. \tag{2.12}$$

2.1.5.2 Polarimetry calibration

Apart from the calibration steps listed in Section 2.1.3.2, to obtain radio images that we can use for polarization studies, we also need to do the following calibration steps:

- Setting polarization model: The polarization calibrator needs to be a source with a well-known polarization angle and degree as a function of frequency. We use the task *setjy* and give the parameters of a polynomial that describes the dependence of the polarization angle and degree as a function of frequency.
- Solving for Cross-hand delays: We use task *gaincal* to calibrate the cross-hand correlations (RL and LR), in order to get accurate Stokes Q and U measurements. If we only need Stokes I and V, it would be sufficient to only calibrate RR and LL.

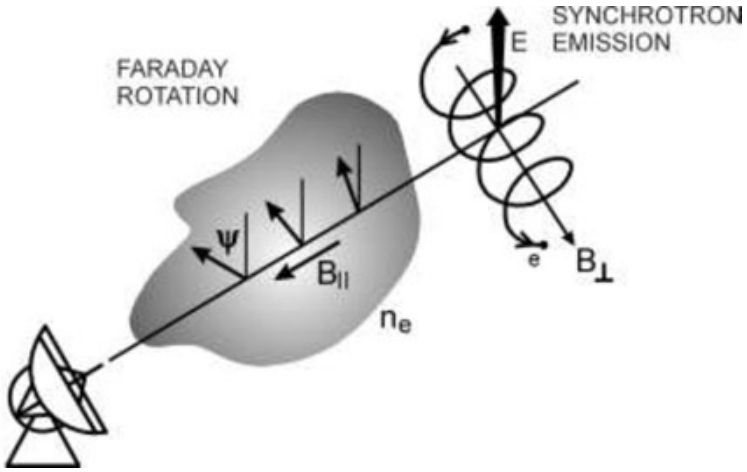

Figure 2.3: The illustration of Faraday rotation. The electromagnetic (synchrotron) radiation goes through a magneto-ionic medium with electron density n_e and a line of sight magnetic field $B_{||}$. The polarization angle changes due to $B_{||}$. Figure from Beck (2013).

- Solving for leakage terms: Some of the right-circular polarization can show up in the left channel, and some of the left-circular polarization can end up in the right channel. To correct this, we need to observe an unpolarized point source. In CASA, we use the task *polcal* to solve for the leakages ('D') on a per channel basis, averaging over all time and scans.
- Solving for the R-L polarization angle: We use *polcal* to set the R-L phase to result in the polarization angle we set in the first step of polarization calibration.
- Scaling amplitude gains: Finally, we transfer the flux scale we determined to the other calibrator sources using the task *fluxscale*.

2.1.5.3 Faraday rotation

Faraday rotation was discovered by Michael Faraday in 1845. He found that the angle of polarization changes when there is a magnetic field in the same orientation (the same or opposite direction) as the path of the light.

The traditional way of determining RM is to plot the observed polarisation angle (PA) as a function of the square of the observing wavelength (λ^2) and perform a least-squares fit:

$$\mathrm{RM} = \frac{\mathrm{dPA}(\lambda^2)}{\mathrm{d}\lambda^2} \tag{2.13}$$

This method was used because the available data were narrowband, being very limited in λ^2 space. However, this can lead to incorrect RMs in the case of multiple polarized emissions with different RMs in one line of sight, regions that both emit synchrotron radiation and cause Faraday rotation, faint sources with high rotation measure, or

bandwidth depolarization. Fitting a simple linear fit to PA as a function of λ^2 is also problematic because of the $n\pi$ ambiguity if we only have data at two frequencies. As PA is measured over a range of 180° , we can not distinguish between PA and PA+$n\pi$, which leads to multiple different RM values.

The physical definition of rotation measure (Faraday depth):

$$\mathrm{RM} = 0.81 \int_{\mathrm{source}}^{\mathrm{observer}} n_e B_{||} \mathrm{d}l, \tag{2.14}$$

where n_e is the electron density, and $B_{||}$ is the line-of-sight magnetic field. For magnetic fields directed towards (away from) the observer, RM is defined as positive (negative) (Ferrière et al. 2021).

2.1.5.4 RM synthesis

To overcome the issues of simply fitting PA versus λ^2 (e.g. nπ ambiguity, and not being able to resolve multiple polarized components), RM synthesis was developed by Burn (1966), implemented by Brentjens & de Bruyn (2005), and further discussed in Heald (2009). As this method needs the measurement of the polarization at multiple wavelengths, it could only begin to be used when broadband radio observations became available.

Burn (1966) introduced the complex Faraday dispersion function ($F(\phi)$), which describes the intrinsic polarized flux as a function of the Faraday depth (ϕ). Burn (1966) defined it through the complex polarization ($P(\lambda^2)$) function:

$$P(\lambda^2) = \int_{-\infty}^{\infty} F(\phi) e^{2i\phi\lambda^2} d\phi. \tag{2.15}$$

The two functions ($F(\phi)$ and $P(\lambda^2)$) can be transformed into each other by the Fourier transformation, so we can retrieve $F(\phi)$ described with observed quantities:

$$F(\phi) = \int_{-\infty}^{\infty} P(\lambda^2) e^{-2i\phi\lambda^2} d\lambda^2. \tag{2.16}$$

However, an issue of this method is that we can not observe at $\lambda^2 < 0$, and also can not observe at all λ^2. To overcome this, Brentjens & de Bruyn (2005) implemented a window function ($W(\lambda^2)$), which is 0 at all λ^2 that are not sampled by the telescope. Then, the observed polarized emission is the product of the window function and $P(\lambda^2)$, and the reconstructed Faraday dispersion function is the convolution of the Faraday dispersion function and the rotation measure spread function (RMSF). The RMSF is defined in the following way:

$$R(\phi) = K \int_{-\infty}^{\infty} W(\lambda^2) e^{-2i\phi(\lambda^2 - \lambda_0^2)} d\lambda^2, \tag{2.17}$$

where K is the inverse of the integral over ($W(\lambda^2)$). Deconvolution schemes must be applied to recover the true Faraday dispersion function (similar to interferometry imaging). The Faraday dispersion function will peak at the Faraday depth corresponding

to the RM of the source. In the case of multiple emissions at different Faraday depths, $F(\phi)$ will have multiple peaks. We note that the Faraday depth derived from RM synthesis is only equal to the rotation measure from Eq. 2.13 if there is only one source along the line of sight and there is no beam depolarization (Brentjens & de Bruyn 2005).

RM synthesis has three main parameters that determine what we will be able to observe with a given observation setup:

- The resolution in Faraday depth space depends on the bandwidth ($\Delta\lambda^2 = \Delta\lambda^2_{\rm max} - \Delta\lambda^2_{\rm min}$):

$$\delta\phi = \frac{2\sqrt{3}}{\Delta\lambda^2}. \tag{2.18}$$

  This is the same as the full-width half maximum of the RMSF, and determines if we can resolve two Faraday depth peaks close by in Faraday space. In the case of our observations of 1–8 GHz, this is 39 rad m^{-2}.

- The largest scale in Faraday depth space, which we are sensitive to, depends on the shortest wavelength ($\lambda^2_{\rm min}$) of our observations:

$$\text{max} - \text{scale} = \frac{\pi}{\lambda^2_{\rm min}}. \tag{2.19}$$

  Sources that are both emitting radiation and causing Faraday rotation will appear as extended structures in $F(\phi)$ (Faraday thick), but we will not be able to recover ones with a scale larger than the max-scale described above. In our observations, this is 2234 rad m^{-2}.

- The maximum observable Faraday depth depends on the channel width ($\delta\lambda^2$, i.e. depends on the spectral resolution of the telescope):

$$||\phi_{\rm max}|| = \frac{\sqrt{3}}{\delta\lambda^2}, \tag{2.20}$$

  which in case of 16 MHz channels is 616 rad m^{-2} at 1 GHz and 307 000 rad m^{-2} at 8 GHz.

In the thesis, I used the CIRADA-Tools package (Purcell et al. 2020) to perform RM synthesis on the data.

2.1.5.5 Stokes QU fitting

The method of Stokes QU fitting was first used by Farnsworth et al. (2011) and O'Sullivan et al. (2012). They fitted the Stokes Q and U (or the fractional values $q = Q/I$ and $u = U/I$) as a function of λ^2. They define different models containing different synchrotron emitting and Faraday rotating components and find the best model by least-squares fitting to derive the polarization properties of these components. This method might have advantages over RM synthesis, as Farnsworth et al. (2011)

found that RM synthesis often gives worse results in the case of multiple interfering RM components compared to Stokes QU fitting.

In the thesis, I use the following models to fit the Stokes QU data:

- Single Faraday thin: In the simplest case, there is a synchrotron emitting region and an external Faraday rotating screen in front of it. We assume the Faraday screens have homogeneous thermal electron density and a uniform magnetic field configuration. It is also possible to have multiple Faraday rotating screens in the line-of-sight, as the RM caused by them simply adds up. The complex polarization of a Faraday thin component can be written as:

$$P = p_0 e^{2i(\phi_0 + \mathrm{RM}\lambda^2)} \tag{2.21}$$

- Double Faraday thin: There are two different synchrotron emitting regions in the background with different polarization fractions and intrinsic RM, and one or multiple external Faraday rotating screens in front of them.

$$P = p_{0,1} e^{2i(\phi_{0,1} + \mathrm{RM}_1\lambda^2)} + p_{0,2} e^{2i(\phi_{0,2} + \mathrm{RM}_2\lambda^2)} \tag{2.22}$$

- Single Burn slab (Burn 1966) with foreground: The synchrotron emitting region also causes Faraday rotation. We assume that this volume's magnetic field and thermal electron density are homogeneous. This means the emission from the far side (further away in the line-of-sight from the observer) of the source experiences more Faraday rotation compared to emission from the near side of the source, as it goes through a longer path in the Faraday rotating media. We also consider that the source can have one or multiple external Faraday screens.

$$P = p_0 \frac{\sin(\mathrm{RM}\lambda^2)}{\mathrm{RM}\lambda^2} e^{2i[\phi_0 + (\frac{1}{2}\mathrm{RM} + \mathrm{RM_{fg}})\lambda^2]} \tag{2.23}$$

- Double Burn slab with foreground: There are two synchrotron emitting regions that cause Faraday rotation, and there are one or multiple external Faraday screens in front of them.

$$P = p_{0,1} \frac{\sin(\mathrm{RM}_1\lambda^2)}{\mathrm{RM}_1\lambda^2} e^{2i[\phi_{0,1} + (\frac{1}{2}\mathrm{RM}_1 + \mathrm{RM_{fg}})\lambda^2]} + p_{0,2} \frac{\sin(\mathrm{RM}_2\lambda^2)}{\mathrm{RM}_2\lambda^2} e^{2i[\phi_{0,2} + (\frac{1}{2}\mathrm{RM}_2 + \mathrm{RM_{fg}})\lambda^2]} \tag{2.24}$$

- Single external dispersion with foreground: There is one synchrotron emitting region with an external Faraday screen which has spatial fluctuations in the electron density and magnetic field configuration due to turbulence, which, additionally to Faraday rotation, also causes Faraday dispersion (σ_{RM}).

$$P = p_0 e^{-2\sigma_{\mathrm{RM}}^2\lambda^4} e^{2i(\phi_0 + \mathrm{RM}\lambda^2)} \tag{2.25}$$

- Double external dispersion with foreground: There are two synchrotron emitting regions with an external Faraday screen that also causes Faraday dispersion.

$$P = p_{0,1} e^{-2\sigma_{\mathrm{RM},1}^2\lambda^4} e^{2i(\phi_{0,1} + \mathrm{RM}_1\lambda^2)} + p_{0,2} e^{-2\sigma_{\mathrm{RM},2}^2\lambda^4} e^{2i(\phi_{0,2} + \mathrm{RM}_2\lambda^2)} \tag{2.26}$$

- Internal dispersion: If the synchrotron emitting and Faraday rotating medium in the Burn slab model is turbulent, we can describe it with this model.

$$P = p_0 e^{(2i\phi_0)}(1 - e^{-s})/s \tag{2.27}$$

$$s = 2\lambda^4 \sigma_{\mathrm{RM}^2} - i\mathrm{RM}\lambda^2 \tag{2.28}$$

We choose the best-fitted model based on which one has the lowest Bayesian information criterion (BIC), which is defined as:

$$\mathrm{BIC} = k\ln(n) - 2\ln(\hat{L}), \tag{2.29}$$

where n is the number of data points, k is the number of parameters in the model, and $\hat{L}$ is the maximized value of the likelihood function of the model. Overfitting (few data points but many model parameters) results in a larger BIC.

2.2 Working with TNG50 simulation data

In Chapters 5 and 6, I use the IllustrisTNG50 simulation to calculate the rotation measure of FRB host galaxies and intervening galaxies, with the aim of predicting the observables of the intergalactic magnetic field and the magnetic field of high redshift galaxies, respectively. In this section, I give an overview on the data structure of the simulation, how we convert units, and calculate integrals (for example, to get the rotation measure of galaxies).

All of the TNG simulations assume a cosmology consistent with the results from the Planck Collaboration (Planck Collaboration et al. 2016b, $\Omega_{\Lambda,0} = 0.6911$, $\Omega_{\mathrm{m},0} = 0.3089$, $\Omega_{\mathrm{b},0} = 0.0486$, $\sigma_8 = 0.8159$, $n_s = 0.9667$, and $h = 0.6774$), with Newtonian self-gravity solved in an expanding Universe (Nelson et al. 2019a).

2.2.1 Structure of TNG50 data

IllustrisTNG data is publicly available (Nelson et al. 2019a) and consists of snapshot data and group catalogs.

The snapshot data are available for 100 simulation snapshots, between $z = 0$ and $z = 20$. However, the magnetic field information was saved for only 20 of these snapshots by the IllustrisTNG team (between $z = 0$ and $z = 12$). In my thesis, I only use these snapshots. In the snapshot data, we can access each gas, star, dark matter, and black hole particle, which have information on their 3D position, mass, velocity, etc. The most important particles for my work are the gas particles, as each has the 3D magnetic field vector, the mass density, and the electron abundance (e_{ab}, fractional electron number density with respect to the total hydrogen number density) of the gas cell saved.

Each snapshot has a group catalog consisting of halos (i.e., galaxy groups) and subhalos (individual galaxies). The galaxies are divided into groups with a friend-of-friends algorithm (FoF, Davis et al. 1985) run on the dark matter particles, and each

group has to consist of a minimum of 32 particles. The gas and other types of particles are sorted to the same halo, as the dark matter particle closest to them is assigned to. The most massive galaxy of a group is considered the primary subhalo, and the others are satellite galaxies. The table of halos contains the IDs of subhalos assigned to them (including the ID of the primary halo), the number of particles associated with the halo, the total mass, SFR, and different definitions of radii. Locally overdense, self-bound particle groups of at least 20 particles are defined by the Subfind algorithm as subhalos (Springel et al. 2001). Gravitationally unbound particles are removed by the Subfind algorithm, which can result in halos without any subhalos. This table contains the different properties of the subhalos, for example, their 3D position, stellar mass, gas mass, SFR, and different definitions of radii.

The data can be accessed via python scripts using the official python package and example scripts on the project website[2]. I also had access to the private (not publicly available) python package of 'arepo-snap-util' developed by Federico Marinacci (and Ruediger Pakmor) to analyze simulation data run with the moving-mesh code AREPO (Springel et al. 2019, which was also used to run IllustrisTNG). These scripts can be used, for example, to load in snapshot and catalog data corresponding to specific galaxy IDs, and the latter package also has a function that can calculate an integral in the snapshot data.

In this thesis, I used the gas particles from the snapshot data to calculate rotation measure (RM), dispersion measure (DM), and magnetic field strength maps. I also use the group catalogs to access the global properties (e.g. mass, SFR) of the selected galaxies.

2.2.2 Conversion of the simulation units into physical unity

Following the recommended procedures for the TNG data (Nelson et al. 2019a), we convert from comoving units (coordinates of cells, gas density, magnetic field strength, masses) to physical units using the scale factor (a) and the Hubble parameter (h). We can obtain kpc from comoving kpc (ckpc) via:

$$1\,\mathrm{kpc} = 1\,\mathrm{ckpc}/h \cdot a. \tag{2.30}$$

After this, the density and magnetic field are converted to CGS units from the physical units in the simulation:

$$\rho[\mathrm{g\,cm^{-3}}] = 6.8 \cdot 10^{-22} \rho_{\mathrm{sim}}[10^{10} M_{\odot}\,\mathrm{kpc}^{-3}], \tag{2.31}$$

and

$$B[\mu\mathrm{G}] = 2.6 \cdot B_{\mathrm{sim}}[(10^{10}\mathrm{M}_{\odot}/\mathrm{kpc})^{1/2} \cdot (\mathrm{km/s})/\mathrm{kpc}]. \tag{2.32}$$

2.2.3 Calculation of integrals

In Chapters 5 and 6, I calculate the rotation measure (RM) of FRB host galaxies and intervening galaxies behind background quasars, respectively. In the case of FRB host

[2] https://www.tng-project.org/data/docs/scripts/

galaxies, also their dispersion measure (DM). Both RM and DM line-of-sight integrals, DM is of the electron density (n_e), and RM is of the n_e and $B_{||}$. Additionally, the magnetic field maps presented in Appendix D of Appendix III are also generated by integrating the magnetic field strength, or its components (azimuthal, radial, vertical), in a face-on or edge-on view of the galaxies.

I used a function from the python package mentioned above ('arepo-snap-util' by Federico Marinacci, Ruediger Pakmor etc.), which is an algorithm that can calculate integrals in the snapshot data. For a given sightline in the simulation, the integrals are replaced by a discrete sum between the two ends of the integral. We use N number of steps of dl stepsize (which is defined in each Chapter). In each step, the algorithm takes the values (e.g. n_e in the case of DM) in the closest cell to the position of the current step in the sightline. When generating maps, the algorithm does this in each pixel of the map.

The DM is the line-of-sight integral, here sum, of n_e:

$$\mathrm{DM} = \sum_{i=0}^{N} n_{e,i} \mathrm{d}l, \tag{2.33}$$

where i is the index for the N steps and $n_{e,i}$ is the electron density at each step.

The RM is the line-of-sight integral, here sum, of n_e and $B_{||}$:

$$\mathrm{RM} = k \sum_{i=0}^{N} B_{||,i} n_{e,i} \mathrm{d}l, \tag{2.34}$$

where $B_{||,i}$ is the line of sight magnetic field at each step.

In the case of the face-on maps of the total magnetic field strength presented in Appendix D of Appendix III , the magnetic field for every pixel is given by:

$$B\left(x,y\right) = \left(\frac{1}{2h} \sum_{i=0}^{N} B^2\left(x,y,-h+i\cdot \mathrm{d}z\right) \mathrm{d}z \right)^{1/2}, \tag{2.35}$$

where we sum from $-h$ kpc below the disk to +1 kpc above the disk, in N steps with a stepsize of dz. The size of a pixel is 80 pc x 80 pc. This corresponds to the average cell size of star-forming gas in the simulation, which is around 70 – 140 pc.

I developed a pipeline that loads in the snapshot data of the 16 000 galaxies studied in this thesis, calculates different integrals (DM, RM, total magnetic field strength), and saves the results into a collection of tables and maps contained in fits files. The final results include tables of DM and RM values of sightlines presented in Chapter 5, RM maps used in Chapter 6, different magnetic field maps presented in Appendix D of Appendix III , electron density maps, and a table of a collection of galaxy properties (utilized in both Chapters 5 and 6): SFR, stellar mass, average total disk magnetic field strength, average n_e, and parameters of the n_e and B profiles. Due to the large number of galaxies (16 500), the pipeline was run in multiple $\sim$ 8-hour blocks with a maximum of 16 computing nodes at a time on the clusters of the Max Planck Computing and

Data Facility (mainly on the **raven** cluster). One block of galaxies usually consists of a few hundred galaxies, but the most massive galaxies require more computational time due to their larger radius (even reaching 100 kpc) and, thus, longer integral path lengths.

Chapter 3

The halo magnetic field of a spiral galaxy at z=0.414

This chapter is based on the in-prep article titled "The halo magnetic field of a spiral galaxy at $z = 0.414$", which is in preparation to be submitted to Astronomy & Astrophysics. The in-prep paper is formatted to fit the template of the thesis. As the lead author of this paper, I have carried out all the data reduction and analysis and wrote the manuscript. The PI of the proposal of the original data is A. Mao, and the PI of the follow-up data is me. The full author list will be T. Kovacs, S. A. Mao, A. Basu, and Y. K. Ma.

Contents

Summary

Even though magnetic fields play an important role in galaxy evolution, the redshift evolution of galactic-scale magnetic fields is not well constrained. In this paper, we aim to constrain the time-scale of the mean-field dynamo and derive the magnetic field in a distant galaxy at $z = 0.414$. We obtained broadband spectro-polarimetric $1 - 8$ GHz Very Large Array observation of the lensing system B1600+434, a background quasar gravitationally lensed by a foreground galaxy into two images. We apply Rotation Measure (RM) synthesis and Stokes QU fitting to derive the RM of the two lensed images and use their RM difference to obtain the magnetic field in the halo of the lensing galaxy, following (Mao et al. 2017). We explore different magnetic field geometry models and parameters to calculate the magnetic field of the lensing galaxy. We measured a coherent magnetic field with a strength of $0.1 - 4.7$ μG field at 0.7 kpc distance from the galactic disk in the halo of a spiral galaxy at $z = 0.414$, adopting different models of the magnetic field geometry (both symmetric and antisymmetric magnetic field) and a wide range of parameters. Such field strength is lower than that in the disk consistent with what has been seen in nearby galaxies and follows the expectation from the mean-field dynamo theory. Our halo and the disk field ratio favors a mean-field dynamo origin over a cosmic ray-driven dynamo origin. We find that the large-scale magnetic field has already built up to the present-day value at $z \simeq 0.4$, with which we derive an upper limit on the dynamo e-folding time: $\tau_{\rm dynamo} < 2.9 \cdot 10^8$ yr.

We provide the highest redshift direct measurement of the magnetic field in the halo of a spiral galaxy and find that galaxies at $z \simeq 0.4$ already have magnetic fields similar to present-day galaxies.

3.1 Introduction

Magnetic fields play an important role in the formation and evolution of galaxies (Beck et al. 2019), as they can affect gas dynamics (Moon et al. 2023), galactic outflows (Hanasz et al. 2013), propagation of cosmic rays (Wiener et al. 2013), star formation rate (SFR, Tabatabaei et al. 2017, Birnboim et al. 2015) and the initial mass function (Rees 1987; Krumholz & Federrath 2019). The strength and structure of magnetic fields in local galaxies can be traced by synchrotron emission: the total synchrotron intensity measures the plane of the sky component of the total magnetic field, and its polarization tells us about the ordered magnetic field (Beck et al. 2019). However, these techniques can only be used in nearby galaxies ($z \ll 0.1$, based on Beck 2013 the highest redshift measurement of an individual galaxy is at $z = 0.009$, and $z = 0.018$ for interacting galaxies), since the polarized synchrotron emission of galaxies at higher redshift is too faint for the current radio facilities. Even with the Square Kilometre Array (SKA), we will only detect it at $z \leq 0.5$ (Beck & Wielebinski 2013). As a result, the redshift evolution of magnetic fields is not well-constrained. Only a handful of measurements exist (Mao et al. 2017, Kronberg et al. 1992, Wolfe et al. 2011), along with some statistical detections in intervening galaxies using samples of absorption line quasar systems (Bernet et al. 2008, Bernet et al. 2013, Farnes et al. 2014, Farnes et al.

2017; and further discussed in Basu et al. 2018). These results suggest galaxies up to $z = 3$ can have comparable magnetic field strengths to local galaxies.

The magnetic field measurements (e.g. magnetic pitch angle and the strength of the mean magnetic field) of nearby galaxies can be reproduced by the mean-field dynamo theory (e.g. Chamandy et al. 2016). The dynamo describes how kinetic energy is transformed into magnetic energy (the amplification of the magnetic field strength), and how the turbulent field is transformed into a regular field. The large-scale dynamo (which operates on kpc scale) requires the large-scale rotation of the galaxy's disk. Disks can already form at high z (e.g. $z \sim 2-3$ based on the observation of ionized gas – Genzel et al. 2006, and $z \simeq 4.4$ based on molecular gas – Tsukui & Iguchi 2021) which allows the possibility of large-scale fields on scales of a few kpc existing in galaxies even at $z = 3$, as there is enough time (~ 2 Gyr) for the large-scale field to develop (Arshakian et al. 2009). To develop a consistent dynamo model, it is crucial to know the evolution of the physical parameters controlling dynamo action (e.g. angular velocity of galactic rotation, disk size, and gas density) and we need to be able to compare the derived magnetic field evolution to observations (Arshakian et al. 2009; Pakmor et al. 2018; Pfrommer et al. 2022).

Mao et al. (2017) demonstrated a new method that directly measured the magnetic field strength in a distant galaxy ($z = 0.4$) by observing a background quasar lensed by a foreground galaxy. If we compare the polarization properties of the lensed images of the background source, we can draw conclusions on the strength and structure of the magnetic field of the lensing galaxy. The polarized light of the background source undergoes Faraday rotation when it passes through the magneto-ionic medium of the galaxy, which causes the polarization angle to change and is characterized by the rotation measure (RM). The RM is defined as the line-of-sight integral of the electron density ($n_{\rm e}$) and the line-of-sight component of the magnetic field ($B_{||}$):

$$\mathrm{RM} = 0.81 \int_{\rm source}^{\rm observer} B_{||} n_e \mathrm{d}l. \tag{3.1}$$

Because of this, the RM of the lensed images consists of the RM of multiple contributors along the line-of-sight: the background quasar ($\mathrm{RM_{qso}}$), the intervening galaxy ($\mathrm{RM_{gal}}$), the intergalactic medium (IGM; $\mathrm{RM_{IGM}}$) and the Milky Way ($\mathrm{RM_{MW}}$). The total observed RM of the polarized light from a quasar at $z_{\rm qso}$ lensed by a galaxy at $z_{\rm gal}$ can be written as:

$$\mathrm{RM_{obs}} = \frac{\mathrm{RM_{qso}}}{(1+z_{\rm qso})^2} + \frac{\mathrm{RM_{gal}}}{(1+z_{\rm gal})^2} + \mathrm{RM_{IGM}} + \mathrm{RM_{MW}}, \tag{3.2}$$

where $\mathrm{RM_{qso}}$ and $\mathrm{RM_{gal}}$ are rest frame RMs, and the $(1+z)^2$ term is the standard conversion factor to the observation's frame. $\mathrm{RM_{qso}}$ is the same in both images, as lensing is achromatic (Schneider et al. 1992) and non-polarizing (Dyer & Shaver 1992), and we assume the background source RM does not vary on the timescale of the gravitational time-delay. The differences in the RM contributions of the IGM and the Milky Way are negligible between the two sightlines because the angular separation between the lensed images is on the scale of arcseconds. The $\mathrm{RM_{MW}}$ does not change on such scales

(Oppermann et al. 2012; Hutschenreuter et al. 2022). Vernstrom et al. (2019) calculated the RM difference between pairs of sources that could be attributed to the IGM and found it decreases with angular separation: on the order of arcseconds, it becomes $< 1\,\mathrm{rad\,m^{-2}}$. As a result, any difference between the RM of the images is caused only by the magneto-ionic medium of the lensing galaxy (Narasimha & Chitre 2004).

In this paper, we estimate the magnetic field properties in another lensing system, B1600+434. In the top panel of Fig. 3.1, we show the optical image of the system from Kochanek et al. (1999). This system was discovered by Jackson et al. (1995), who found it is a two-image lensing system with an image separation of 1.39". The redshift of the background quasar is $z = 1.589$, and the lensing galaxy is at $z = 0.414$ (Fassnacht & Cohen 1998). The galaxy is an edge-on spiral: its axis ratio (a/b, where a and b are the major and minor axis) is 2.4 ± 0.2, and its position angle is $46° \pm 3°$ (Jaunsen & Hjorth 1997). Based on this, the inclination is at least 65° (Maller et al. 1997). According to the Hutschenreuter et al. (2022) RM map, the Milky Way's contribution is 16.6 $\mathrm{rad\,m^{-2}}$ along the line-of-sight towards B1600+434, but the variation in a 10 arcmin radius around the source is only 1.4 $\mathrm{rad\,m^{-2}}$, implying variation on smaller scales should be even lower. Based on the North Galactic Pole's structure-function (Stil et al. 2011) we expect the Galactic RM fluctuation to be $\lesssim 1\,\mathrm{rad\,m^{-2}}$. The sight lines of the lensed images go through the halo, one below and the other above the disk. This system complements the results of the lensing galaxy of B1152+199 from Mao et al. (2017), as the two lensing galaxies are at a similar redshift, but the sightlines of B1152+199 probe a different part of the magneto-ionic medium, namely the disk of its lensing galaxy. These two systems allow us to investigate the general magnetic field properties of a typical galaxy at $z \simeq 0.4$.

The paper is organized as follows: in Section 3.2, we describe the data reduction of our observations with the Very Large Array (VLA), and in Section 5.3, we show the results of the RM synthesis and Stokes QU fitting. In Section 5.4, we estimate the magnetic field strength of the lensing galaxy, investigate how typical the lensing galaxy's properties are, and the implications of the derived B field properties on the magnetic field generation mechanism in galaxies. Finally, we show an overview on the typical magnetic fields of galaxies at $z \simeq 0.4$ using the two systems. We summarize our findings in Section 5.7.

3.2 Data analysis

3.2.1 VLA data and imaging

We performed broadband spectro-polarimetric observations at $1 - 8$ GHz (L-, S-, and C-band) of the lensing system B1600+434 with the VLA in A configuration. We chose a secondary polarization calibrator, J2202+4216, which is one of the suggested polarization calibrators for the VLA, with the caveat that it can have moderate variabilities and, therefore, does not have a standardized model of its polarization properties. Thus, in addition to our science observation (from here on the science dataset), we also performed an observation to obtain a model for the polarization properties of

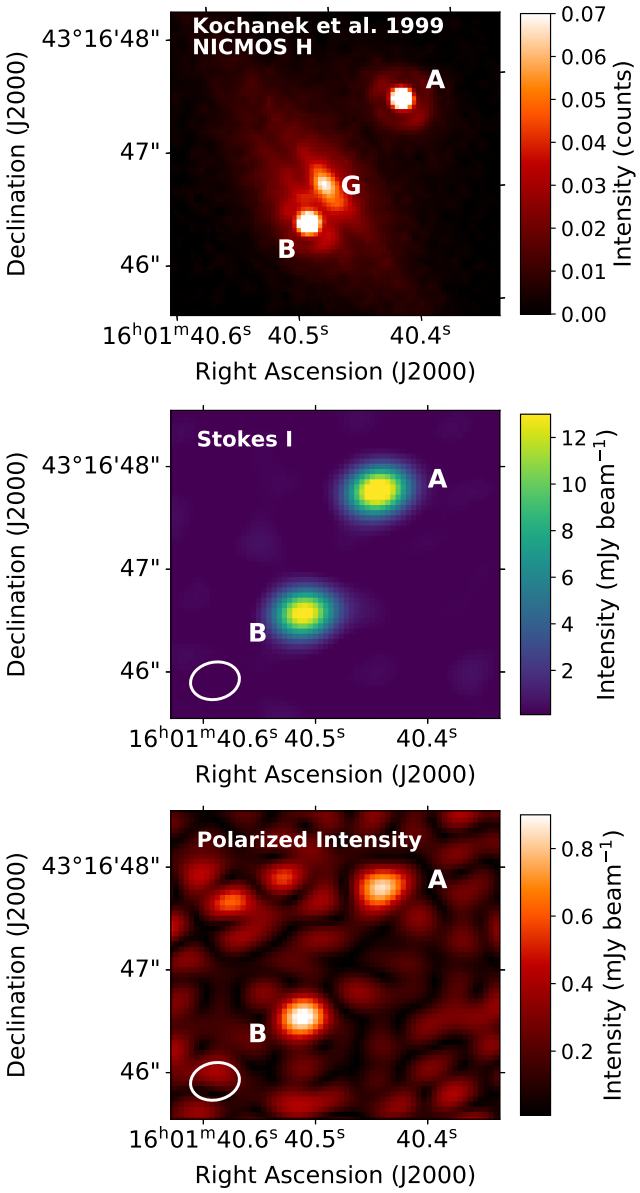

Figure 3.1: The Near Infrared Camera and Multi-Object Spectrometer (NICMOS) H band image of the lensing system from Kochanek et al. (1999), and the Stokes I and polarized intensity (PI) maps from our VLA data. A and B indicate the lensed images of the background quasar, and G shows the lensing galaxy. The galaxy can only be seen in the NICMOS H image; in our VLA images, the lensing galaxy is too faint to be detected. The Stokes I and PI maps are 16MHz channel maps at 3.7 GHz. The beam size is shown in the lower left corner.

J2202+4216 (calibration dataset). The science and calibration datasets were observed on 29 October 2012 and 27 October 2012, respectively.

First, we used the calibration dataset to obtain the polarization information of J2202+4216, which we would utilize for calibrating the science dataset. We observed 3C138 as the flux and polarization calibrator for the calibration dataset and J0319+4130 as the leakage calibrator.

We used the Common Astronomy Software Applications package (CASA, version 5.3.0-143, McMullin et al. 2007, Emonts et al. 2020) to calibrate the data and to form images. We first did basic flagging (shadowing, flagging for zeros, quack flagging, and bad antennas based on the observer's log) and flagged the end channels for each spectral window (first and last eight channels). Next, we calibrated the antenna positions and did the initial flux scaling using the Perley & Butler (2013a) models, the initial phase calibration, and delay and bandpass calibration. After applying these calibration solutions, we inspected the data for strong Radio Frequency Interferences (RFI), and flagged them manually. We also used the automatic flagging methods `tfcrop` and `rflag`. We then extended these flags to all polarizations and re-determined the flux, delay, and bandpass solutions.

After this initial calibration and flagging, we performed gain calibration and polarization calibration, which consists of setting a polarization model of the polarization calibrator and solving for the cross-hand delays, the leakage terms, and the cross-hand phase offset. The polarization model for 3C138 was taken from Perley & Butler (2013b). In the end, we scaled the amplitude gains and applied the solutions to the calibrators and the targets. We did additional flagging until the resulting images were free of obvious artifacts.

We formed Stokes I, Q, and U images of J2202+4216 with 16 MHz channel width across 1 to 8 GHz. We used the Clark deconvolver and Briggs weighting (Briggs 1995b), with a robust parameter of -2 We used the task `imfit` to fit J2202+4216 on the channel images and determine their flux density. In Stokes I, we fixed the minor and major axis and the position angle for the fitted Gaussians to be the same as the synthesized beam, and we only let the position and amplitude change. The errors of the flux densities are given by the root mean square (rms) noise of a source-free region in each image. We fitted the polarization angle and the polarization fraction of J2202+4216 as a function of frequency, and we would use this as a polarization model in the science dataset.

For the science dataset, the flagging and calibration procedures are similar to those done for the calibration dataset. The difference is in the used calibrators: we used 3C48 as the flux density calibrator, J2202+4216 as the polarization calibrator, J2355+4950 as the leakage calibrator, and J1545+4751 as the phase calibrator. We note that we could not use 3C48 as a polarization calibrator for the whole dataset, as it is depolarized below 4GHz[1], which is why we had to use J2202+4216. For the flux calibration, we use the Perley & Butler (2013a) models, and for the polarization calibration, we use the model of J2202+4216 that we determined from our calibration dataset. As a quick independent check to see if the calibration was done correctly, we imaged 3C48 in

[1] https://science.nrao.edu/facilities/vla/docs/manuals/obsguide/modes/pol

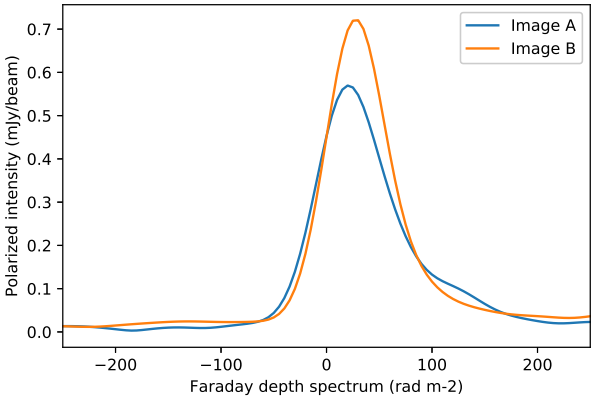

Figure 3.2: The Faraday depth spectrum of image A and image B.

Stokes I, Q, and U, as this source has not been used in the polarization calibration. We found that the PA and polarization fraction are consistent with the reported values from Perley & Butler (2013b).

We formed images in the same way for our target, the lensing system B1600+434, as we did for the calibration dataset. However, below 1.5 GHz, the lower angular resolution leads to the spatial blending of the two lensed images. Therefore, we also fixed the positions of the fitted Gaussians in this frequency range based on their positions between 1.5 and 2 GHz. We show the Stokes I in the middle panel and the polarized intensity image in the bottom panel of Fig. 3.1.

3.3 Results

3.3.1 Rotation Measure Synthesis

To estimate the polarization properties of the lensed images, we performed Rotation Measure synthesis (Brentjens & de Bruyn 2005) on our target source, using the python package RM-Tools (Purcell et al. 2020). To constrain the residual polarization leakage of our observations, we performed RM synthesis on our leakage calibrators. We found that the polarized intensity (PI) of J2355+4950 is 0.0001 Jy, and its Stokes I is 1.5 Jy. This corresponds to an upper limit in the residual polarization leakage of 0.01%. The leakage calibrator J0319+4130 in the 27 October 2012 calibrator dataset has an even lower residual polarization: 0.003%.

In Fig. 3.2, we show the Faraday depth spectra of the lensed images, revealing only a small difference between the peaks. We derive a peak Faraday depth of $\phi_A = 27.4 \pm 0.2\,\mathrm{rad\,m^{-2}}$ and $\phi_\mathrm{B} = 21.0 \pm 0.4\,\mathrm{rad\,m^{-2}}$ for the two lensed images. However, there is an indication that the spectra are not Faraday thin.

3.3.2 Stokes QU fitting

We used Stokes QU fitting (see e.g. Farnsworth et al. 2011, O'Sullivan et al. 2012, and Ma et al. 2019) to fit the fractional Stokes parameters $q = Q/I$ and $u = U/I$ as a function of frequency for both the lensed images. This method is better at disentangling multiple polarized components, as Farnsworth et al. (2011) previously showed.

We fitted several models independently to the Stokes Q and U of the lensed images. This included Faraday thin models, where a synchrotron emitting source is behind a Faraday rotating screen with a homogeneous magnetic field and thermal electron density, Burn slab models (Burn 1966) with a foreground rotating screen, where the synchrotron emitting volume is also Faraday rotating, external dispersion models, where we have a turbulent Faraday screen in the foreground that cause depolarization effects, internal dispersion with foreground, where the synchrotron emitting volume is also Faraday rotating and has a turbulent magnetic field, and a model including both external and internal dispersion. In the case of Faraday thin, Burn slab, external dispersion, and internal dispersion models, we tried both single and double models, where there are one and two spatially unresolved synchrotron emitting sources (i.e. polarized components), respectively. For more details on the specific models, see, for example, Ma et al. (2019).

We chose the best model to be the one with the lowest resulting Bayesian Information Criterion (BIC) value. The best model was the double external dispersion model for both lensed images, shown in Figs. 3.3 and 3.4. This model describes a background source with two spatially unresolved polarized components, both of which experience external Faraday dispersion ($\sigma_{\rm RM}$) along the line-of-sight, contributing to the observed RM and $\sigma_{\rm RM}$. The complex polarization as a function of λ^2 is given by:

$$P = {\rm PF}_1 e^{-2\sigma^2_{\rm RM,1}\lambda^4} e^{2i({\rm PA}_1+{\rm RM}_1\lambda^2)} + {\rm PF}_2 e^{-2\sigma^2_{\rm RM,2}\lambda^4} e^{2i({\rm PA}_2+{\rm RM}_1\lambda^2)}, \tag{3.3}$$

where λ is the wavelength, ${\rm PF}_1$ and ${\rm PF}_2$ are the intrinsic polarization fractions, ${\rm PA}_1$ and ${\rm PA}_2$ are the intrinsic polarization angles, ${\rm RM}_1$ and ${\rm RM}_2$ are the RM values, and $\sigma_{\rm RM,1}$ and $\sigma_{\rm RM,2}$ represent the Faraday dispersions of the two components. The fitted parameters are listed in Table 3.1. The presence of two polarization components is consistent with observations from the Very Large Baseline Array (VLBA) that show the substructure of the background source (Biggs 2021), with two sub-arcsecond scale spatial components in both images.

In the rest of the paper, we refer to the polarized component with the larger PF as the main polarized component and the other component as the secondary component. The PA and PF of both polarized components are consistent between images A and B, suggesting that we truly see the same background source and its components in both lensed images. We find only a small difference in the RM (${\rm RM}_{\rm A,1}$ vs. ${\rm RM}_{\rm B,1}$, and ${\rm RM}_{\rm A,2}$ vs. ${\rm RM}_{\rm B,2}$) and $\sigma_{\rm RM}$ ($\sigma_{\rm RM,A,1}$ vs. $\sigma_{\rm RM,B,1}$, and $\sigma_{\rm RM,A,2}$ vs. $\sigma_{\rm RM,B,2}$) of both components between the two images, which is possibly caused by the lensing galaxy's magneto-ionic medium. The RM of both components is larger in image A, and $\sigma_{\rm RM}$ is slightly larger in image B (although for the secondary component, the values agree within the errors). As we usually see larger RMs in AGNs (Hovatta et al. 2019), the

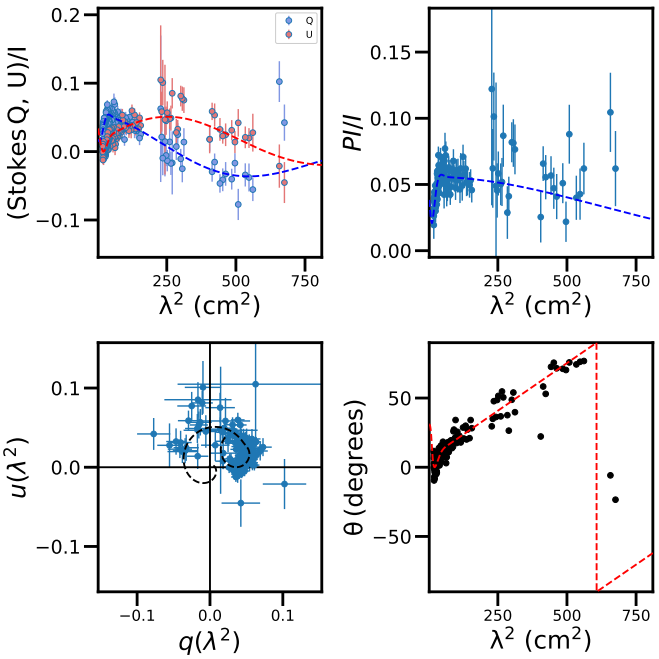

Figure 3.3: *QU* fitting results of image A.

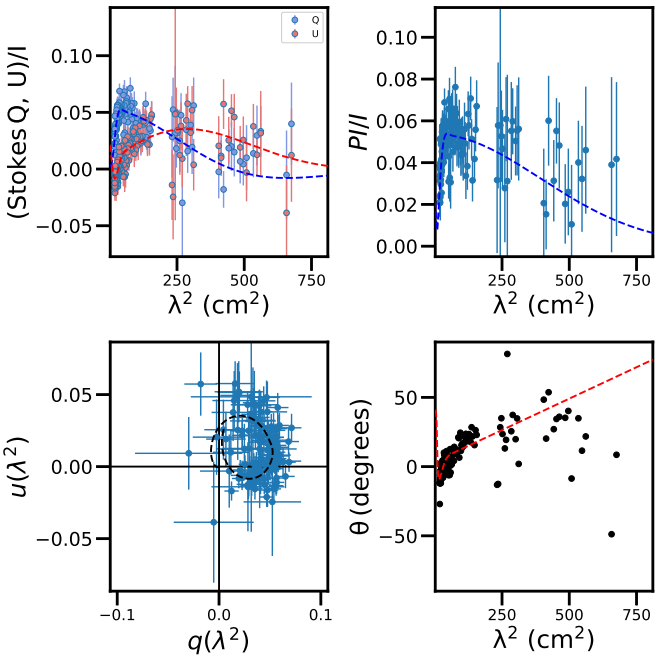

Figure 3.4: *QU* fitting results of image B.

Table 3.1: The polarization angle (PA), polarization fraction (PF), Rotation Measure (RM) and Faraday dispersion (σ) of the two polarized components of B1600+434 for the two lensed images.

	Image A	Image B
PA_1 (deg)	6.3 ± 1	3.7 ± 1.4
PA_2 (deg)	71 ± 8	79 ± 9
PF_1 (%)	5.6 ± 0.1	5.4 ± 0.2
PF_2 (%)	4.2 ± 0.6	5.2 ± 0.8
RM_1 ($\mathrm{rad\,m^{-2}}$)	24.0 ± 1.2	15.9 ± 2.1
RM_2 ($\mathrm{rad\,m^{-2}}$)	342 ± 62	271 ± 71
$\sigma_{RM,1}$ ($\mathrm{rad\,m^{-2}}$)	8.4 ± 1.5	12.7 ± 1.8
$\sigma_{RM,2}$ ($\mathrm{rad\,m^{-2}}$)	243 ± 26	273 ± 29

main polarized component which has a lower RM is possibly from the jet, and the secondary component with a high RM corresponds to emission near the core of the AGN. We note that the emission from the core would have a flatter spectrum than that of the jet. This would mean that the main component is mainly seen at low frequencies and the secondary component at high frequencies. The large $\sigma_{RM,2}$ values might be due to this effect (in contrast to being caused by a depolarising medium), as it would result in a fit where the secondary component is suppressed at low frequency. Nevertheless, this would not affect the main component's RM difference between the lensed images, and in the rest of the paper, we do not use $\sigma_{RM,2}$, so this would not affect the results of our paper.

Gravitational lensing only introduces additional changes in the polarization angle in the case of a rotating or non-spherical lens. This effect is less than 0.1 degrees if the image is $r = 100\ m$ away from the lens (Dyer & Shaver 1992), where m is the geometrized mass (in geometrized unit system). In the case of a galaxy with a stellar mass of $\log(M_*/\mathrm{M}_\odot) = 12$, m is 0.05 pc, and r=5 pc, which is significantly less than the distance of the lensed images from the lensing galaxy (0.7 and 6.2 kpc). This means we do not expect a change in the polarization angle between the lensed images of the background quasar due to gravitational lensing.

3.3.3 RM difference

After deriving the observed RM of the two quasar images, we get an RM difference of 8 ± 2 $\mathrm{rad\,m^{-2}}$ and 30 ± 26 $\mathrm{rad\,m^{-2}}$ from the two components. These two results are consistent; however, due to the large uncertainty of the RM difference from the secondary polarized component, we only consider the RM difference of the main component.

3.3.4 Variability of B1600+434

Biggs (2021) showed that B1600+434 has a time delay of 42.3 ± 2.1 days, and the background source also exhibits variability in polarization on similar time scales.

Table 3.2: The polarization properties of the two images of B1600+434 based on the new observations in L-band.

	image A	image B
PA (°)	-0.7 ± 6.9	-10.7 ± 6.8
PF (%)	3.6 ± 0.2	4.8 ± 0.6
RM ($\mathrm{rad\,m^{-2}}$)	19.6 ± 3.2	17.1 ± 3.3
σ_{RM}($\mathrm{rad\,m^{-2}}$)	0	9.2 ± 2.5

Previous measurements of time delay in this system were 47^{+5}_{-6} days by Koopmans et al. 2000 in radio and 51 ± 4 days by Burud et al. 2000 in optical. As the joint effect of time delay and RM time variability of the background source can also change the observed RM difference, we conducted follow-up observations in L-band. If the RM difference is caused by the magneto-ionic medium of the lensing galaxy, it should remain constant between the images, independently of the time of observation. If this is not the case, we can determine the RM variability of the background source by monitoring the lensing system in polarization. With these measurements, we can separate the RM difference caused by the galaxy.

We also performed follow-up observations of the lensing system in L-band on 17 February 2021. The flagging, calibration, and imaging essentially follow the steps for the main science dataset, described in Section 3.2, and we used 3C286 as the flux and polarization calibrator, J1407+2827 as the leakage calibrator, and J1545+4751 as the phase calibrator. We also applied *QU*-fitting and again chose the model with the lowest BIC as the best-fit model. In the case of image A, the best-fit model was a single Faraday thin model, and for image B, we found the single external dispersion model to be the best. As we found a single model to be the best in both images, we concluded that we could not observe one of the polarized components found in the main science data. Based on the similarities of the polarization properties, we argue that we found the same main polarized component, but we could not observe the secondary component. This is supported by how the secondary component most likely could only be observed with higher frequency data due to its large σ_{RM} (or due to its flat spectrum). Even though the observations were taken nine years apart, the polarization properties of the images do not show a significant variation. However, note that our follow-up observations have higher uncertainties since we only used a narrower frequency range, which reduces the precision in Faraday space. We compare the Stokes *QU* fitting results of the new observations (see Figs. 3.5 and 3.6, and Table 3.2) to the Stokes *QU* fitting results of only L-band of our earlier observations.

We find that the RM has not changed significantly over time, and therefore, likewise for the RM difference. This suggests that the RM difference between the images reflects the magneto-ionic medium of the foreground galaxy (i.e., there is no significant contribution by the RM time variability of the background source).

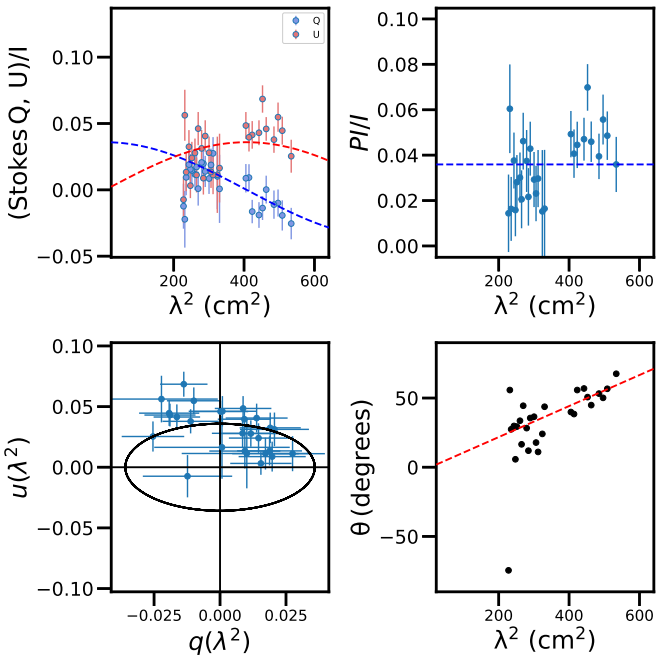

Figure 3.5: *QU* fitting results of image A in L-band from follow-up data taken in 2021.

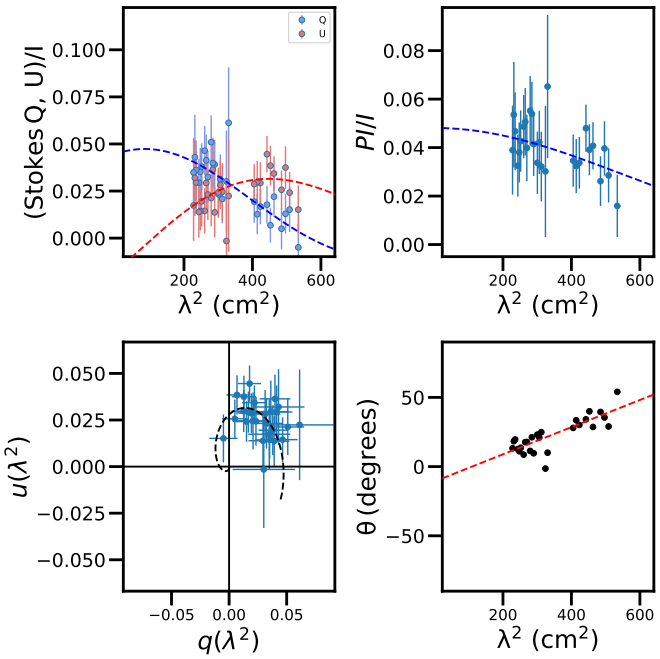

Figure 3.6: *QU* fitting results of image B in L-band from follow-up data taken in 2021.

3.4 Discussion

After deriving the observed RM (RM_{obs}) of the two quasar images ($RM_{A,obs}$= 24 ± 1 rad m^{-2}, $RM_{B,obs}$ = 16 ± 2 rad m^{-2}) we have to correct for the redshift dilution to obtain the rest frame RM (RM_{rf}):

$$RM_{rf} = (1 + z_{gal})^2 \cdot RM_{obs}, \tag{3.4}$$

where z_{gal} is the redshift of the lensing galaxy. This increases the RMs by a factor of ∼2: $RM_{A,rf} = 48\,\mathrm{rad\,m^{-2}}$ and $RM_{B,rf} = 32\,\mathrm{rad\,m^{-2}}$. The rest-frame RM difference is related to the electron column density (N_e) and the line of sight magnetic field component ($B_{||}$) in the following way:

$$\Delta RM = RM_B - RM_A = k(N_{e,B}B_{||,B} - N_{e,A}B_{||,A}), \tag{3.5}$$

where the quantities with subscripts A and B correspond to the positions probed by sightlines A and B, respectively, and $k = 0.812\,\mathrm{rad\,m^{-2}\,pc\,cm^{-3}\,\mu G^{-1}}$. We assumed that $B_{||}$ is constant along the LOS, and the magnetic field and the electron density are uncorrelated.

We note the possibility that the RM difference is due to the small-scale field, as opposed to the large-scale field. The differential Faraday dispersion ($\Delta\sigma_{RM,obs}$ = 9.5 rad m^{-2}) from the small-scale field in the lensing galaxy could also cause an RM difference between the images: $|RM| = \frac{\sigma_{RM}}{\sqrt{N}}$, where N is the number of turbulent cells. However, this only results in |RM| = 1 rad m^{-2} in the case of N = 100 (e.g. 50 pc turbulent cells in 5 kpc), which is lower than the differential $RM_{obs} = 8\,\mathrm{rad\,m^{-2}}$, which means the RM difference is most likely to be due to the large-scale field of the lensing galaxy.

To estimate the magnetic field strength, first we make assumptions about the electron density and the geometry of the large-scale magnetic field, as discussed below.

3.4.1 Assumptions on electron density

3.4.1.1 General assumptions

This lensing system has been observed by the *Chandra X-ray Observatory*, and Dai & Kochanek (2005) derived the differential hydrogen column density from the X-ray absorption ($\Delta N_H = \Delta N_{H,B} - \Delta N_{H,A} \sim 3{\cdot}10^{21}\mathrm{cm^{-2}}$). This can be converted into differential electron column density if we assume an ionization fraction (f_{ion}). By assuming a wide range of f_{ion} = 5% − 50%, we get $\Delta N_e = N_{e,B} - N_{e,A}$=48.6−486.1 pc cm^{-3}. This can be directly used in a constant antisymmetric magnetic field geometry model to get a B field strength estimate (see Section 3.4.2, item 2). However, this assumption is insufficient for all other magnetic field geometry models. We also need to make another assumption about the electron column density of sightline A. In those models (see Section 3.4.2, item 3–6), we need the sum of the electron column densities instead of the differential column densities. We assume a wide range of 1 − 100 pc cm^{-3} for $N_{e,A}$, which means $N_{e,B} = N_{e,A} + \Delta N_e$ = 49.6 − 586.1 pc cm^{-3}, and

$N_{\rm e,A} + N_{\rm e,B} = 50.6 - 686.1\,{\rm pc\,cm^{-3}}$. For all assumed values above, we consider the wide range of parameters to take into account the possibility that high redshift galaxies behave differently than local ones.

3.4.1.2 Electron density in MW-like galaxies

We also investigate the scenario where we assume Milky Way like properties for our lensing galaxy, for which we have devised two approaches.

With our first approach, we use an ionization fraction of $10^{+4}_{-3}\%$ (He et al. 2013, which is the ionization fraction of the Galactic interstellar medium derived from the dispersion measure and X-ray column density of radio pulsars). We calculate a differential electron column density $\Delta\,N_e = 97\,{\rm pc\,cm^{-3}}$ (68–136 ${\rm pc\,cm^{-3}}$). Assuming the same range of $1 - 100\,{\rm pc\,cm^{-3}}$ for $N_{\rm e,A}$ as previously, we find $N_{\rm e,A} + N_{\rm e,B} = 70 - 336\,{\rm pc\,cm^{-3}}$.

In our second approach, we estimate the electron column densities in a different way: by using the electron density profile derived by Gaensler et al. (2008) in the Milky Way halo:

$$n_e = n_0 \exp(-h/h_{\rm scale}), \tag{3.6}$$

where $n_0 = 0.014 \pm 0.001$ cm^{-3}, $h_{\rm scale} = 1.83^{+0.12}_{-0.25}$ kpc and h is the vertical distance from the Galactic plane. If we assume an integral path length of 10 kpc through the halo (e.g. see Badole et al. 2022 with similar path length assumption), we derive electron column densities of $N_{\rm e,A} = 2 - 5\,{\rm pc\,cm^{-3}}$ and $N_{\rm e,B} = 83 - 105\,{\rm pc\,cm^{-3}}$ at a distance from the plane of the galaxy at 6.2 kpc (image A) and -0.7 kpc (image B), respectively. This gives us a differential electron column density $\Delta\,N_{\rm e} = 78 - 103\,{\rm pc\,cm^{-3}}$ (a value consistent with $f_{\rm ion} = 8 - 10\%$), and $N_{\rm e,A} + N_{\rm e,B} = 85 - 110\,{\rm pc\,cm^{-3}}$. Our calculations based on Gaensler et al. (2008) suggest that $N_{\rm e,A}$ is more likely to be much less than 100 ${\rm pc\,cm^{-3}}$, unless n_e is an order of magnitude higher in galaxy halos at $z \sim 0.4$ compared to the Milky Way.

These two estimates of ΔN_e in the case of MW-like galaxy properties are very close to each other, even though we started from different assumptions. $N_{\rm e,A} + N_{\rm e,B}$ have a larger difference, as in the case of He et al. (2013) we assumed the same wide range for $N_{\rm e,A}$ as previously. When deriving the magnetic field strength of a MW-like galaxy, we focus on the electron densities derived from Gaensler et al. (2008), as it overlaps but has a narrower range than the results based on He et al. (2013). Our electron density ranges from the general assumptions overlap these cases but have a wide range, thus we decide to calculate the magnetic field properties with the widest (full parameter range) and narrowest (MW-like parameters) range of parameters.

3.4.2 Magnetic field geometries

In this section, we explore the magnetic field strength of the lensing galaxy using different, simplified magnetic field geometry models.

The inclination of the galaxy is important to know as we calculate the magnetic field strengths using our simple models. Maller et al. (2000) derived an inclination of $81.7^{\circ+0.4^{\circ}}_{-0.5^{\circ}}$ by fitting elliptical isophotes to an HST image of the galaxy. We consider

Table 3.3: The derived magnetic field strengths for different magnetic field geometry models. Image A is 6.2 kpc and image B is −0.7 kpc away from the plane of the galaxy.

Model	Symmetry	Full parameter range			MW-like parameters		
		B_0 (μG)	B_A (μG)	B_B (μG)	B_0 (μG)	B_A (μG)	B_B (μG)
Toroidal		0.04 - 0.4	0.04 - 0.4	0.04 - 0.4	0.15 - 0.3	0.15 - 0.3	0.15 - 0.3
Constant	anti	−3.0 - −0.3	−3.0 - −0.3	−3.0 - −0.3	−1.8 - −1.3	−1.8 - −1.3	−1.8 - −1.3
Constant	sym.	0.2 - 2.8	0.2 - 2.8	−0.2 - −2.8	1.2 - 1.7	1.2 - 1.7	−1.2 - −1.7
B/h	anti	0.2 - 2.0	0.02 - 0.3	0.2 - 2.9	0.9 - 1.2	0.1 - 0.2	1.2 - 1.7
B/h	sym.	0.2 - 2.0	0.03 - 0.3	−2.9 - −0.2	0.9 - 1.2	0.1 - 0.2	−1.7 - −1.2
Exponential	anti	0.2 - 4.1	0.01 - 2.2	0.2 - 2.9	1.4 - 2.5	0.1 - 0.9	1.2 - 1.7
Exponential	sym.	0.3 - 4.1	0.01 - 2.2	−2.9 - −0.2	1.3 - 2.5	0.1 - 0.9	−1.8 - −1.2
All ($\|B\|$)		0.2 - 4.1	0.01 - 2.8	0.2 - 3.0	0.9 - 2.5	0.1 - 1.8	1.2 - 1.8

image A to be above the disk with a vertical distance from the midplane of $h_{\rm A} = +6.2$ kpc and image B to be below the disk with a vertical distance from the midplane of $h_{\rm B} = -0.7$ kpc.

First, we assume that there is a dominating toroidal field in the halo, and the RM we see is mainly due to the toroidal field. In this case, $B_{||} = B_t \sin(i)$, where B_t is the strength of the toroidal magnetic field, which we assume to be constant. We find this to be low: < 0.4 μG.

It is more likely that the halo only has a vertical magnetic field. In this case, the line-of-sight magnetic field component is given by

$$B_{||} = B_{\rm vert} \cos(i). \tag{3.7}$$

We examine different large-scale magnetic field configurations in the halo (from simple constant fields to fields that scale with distance from the galaxy's plane) and calculate their magnetic field strengths. We show the derived magnetic field strengths both at position A and B in Table 3.3.

Below we list the different geometry models that we used, going from the simplest models to the more physical ones:

1. Constant vertical magnetic fields in the halo, with the same direction below and above the disk (constant, antisymmetric). For this case, the vertical magnetic field strength is given by:

$$B_{\rm vert} = B_0 (= B_{\rm A} = B_{\rm B}). \tag{3.8}$$

   In the simplest case, where the magnetic field has the same direction below and above the disk, and has no height dependence, we derive

$$B_0 = \frac{\Delta {\rm RM}}{k \cos(i)(N_{\rm e,B} - N_{\rm e,A})} \tag{3.9}$$

2. Constant vertical magnetic fields in the halo, with opposite directions below and above the disk (constant, symmetric). For this case, the vertical magnetic field

strength is given by:

$$B_{\rm vert} = \begin{cases} +B_0 = B_{\rm A}, & \text{if } h > 0 \\ -B_0 = B_{\rm B}, & \text{if } h < 0. \end{cases} \tag{3.10}$$

In this case

$$B_0 = \frac{-\Delta{\rm RM}}{k\cos(i)(N_{\rm e,B} + N_{\rm e,A})}. \tag{3.11}$$

3. Vertical magnetic field strengths with linear scaling with distance from the midplane, with the same direction below and above the disk (B/h, antisymmetric). For this case, the vertical magnetic field strength is given by:

$$B_{\rm vert} = \frac{B_0}{|h|}. \tag{3.12}$$

In this case

$$B_0 = \frac{\Delta{\rm RM}}{k\cos(i)\left(\frac{N_{\rm e,B}}{|h_{\rm B}|} + \frac{N_{\rm e,A}}{|h_{\rm A}|}\right)}. \tag{3.13}$$

4. Vertical magnetic field strengths with linear scaling with distance from the midplane, with opposite directions below and above the disk (B/h, symmetric). For this case, the vertical magnetic field strength is given by:

$$B_{\rm vert} = \frac{B_0}{h}. \tag{3.14}$$

In this case

$$B_0 = \frac{\Delta{\rm RM}}{k\cos(i)\left(\frac{N_{\rm e,B}}{h_{\rm B}} + \frac{N_{\rm e,A}}{h_{\rm A}}\right)}. \tag{3.15}$$

5. Vertical magnetic field strengths scale exponentially with distance from the midplane, with the same direction below and over the disk (exponential, antisymmetric). For this case, the vertical magnetic field strength is given by:

$$B_{\rm vert} = B_0 \exp\left(-\frac{h}{h_{\rm B,scale}}\right), \tag{3.16}$$

where $h_{\rm B,scale}$ is the scale height of the halo magnetic field. We note that based on the synchrotron scale height in most nearby edge-on spiral galaxies ($H_{\rm syn}$ = 1−2 kpc), we would expect $h_{\rm B,scale}$=2−8 kpc (Beck et al. 2019). However, we again consider a wider range of parameters (between 2 and 20 kpc) to account for very different environments at large z.

In this case

$$B_0 = \frac{\Delta{\rm RM}}{k\cos(i)\left[N_{\rm e,B}\exp\left(-\frac{h_{\rm B}}{h_{\rm B,scale}}\right) + N_{\rm e,A}\exp\left(-\frac{h_{\rm A}}{h_{\rm B,scale}}\right)\right]}. \tag{3.17}$$

6. Vertical magnetic field strengths scale exponentially with distance from the mid-plane, with opposite signs below and above the disk (exponential, symmetric). For this case, the vertical magnetic field strength is given by:

$$B_{\rm vert} = \begin{cases} B_0 \exp\left(-\frac{h_{\rm A}}{h_{\rm B,scale}}\right), & \text{if } h > 0 \\ -B_0 \exp\left(-\frac{h_{\rm B}}{h_{\rm B,scale}}\right), & \text{if } h < 0. \end{cases} \tag{3.18}$$

In this case

$$B_0 = \frac{-\Delta{\rm RM}}{k\cos(i)\left[N_{\rm e,B}\exp\left(-\frac{h_{\rm B}}{h_{\rm B,scale}}\right) - N_{\rm e,A}\exp\left(-\frac{h_{\rm A}}{h_{\rm B,scale}}\right)\right]}. \tag{3.19}$$

We find that if we use models that only assume a vertical field, the magnetic field strength B_0 is between 0.2 and 4.1 μG. Assuming only a toroidal field, we get 0.03 and 0.6 μG. We obtained such a wide range of magnetic field strength values because of the wide parameter range. We explore in detail how each parameter affects the results in Appendix I.1.

We find that all models give similar ranges of magnetic field strength, apart from the toroidal model, which results in low field strengths. However, we can not rule out any of the models above based on our data, as all of them give reasonable results.

3.4.3 Magnetic field strength in the case of MW-like properties

We investigate what our results would be with restricted parameter ranges that correspond to MW-like galaxies and electron column densities ($\Delta N_e = 68{-}136 \mathrm{pc\,cm^{-3}}$) calculated in Section 3.4.1 based on the n_e profile from Gaensler et al. (2008), and assuming a scale height of $h_{\rm B,scale} = 2 - 8$ kpc for the exponential magnetic field geometry (Beck et al. 2019). We investigated the different geometry models for this parameter case and listed the results in Table 3.3. The exponential model is the most realistic model based on what we see in nearby galaxies. This results in an absolute vertical magnetic field strength of 1.2 – 1.8 μG at 0.7 kpc away from the plane of the disk and 0.1 – 0.9 μG at 6.2 kpc.

3.4.4 Properties of the lensing galaxy of B1600+434

The lens galaxy of B1600+434 is an edge-on spiral galaxy at $z = 0.414$. From lens modeling, the total mass (which includes dark matter, stars, gas, and dust) enclosed within the Einstein radius (which is half of the image separation, $\theta_E = \theta/2$) can be determined. In the case of B1600+434, $\theta = 1.4$", which means the Einstein radius is 3.85 kpc at the redshift of the lensing galaxy. This enclosed total mass ($\log(M/\mathrm{M}_\odot)$) is estimated to be between 10.97 and 11.11 (Jaunsen & Hjorth 1997; Fassnacht & Cohen 1998; Koopmans et al. 1998). Girelli et al. (2020) found that according to the stellar-to-halo mass relation (derived from combining stellar mass functions from the COSMOS field with a cosmological N-body simulation), a halo with $\log(M/\mathrm{M}_\odot) \sim 11$ has a stellar mass of $\log(M_*/\mathrm{M}_\odot) \sim 8.5$. As the Einstein radius does not enclose the

whole galaxy, the galaxy is suspected to have a larger stellar mass than $\log(M_*/\mathrm{M}_\odot) \sim 8.5$.

3.4.5 Implications on the field generation mechanism in the lensing galaxy of B1600+434

The mean field dynamo has a theoretical amplification time-scale (e-folding time) of $\sim 2.5 \cdot 10^8$ yrs (Arshakian et al. 2009), in the case of a disk galaxy with an average angular velocity of $\Omega = 20$ km s^{-1} kpc^{-1}. This time scale describes the time needed to spatially order the field on the scale of a few kpc. However, the time (ordering time-scale) needed for a large-scale field to be ordered on the scale of the entire galaxy disk (10s of kpc) without reversals is only a few times shorter than the lifetime of a galaxy (Arshakian et al. 2009).

Magnetic field strengths in the order of μG are expected from the mean-field dynamo theory (Ruzmaikin et al. 1988). We find that the large-scale magnetic field has already built up to present-day structure and magnitude at $z = 0.4$. The measured magnetic field strength can constrain the amplification time scale of the large-scale magnetic field of galaxies. To derive the e-folding time, we use the following equation (similar to Mao et al. 2017):

$$\tau_{\mathrm{dynamo}}[\mathrm{Gyr}] = \frac{t}{\ln(B_{\mathrm{disk,z=0.414}}/B_{\mathrm{seed}})}, \tag{3.20}$$

where B_{seed} ($3 \cdot 10^{-16}$ G, Neronov & Vovk 2010) is the seed magnetic field of the mean-field dynamo, t is the time that passed between when the disk settled into equilibrium ($z = 2$) and the redshift of the lensing galaxy ($z = 0.414$), and $B_{\mathrm{disk,z=0.4}}$ is the disk field strength at $z = 0.414$, assuming that $B_{\mathrm{halo}} = 0.4\ B_{\mathrm{disk}}$ (Beck et al. 2019, based on the densities and energy densities). We also assume that the magnetic field has already saturated before $z = 0.4$. In this case, $t = 5.97$ Gyr, and we derive an upper limit on the dynamo e-folding time: $\tau_{\mathrm{dynamo}} < 2.9 \cdot 10^8$ yr.

3.4.6 Comparison to cosmological MHD simulations

We select analog galaxies at $z = 0.4$ from IllustrisTNG50 simulation (we can assume that the lens galaxy is not quenched but star-forming). From the average vertical magnetic field profile of galaxies, we find that the vertical magnetic field strength is 0.55 μG at 0.7 kpc and 0.2 μG at 6.2 kpc. This is consistent with some of the lower magnetic field strength values that we derived from the observations. We note that this comparison between the derived large-scale field strengths from the observations and the magnetic field strengths in the simulation is comparing similar quantities, as TNG50 mainly has a large-scale field and does not include most random magnetic fields.

3.4.7 Typical magnetic fields at $z \simeq 0.4$

Mao et al. (2017) has used the same method for a lensing system (B1152+199) with a lensing spiral galaxy at $z = 0.439$, where the sightlines of the lensed quasar images pass through the disk of the galaxy. They detected a coherent magnetic field with field strengths between 4 and 16 μG, and found that the scenario of axisymmetric fields in the disk is favored over the presence of bisymmetric fields. Their results are consistent with the dynamo model, because the model predicts the axisymmetric mode is the strongest in the disk (Mao et al. 2017, Shukurov 2005, Arshakian et al. 2009).

The sightlines of B1600+434, on the other hand, pass through the halo of the lensing galaxy, providing us with information about the halo magnetic fields. Assuming both galaxies are typical spirals at $z \simeq 0.4$, we can draw an overall view of galactic magnetic fields at that redshift, including the halo and the disk. We find that the halo B field strength in the case of Milky Way-like galaxy (0.9 – 2.5 μG) is lower by a factor of 1.6–19 compared to the disk field (4 – 17 μG) in the lensing galaxy of B1152+199 (Mao et al. 2017). In most cases, the magnetic field strength is also lower when we consider the full parameter range (0.2 – 4.1 μG). This is also in agreement with the dynamo theory.

Our result of the halo and disk field ratio favors a mean-field dynamo origin over a cosmic ray-driven dynamo origin, which would produce a stronger halo magnetic field (right below and above the center of the galaxy) than the one in the disk (e.g. see Pfrommer et al. 2022, Fig 14).

3.4.8 Comparison to the halo field of nearby galaxies and the Milky Way

In the past years, the Continuum Halos in Nearby Galaxies - an EVLA Survey (CHANG-ES, Irwin et al. 2012) has conducted observations of nearby edge-on galaxies and derived their magnetic field properties. Mora-Partiarroyo et al. (2019) found a magnetic field coherent over 2 kpc in height, which reverses on a scale of 2 kpc in radius, and is about 4 μG strong (lower than its disk, which is 9 μG) in NGC 4631.

Taylor et al. (2009) studies the halo of the Milky Way and derived -0.14 μG for $h > 0$ (in the northern Galactic hemisphere), and $+0.30$ μG for $h < 0$ (in the southern Galactic hemisphere). Later Mao et al. (2010) found the same vertical magnetic field strength towards the south Galactic pole as Taylor et al. (2009), but found the strength towards the north Galactic pole to be consistent with zero.Mao et al. (2012a) assumed that there is a constant, coherent azimuthal halo magnetic field parallel to the Galactic plane, but with different strengths below and above the disk. They calculated 7 μG below the galaxy's plane and 2 μG above it (from 0.8 to 2 kpc).

The ranges of these B field strengths are consistent with our result of $0.2 - 4.1$ μG. However, we cannot implement models with more free parameters because we only have one ΔRM to work with. This is why we assumed that only the direction of the magnetic field can change below and above the disk, not its strength (e.g. it can not be 7 μG below and 2 μG above the disk).

3.5 Conclusions

We performed broadband radio polarization observations with the VLA of the gravitational lensing system B1600+434. We directly measure the RM difference between the lensed images, from which we infer the coherent magnetic field strength in the halo of the lensing spiral galaxy at the highest redshift ($z = 0.414$) to date.

Assuming Milky-Way-like galaxy properties and an exponential model, we find the vertical magnetic field strength to be 1.2 – 1.8 μG at a vertical distance of 0.7 kpc from the plane of the galaxy and 0.2 – 0.9 μG at 6.2 kpc. Even with broader parameter ranges and different geometry models, we find 0.01 – 2.8 μG at 0.7 kpc and 0.2 – 3 μG at 6.2 kpc. The strength of the halo field is comparable to halo fields measured in nearby galaxies (Beck 2015a, Beck & Wielebinski 2013, CHANG-ES - Irwin et al. 2012) and the Milky Way. We note that in contrast to other magnetic field measurements of nearby galaxies, which are based on the equipartition assumption, our measurements are independent and not based on that assumption but still show consistent results.

The mechanism generating the large-scale magnetic field has already built up the field strength and structure to what we see in present-day galaxies at a redshift of 0.4. We derive a dynamo e-folding time of $< 2.9 \cdot 10^{8}$ yr. Furthermore, we find the halo magnetic field is lower compared to the disk field of a similar galaxy at $z \simeq 0.4$ (Mao et al. 2017), which is consistent with the prediction of the dynamo theory.

Chapter 4

Magnetic field in a face-on lensing galaxy: B0218+357

Contents

4.1 Introduction

In this Chapter, we investigate the magnetic field structure and strength of another two-image lensing system, B0218+357, using the method described in Chapter 1 and applied in Chapter 3 to B1600+434. This lensing system is at a higher redshift than the system in the previous chapter, thus we can probe galactic magnetic fields to a redshift of $z = 0.685$.

4.1.1 Previous observations of the lensing system

B0218+357 was first discovered by Patnaik et al. (1992), who carried out a survey of flat-spectrum radio sources at 8.4 GHz to search for sources suitable for phase calibration. Patnaik et al. (1993) proved it to be a lensing system: the bright components have similar spectral indices of -0.2 between 5 and 22 GHz, and the elongation of image A is approximately orthogonal to the line of separation between the lensed images, which is expected from a simple lens model. The separation between images A and B

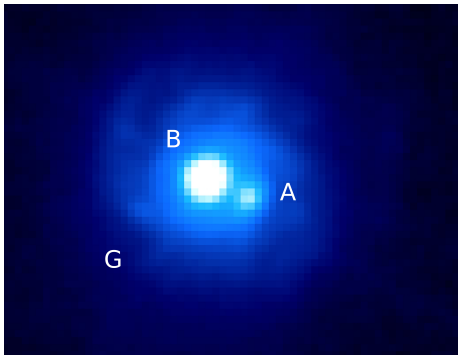

Figure 4.1: The optical image of the lensing system B0218+357. "G" indicates the lensing galaxy, which can be seen as a faint spiral. The lensed images of the background quasar are indicated by "A" and "B", which are 2 and 0.26 kpc away from the center of the lensing galaxy. Image credits: NASA/ESA and the Hubble Legacy Archive.

is 300 mas. This is very small compared to other known lensing systems, with only one known lensing system with a smaller separation (J0439+1634, 200 mas). Patnaik et al. (1993) measured the differential rotation measure between A and B based on narrow-band data at 8.4, 15, and 22 GHz, and found it to be 910 rad m^{-2} in the observer's frame. This RM value was derived using a simple linear fit of three polarization angles, consequently, the RM can be affected by the $n\pi$ ambiguity and by the presence of multiple polarized components.

The William Herschel Telescope measured the lensing galaxy's redshift by detecting narrow absorption and emission lines at $z = 0.684$ (Browne et al. 1993). The redshift of the lensed quasar was measured to be $z = 0.944 \pm 0.002$ based on five broad emission lines detected from observations obtained at the W.M. Keck Observatory by Cohen et al. (2003). York et al. (2005) found the lensing galaxy to be a face-on spiral using Hubble Space Telescope (HST) imaging.

Image A was found to be stronger in the radio, and it lies to the west. The weaker B image is surrounded by not well-resolved extended emission based on observation at 8.4 GHz with a resolution of 200 mas (Patnaik et al. 1993). They found the A/B flux density ratio to be 3.7:1. Both components have similar fractional polarizations of $\sim$ 7%. There is a change in flux density ratio by 10% in <1 yr. The lensing object in B0218+357 may be the bulge of a spiral galaxy. We note that Falomo et al. (2017) suggested that the face-on spiral galaxy is not the lensing galaxy but rather the emission of the host galaxy, as the absolute magnitude of the spiral galaxy is consistent with that of quasar host galaxies. Nevertheless, in this chapter, we assumed the general consensus presented above, that the lensing galaxy is a face-on spiral galaxy at $z = 0.684$.

Apart from its high redshift, this system is also interesting due to the rotation measure difference between the two lensed images. It is extremely large based on the narrow band polarization data, making it important to further investigate with broad-band polarization data to uncover the magnetic field strength of the lensing galaxy.

4.1.2 HII region in the lensing galaxy

The lensing system showed some unusual behavior in previous observations: image B is brighter in optical than image A (which can be due to dust obscuration in image A), but image A is brighter in the radio (Lehár et al. 2000; Jackson et al. 2000). The ISM in front of image A is rich in gas and dust. Falco et al. (1999) measured high differential (and total) extinction between the two images.

There is evidence of an HII region at $z = 0.684$ in the lensing galaxy in the sightline of image A. This was first proposed by Grundahl & Hjorth (1995), who argued a molecular cloud could absorb the optical light in image A, making it fainter than image B. HII regions are heated up and ionized by the ultraviolet radiation of young stars. They are a good tracer of the spiral arms in the Milky Way (Hou et al. 2009), and there are more HII regions in the spiral arms of external galaxies (e.g. M31, Azimlu et al. 2011). HII regions form embedded in or at the edge of molecular clouds (Zuckerman 1973; Krumholz & Matzner 2009).

Menten & Reid (1996) observed H_2CO absorption at $z = 0.685$ towards image A, but not towards image B. The HII region scenario is also supported by the location of image A: the line-of-sight might pass through a spiral arm of the lensing galaxy (2 kpc from the center).

Finally, Mittal et al. (2007) found that the (A/B) image flux-density ratio in the radio decreases from 3.9 to 2.0 over the observed frequency range from 15 GHz to 1.65 GHz. They argue this is due to free-free absorption by an HII region embedded in a molecular cloud in the lensing galaxy covering the entire structure of image A at 1.65 GHz. They assumed the HII region's temperature is in the range of 4 000 K and 10^4 K, and calculated the emission measure (EM) for these two extremes: 5.3 ± 0.9 and x 10^6 to 1.8 ± 0.3 x 10^7 cm^{-6}pc. This corresponds to $163 < n_e < 4243$ cm^{-3}, considering HII region sizes of 1 - 200 pc. The most meaningful values are the ones corresponding to a size of 200 pc as the assumption was that it completely covers image A: $163 < n_e < 300$ cm^{-3}. In reality, it can also be multiple HII regions in one molecular cloud.

The presence of an HII region or giant molecular cloud (GMC) is further supported by Hada et al. (2020), who found evidence of substructure lensing using millimeter VLBI observations. They argue that a compact clump of the size of $\sim$ 10 pc in the sightline of image A can explain the difference between the predicted and observed magnification ratios.

4.2 Data analysis and results

We analyzed the broadband spectro-polarimetric observations of the lensing system B0218+357 at 2 - 8 GHz taken by the VLA on 27.10.2012. The standard flagging and data reduction were done accordingly to Section 2.1.3. The flux and polarization calibrator was 3C138, the phase calibrator was J0204+3649, and the leakage calibrator was J0319+4130. We detect the two lensed images in total and polarized intensity, and we do not detect the lensing galaxy, as expected. The average signal to noise (S/N) is 43 in Stokes I, 35 in Stokes Q, and 25 in Stokes U. The two images start to blend

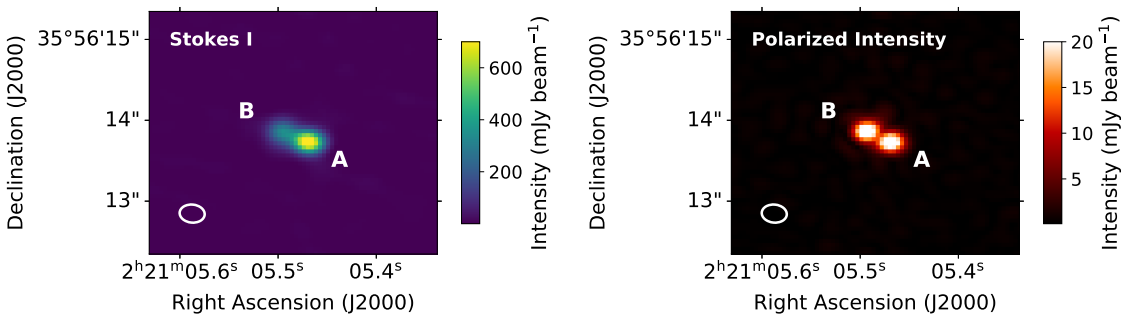

Figure 4.2: The Stokes I and PI image of the lensed images.

Table 4.1: Stokes QU fitting results of the lensing system B0218+357

	Image A	Image B
PF_1	0.03 ± 0.002	0.02 ± 0.001
PF_2	0.1 ± 0.003	0.09 ± 0.001
$PA_{0,1}$ (°)	10 ± 2	40 ± 1
$PA_{0,2}$ (°)	49 ± 2	41.5 ± 0.3
RM_1 (rad m^{-2})	-22 ± 7	90 ± 4
RM_2 (rad m^{-2})	-111 ± 25	656 ± 1
$\sigma_{RM,1}$ (rad m^{-2})	120 ± 3	71 ± 2
$\sigma_{RM,2}$ (rad m^{-2})	400 ± 9	80 ± 1

together at frequencies below ~ 7 GHz, but we can still separate them by jointly fitting two 2D-Gaussian functions at the positions of the images.

4.2.1 RM synthesis

We used CIRADA RM-tools (Purcell et al. 2020) to perform RM synthesis on the data. The leakage calibrator J0319+4130 has a residual polarization of 0.003%, which is the upper limit of the residual polarization leakage of the dataset.

The Faraday depth spectrum of the two images is shown in Fig. 4.3. We find that the peak of the Faraday depth spectrum in image A is $\phi_A = -30.7 \pm 0.8\,\mathrm{rad\,m^{-2}}$ and in image B is $\phi_B = 543.6 \pm 1.4\,\mathrm{rad\,m^{-2}}$. There is a clear difference in the Faraday depth spectrum of the two images.

4.2.2 Stokes QU fitting

We also perform Stokes QU fitting to retrieve the polarized properties of the lensed images. It was shown before that in the case of Faraday complex sources, Stokes QU fitting provides more accurate RMs (Farnsworth et al. 2011). I fitted several different models independently to the Stokes Q and U of the two lensed images, including single Faraday thin, double Faraday thin, single and double Burn slab with foreground, single and double external dispersion, single and double internal dispersion with foreground,

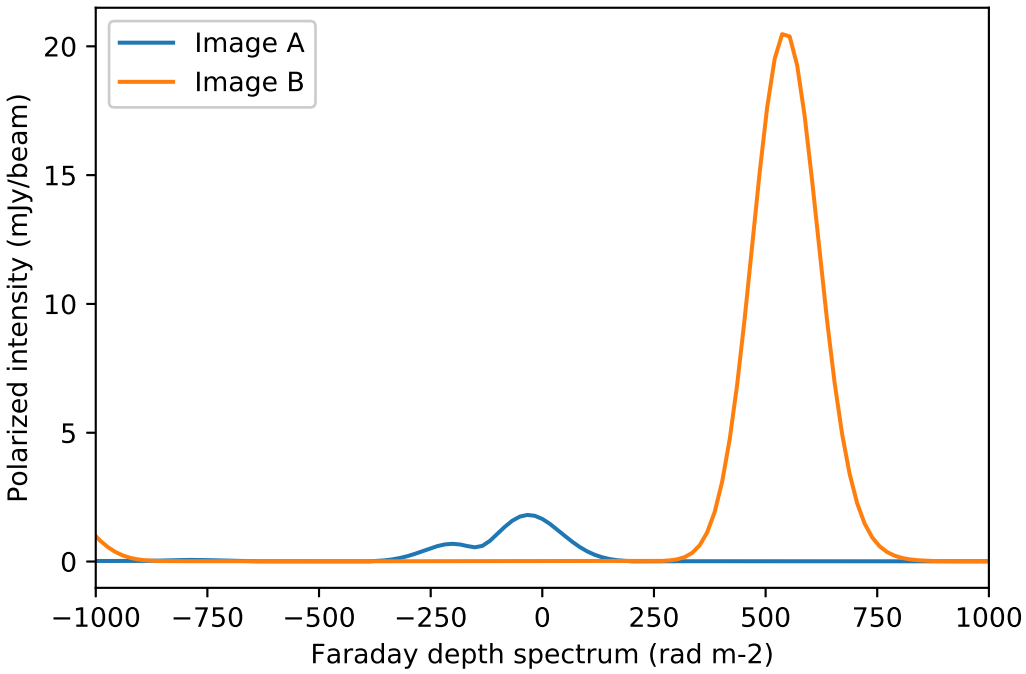

Figure 4.3: The clean Faraday depth spectrum of the two images.

and a model including both external and internal dispersion, which are all described in Chapter 2. The best model based on the Bayesian information criterion (BIC) was the double external dispersion model for both images. We show the final fits in Figs. 4.4 and 4.5, and the fitted parameters are listed in Table 4.1. The PF of the two polarized components is consistent between the two images, which suggests we found the same components in both. The Stokes QU fits of image B are well represented by the model, however, the fits of image A are less satisfactory.

The derived RMs are different from $\phi_{\rm A}$ and $\phi_{\rm B}$ from RM synthesis but still show a broad agreement. As Stokes QU fitting can lead to more accurate RMs (Farnsworth et al. 2011), we will use the RMs from our QU fitting to derive the magnetic field properties of the lensing galaxy.

In the rest of the chapter, we consider the polarized component with PF ~ 0.1 as the main component, as the other component's PF is very low (< 0.03).The RMs of the main polarization components are $+656 \pm 1$ and -111 $\pm$ 25 rad m^{-2}.

It is not surprising that the best polarization model has two polarized components, as previous high angular resolution radio VLBI observations (at 8.4 GHz, 15GHz, and millimeter wavelengths) show the core-jet structure of the background source in both lensed images (Patnaik et al. 1995; Biggs et al. 2003; Hada et al. 2020). This demonstrates the power of broadband polarization data and QU fitting: polarized components can be disentangled without having to resolve them spatially.

4.3 Discussion

4.3.1 RM difference between the lensed images

The RM difference between the main polarized components of the lensed images is $\Delta{\rm RM}_{\rm obs} = 767 \pm 25$ rad m^{-2} in the observer's frame. This is in broad agreement with the $\Delta{\rm RM}_{\rm obs} = 910$ rad m^{-2} from Patnaik et al. (1993) (they did not report uncertainty). The difference can be due to the different methods of deriving the RM. While Patnaik et al. (1993) only had three data points and derived RM with the linear fitting of PA vs. λ^2, we conducted broadband spectro-polarimetric observations and used QU fitting to Q and U vs. λ^2. The wavelength range of the two data sets is also different ($1 - 8$ GHz versus $8.4 - 22$ GHz), which can cause different RMs due to the Faraday complexity of the source. Patnaik et al. (2001) reported significantly higher absolute RMs, ${\rm RM_A} = -8920 \pm 250$ and ${\rm RM_B} = -7920 \pm 220$ rad m^{-2} from narrow band VLA observations in six bands between 1.4 and 43 GHz. However, Biggs & Browne (2018) reanalyzed their data and derived ${\rm RM_A} = -166 \pm 20$ and ${\rm RM_B} = 693 \pm 11$ rad m^{-2}. Biggs & Browne (2018) suggests Patnaik et al. (2001) accidentally switched Stokes Q and U, which led to the different RMs. Interestingly, Biggs & Browne (2018) also analyzed narrow band data at 5, 8.4, and 15 GHz, and found ${\rm RM_A} = -112 \pm 11$ and ${\rm RM_B} = 720 \pm 18$ rad m^{-2} from simple linear fitting, with values that are very close to the RM of the main polarized components from our QU fitting results.

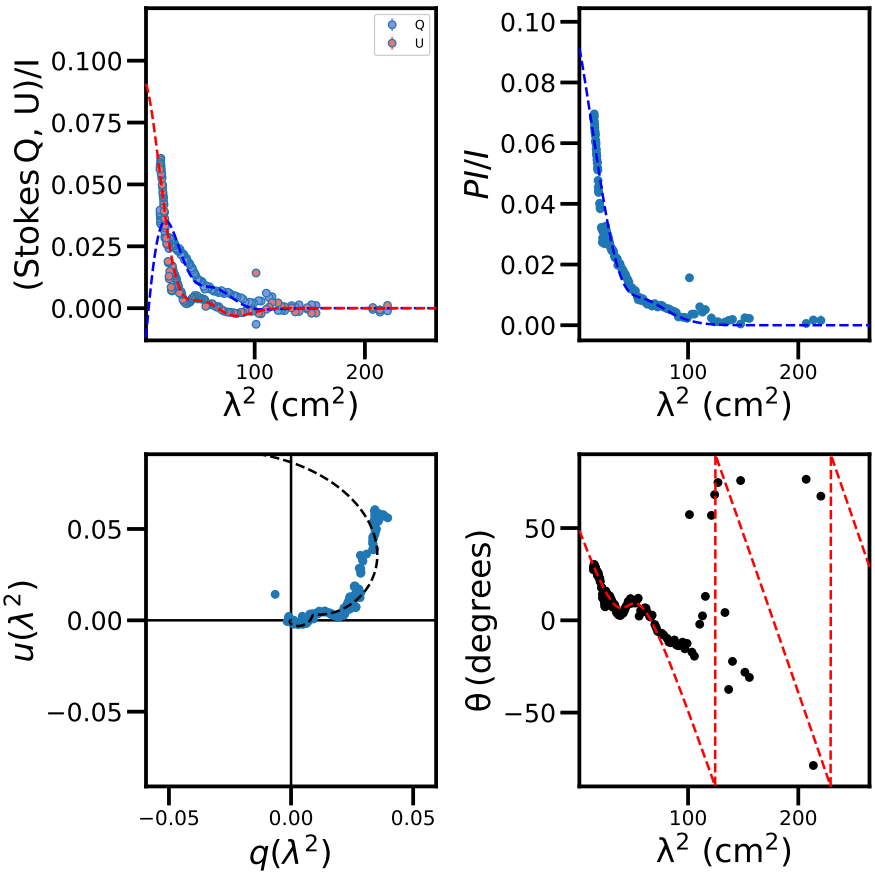

Figure 4.4: The Stokes QU fitting results of image A

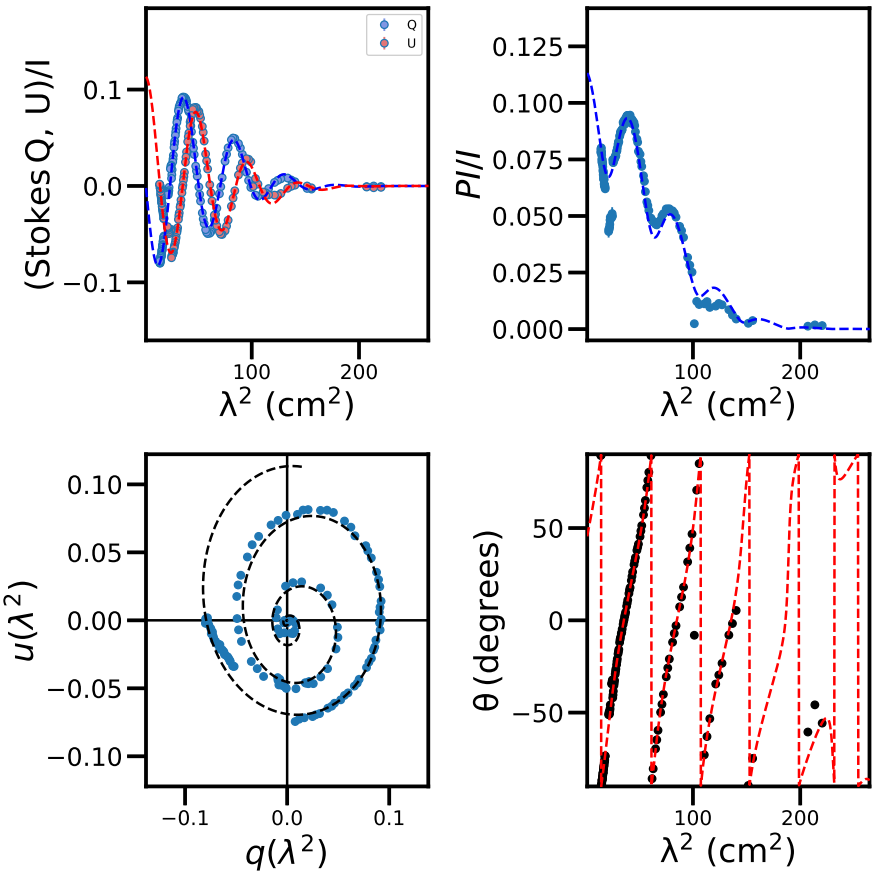

Figure 4.5: The Stokes QU fitting results of image B

$\Delta\mathrm{RM}_{\mathrm{obs}}$ can be converted to rest frame by

$$\Delta\mathrm{RM}_{\mathrm{rf}} = (1+z)^2\Delta\mathrm{RM}_{\mathrm{obs}} = 2217 \pm 72\,\mathrm{rad\,m^{-2}}. \tag{4.1}$$

If we assume that N_e and B are uncorrelated:

$$\Delta\mathrm{RM}_{\mathrm{rf}} = k(N_{e,\mathrm{B}}B_{||,\mathrm{B}} - N_{e,\mathrm{A}}B_{||,\mathrm{A}}). \tag{4.2}$$

4.3.2 Variability of the background source

The RM of the lensing images can be affected by the variability of the background source. Biggs & Browne (2018) obtained VLA monitoring data, which we use to explore this possibility. The changes in polarization properties are small on the scale of the time delay (11.3 ± 0.2 day). The largest changes in the observations show a PA variation of 2.5°, a PF variation of 0.5%, and an RM variation of 2 $\mathrm{rad\,m^{-2}}$ over 10 days. This RM variation is insignificant compared to the error of $\Delta\mathrm{RM}_{\mathrm{obs}}$ (25 $\mathrm{rad\,m^{-2}}$). Therefore, the variability of the background source does not affect the differential RM, and thus, the derived magnetic field strengths for the lensing system.

4.3.3 RM difference due to HII region or large-scale field?

The large RM difference of the lensing images is most likely due to either the large-scale magnetic field of the galaxy or the magneto-ionic medium of the HII region in image A. The RM difference is less likely to be due to a small-scale turbulent field in the galaxy (not related to the HII region), as the RM difference is large. From the small-scale field, σ_{RM} can cause an absolute $|\mathrm{RM}| = \frac{\sigma_{\mathrm{RM}}}{\sqrt{N}}$, where N is the number of turbulent cells. We can calculate $\Delta\sigma = \sqrt{\sigma_A^2 - \sigma_B^2} = 390\,\mathrm{rad\,m^{-2}}$, which is the additional Faraday dispersion image A undergoes. In the case of $N \sim 100$ (e.g. 50 pc cells in a path length of 5 kpc), this results in $|\mathrm{RM}| = 32\,\mathrm{rad\,m^{-2}}$, which is significantly smaller than the $\sim 800\,\mathrm{rad\,m^{-2}}$ difference between the lensed images.

4.3.4 RM due to the large-scale magnetic field

To derive the large-scale magnetic field strength, we need to know the inclination of the galaxy as precisely as possible, we need to have an assumption on the electron densities of the two sightlines and assume different large-scale magnetic field geometries. This subsection explores the different assumptions and the resulting magnetic field strengths.

Inclination The galaxy appears to be face-on. Wiklind & Combes (1995) determined a constraint on the inclination (i) based on the line width of the molecular absorption line observed toward the lensing system:

$$\sin(i) \leq \frac{0.05}{\cos(\theta)}, \tag{4.3}$$

Table 4.2: The derived magnetic field strengths for different magnetic field geometry models in the lensing galaxy of B0218+357. Image A is 2 kpc and image B is 0.2 kpc away from the plane of the galaxy. The halo field is assumed to be antisymmetric.

	Model	B_0 (μG)
Halo field	Constant	3 – 8
Disk field	Axisymmetric	2 – 20
	Bisymmetric	2 – 180

where θ is the azimuthal angle of image A (the angle measured from the major axis of the lensing galaxy). If image A is not near the minor axis of the lensing galaxy ($\theta = 90 \pm 15°$ or $270 \pm 15°$), the galaxy's inclination is $i < 10°$. Based on the lens modeling of Wucknitz et al. (2004), the position angle of the major axis of the lensing galaxy is $\sim -47°$. From this, we can calculate the azimuthal angle of image A, which results in $\theta \sim 133°$. This, in turn, gives us an inclination of $i < 4°$.

Assumptions on electron density One way we can estimate the electron density is by using X-ray absorption measurements. Acciari et al. (2022) measured that the hydrogen column density in image A at $z = 0.685$ is $0.81 \pm 0.09 \cdot 10^{22}$ cm^{-2} by assuming a model with hydrogen absorption in the lens in the sightline of image A. Ahnen et al. (2016) found strong hydrogen absorption at the lens in image A, but no strong absorption in image B. They modeled the X-ray spectrum with a hydrogen absorption at the redshift of the lens in image A, and no absorption in image B - they derived $N_{\mathrm{H,A}} = 2.4 \pm 0.5\ 10^{22}$ cm^{-2}. The two values only broadly agree, and Acciari et al. (2022) notes the actual absorption in the lens could have changed since the observations of Ahnen et al. (2016). This could be due to a change in the X-ray emitting source's size or its movement along the jet. In the rest of the Chapter, we use the results of Ahnen et al. (2016) because of the chance of changes in the absorption with time, and it is closer to when our observations were taken (2012).

We can turn this into the electron column density (N_e) by assuming an ionization fraction (f_{ion}). He et al. (2013) derived $f_{\mathrm{ion}} = 10^{+4}_{-3}\%$, which is the ionization fraction of the Galactic interstellar medium derived from the dispersion measure and X-ray column density of radio pulsars. With this ionization fraction, $N_H = 2.4 \pm 0.5 \cdot 10^{22}$ cm^{-2} turns into $N_e = 778 \pm 162$ pc cm^{-3}. However, since there may be an HII region in the sightline, f_{ion} can be much higher, so we should consider another extreme case of $f_{\mathrm{ion}} = 1$, and thus $N_e = 7777 \pm 1620$ pc cm^{-3}.

We also need an assumption on the N_e of image B. Based on Xu & Han (2015), who used the Milky Way n_e model NE2001 (Cordes & Lazio 2002), the range of electron column densities in a face-on spiral galaxy is ~ 5 – 100 pc cm^{-3}. This is much lower than the N_e calculated from absorption in image A (which could be excessive due to an HII region).

Different magnetic field geometry models We investigate different magnetic field geometry models to derive the magnetic field strength of the lensing galaxy.

The inclination plays an important role in the type of model we need to consider:

- if $i = 0°$, the RM difference is only due to the vertical magnetic fields in the halo of the galaxy. We can consider different models for the halo field: constant, $1/h$, and exponential scaling, all with symmetric and antisymmetric cases, same as in Chapter 3. However, for these, we need the vertical distance of the images from the plane of the lensing galaxy (h); we assumed $h = 0$ kpc. This means the different geometry models will give the same result (the vertical scaling does not matter), and we only consider the constant model. It is interesting to note that in the case of symmetric vertical magnetic fields if the n_e is also symmetric below and above the plane, we would not be able to detect RM from the lensing galaxy (not only the RM difference but any RM at all, as the RM would get canceled from below and above the disk in each line of sight). Thus, if we assume that n_e is not different below and above the disk, the magnetic field has to be antisymmetric (i.e. it has a different direction below and above the disk). However, this is only true if i is exactly 0. With the assumptions listed above, the antisymmetric constant model and assuming $f_{\rm ion} = 0.1$ gives a vertical magnetic field of $3 - 8$ μG.

- if $0 < i < 10°$, the RM difference is due to both the disk field and the halo field. This scenario is more realistic, as the lensing galaxy is unlikely to be precisely face-on. For simplicity, in this case, we assume the RM is only due to the disk field.

  Disk fields:

  B field strength is described with an exponential: $B_c(r) = B_0 \exp -r/r_{\rm mag}$.

  The field structure can be

  – axisymmetric

  $$\begin{aligned} C_1 &= \cos p_0 \cos\theta_A + \sin p_0 \sin\theta_A \\ C_2 &= \cos p_0 \cos\theta_B + \sin p_0 \sin\theta_B, \end{aligned} \tag{4.4}$$

  – or bisymmetric

  $$\begin{aligned} C_1 &= \cos p_1 \cos\theta_A \cos(\theta_A - \beta_1) + \sin p_1 \sin\theta_A \cos(\theta_A - \beta_1) \\ C_2 &= \cos p_1 \cos\theta_B \cos(\theta_B - \beta_1) + \sin p_1 \sin\theta_B \cos(\theta_B - \beta_1), \end{aligned} \tag{4.5}$$

  where θ_A and θ_B are the azimuthal angles of the sightlines A and B, C_1 and C_2 depend on the field geometry, $p_0 = -20°$ (typical for galaxies in the local volume), $p_1 = 20°$ (adopted to be this), and $\beta_1 = 0°$ determines the azimuth where the bisymmetric mode is maximum (which gives a lower limit on the bisymmetric field strength). The equations were taken from Mao et al. 2017).

  These models, when used together with the assumption of $f_{\rm ion} = 10\%$, give unrealistically high magnetic field strengths of > 20 μG, reaching up to ~ 100 μG

in the axisymmetric and up to a few 1000 μG in the bisymmetric case. (This is the case even when trying with different azimuthal angles.) In the case of $f_{\rm ion} = 1$, and $i = 10°$, the B field strength is $2 - 8$ μG in an axisymmetric, and $2 - 73$ μG in a bisymmetric case (if the images are not exactly on the minor axis). In the case of a smaller inclination $i = 4°$, the B field strength is $5 - 20$ μG in an axisymmetric and $5 - 180$ μG in a bisymmetric case.

For the disk field models, apart from the inclination, the azimuthal angles also significantly affect the results.

In summary, the most realistic scenario among the above models is that the lensing galaxy is not precisely face-on, and we detect the disk field. The bisymmetric model often results in unrealistically high magnetic field strengths, as we would expect at most a few times 10 μG based on the dynamo theory and nearby galaxies. The axisymmetric model results in realistic values for most of the parameters.

Implications on dynamo theory The mean-field dynamo theory (Ruzmaikin et al. 1988) predicts large-scale magnetic field strengths of $\sim$ μG. We can constrain the large-scale magnetic field's amplification time scale using the measured magnetic field strength. The e-folding time can be derived using the equation (similar to Mao et al. 2017):

$$\tau_{\rm dynamo}[\rm Gyr] = \frac{t}{\ln(B_{\rm disk,z=0.7}/B_{\rm seed})}, \tag{4.6}$$

where $B_{\rm seed}$ ($3 \cdot 10^{-16}$ G, Neronov & Vovk 2010) is the seed magnetic field of the mean-field dynamo, $t = 4.12$ Gyr is the time that passed between when the disk settled into equilibrium ($z = 2$) and the redshift of the lensing galaxy ($z = 0.685$), and $B_{\rm disk,z=0.7}$ is the disk field strength at $z = 0.685$. Using the lowest B strength of 2μG, and assuming the magnetic field has already saturated before $z = 0.685$, we derive an upper limit on the dynamo e-folding time: $\tau_{\rm dynamo} < 2 \cdot 10^8$ yr.

Considering a disk galaxy with an average angular velocity of $\Omega = 20$ km s^{-1} kpc^{-1} and total mass of $M \sim 10^{11} M_\odot$, Arshakian et al. (2009) derives an e-folding time of $\sim 2.5 \cdot 10^8$ yrs, which is larger than our result. If our magnetic field strengths are not overestimated, this would mean the amplification of the magnetic field was faster than expected from the dynamo theory. This could be due to various reasons; for example, the disk settled into equilibrium earlier than $z = 2$. This is not impossible; calculating with $\tau_{\rm dynamo} \sim 2.5 \cdot 10^8$ yrs, it would mean the disk settled into equilibrium at $z \sim 3.5$. Recent results of the *James Webb Space Telescope* show galaxy disks at very high redshifts ($z \sim 2 - 3$, Ferreira et al. 2022; Labbé et al. 2023).

Dwarf galaxies (i.e. low mass halos) also develop a large-scale field earlier than normal-size galaxies (Arshakian et al. 2009), which they define as having a total mass of $M \sim 10^{10}\, M_\odot$. However, the total mass enclosed in the Einstein radius of the lensing galaxy is $1.8 \cdot 10^{10}$ M$_\odot$ (Wiklind & Combes 1995), which is already larger than that, even though it only accounts for the mass within the Einstein radius ($\sim$ 1 kpc). Thus,

our lensing galaxy is possibly closer to the case of a galaxy of $M \sim 10^{11} M_{\odot}$, and not a dwarf galaxy, so this can not cause the earlier development of a large-scale field.

Comparison with nearby galaxies The average equipartition field strength is 4 - 19 μG in nearby galaxies (Beck & Wielebinski 2013; Beck 2015a), which is close to the possible magnetic field strengths from the axisymmetric model. The bisymmetric model often results in magnetic field strengths that are significantly stronger but also cover the range of values found in nearby galaxies. Observations of nearby galaxies show most have an axisymmetric field (e.g. M31, NGC 253, IC 342 - Fletcher et al. 2004; Heesen et al. 2009; Beck 2015b), and Mao et al. (2017) also found that an axisymmetric field is more likely in the case of the lensing galaxy of CLASS B1152+199. Our results are also consistent with this, as a wider range of parameters result in realistic magnetic field strengths in the axisymmetric case.

4.3.5 RM difference due to the HII region

Mittal et al. (2007) found the most likely electron densities in the HII region are in the range of $163 < n_e < 300$ cm^{-3}. To get the average electron density along the line of sight ($\langle n_e \rangle$), we need to know the filling factor (f). According to Harvey-Smith et al. (2011):

$$\langle n_e \rangle = f n_e, \tag{4.7}$$

and $f = 0.1$.

The assumption of Mittal et al. (2007) was that the HII region or the molecular cloud it is associated/embedded in covers the entire image A at the redshift of the lensing galaxy. This size is 200 pc, so we assume the path length is $L = 200pc$.

Finally, if we assume the RM difference is entirely due to the HII region in sightline A (i.e. there is no RM from the lensing galaxy in the sightline of image B):

$$B_{||} = \frac{\mathrm{RM}}{0.81 \langle n_e \rangle L} = 0.4 - 0.7\,\mu\mathrm{G} \tag{4.8}$$

In the case of smaller HII region sizes, the n_e would be larger (Mittal et al. 2007). The highest possible $B_{||}$ would be 9.6 μG (L = 1 pc, n_e = 2302 cm^{-3}).

Previous studies suggest that the large-scale field structure is preserved in molecular clouds (see Li et al. 2014, Clemens et al. 2018, and Devaraj et al. 2021). Therefore, the $B_{||}$ can be representative of the large-scale field in the line of sight, which is mostly the vertical field.

Observations of HII region RMs - comparison to our HII region scenario Based on observations of Galactic HII regions, the typical magnetic field strength of HII regions is between $\sim$ 2 to 6 μG. The excess RM from HII regions can be up to $\sim$ 1200 rad m^{-2} (if we do not consider the large RM from Rodríguez et al. 2012, as it might be due to the background source, not the HII region). The RM difference in our system is almost double the largest value reported by Costa et al. (2016). The small $B_{||}$

is likely due to the galaxy's face-on orientation and, thus, the HII region's orientation, as the vertical fields of a galaxy are weaker than the azimuthal fields in the disk. It is also worth noting that the n_e values from previous works are smaller on average than the results from Mittal et al. (2007), which could also cause a smaller RM compared to previous works.

In the rest of this subsection, we give an overview of previous studies on the RM and magnetic field of HII regions:

- Sun et al. (2007) used Faraday rotation to estimate the strength of the ordered magnetic field along the line of sight to two diffuse H II regions, G124.9+0.1 and G125.6-1.8. In the case of G124.9+0.1 (with an estimated electron density of 1.6 cm^{-3}), this magnetic field was found to be +3.9 μG, while in the case of G125.6-1.8 (with an upper limit of the electron density of 0.84 cm^{-3}), a lower limit of +6.4 μG was obtained.

- Harvey-Smith et al. (2011) investigated the line-of-sight magnetic fields in five large-diameter Galactic H II regions. They estimated the strength and orientation of the magnetic field along 93 individual sight lines through the H II regions and found $75 < |\mathrm{RM}| < 300$ rad m^{-2}, which corresponds to 2 to 6 μG.

- Rodríguez et al. (2012) measured RM = $+5100 \pm 900$ rad m^{-2} (total observed RM) of NGC6334A, which corresponds to a line-of-sight average magnetic field of $B_{||} = +36 \pm 6 \mu$G. We note that some of the RM might be due to the extragalactic background source, and the magnetic field strength of the HII region might be overestimated.

- Costa et al. (2016) measured an excess RM of +40 to +1200 rad m^{-2} in the Rosette nebula.

- Raycheva et al. (2022) combined polarized radio synchrotron emission data from the S-band Polarization All-Sky Survey (S - PASS) at 2.3 GHz with Hα data from the Southern Hα Sky Survey Atlas. They found that Sh2-27 has an excess RM median of 126 $\pm$ 3.1 rad m^{-2}, and $59 < |\mathrm{RM}| < 443$ rad m^{-2}. They estimated the median value of n_e as 7.3 $\pm$ 0.1 cm^{-3}, and the median value of $B_{||}$ as -4.5 ± 0.1 μG, which is comparable to the magnetic field strength in diffuse ISM.

4.4 Conclusions

We measure the differential RM between the lensed images of the lensing system B0218+357, which is either due to the large-scale field of the lensing galaxy ($z = 0.685$) or the magneto-ionic medium of an HII region in the lensing galaxy. Depending on which of these scenarios is true, this is the highest redshift detection of the coherent large-scale field of a galaxy or the magnetic field of an HII region to date at $z = 0.685$.

We explore the possible magnetic field strengths using different large-scale magnetic field geometry models. The most likely scenario is that the RM is due to an axisymmetric disk field of 2 – 20 μG. This is consistent with nearby galaxies, and we find that

the mean-field dynamo has already built up a large-scale field at $z = 0.685$. Based on this, the e-folding time of the dynamo is lower than expected, possibly meaning that the disk settled into equilibrium sooner, at $z \sim 3.5$. This is not surprising in the light of recent JWST detections of disk galaxies at high redshift ($z \sim 3 - 6$, Ferreira et al. 2022).

Assuming the RM difference is due to the magneto-ionic medium of the HII region, its line-of-sight magnetic field strengths also fall into a similar range of 0.4 – 9.6 μG, and is also in broad agreement with the magnetic field strength of Galactic HII regions.

Chapter 5

The dispersion measure and rotation measure from fast radio burst host galaxies based on the IllustrisTNG50 simulation

This chapter is based on the article titled "The dispersion measure and rotation measure from fast radio burst host galaxies based on the IllustrisTNG50 simulation", which was submitted to Astronomy & Astrophysics on 13$^{\text{th}}$ July 2023. The manuscript in its original format can be found in Appendix III. In this Section, I provide a summary, and the content of the submitted manuscript formatted to fit the template of the thesis. As the lead author of this paper, I have carried out all the data reduction and analysis. The full author list is T. Kovacs, S. A. Mao, A. Basu, and Y. K. Ma, R. Pakmor, L. Spitler, and C. R. H. Walker.

Contents

Summary

Fast radio bursts (FRB) will become important cosmological tools in the near future (Akahori et al. 2016; Macquart et al. 2020), as the number of observed FRBs is increasing rapidly with more surveys being carried out (Hallinan et al. 2019; CHIME Collaboration et al. 2022). Soon a large sample of FRBs will have available dispersion measures (DM) and rotation measures (RM), which can be used to study the cosmic baryon density and the intergalactic magnetic field (IGMF). However, the observed DM and RM of FRBs consists of multiple contributions which must be quantified to estimate the DM and RM of the intergalactic medium (IGM).

In this paper, we estimate one such contribution to DM and RM using a simulation: that of FRB host galaxies (DM_{host}, RM_{host}). This contribution is difficult to constrain observationally, thus it is important we derive it in a different way. We show how DM_{host} and RM_{host}) changes with redshift, galaxy type, and the stellar mass of the galaxies. We also investigate its dependence on galaxy inclination, and on an FRB's offset from the center of the galaxy.

We used the IllustrisTNG50 state-of-the-art cosmological MHD simulations (Pillepich et al. 2018; Nelson et al. 2019a). We selected 16 500 galaxies at redshifts of $0 \leq z \leq 2$, with stellar masses in the range $9 \leq \log(M_*/M_\odot) \leq 12$. In each galaxy, we calculate the DM and RM contributions of 1000 sightlines, and from these, construct DM and RM probability density functions. We also calculate magnetic field maps, including the total magnetic field strength, and the strength of the different components (radial, azimuthal, and vertical) of the magnetic field for each galaxy.

We find that the rest frame DM distributions of all galaxies at a given redshift can be fitted by a lognormal function, and its median and width increases as a function of redshift: median $DM_{host,rf} = 89 \cdot z^{0.77} + 41$ pc cm^{-3}. The rest frame RM distribution is symmetric, with median $RM_{host,rf}$=0 rad m^{-2}, and it can be fitted by the combination of a Lorentzian and two Gaussians. We define distribution width of the rest frame RM PDF ($w_{RM,rf}$) as the difference between the 84th and 16th percentile, where the PDF contains 68% of the data. The redshift evolution of this width can be fitted by a curved power law: $w_{RM,rf} = 270 \cdot z^{1.3-0.6 \cdot z} + 123$ rad m^{-2} The parameters of these functions change for different subsets of galaxies with different stellar mass, inclination, and FRB

offset. These changes are due to an increasing n_e with redshift, SFR, and stellar mass, and we find a more ordered B field at lower z compared to higher z, suggested by more galaxies with B field reversals and B fields dominated by random B field at higher z.

We apply our method to a localized FRB, FRB190608. We obtain DM and RM host contributions that are consistent with observations.

We estimate the FRB host DM and RM contributions in the observer's frame, which can be used in the future to isolate the IGM's contribution from the observed DM and RM of FRBs. The observed DM stays constant, while the observed RM PDF becomes narrower with redshift. This means that the absolute value of the observed RM of host galaxies becomes lower, closer to 0 $\mathrm{rad\,m^{-2}}$, at higher redshift, making it easier to constrain their RM contribution. We predict that to constrain an $\sigma_{\mathrm{RM,IGM}}$ of 2 $\mathrm{rad\,m^{-2}}$ to 95% confidence level we need to observe 95 000 FRBs at $z = 0.5$, but only 9 500 FRBs at $z = 2$.

As the lead author of this manuscript, I wrote the pipeline used to calculate RM, DM, and the magnetic field strength maps of galaxies, and ran it on 16 500 galaxies. In my pipeline, I used functions from a python package coded by R. Pakmor to load in simulation snapshot and halo catalog data, and to calculate integrals in the simulation. I carried out the analysis, constructed probability density functions of RM and DM, inspected the changes in them across redshift and other galaxy properties, and interpreted these changes. During the creation of the pipeline and while doing the analysis I had meetings with the co-authors, and considered and implemented their suggestions. I wrote the manuscript, and received and implemented comments from the co-authors.

5.1 Introduction

The seeds of intergalactic magnetic fields (IGMF) are an open question in astrophysics (Baym et al. 1996; Brandenburg & Subramanian 2005; Kahniashvili et al. 2012, 2013). They could be primordial (magnetic fields that already existed soon after the Big Bang), astrophysical (magnetic fields that were caused by galaxy evolution, e.g. feedback processes, star formation, active galactic nuclei), or both. The true scenario could also have implications on the dynamics of inflation (due to inflationary magnetogenesis, e.g. Ferreira et al. 2013; Vazza et al. 2021) and the physics of the early Universe. Recent measurements exclude purely astrophysical and purely primordial origins, and find an upper limit of $\sim 4\,\mathrm{nG}$ on the co-moving magnetic field strength based on Cosmic Microwave Background (CMB) anisotropies (Planck Collaboration et al. 2016c) and low-frequency radio observations with the Low-Frequency Array (LOFAR) of close pairs of extragalactic radio sources (O'Sullivan et al. 2020). Hackstein et al. (2016) found 0.1 nG magnetic field in voids based on the observed degree of isotropy of ultra high energy cosmic rays (UHECR, Sigl et al. 2003). Carretti et al. (2023) measured the magnetic field of filaments with LOFAR, and inferred an IGMF of 0.04–0.11 nG on Mpc scales. Many of these methods measure the magnetic field only in filaments, thus we have limited constraints on the low density Universe. Fast radio bursts (FRB) are a promising, unique tool for measuring the IGMF as they account

for every ionized baryon along a line of sight (Akahori et al. 2016, Zheng et al. 2014).

FRBs are millisecond radio transients; some are one-off sources and some are confirmed repeaters. Since the first discovery by Lorimer et al. (2007), an increasing number of FRBs have been observed; for example, there are 118 unique FRB sources listed in the FRB catalogue by Petroff et al. (2016)[1], and the Canadian Hydrogen Intensity Mapping Experiment (CHIME) observed over 400 one-off FRBs (CHIME/FRB Collaboration et al. 2021). The Five-hundred-meter Aperture Spherical radio Telescope (FAST) observed 1652 bursts by one repeating FRB, FRB121102 alone (Li et al. 2021, Spitler et al. 2016).The most complete catalogue is the Transient Name Server (Yaron et al. 2020).

FRBs experience propagation effects due to the intervening material they pass through, causing a dispersion in the observed pulse (Cordes & Chatterjee 2019), which is characterized by the dispersion measure (DM, see below for more details). Some FRBs are linearly polarized (∼20 known to date), and thus also undergo Faraday rotation (Masui et al. 2015), which causes the angle of polarization to change upon passing through a magneto-ionic medium. This is characterized by the rotation measure (RM, see below for more details). The observed DM of FRBs (100 – 2600 pc cm^{-3}, based on the FRB catalogue, Petroff et al. 2016) are larger than expected due to the Milky Way material alone, suggesting they are extragalactic (Thornton et al. 2013). Recently, more and more FRBs have been localized to distant galaxies (see e.g. Chatterjee et al. 2017, Bannister et al. 2019, and Marcote et al. 2022). The |RM| of FRBs have a wide range from 1.5 to 10^5 rad m^{-2} (Petroff et al. 2019, Michilli et al. 2018). Unfortunately, many early FRB detections did not record polarization data, resulting in only a small sample of FRBs (∼20) with measured RMs. In the future many surveys will also analyze the polarized signals of their detections (e.g. CHIME, Mckinven et al. 2021). Due to their extragalactic origin and high event rate (predicted to be $10^3 - 10^4$ per day over the whole sky above a fluence of ∼2 Jy ms, Bhandari et al. 2018), FRBs can be used as cosmological probes. They can detect the baryonic content along the line-of-sight (LOS) into the distant Universe, and are a powerful tool of cosmic magnetism (e.g. IGMF, Akahori et al. 2016, Zheng et al. 2014), because they provide information on both DM and RM simultaneously. Furthermore, they provide a unique tool for the study of the missing baryons (McQuinn 2014), cosmological parameters (Macquart et al. 2015, Gao et al. 2014, Zhou et al. 2014), Hubble constant (H_0) measurements (James et al. 2022), the intergalactic medium (IGM), and the interstellar medium (ISM) of our or other galaxies (e.g. Mannings et al. 2022).

The DM is the integral of the free electron density (n_e [cm^{-3}]) along the LOS (l [pc]) from a source to the position of an observer:

$$\mathrm{DM} = \int_{\mathrm{source}}^{\mathrm{observer}} n_e \mathrm{d}l. \tag{5.1}$$

Because DM is an integral along the entire LOS, there are multiple contributors to the observed DM of FRBs ($\mathrm{DM_{obs}}$): the immediate source environment ($\mathrm{DM_{source}}$),

[1] http://www.frbcat.org

the host galaxy ($\mathrm{DM_{host}}$), the IGM ($\mathrm{DM_{IGM}}$), and the Milky Way ($\mathrm{DM_{MW}}$). Thus the observed DM of a source at redshift z_{host} (i.e. $z_{\mathrm{source}} = z_{\mathrm{host}}$) can be described in the following way:

$$\mathrm{DM_{obs}} = \frac{\mathrm{DM_{source,rf}}}{(1+z_{\mathrm{host}})} + \frac{\mathrm{DM_{host,rf}}}{(1+z_{\mathrm{host}})} + \mathrm{DM_{IGM}} + \mathrm{DM_{MW}}, \tag{5.2}$$

where $\mathrm{DM_{source,rf}}$ and $\mathrm{DM_{host,rf}}$ are in the rest-frame, and can be converted to the observer's frame by the standard correction of $1/(1+z_{\mathrm{host}})$, because of the cosmological time dilation and the frequency shift. Below, we discuss the magnitude of the different components' DM contributions. There are many different FRB progenitor models, but the majority assume a connection to neutron stars (Platts et al. 2019).In the case of a young neutron star progenitor, the local environment of an FRB can be a supernova remnant (SNR), which theoretical models predict can result in a wide range of DMs (0.1 – 1000 $\mathrm{pc\,cm^{-3}}$, Piro & Gaensler 2018). In the case of a magnetar, its near wind zone would only contribute $10^{-6}\,\mathrm{pc\,cm^{-3}}$ to $\mathrm{DM_{source}}$ (Lyutikov 2022). $\mathrm{DM_{MW}}$ has contributions of the Milky Way and its dark matter halo. The DM from the Milky Way can be estimated from models based on Galactic pulsar measurements (e.g. NE2001: Cordes & Lazio 2002, YMW: Yao et al. 2017) and is usually below $\sim 200\,\mathrm{pc\,cm^{-3}}$ at Galactic longitudes $|l| > 120°$, but can reach $\sim 1700\mathrm{pc\,cm^{-3}}$ at $|l| < 60°$. However, these lack the virialized dark matter halo with a hot gaseous atmosphere, which would give an additional contribution to the DM. Dolag et al. (2015) estimate this to be $30\,\mathrm{pc\,cm^{-3}}$, but Keating & Pen (2020) suggest it could be as small as $10\,\mathrm{pc\,cm^{-3}}$. The contribution of the host galaxy can vary from $\sim$10 pc $\mathrm{cm^{-3}}$ to a few thousand pc $\mathrm{cm^{-3}}$ and depends on the galaxy type and FRB location (see e.g. Zhou et al. 2014, Walker et al. 2020, and Zhang et al. 2020). $\mathrm{DM_{IGM}}$ increases with redshift (Macquart et al. 2020), and Akahori et al. (2016) shows it can reach $\sim$ 1000 pc $\mathrm{cm^{-3}}$ at z=1, and a few thousand pc $\mathrm{cm^{-3}}$ at z=5. However, its exact value can be different if the LOS goes through a dense region, e.g. a cluster or a filament.

Once we can isolate the DM contribution of the IGM, it can be an excellent tracer for the ionized cosmic baryon density (Akahori et al. 2016, Macquart et al. 2020). The majority of the baryonic content of the Universe is in a diffuse state, which is difficult to directly observe (Cen & Ostriker 1999, Kovács et al. 2019). Various techniques have been used previously to detect this component of baryonic matter: absorption studies of quasars (Nicastro et al. 2018), the Sunyaev-Zel'dovich effect (de Graaff et al. 2019) and direct X-ray observation of filaments (Eckert et al. 2015). Recently, Anderson et al. (2021) showed RM grid studies can also trace these baryons. However, absorption studies are more sensitive to lower temperature gas ($<10^5$ K), while X-ray measurements only detect hot ionized plasma (10^7 K), and the Sunyaev-Zel'dovich method can only study the gas in filaments, missing some of the baryons. On the other hand, FRBs are a powerful cosmological probe that considers every ionized baryon, both in the cold and hot (but not relativistic) media, as the DM of FRBs provides us with information about the electron column density along the full line-of-sight (McQuinn 2014; Macquart et al. 2020).

The RM of a source is defined similarly to DM, but the integral is weighted by the

LOS component of the magnetic field ($B_{\parallel}$ [μG], parallel to the LOS):

$$\mathrm{RM} = k \int_{\mathrm{source}}^{\mathrm{observer}} B_{\parallel} n_e \mathrm{d}l, \tag{5.3}$$

where $k = 0.81\ \mu\mathrm{G}^{-1}$.

Similar to DM, the observed RM of a source at redshift z_{host} also consists of the components from the source ($\mathrm{RM_{source}}$), host ($\mathrm{RM_{host}}$), IGM ($\mathrm{RM_{IGM}}$), and the Milky Way ($\mathrm{RM_{MW}}$):

$$\mathrm{RM_{obs}} = \frac{\mathrm{RM_{source,rf}}}{(1+z_{\mathrm{host}})^2} + \frac{\mathrm{RM_{host,rf}}}{(1+z_{\mathrm{host}})^2} + \mathrm{RM_{IGM}} + \mathrm{RM_{MW}}. \tag{5.4}$$

where $\mathrm{RM_{source,rf}}$ and $\mathrm{RM_{host,rf}}$ are in the rest-frame, and can be converted to the observer's frame by the standard correction of $1/(1+z_{\mathrm{host}})^2$. $|\mathrm{RM_{source}}|$, considering again a neutron star progenitor, could be between 10^{-2} and 10^{6} rad m^{-2} (Piro & Gaensler 2018). The near wind zone of magnetars can produce large RMs (magnitude of 10^5 rad m^{-2}, Lyutikov 2022), and the RM can vary greatly, even changing sign with time. The RM contribution of the MW can be estimated from all-sky Galactic RM maps (e.g. Oppermann et al. 2012; Hutschenreuter et al. 2022). $|\mathrm{RM_{MW}}|$ is below 150 rad m^{-2} in a large fraction of the sky, but can exceed 3000 rad m^{-2} towards the inner disk ($l \in (270°, 90°)$). The RM contribution of the host galaxy can vary widely depending on the type of the host galaxy: Hackstein et al. (2019) showed the different $|\mathrm{RM_{host}}|$ contributions from galaxy models of a Milky Way-like galaxy and a starburst dwarf galaxy, which can range from 10^{-4} to 10^{4} rad m^{-2}, and Hackstein et al. (2020) found an $|\mathrm{RM_{host}}|$ contribution of ≤ 1000 rad m^{-2} using galaxy models from Rodrigues et al. (2019). Both Hackstein et al. (2019) and Akahori et al. (2016) show that $|\mathrm{RM_{IGM}}|$ increases towards higher redshift, predicting it to be ≤ 10 rad m^{-2}. If we can isolate the contribution of the IGM from the other contributions in the observed RM, we can study the IGMF.

To be able to study the cosmic baryon density and the IGMF using the DM and RM measurements of FRBs, we need to constrain the other components, as they can all contribute significantly to the observed DM and RM mentioned above. In this paper, we focus on constraining the contribution of host galaxies. To do this, we calculated the DM and RM contribution of galaxies selected from the TNG50 simulation of the IllustrisTNG project (Pillepich et al. 2018, Nelson et al. 2019a), a state-of-the-art cosmological magnetohydrodynamic simulation, which contains thousands of galaxies at every redshift, of different types of galaxies, with relatively high resolution (70-140 pc), allowing us to provide good DM and RM estimates. We used 16.5 million sightlines to construct DM and RM Probability Density Functions (PDF) for different galaxy types to account for a large variety of possible FRB host galaxies.

This paper is organized as follows: in Section 5.2, we describe the simulation we used, our galaxy selection, and our DM and RM calculation methods. In Section 5.3, we show how the DM and RM distributions depend on different galaxy properties, for example, redshift, stellar mass, and inclination. In Section 5.4, we discuss the possible

reasons behind the trends we show in Section 5.3 and compare our results to previous works. In Section 5.5, we investigate how the observed DM and RM of hosts changes with redshift, and its implications on measuring the RM of the IGM. In Section 5.6, we show an example of how we can estimate the host contribution of a localized FRB (using FRB190608). In Section 5.7, we summarize our findings.

5.2 Methods

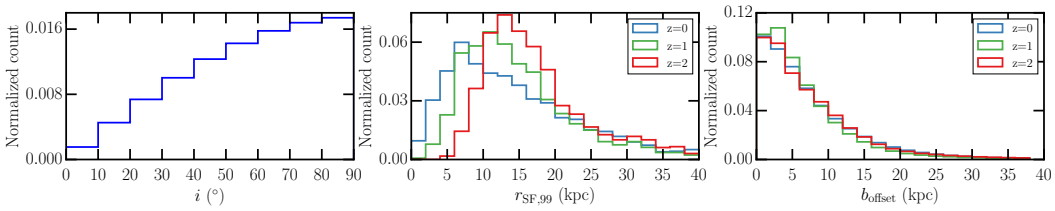

Figure 5.1: **Left:** The inclination distribution of the galaxies, which is the same at every redshift. We define the inclination as the angle between the total angular momentum vector of the galaxy's stars and the LOS. **Middle:** The distribution of galaxy radii at different redshifts. This changes slightly with redshift, with larger radii at higher redshift. **Right:** The distribution of the projected offsets ($b_{\rm offset}$) of the FRBs with respect to the center of their host galaxy. There are more FRBs in the center of galaxies, and the distribution does not change significantly with redshift.

In this section we summarize the TNG50 simulation of the IllustrisTNG project, we describe the selection process for our sample galaxies, and how we place FRBs within these galaxies. Finally, we show how we calculate the rest frame DM and RM host contributions of the galaxies.

5.2.1 TNG50

We have used IllustrisTNG, a state-of-the-art cosmological magnetohydrodynamical (MHD) simulation (Pillepich et al. 2018, Nelson et al. 2019a) to estimate the distribution of the DM and RM contribution of FRB host galaxies. The TNG project consists of three different simulation cubic volumes: TNG300, TNG100, and TNG50 with side length of approximately 300, 100, and 50 Mpc, respectively. We chose TNG50-1 because it has the highest physical resolution compared to the TNG300 and TNG100, and the other subruns of TNG50: TNG50-2 etc. (Pillepich et al. 2019, Nelson et al. 2019b).

In these simulations, the physical resolution depends on the gas density, which results in higher resolutions and larger numbers of cells in high-density regions (e.g. galaxies), and lower resolutions and numbers of cells in the IGM. Since the DM and RM of FRBs are calculated as a LOS integral, passing through the galaxy as a pencil beam, we need the highest physical resolution possible for our study, as in reality both n_e and $B_{||}$ can change on small scales (a few 10s of pcs) due to turbulence (Haverkorn

Table 5.1: The number of galaxies selected at each redshift. All galaxies have a stellar mass ($\log(M_*/\mathrm{M}_\odot)$) between 9 and 12.

z	N_{halos}
0.0	1849
0.1	1834
0.2	1813
0.3	1752
0.4	1707
0.5	1695
0.7	1658
1.0	1607
1.5	1389
2.0	1208
3.0	676
4.0	301
5.0	105

et al. 2008). We want to calculate a DM and RM from n_e and $B_{||}$ that are realistic on all scales, down to as small of a scale as possible. In the simulation volume of TNG50, the magnetic fields are also modeled with the highest physical resolution in cosmological MHD simulations at the moment: the average cell size is 70 – 140 pc in the star-forming regions of galaxies. In comparison, the mean cell size of star-forming cells is 355 pc in TNG100, and 715 pc in TNG300 (Nelson et al. 2019a), and 370 pc in zoom-in simulations of the Auriga galaxies (Grand et al. 2017). The magnetic field information in TNG50 was saved in 20 snapshots by the TNG team, and the redshifts of these snapshots that we used in our study are listed in Table 5.1.

5.2.2 Galaxy selection

The TNG50 simulation includes a large number of galaxies (also called 'subhalos'[2]) at various redshifts, from $z = 0$ to $z = 12$. These include a wide variety of galaxies, for example spiral galaxies and early-type galaxies. To be able to provide DM and RM contribution estimates for different possible FRB host galaxies, we assume that different types of galaxies with different properties could be a host to an FRB. How DM and RM depend on these properties is described in Sections 5.3 and 5.4. Due to computational limitations, we do not analyze every galaxy in the TNG50 simulation, but restrict our study to a subset of galaxies, which we describe below.

Of the 18 currently known FRB-hosts, 15 have $9 < \log(M_*/\mathrm{M}_\odot) < 11$ (Heintz et al. 2020)[3]. We include galaxies with a stellar mass (M_*) in the range $\log(M_*/\mathrm{M}_\odot) = 9$ –

[2]The friends-of-friends algorithm organizes the dark matter particles into halos, and the subfind algorithm separates the halos into subhalos.

[3]https://github.com/FRBs/FRBhostpage

12, so we not only can study normal spiral galaxies as possible hosts, but we can also account for possible future hosts with high masses, such as large elliptical galaxies.

The capabilities of current and near-future surveys are expected to be sensitive to FRBs up to a high redshift. For example the Parkes radio telescope and CHIME will detect FRBs up to a redshift of $z = 2$, while the Australian Square Kilometre Array Pathfinder (ASKAP) can detect FRBs up to $z = 1$ (predicted by Hackstein et al. 2020 using FRBPOPPY Gardenier 2019), and SKA-mid will also detect high redshift FRBs (Macquart et al. 2015). To date, the highest measured FRB host galaxy redshift is only $z = 0.66$ (Ravi et al. 2019). For FRBs without identified host galaxies we can only estimate the redshift based on their DM, however, this method is less certain, since the measured DM can have a significant contribution from the source environment and the host galaxy. Walker et al. (2020) constrained the redshift of unlocalised FRBs (from the FRB catalogue in 2020), accounting for uncertainties due to different potential host galaxies and progenitor scenarios, finding that in all cases the most probable redshifts are $z \leq 1.6$, except for one FRB for which it was $z \sim 2.5$. Therefore based on present and future observational capacities, we decided to constrain our sample to galaxies at $z \leq 2$.

In addition to these observational constraints, our choice of $z = 2$ as our upper redshift range is also due to the rapid falloff of the number of galaxies in the simulation beyond $z = 2$. This is as expected, because of hierarchical structure formation there are fewer massive galaxies at higher redshifts. We note that recent results from the *James Webb Space Telescope* might challenge this view. Ferreira et al. (2022) and Labbé et al. (2023) show the presence of massive galaxies and a higher rate of galaxy disks at earlier cosmological times than expected from the lambda cold dark matter (ΛCDM) model, which IllustrisTNG is based on. Our results at $z < 2$ should not be significantly affected, but at higher redshifts DM and RM might be higher in reality than our results from the simulation. At $z \leq 2$ there are more than 1000 galaxies per redshift with stellar mass $\log(M_*/\mathrm{M}_\odot) = 9 - 12$, vs. 676, 301, 105 at $z = 3, 4, 5$, respectively. We briefly investigate the overall redshift dependence of galaxies at these redshifts in Section 5.3, but do not include them in the statistical studies where we divide the galaxies/sightlines into groups.

We excluded satellite galaxies, which are defined as the galaxies that are not the most massive subhalos of their parent halo. Subhalos which are flagged by the simulation as unsuitable for most analysis were also left out from our study, as they are not of cosmological origin. These are defined as satellite galaxies that form within the virial radius of their parent halo, and their ratio of dark matter mass to total subhalo mass is less than 0.8 (Nelson et al. 2019a). Furthermore, we also excluded galaxies labeled with star formation rate (SFR) = 0 in the simulation output. These galaxies have an SFR below the SFR resolution limit of TNG50, 10^{-5} M_*/yr. Other galaxy types that may be of interest to study are satellite galaxies and dwarf galaxies ($\log(M_*/\mathrm{M}_\odot)<9$), but these are not included in this paper.

In summary, we select galaxies from $z = 0$ out to $z = 2$, with $\log(M_*/\mathrm{M}_\odot)$ in the range of 9 – 12, resulting in a total of 16 500 galaxies (Table 5.1).

5.2.3 Positions of FRBs

Although there are many different possible progenitors of FRBs, recent evidence suggests some progenitors are likely young magnetars (Wang et al. 2020, CHIME/FRB Collaboration et al. 2020, Zanazzi & Lai 2020), which are typically found in star-forming regions (Bochenek et al. 2021).

We therefore place FRBs in our selected galaxies according to this paradigm, as follows. We define a radius for each galaxy that encloses 99% of the star-forming gas of the subhalo ($r_{\rm SF,99}$). Fig. I.4 (middle) shows the distribution of $r_{\rm SF,99}$ at different redshifts are, with slightly larger radii at higher redshifts, where the star-forming gas is not yet confined to the inner parts of the galaxies. We then randomly select 1000 gas cells inside this radius, which we adopt as the positions of our FRBs. As the physical resolution of the simulations is adaptive, this means we have more FRBs in denser regions of the galaxies, closer to regions where magnetars could be found, and most FRBs are in the disk. In Fig. I.4 (right) we show the distribution of the projected offset of FRBs from the center of their host galaxies ($b_{\rm offset}$), and we show three example illustrations of $b_{\rm offset}$ in galaxies with different inclinations in Fig. 5.2. These distributions do not change significantly with redshift. We point out that among the current sample of FRBs that have been observationally localized, the FRB with the smallest $b_{\rm offset}$ is at 0.6 ± 0.3 kpc (Heintz et al. 2020) and the FRB with the largest $b_{\rm offset}$ is at 27.2 ± 22.6 kpc (Bhandari et al. 2022) away from the center of their host galaxies (where the errors are due to the uncertainties of the localization of the FRBs). This is consistent with our resulting range of $b_{\rm offset}$. We note that different progenitors could have different spatial distribution in galaxies (see e.g. Walker et al. 2020; Mo et al. 2023).

5.2.4 Inclination of galaxies

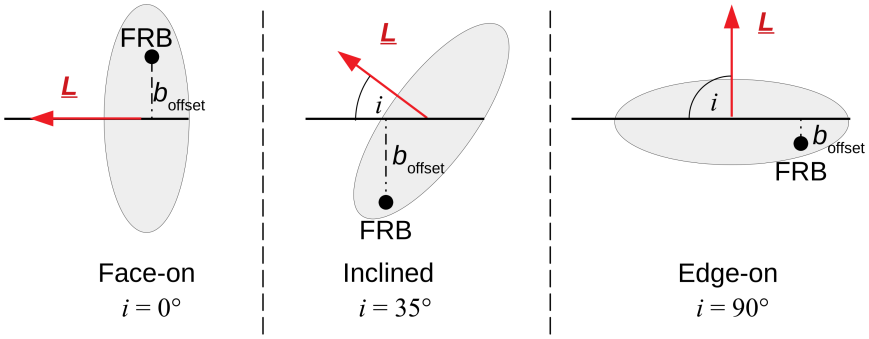

Figure 5.2: Illustration of the inclinations of host galaxies and the projected distance of FRBs from the center of the host galaxy ($b_{\rm offset}$), showed for face-on, inclined, and edge-on galaxies. The observer is on the left side. The total angular momentum vector of the host galaxy ($\boldsymbol{L}$) is perpendicular to the plane of its disk. The inclination is the angle between the line of sight and $\boldsymbol{L}$. The filled circles indicate the positions of the FRBs.

We assume that galaxies are randomly oriented with respect to the line of sight. To ensure this, first we rotate each galaxy to face-on view, by rotating the total angular momentum vector of its stars ($\boldsymbol{L}$, which is perpendicular to the plane of the galaxy) to point to the observer. For more details about the inclination distribution and rotation of galaxies, see Appendix II.1. Then for each galaxy, we generate 1000 random rotation matrices using Fast Random Rotation Matrices (Arvo 1992), so that for each FRB position, the same galaxy has a unique orientation. After the rotations, the total angular momentum vectors are uniformly distributed on a sphere. We define the inclination as the angle between the total angular momentum vector and the line-of-sight, and we show three example illustrations of different inclinations in Fig. 5.2. Multiple orientations can result in the same inclination. An example of the distribution of the inclinations is shown in Fig. I.4 (left). The magnetic field vectors and the position vectors of the cells of the galaxies are rotated by the same matrices.

5.2.5 Conversion of the simulation units

Following the recommended procedures for the TNG data (Nelson et al. 2019a), we convert from comoving units (coordinates of cells, gas density, magnetic field strength, masses) to physical units using the scale factor (a) and the Hubble parameter (h). We can obtain kpc from comoving kpc (ckpc) via:

$$1\,\mathrm{kpc} = 1\,\mathrm{ckpc}/h \cdot a. \tag{5.5}$$

After this, the density and magnetic field are converted to CGS units from the physical units in the simulation:

$$\rho[\mathrm{g\,cm^{-3}}] = 6.8 \cdot 10^{-22} \rho_{\mathrm{sim}}[10^{10} M_{\odot}\,\mathrm{kpc}^{-3}], \tag{5.6}$$

and

$$B[\mu\mathrm{G}] = 2.6 \cdot B_{\mathrm{sim}}[(10^{10}\mathrm{M}_{\odot}/\mathrm{kpc})^{1/2} \cdot (\mathrm{km/s})/\mathrm{kpc}]. \tag{5.7}$$

5.2.6 Calculating n_e

The ionisation in the simulation that sets n_e is computed as the equilibrium state given radiative cooling and heating from the UV background and nearby AGN. The electron density (n_e) must be calculated differently for star-forming and non star-forming cells (where SFR = 0 $\mathrm{M}_{\odot}$/yr, i.e. below the SFR resolution of the simulation). For non star-forming cells, it can simply be computed from the electron abundance (e_{ab}, the fractional electron number density with respect to the total hydrogen number density) and the hydrogen number density (n_{H}):

$$n_e[\mathrm{cm^{-3}}] = e_{\mathrm{ab}} \cdot n_{\mathrm{H}}. \tag{5.8}$$

e_{ab} is available in the IllustrisTNG particle data. However, n_{H} has to be calculated using the total gas density of the cells (ρ):

$$n_{\mathrm{H}}[\mathrm{cm^{-3}}] = \rho \cdot X_{\mathrm{H}}/m_{\mathrm{p+}}, \tag{5.9}$$

where we assume the fraction of hydrogen to be $X_{\rm H} = 0.76$ (based on the initial conditions of TNG, Pillepich et al. 2018), and $m_{\rm p+}$ is the mass of a proton.

For star-forming cells, we must consider the sub-grid model for star formation and the multi-phase interstellar medium used by the simulation (Springel & Hernquist 2003). Following Springel & Hernquist (2003) (see also e.g. Pakmor et al. 2018, Zhang et al. 2020) we calculate n_e assuming each cell's interstellar medium consists of volume-filling hot ionized gas ($T \sim 10^7$ K) and small neutral cold clouds ($T \sim 10^3$ K), that our sightlines do not cross the cold clouds, and the temperature in the warm phase is hot enough to fully ionize hydrogen and helium.

Then by finding the mass fraction of the warm gas ($x_{\rm warm}$), and assuming it is 100% ionized:

$$n_e[{\rm cm}^{-3}] = x_{\rm warm} \cdot [X_{\rm H} + (Y_{\rm He}/4 \cdot 2)] \cdot \rho / m_{\rm p+}, \tag{5.10}$$

where $Y_{\rm He}$ (the fraction of helium) is 0.23. We note that the n_e calculated using this subgrid model might be uncertain by a factor of 2–3, but a better estimate would require resolving the ISM. Pellegrini et al. (2020) presented a new method of postprocessing galaxies from MHD simulation to obtain better estimates on the small-scale ISM properties by including stellar clusters and their impact on the ISM. Comparing their radial and vertical profiles of $n_{\rm e}$ with a single galaxy from the Auriga simulations, they found that n_e can vary by a factor of 2 lower or higher in different parts of the galaxy compared to when computed using Eq. 5.10. We argue that because for most sightlines we integrate across a large part of the galaxies, these differences would average out, and our DMs and RMs are not affected significantly.

5.2.7 Calculating DM and RM

The DM is the line-of-sight integral of the electron density (n_e). For a given sightline in the simulation, we compute this by replacing the integral with a discrete sum between the FRB position in the inclined galaxy and $r_{\rm SF,99}$ of the galaxy. We use N steps of dl=20 pc stepsize, and the integration takes the closest cell to the position on the sightline in every step:

$$\mathrm{DM} = \sum_{i=0}^{N} n_{e,i} \mathrm{d}l, \tag{5.11}$$

where i is the index for the N steps and $n_{e,i}$ is the electron density at each step. We also assume that the origin of the FRB is a point source, and its emission originates from scales smaller than 20 pc. For a discussion on the effect of different parameter choices (integral length, integral stepsize, number of rotations), see Appendix B of the paper (attached as Appendix III).

The RM is calculated similarly as DM:

$$\mathrm{RM} = k \sum_{i=0}^{N} B_{||,i} n_{e,i} \mathrm{d}l, \tag{5.12}$$

where $B_{||,i}$ is the line of sight magnetic field at each step. The same parameter tests

were performed as during DM calculations (see Appendix B of the paper, attached as Appendix III)

5.2.8 Pipeline summary

In summary, we selected 16 500 galaxies, rotated each to a random inclination 1000 times and randomly chose 1000 FRB positions in each galaxy. Then we calculated the DM and RM contribution by the host galaxy for each FRB sightline.

For each sightline we save the galaxy ID, the position of the FRB, the n_e of that cell, the calculated DM and RM, and the used rotation matrix. For each galaxy we save the stellar mass, star formation rate, $r_{\mathrm{SF},99}$, the properties of its magnetic field (average total magnetic field of the disk, and the average of its components – azimuthal, radial and vertical), and the radial and vertical profile for the magnetic field and its components (for details see Appendix D of Appendix III). We also calculate these profiles for n_e and ρ.

5.3 Results

In this section, we calculate the $\mathrm{DM_{host,rf}}$ and $\mathrm{RM_{host,rf}}$ PDFs[4] for different subsets of galaxies, and investigate how the properties of these distributions change with redshift. First we show the redshift dependence of the full sample, then the differences between star-forming and red galaxies (i.e. 'quenched'), and how the distributions change with stellar mass. Assuming we also have information about the inclination of observed host galaxies, or the b_{offset} of the FRB from the center of the galaxy, we also provide PDFs for different inclinations and offsets. Finally, we also investigate if the overall redshift evolution of $\mathrm{DM_{host,rf}}$ and $\mathrm{RM_{host,rf}}$ up to z=5 is well described by our fits for hosts below z=2. We discuss the possible reasons behind these trends in Section 5.4.

5.3.1 Redshift evolution of $\mathrm{DM_{host,rf}}$ and $\mathrm{RM_{host,rf}}$

We show the PDFs of $\mathrm{DM_{host,rf}}$ and $\mathrm{RM_{host,rf}}$ individually for each redshift, explore their functional forms and investigate how their parameters change across redshift. We provide these functional forms in the paper for easier application. The PDFs for redshifts 0.0, 0.2, 0.4, 1.0, and 2.0 are shown in Fig. 5.3. We only show the PDFs for half of the snapshots in our analysis to make the plot clearer, but we will show below that the parameters of the distributions change smoothly with redshift. We calculate the PDFs individually for each redshift, and for each PDF we take into account the DM and RM of every FRB at the given redshift.

We found that the PDF of $\mathrm{DM_{host,rf}}$ can be described by a lognormal distribution:

$$f_{\mathrm{DM,host}}(x) = \frac{1}{\sqrt{2\pi}x\sigma} \exp(-(\ln(x) - \mu)^2/(2\sigma^2)), \tag{5.13}$$

[4] All histograms presented in this work have been normalized to unit area.

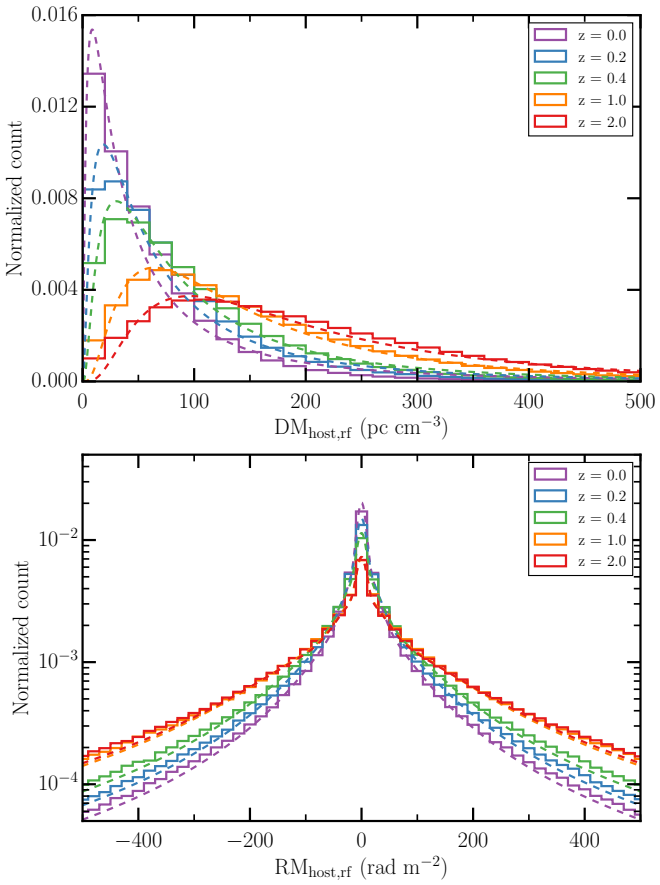

Figure 5.3: **Top:** The PDF of the rest frame DM contribution of host galaxies, using FRBs at different redshifts. The distributions are lognormal, with a long positive tail. The fits are shown by the dashed lines, and the colors correspond to the different redshifts. The PDFs become broader at higher redshifts, with larger possible DM values. **Bottom:** The PDF of the rest frame RM contribution of host galaxies, using FRBs at different redshifts. The distributions are symmetric with a sharp peak at 0 rad m^{-2}, similar to a Lorentzian. The fits are shown by the dashed lines, and the colors correspond to the different redshifts. The PDFs become broader at higher redshifts up to $z = 1$, with larger RMs. After $z = 1$, the distributions do not change significantly.

parametrized with μ and σ, which are the mean and standard deviation of the DM's natural logarithm, and not the DM itself.

We find broader distributions at higher redshifts. We note that other distributions that can be fitted to the data include the gamma function, however this overestimates the 16th percentile by a factor of 4. The median of DM also increases with redshift, following a power law:

$$\text{median DM}_{\rm host,rf}(z) = a \cdot z^b + c, \tag{5.14}$$

with fitting parameters $(a, b, c$, see in Table in Table A.1 of Appendix III . The difference

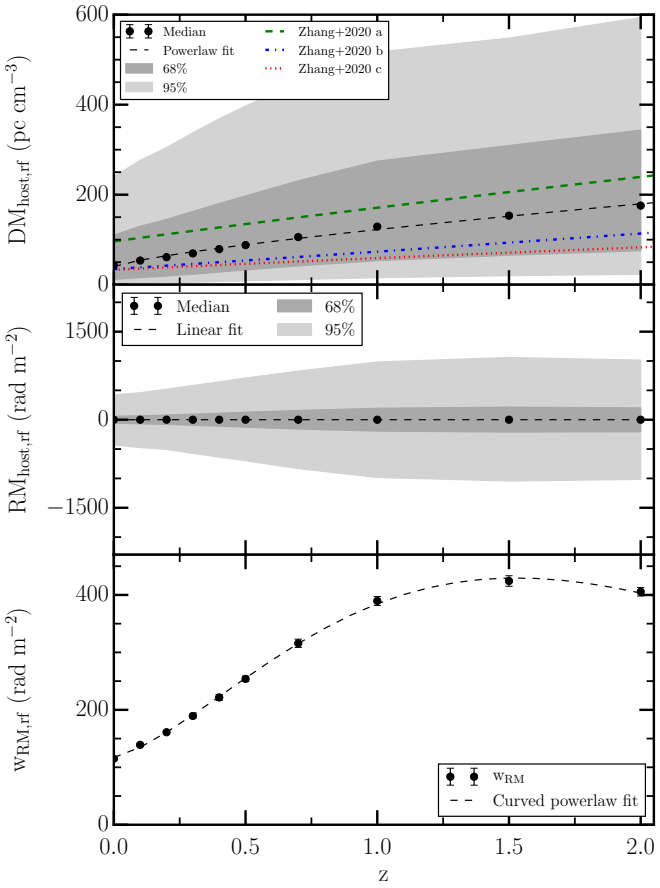

Figure 5.4: **Top:** The median of $\mathrm{DM_{host,rf}}$ increases at larger redshifts. The shaded regions correspond to the 1σ and 2σ width of the distributions. This relation can be fitted by a power law. For comparison we also plotted the results from Zhang et al. (2020), in the case of host galaxies like the host of FRB180916 (a), galaxies similar to the hosts of non repeating FRBs (b) - hosts known at the time of Zhang et al. (2020)'s paper, and galaxies similar to the host of the repeating FRB121102 (c). For further details on the comparison see Section 5.4.3.1. **Middle:** The median of $\mathrm{RM_{host,rf}}$ stays the same at all redshifts. The shaded regions correspond to the 1σ and 2σ width of the distributions, which increases until $z = 1$. **Bottom:** The 1σ width of the distributions of $\mathrm{RM_{host,rf}}$ increases at larger redshifts, but it stays the same after $z = 1$. This relation can be fitted by a curved power law (black dashed line). The errors are from the bootstrap method.

between the median of the actual PDF and the median from the lognormal fit ($\exp(\mu)$) is below 10 pc cm^{-3} at all redshifts. We define the 1σ width of the distribution as the difference between the 84th and 16th percentile ($w_{\rm DM,rest}$). The $w_{\rm DM,rest}$ also increases with redshift, and its redshift evolution can also be fitted by Eq. 5.14, with fitting parameters listed in Table A.1 of Appendix III . We note that the tail of the distribution is slightly overestimated by the lognormal fit The μ and σ parameters of

the fitted PDFs also change with redshift, we find they are better described by an exponential function:

$$\mu(z) = A_{\mathrm{DM},\mu} \exp(-B_{\mathrm{DM},\mu} z) + C_{\mathrm{DM},\mu}, \tag{5.15}$$

$$\sigma(z) = A_{\mathrm{DM},\sigma} \exp(-B_{\mathrm{DM},\sigma} z) + C_{\mathrm{DM},\sigma}, \tag{5.16}$$

where A_{DM}, B_{DM} and C_{DM} are the parameters of the fit (see Table A.2 of Appendix III. We note that the difference of best fit function form (exponential instead of power law) is due to the fact that μ and σ are related to the variable's natural logarithm.

We find that the PDF of $\mathrm{RM}_{\mathrm{host,rf}}$ (shown in Fig. 5.3 bottom) is symmetric, with both peak and median at $\mathrm{RM} = 0.00 \pm 0.03\ \mathrm{rad\,m^{-2}}$ at every redshift. It can be fitted by the sum of one Lorentzian and two Gaussian functions, similar to the results of Basu et al. (2018) (for more details see Section 5.4):

$$f_{\mathrm{RM,host}}(x) = a_1 \cdot \left[\frac{\gamma^2}{\pi\gamma(\gamma^2 + x^2)}\right] + a_2 \exp\left[-\frac{1}{2}\left(\frac{x}{\sigma_1}\right)^2\right] + a_3 \exp\left[-\frac{1}{2}\left(\frac{x}{\sigma_2}\right)^2\right], \tag{5.17}$$

where a_1, a_2 and a_3 are normalization fractions, γ is the parameter of the Lorentzian function, and σ_1 and σ_2 are parameters of the Gaussian functions. We note that the exact definition of the function is different from that of Basu et al. (2018), for example we did not define a variable for the mean, but assumed it to be 0 $\mathrm{rad\,m^{-2}}$. We also experimented with a purely Lorentzian fit, and different combinations of Gaussian and Lorentzian fits, but the combination from Basu et al. (2018) captured the long tails and peak of the distribution best.

We find that the RM distribution becomes broader with redshift, up to $z = 1$, where it flattens, and turns over at $z = 2$. The 1σ width of the distributions ($w_{\mathrm{RM,rest}}$, containing 68% of the data) as a function of redshift can be fitted by a curved power law:

$$w_{\mathrm{RM,rf}}(z) = A_{\mathrm{RM}} \cdot z^{D_{\mathrm{RM}} + B_{\mathrm{RM}} \cdot z} + C_{\mathrm{RM}}, \tag{5.18}$$

and the fitted parameters (A_{RM}, B_{RM}, C_{RM} and D_{RM}) are in Table A.1 of Appendix III. We estimate the uncertainty of $w_{\mathrm{RM,rf}}$ with the bootstrapping method. $w_{\mathrm{RM,rf}}$ can also be fitted by a broken power law, but the curved power law has the advantage of the fit changing more smoothly, without a sharp peak. We use the curved power law for the remainder of the paper.

We find that the parameters of the fitted RM PDFs (a_1, a_2, a_3, γ, σ_1, and σ_2) also change as curved power laws. Apart from the normalization parameters of the Gaussian components (a_1 and a_2), all parameters increase towards higher redshift. We list the results of the fits in Table A.3 of Appendix III. The 1σ width of the fitted PDFs differs from that of the real PDFs by less than 20 $\mathrm{rad\ m^{-2}}$.

If the redshift of an FRB is known, the relations above can be used to derive the possible $\mathrm{DM}_{\mathrm{host,rf}}$ and $\mathrm{RM}_{\mathrm{host,rf}}$ contribution.

5.3.2 $DM_{host,rf}$ and $RM_{host,rf}$ in star-forming and red galaxies

The structure and properties (e.g. SFR, stellar mass) of star-forming spiral and red elliptical galaxies are different (see e.g. Conselice 2014 for a review), and their electron densities and magnetic field strength and structure can also differ: ellipticals might have weaker large-scale fields because they lack a differentially rotating disk (Beck 2012). Considering this, we would expect the DM and RM contribution of these galaxies to also be different. It is relatively easy to separate them observationally based on their color-magnitude diagram (Bell et al. 2004), which means FRB host galaxies could easily be divided based on this property in the future.

To separate them in the simulation we adapt a method from Donnari et al. (2019), who derived the Main Sequence (MS) of galaxies in TNG100. We describe this in Appendix C of Appendix III. The MS is a tight relation between the stellar mass and SFR of star-forming galaxies based on observations (e.g. Noeske et al. 2007), and this relation also scales with redshift.

We separated the galaxies based on the MS, and in Fig. C.1 of Appendix III we show the DM and RM distributions of quenched and star-forming galaxies at z=0.5. In the top panels of Fig. 5.5 and Fig. 5.6, we show how the median DM and the RM distribution width ($w_{RM,rf}$) changes with redshift, respectively. We fit the former with a power law and the latter with a curved power law. At high redshifts ($z \geq 1.5$), we have fewer than ten quenched galaxies in a redshift bin. Because of this, the trends at high redshift for quenched galaxies can not be seen clearly.

We find that quenched galaxies have a lower median DM and RM contribution on average, compared to star-forming galaxies. Star-forming galaxies have a wider DM and RM distribution, and a larger median DM. The same trend can be seen at all redshifts.

Both the DM and RM PDFs of star-forming galaxies closely follow the DM and RM PDF of all galaxies, as most of the sampled galaxies are star-forming (97% in total, with 95% at z=0 and 99% at z=2). To test if the different distribution shape is caused by the small sample size of the quenched galaxies, we randomly selected the same number of galaxies from the star-forming sample as there are in the quenched sample. The resulting DM and RM PDFs also closely resemble the PDFs of all star-forming galaxies, suggesting the quenched galaxies have a different PDF unrelated to the sample size.

5.3.3 $DM_{host,rf}$ and $RM_{host,rf}$ in different stellar mass bins

We investigate how the properties of the DM and RM PDFs change if we separate the sightlines by the stellar mass of the host galaxies. We divided the galaxies into five stellar mass bins at each redshift (the bins are listed in Table A.1 of Appendix III). and constructed PDFs for each group.

We show an example of these DM and RM PDFs for galaxies at z=0.5 in Fig. F.1 of Appendix III. The shapes of the distributions are the same as the ones for the full sample; the DM distributions are lognormal, and the RM distributions are Lorentzian-

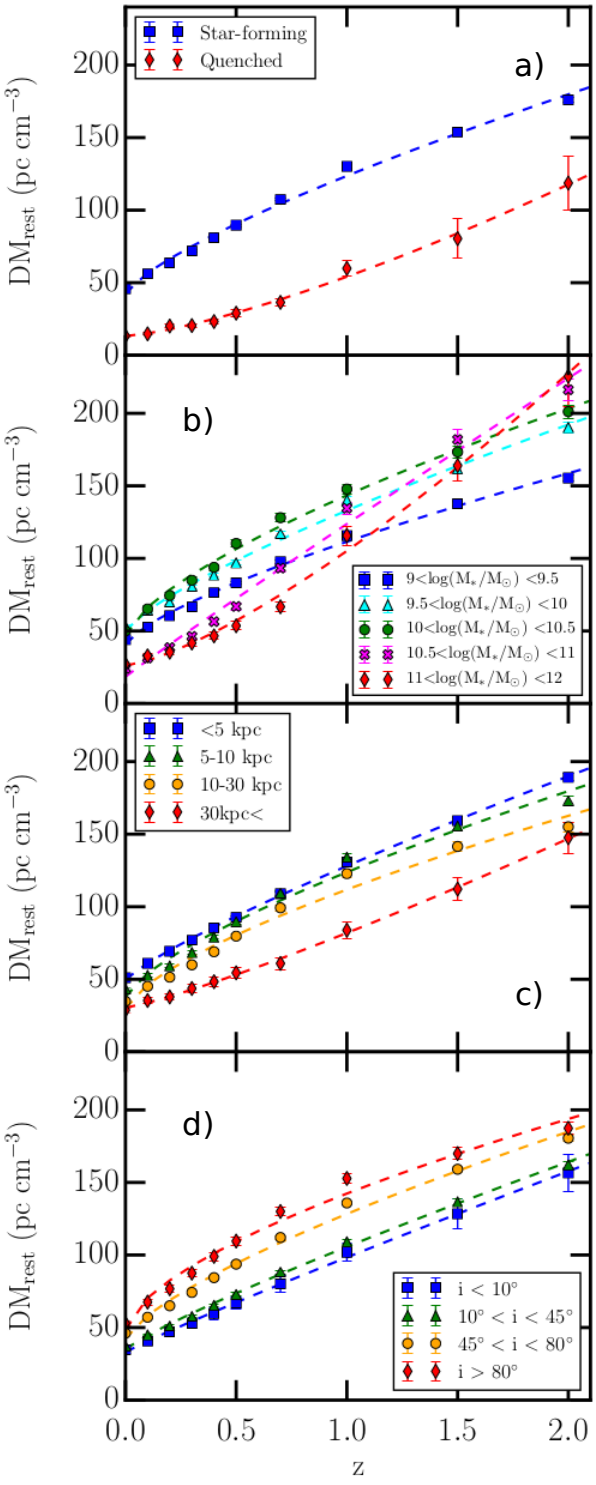

Figure 5.5: The redshift evolution of median $DM_{host,rf}$ of different subsets of galaxies. A power law can be fitted to each group. The error bars are from bootstrapping. **a**: Quenched and star-forming galaxies. **b**: Different stellar mass bins. **c:** Sightlines with different inclinations. **d**: Sightlines with different b_{offset}.

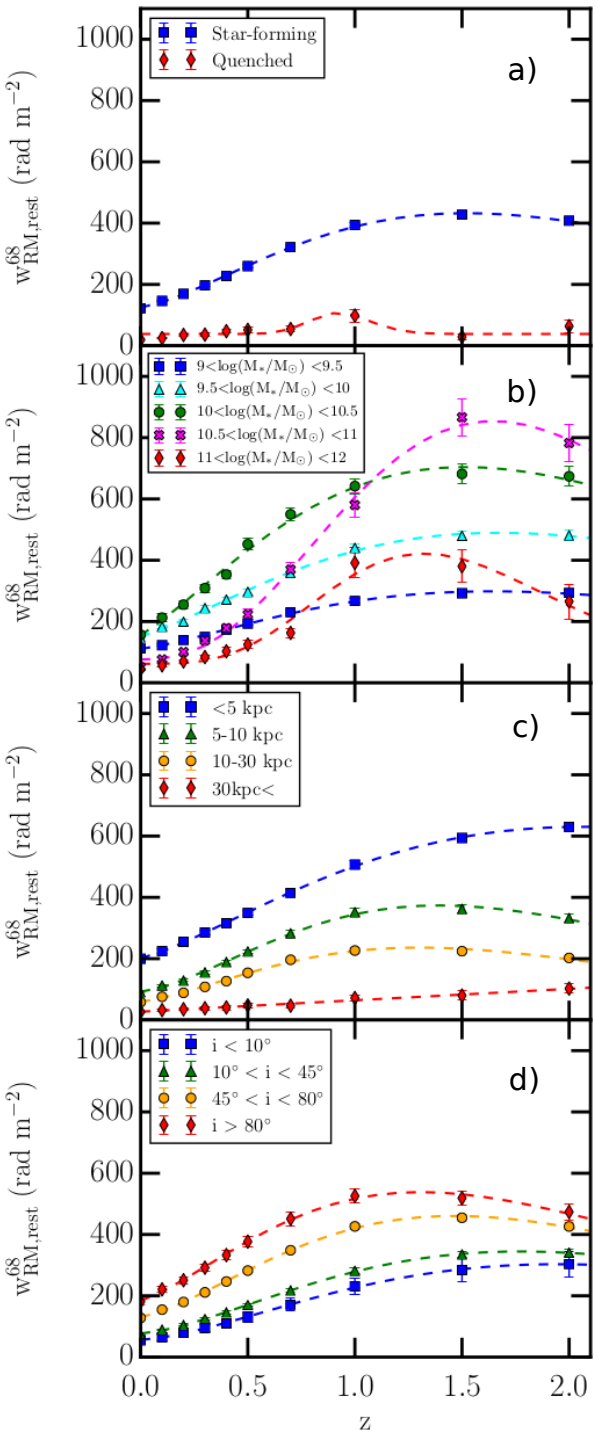

Figure 5.6: The redshift evolution of the width of the rest frame RM distribution ($w_{\mathrm{RM,rest}}$) of different subsets of galaxies. A curved power law can be fitted to each group. The error bars are from bootstrapping. **a**: Quenched and star-forming galaxies. At high z we only have a few (<10) quenched galaxies, which makes it difficult to obtain a good fit. **b**: Different stellar mass bins. **c:** Different inclinations. **d:** Sightlines with different b_{offset}.

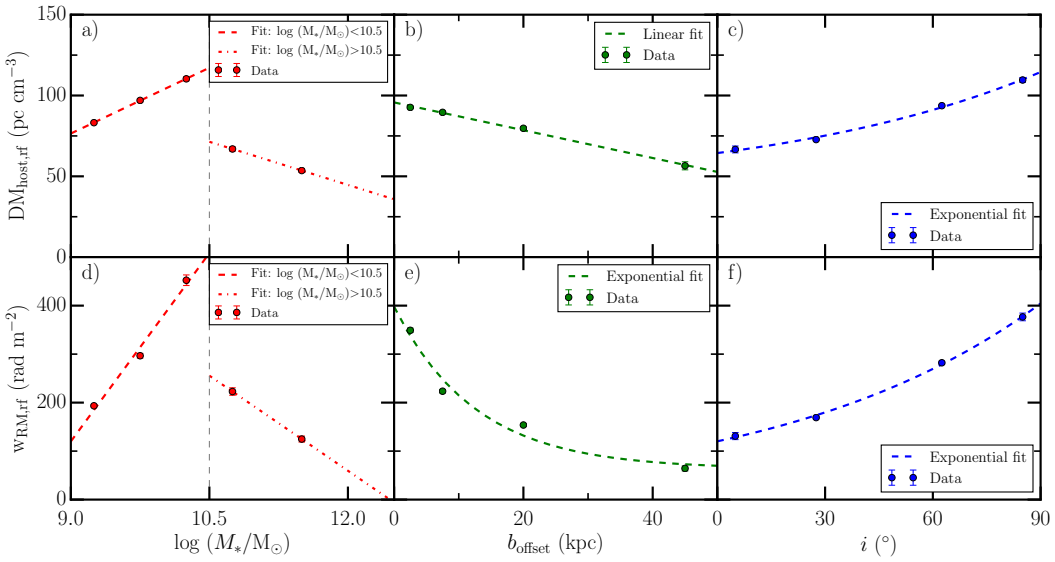

Figure 5.7: The top row shows how the median $\mathrm{DM_{host,rf}}$ changes as a function of stellar mass, b_{offset} and galaxy inclination. The bottom row shows the same for the $\mathrm{RM_{host,rf}}$ distribution width ($w_{\mathrm{RM,rf}}$). This figure shows these trends for galaxies at z=0.5. **Left column:** The median $\mathrm{DM_{host,rf}}$ and $w_{\mathrm{RM,rf}}$ linearly increases with stellar mass, but suddenly drops for galaxies with very high stellar masses ($\log(M_*/\mathrm{M}_\odot) > 10.5$), and after that linearly decreases with increasing stellar mass. **Middle column:** The median $\mathrm{DM_{host,rf}}$ decreases linearly, and the $w_{\mathrm{RM,rf}}$ decreases exponentially with b_{offset}. **Right column:** The median $\mathrm{DM_{host,rf}}$ and $w_{\mathrm{RM,rf}}$ increases exponentially with host galaxy inclination.

like. While the shape of the PDFs remains the same, the parameters of the PDFs change with stellar mass. We show these changes in Fig. 5.7 a) and d). The median of DM increases linearly with stellar mass, up to very high mass galaxies ($\log(M_*/\mathrm{M}_\odot) > 10.6$). But for galaxies with very large stellar masses the PDF becomes narrower, the median DM drops significantly, and the RM distribution width ($w_{\mathrm{RM,rf}}$) also follows the same trend. This can be seen at every redshift, but for $z > 1$ the drop occurs at a larger stellar mass $\log(M_*/\mathrm{M}_\odot) > 11$). The $w_{\mathrm{RM,rf}}$ decreases linearly after the drop at every redshift. The median DM does not always follow this trend.

In panel b) of Figs. 5.5 and 5.6 we show that the median DM and $w_{\mathrm{RM,rf}}$ of the different stellar mass bins as a function of redshift can be fitted by a power law and a curved power law, respectively. The fit parameters for the different stellar mass bins can be found in Table A.1 of Appendix III. The difference between the fits are more visible in the case of RM. For galaxies below $\log(M_*/\mathrm{M}_\odot) = 10.5$, the exponents are similar, but the scaling parameters are higher at higher stellar mass. For massive galaxies, the exponents are also different. At low redshifts (z<0.2), the galaxies with lower stellar mass have a higher median DM and $w_{\mathrm{RM,rf}}$ than galaxies with larger masses.

5.3.4 $DM_{host,rf}$ and $RM_{host,rf}$ at different inclinations

We expect $DM_{host,rf}$ and $RM_{host,rf}$ contributions to differ for face-on vs. edge-on hosts. For edge-on galaxies, we expect sightlines to propagate through more ISM, resulting in higher DMs and affected RMs. In real observations, if a host galaxy is identified and assumed to be a circular disk galaxy, its inclination can be measured by the ratio of its major and minor axis. For our TNG50 galaxy sample, we define the inclination angle as the angle between the total angular momentum vector of the galaxy's stars and the line of sight (see Section 5.2).

We divide the galaxies into four inclination bins, which are listed in Table A.1 of Appendix III, and their DM and RM distributions at z=0.5 are shown in Fig. F.3 of Appendix III. The distributions for galaxies at other redshifts can be found in Appendix G of Appendix III.

We find that the median DM increases exponentially with inclination, shown in Fig. 5.7 c): face-on galaxies ($i < 10°$) have a smaller median DM than galaxies with larger inclinations ($10° < i < 80°$), while edge-on galaxies ($i > 80°$) have the highest DM range (larger by a factor of ~ 2 compared to face-on galaxies). The same trends are found at all other redshifts (see Appendix G of Appendix III).

In Fig. 5.7 f) we also see the RM distribution width ($w_{RM,rf}$) increasing exponentially with galaxy inclination: edge-on host galaxies have an $w_{RM,rf}$ a factor of ~ 4 larger compared to face-on galaxies. The increase with inclination can be seen at every redshift (see Appendix G of Appendix III), but at $z \geq 1.5$, the increase is only linear in contrast to the exponential increase at $z < 1.5$.

The median DM and $w_{RM,rf}$ from each inclination group can be fitted by a power law and a curved power law, respectively, as a function of redshift. The fits can be found in Figs. 5.5 and 5.6, and the fitted parameters are listed in Table A.1 of Appendix III.

5.3.5 $DM_{host,rf}$ and $RM_{host,rf}$ at different FRB b_{offset}

We expect both n_e and B field to change as a function of distance from the center of the galaxy (see e.g. Beck 2007 regarding how the energy densities of magnetic fields and ionized gas decrease with radius in NGC6946). As a result, the DM and RM distributions can also be affected. We define the projected offset (b_{offset}) as the projected distance of the FRB position from the center of the galaxy, which should be readily available for well-localized observed FRBs. Therefore, we investigate how $DM_{host,rf}$ and $RM_{host,rf}$ distributions are affected by b_{offset}.

In Fig. F.4 of Appendix III we show the distributions of $DM_{host,rf}$ and $RM_{host,rf}$ with different FRB offsets for galaxies at $z = 0.5$. We find that the median $DM_{host,rf}$ and the RM distribution width ($w_{RM,rf}$) decrease with larger FRB offsets. In Fig. 5.7 b), we show that the median of DM decreases linearly, and in Fig. 5.7 e) we see how $w_{RM,rf}$ decreases exponentially. The magnitude of the change from $b_{offset} = 0$ kpc to $b_{offset} = 50$ kpc is more significant in the case of $w_{RM,rf}$ (decrease by a factor of $\sim$8), compared to the median $DM_{host,rf}$ (factor of $\sim$2).

The median $\mathrm{DM_{host,rf}}$ and $w_{\mathrm{RM,rf}}$ of the sightlines in the different offset bins may also be fitted by a power law and broken power law as a function of redshift, as shown in Figs. 5.5 and 5.6 (d). The fitted parameters are listed in Table A.1 of Appendix III. The exponents stay similar for all offset bins, but the scaling changes more significantly from the smallest to the largest offset bin: a factor of ∼1.5 in the case of DM, and ∼7 in the case of RM.

5.3.6 $\mathrm{DM_{host,rf}}$ and $\mathrm{RM_{host,rf}}$ above z=2

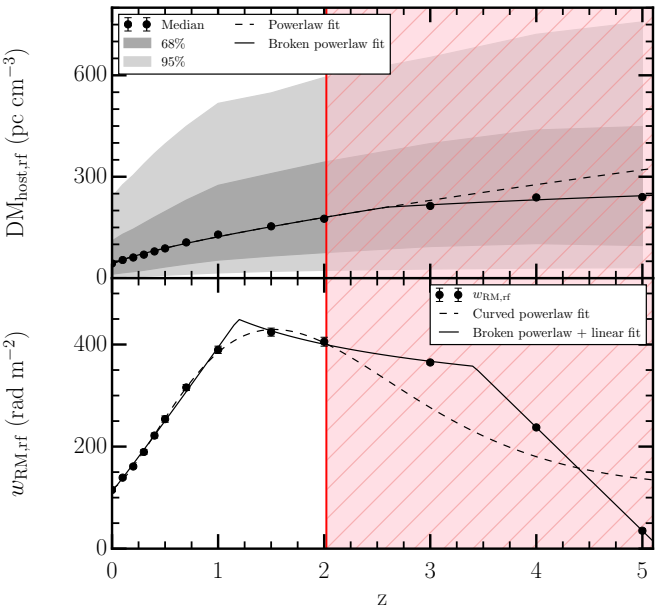

Figure 5.8: **Top**: The median $\mathrm{DM_{host,rf}}$ as a function of redshift, including FRBs at $3 \leq z \leq 5$. These high redshift sightlines are not included in the further analysis, indicated by the red hashed pattern. $\mathrm{DM_{host,rf}}$ at $z \geq 3$ changes differently compared to our fit based on sightlines in galaxies at $z \leq 2$ (black dashed line). It increases more slowly, and can be fitted by a broken power law (black solid line). **Right:** The $\mathrm{RM_{host,rf}}$ distribution width ($w_{\mathrm{RM,rf}}$) as a function of redshift, including FRBs at $3 \leq z \leq 5$. These high redshift sightlines are not included in the further analysis, indicated by the red hashed pattern. The $w_{\mathrm{RM,rf}}$ changes differently than our fits based on $z \leq 2$ (black dashed lined) predicted, and drops significantly after $z = 3$. It can be fitted by the combination of a broken power law and a linear decrease after $z = 3.3$, indicated by the black solid line.

As we might observe FRBs at higher redshifts in the future with the SKA (Hashimoto et al. 2020), we investigate how the $\mathrm{DM_{host,rf}}$ and $\mathrm{RM_{host,rf}}$ trends evolve over redshift above z=2, and whether it follows the functions we found based on galaxies at $z \leq 2$. However, these snapshots contain significantly fewer galaxies than the ones discussed in the previous sections (see Table 5.1), hence it is harder to split them into subgroups. Therefore, we only discuss their overall redshift evolution.

We calculated $\mathrm{DM_{host,rf}}$ and $\mathrm{RM_{host,rf}}$ at redshifts of 3, 4, and 5. We show the evolution of median DM as a function of redshift in Fig. 5.8 (right) and find that the DM does not increase as much as we would expect based on the fit from DMs at lower redshift. Between z=4 and z=5 median $\mathrm{DM_{host,rf}}$ has only a few pc cm^{-3} difference. The redshift evolution of the median $\mathrm{DM_{host,rf}}$ as a function of redshift can be fitted by a broken power law:

$$\mathrm{DM_{host,rf}}\,(z) = \begin{cases} 82.2 \pm 5.3 \cdot z^{0.8\pm0.1} + 40.2 \pm 4.2, \\ \qquad\qquad\qquad \text{if } z < 2.6 \pm 0.3; \\ 130.7 \pm 15.9 \cdot z^{0.3\pm0.1} + 40.2 \pm 4.2, \\ \qquad\qquad\qquad \text{if } z \geq 2.6 \pm 0.3, \end{cases} \tag{5.19}$$

with a break at z=2.4, and the power law below this redshift is the same as the one we found before using $z \leq 2$ galaxies.

We previously found that the RM distribution width ($w_{\mathrm{RM,rf}}$) turns over for $z > 1.5$ (see Section 5.3.1). In Fig. 5.8 (right) we see that it continues to slowly decrease until z=3, and at z=4 it drops significantly (by about 50%), and continues to quickly decrease. At z=5, it becomes even lower than it is at z=0. Our fit to $w_{\mathrm{RM,rf}}$ below $z \leq$2 can not predict $w_{\mathrm{RM,rf}}$ at $z \geq$2, and we find that the redshift evolution could be described by a broken power law (with a break at z=1.2) and a linear fit after z=3.4:

$$w_{\mathrm{RM,rf}}\,(z) = \begin{cases} 282.3 \pm 6.6 \cdot z^{1.0\pm0.05} + 112.2 \pm 4.9, \\ \qquad\qquad\qquad \text{if } z < 1.2 \pm 0.03; \\ 357.8 \pm 7.2 \cdot z^{-0.3\pm0.04} + 112.2 \pm 4.9, \\ \qquad\qquad\qquad \text{if } 1.2 \pm 0.03 \leq z < 3.4 \pm 0.06; \\ 1048.6 \pm 33.5 - 202.5 \pm 8.0 \cdot z, \\ \qquad\qquad\qquad \text{if } z \geq 3.4 \pm 0.06. \end{cases} \tag{5.20}$$

5.4 Discussion

In this section, we discuss the possible physical reasons behind the trends of $\mathrm{DM_{host,rf}}$ and $\mathrm{RM_{host,rf}}$ we described in Section 5.3. To be able to interpret the role of n_e and B in the resulting DM and RM, we calculated the electron density, gas density, and magnetic field radial and vertical profiles, and other properties of the magnetic field. To calculate the magnetic field properties we followed the methods in Pakmor et al. (2017) and Pakmor et al. (2018), who studied Milky-Way-like galaxies from the Auriga simulations. The range of magnetic field strengths are in agreement with what we have found in the examined galaxies (see Appendix D of Appendix III. Finally, we compare our results to previous works.

5.4.1 Interpretations of $\mathrm{DM_{host,rf}}$ trends

As DM is calculated by Eq. 5.11, it depends on the electron density and path length, and any changes we see in DM should be caused by one or both of these quantities.

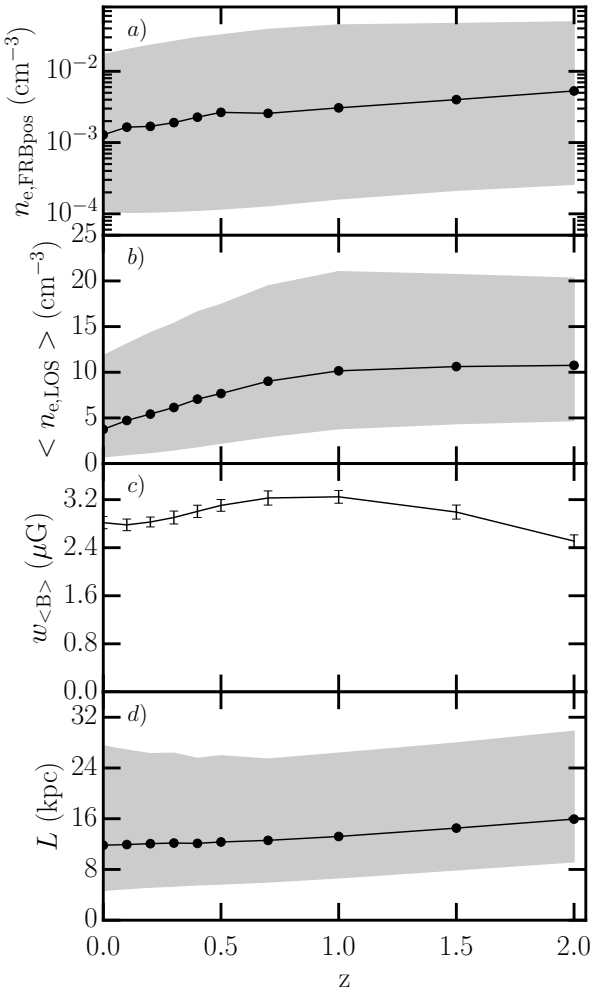

Figure 5.9: We show how different properties change with redshift, in order to help to understand what drives the DM and RM trends. **a:** The median of the n_e of the position of the FRBs across redshift, and the ranges of values between the 16th and 84th percentile. It increases by a factor of $\sim$4, and the range of values increases by a factor of $\sim$3. **b:** The median of $\langle n_{\rm e,LOS} \rangle$ increases with redshift up to $z = 2$ by a factor of 2.9, but between $z = 1$ and $z = 2$ only increases by a few %. **c:** The distribution width of $\langle B_{||,\rm LOS} \rangle$ increases until $z = 1$ by a factor of 1.15. From $z = 1$ to $z = 2$ it decreases by 20%, becoming smaller than at $z = 0$. **d:** The median of path lengths increase by a factor of 1.15$-$1.3 at higher redshifts ($z > 1$) with respect to $z < 1$, but at lower redshifts it only changes by a few %.

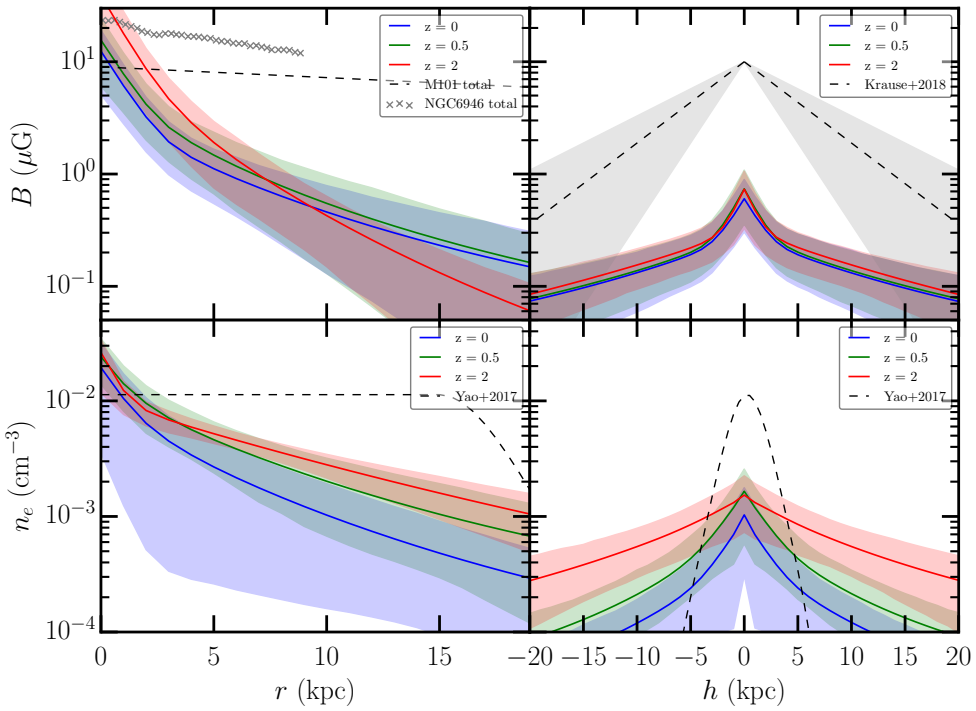

Figure 5.10: **Top row**: The averaged radial and vertical profile of B of galaxies at various redshifts, and their 1σ width. In the top left panel, we show the total magnetic strength profile of NGC6946 (Beck 2007) and M101 (Berkhuijsen et al. 2016). In the top right panel, we show the average vertical B profiles of CHANG-ES galaxies (Krause et al. 2018) with a scale-height of 6 ± 3 kpc. **Bottom row**: The averaged radial and vertical profile of n_e of galaxies at various redshifts, and their 1σ width. We overplotted the n_e profiles of the thick disk from Yao et al. (2017).

5.4.1.1 $\mathrm{DM_{host,rf}}$ changes versus redshift – the role of n_e

The median and 1σ width of the DM distribution increases with redshift (see Fig. 5.3), with both the lower and upper bound increasing at higher redshifts. We see that the median DM increases by a factor of $\sim$4 from z=0 to z=2, and the 1 sigma width of the distribution changes by a factor of $\sim$2.5.

We also find that from $z = 0$ to $z = 2$, the median n_e of the locations of FRBs ($n_{\mathrm{e,FRBpos}}$) increases by a factor of $\sim$4, and the range of values increases by a factor of $\sim$3 (shown in panel a of Fig. 5.9). As the 1000 positions for each galaxy were randomly selected, their properties can tell us about the general environment in these galaxies. In summary, we find that $n_{\mathrm{e,FRBpos}}$ significantly increases with redshift, which can cause a significant increase in DM.

Another cause of larger DMs at higher redshifts may be a longer integral path length through the host galaxy. We find that the median of path lengths increase by a factor of 1.15−1.3 at z>1 (shown in panel d of Fig. 5.9) with respect to $z < 1$, but at lower redshifts it only changes by a few %. The reason behind larger path lengths can be due to the radius of the galaxies. Since we calculate the integral until the $r_{\mathrm{SF,99}}$ radius, a larger radius can cause larger path lengths, thus larger DMs. We find that indeed, the median of the $r_{\mathrm{SF,99}}$ increases by 10−25% at redshifts above $z = 1$ with respect to $z < 1$, and it only changes by a few % at $z < 1$, which can cause a small increase in path lengths and thus DM.

We also note that we can calculate the average electron density along an FRB sightline as we know the path length (L), if we rearrange Eq. 5.11: $\langle n_{\mathrm{e,LOS}} \rangle = \frac{\mathrm{DM}}{L}$ $\mathrm{cm^{-3}}$. We find that this increases with redshift up to $z = 2$ by a factor of 2.9, but between $z = 1$ and $z = 2$ only increases by a few % (shown in panel b of Fig. 5.9). We previously saw that at $z > 1$ the path length increases, which could explain why DM keeps increasing despite $\langle n_{\mathrm{e,LOS}} \rangle$ only increasing slightly. This could mean that at higher redshifts the galaxies have star-forming gas out to a larger distance compared to lower redshifts, but n_e is low in the outskirts of galaxies, causing us to measure a lower $\langle n_{\mathrm{e,LOS}} \rangle$ than expected from DM. This idea is supported by the fact that the difference between the radius containing 95% and 99% of the star-forming gas in galaxies are larger at higher redshifts. At $z = 2$, the difference is 40% of $r_{\mathrm{SF,99}}$ on average, while it is only 20% at $z = 0$.

We performed a simple test to see if the increase in electron density plays the major part in the increase in the median DM: we select a galaxy at z=0 (ID = 1004, $\log(M_*/\mathrm{M_\odot}) = 9.8$, SFR=0.5 $\mathrm{M_\odot/yr}$) with a $\mathrm{DM_{median}} = 49$ pc $\mathrm{cm^{-3}}$ close to the median DM of the whole sample at z=0 (43 pc $\mathrm{cm^{-3}}$). This galaxy was selected to have average properties of the sample. As there might be a more complicated relation between n_e and DM (e.g. n_e changes with radius), we conducted three tests: 1) scaling up the n_e of each cell by a factor of 4, 2) increasing the integration limit by a factor of 1.25, and 3) and increasing both. As expected, the median DM increases by 3.9, 1.3, and 4.1, respectively. Thus we conclude that the increasing trend of median DM with increasing redshift can be mainly explained by higher electron densities, but an increase in path lengths can also contribute to a lesser degree.

The higher electron densities are possibly caused by higher star formation rates at higher redshifts. In the sub grid star formation model from Springel & Hernquist (2003) the star forming process converts matter in the cold cloud phase to stars if the density exceeds a certain limit, and by the feedback of supernovae heats up the warm phase of the ISM. This depletes the cold gas that is used in star formation, which causes a decrease in SFR and electron densities as a function of time. This is why we see larger SFR and electron densities at higher redshifts, when there is still a large amount of star-forming gas available in these galaxies. This interpretation is supported by how the median SFR of the selected galaxies is also larger by a factor of ∼9 at $z = 2$ compared to $z = 0$, similarly to observed galaxies (see Fig. E.1 of Appendix III). The 1σ width of the SFR distribution increases by a factor of ∼10 from $z = 0$ to $z = 2$, which could contribute to the increasing $w_{\rm DM,rest}$ towards higher redshift. The fraction of star-forming cells in each galaxy also increases from a few % at z=0 to ∼ 20 % at z=2. Furthermore, we find the number of quenched galaxies decreases towards higher redshift, which is in agreement with observations: at high redshifts most galaxies are star-forming, and the fraction of red galaxies increases towards lower redshift. If the fraction of quenched galaxies is larger, the fraction of low DM values is also higher, resulting in a lower median DM.

There is also observational evidence of a connection between the SFR and the n_e of galaxies. Based on optical spectroscopic observations of galaxies at z=2.5, Shimakawa et al. (2015) found that n_e is correlated with the surface density of SFR, and found that highly star-forming galaxies have higher n_e. Kaasinen et al. (2017) compared galaxies at z=1.5 to local ones, and found that the n_e for the former is a factor of 5 greater than that of the latter. They found that n_e for galaxies with similar SFRs was the same, independently of their redshift. A high SFR density increases the number of young massive stars, which in turn, by stellar winds and shocks will have a larger energy input to HII regions, and the diffuse ionized gas, increasing the electron density of galaxies.

5.4.1.2 $\mathbf{DM_{host,rf}}$ changes versus star formation activity – the role of n_e

In galaxies that we classified as star-forming, the median DM and $w_{\rm DM,rf}$ is larger than in the case of quenched galaxies by a factor of ∼ 3 (see Fig. 5.5). In spite of this, we find that the path length in quenched galaxies is usually two times larger on average. However, this is not surprising, as the quenched galaxies have large stellar masses (∼ 10 times larger than average SF galaxies) and galaxy sizes (∼ 3 times larger), similar to large ellipticals. Only a few quenched galaxies (∼ 15%) have radii below 5 kpc, and we found that 95% of these galaxies have log $(\mathrm{M_*/M_\odot}) < 10.5$. The average radial profile of n_e of red galaxies is 1.5–3 times lower at all radii, and the average vertical profile is 2 times lower than that of SF galaxies. We also find that the average $n_{\rm e,FRBpos}$ is 4 times larger in star-forming galaxies than in quenched galaxies. The $\langle n_{\rm e,LOS}\rangle$ is 5 times smaller for quenched galaxies. So in summary while the path lengths are larger, the electron densities are lower in red galaxies, which causes their smaller DM contributions.

The red galaxies have already started or gone through quenching, their cold star-forming gas is depleted and the electron densities decreased. As we already described in the previous subsection, there is a connection between the SFR and the n_e of galaxies based on observations (see Section 5.4.1.1), We also find that in galaxies with similar SFR at different redshifts, the median of DM is almost the same (the difference is a few $\mathrm{pc\,cm^{-3}}$).

5.4.1.3 $\mathrm{DM_{host,rf}}$ changes versus stellar mass – the role of n_e

The increase in median DM and width with stellar mass (see Fig. 5.7) can be explained by the MS relation between stellar mass and SFR, as SFR increases with stellar mass, thus the electron densities do too. This increase in median DM continues up to very high mass galaxies ($\log(M_*/\mathrm{M_\odot})$=10.5), where it suddenly drops to half of its value. Here we investigate what causes this sudden drop.

We find that the magnitude of the radial and vertical n_e profiles of galaxies with $\log(M_*/\mathrm{M_\odot})$>10.5 is half of that of galaxies with lower stellar masses, and $\langle n_{\mathrm{e,LOS}} \rangle$ also decreases by a factor of 2. Although the path length increases as a function of stellar mass, the n_e decrease is more prominent, producing low DMs in very massive galaxies.

These massive galaxies are analogous to large ellipticals with low electron densities and star formation rates. The supermassive blackhole (SMBH) feedback mechanism in the simulation (described in Weinberger et al. 2017, Weinberger et al. 2018) becomes very efficient at larger black hole masses ($\sim 10^8 M_\odot$). At lower black hole masses (found in galaxies with lower stellar masses), kinetic energy is injected in pulses, and it is proportional to the surrounding density. The change in the feedback mechanism occurs in galaxies with a stellar mass of around $\log(M_*/\mathrm{M_\odot}) \sim 10.5$: then thermal energy is continuously injected, subsequently lowering the gas densities, electron densities and SFR. The feedback mechanism at large black hole masses is consistent with X-ray observations that show strong outflows are possible from AGNs (Tombesi et al. 2010), which could cause the expulsion of gas from their host galaxies and the suppression of star formation (Combes 2017).

We investigated if the massive galaxies in our sample are truly undergoing quenching. We find that 70% to 90% (corresponding to different redshifts) of galaxies we classified as quenched have a stellar mass above $\log(M_*/\mathrm{M_\odot}) \sim 10.5$. However only <30% of $\log(M_*/\mathrm{M_\odot}) > 10.5$ galaxies are classified as quenched. This is because we only consider galaxies red if they are 1 dex below the MS. So while for galaxies with smaller stellar masses we find an average SFR close to the SFR of the main sequence, for massive galaxies we find SFRs that lie below the MS. These galaxies might have already started the quenching process. The fraction of quenched galaxies decreases at higher redshift, and more massive galaxies are classified as star-forming. We also note that <4% of star-forming galaxies are massive and very active in star formation: with $\log(M_*/\mathrm{M_\odot}) > 11$ and a mean SFR $\sim 10\ \mathrm{M_\odot/yr}$. As we showed in Section 5.4.1.2, n_e is correlated with SFR, and a lower SFR can explain lower DMs.

5.4.1.4 $\mathrm{DM_{host,rf}}$ changes versus inclination – the role of n_e

Galaxies viewed at larger inclinations have larger average DM contributions: the median DM is higher by a factor of $\sim$ 1.5 for edge-on galaxies compared to face-on galaxies (see Fig. 5.7). This is because those sightlines have a longer path through the dense ISM inside the galaxy's disk, compared to the case of face-on galaxies, where the sightline only passes through a short path in the disk. We divided the sightlines, consisting of 1000 sightlines with different inclinations for each galaxy, into four inclination bins at each redshift, resulting in each bin having the same galaxy property (e.g stellar mass, SFR) distribution. This also means there are no differences in the radial and vertical profiles of n_e and B field strength of galaxies in these bins. And, as we select the FRB positions randomly, $n_{\mathrm{e,FRBpos}}$ only fluctuates by 4% for the different inclination bins. Thus we conclude that the trend with inclination is a geometric effect, and is independent of the physical properties of individual galaxies.

We find the $\langle n_{\mathrm{e,LOS}} \rangle$ is larger by a factor of $\sim$ 1.5-2 for edge-on compared to face-on galaxies, which is due to larger n_e in galaxy disks. The median path length decreases slightly with inclination, but the mean path length stays the same. This could be explained by how in edge-on view, both small and long path lengths are possible depending on the line of sight. As our FRB sources are mostly found in a disk, an FRB from a source at the edge of the disk can go through the whole disk and the halo of the galaxy, or only the halo, depending on whether the source is on the near-side or the far-side of the disk with respect to the observer. In face-on view the path lengths are closer to each other, as all sightlines go through the halo.

5.4.1.5 $\mathrm{DM_{host,rf}}$ changes versus b_{offset} – the role of n_e

Sightlines with large b_{offset} have smaller DM on average (see Fig. 5.7), than sightlines with small offsets, and the median DM decreases linearly with increasing b_{offset}. The reason behind this is that at the center of galaxies in the simulation the electron density is higher, and it decreases by a double exponential as a function of radius and distance from the midplane (see the profiles in Fig. 5.10). We find that the path lengths increase with b_{offset}, along with galaxy radius, because galaxies with larger radii have a higher chance of having an FRB with larger offset.

We find that the fitted radial profiles of n_e averaged by redshift (shown in Fig. 5.10, and see Section 5.2) show that in the outskirts of galaxies (outside of the inner 5 kpc) n_e is higher at higher redshifts. At a radial distance of 20 kpc, n_e at z=2 is higher than at z=0 by factor of $\sim$2, but in the center of galaxies it decreases by $\sim$20%. The 1σ width changes only by a factor of $\sim$1.2. The vertical profile of n_e shows a similar behaviour, with a slight decrease in the center ($\sim$20%), but larger n_e beyond 2.5 kpc at higher redshifts. At a vertical distance of 15 kpc from the midplane of the galaxy, the n_e is $\sim$2.3 times larger at z=2 compared to galaxies at z=0, and the 1σ range of values changes by a factor of $\sim$ 1.7.

5.4.2 Interpretation of $\mathrm{RM}_{\mathrm{host,rf}}$ trends

As RM is calculated using Eq. 6.3, in addition to the electron density and path length, it also depends on the strength and direction of the line-of-sight magnetic field, and any change we see in RM should be caused by these quantities. However, considering the large number of galaxies with different field directions, we will see that the magnetic field direction of large-scale fields without reversals will not have an effect on the PDFs. Changes in the direction of the magnetic field in the LOS (due to random fields and field reversals) can cancel out along the LOS thus can lower RM. The way the magnetic field properties were calculated can be found in Appendix D of Appendix III. Here we investigate the reasons behind the changes in the width of $\mathrm{RM}_{\mathrm{host,rf}}$ ($w_{\mathrm{RM,rf}}$) with different parameters.

5.4.2.1 $w_{\mathrm{RM,rf}}$ changes versus redshift – the role of B fields

One main question is whether the change in RM is dominated by changes in n_e or $\vec{B}_{||}$. Similarly to DM, the width of the RM distribution ($w_{\mathrm{RM,rf}}$) also increases as a function of redshift for $z < 1.5$ (see Fig. 5.7), by a factor of ~ 3.5. The $w_{\mathrm{RM,rf}}$ increase below $z = 1$ can be partly attributed to increasing electron densities, but for $1 < z < 1.5$ the $w_{\mathrm{RM,rf}}$ does not increase as rapidly as before. For $z > 1.5$ it starts decreasing, and for $z > 3$, it drops even further (see right panel of Fig. 5.8). The average of the total magnetic field strength in the disk (calculated from the thin projections of the magnetic field strength, details in Appendix D of Appendix III. increases by a factor of 1.2 up to $z = 1$, and at $z = 2$ it drops to the same value as at $z = 0$ (Fig. E.1).Although this is only a small factor, we also need to consider the factor of 4 increase we see in DM. Until $z = 1$, both n_e and the average B field strength increase, so $w_{\mathrm{RM,rf}}$ also increases. For $z > 1$ only n_e increases and the average B field strength decreases, which is partly the reason why the $w_{\mathrm{RM,rf}}$ stops its steep increase.

In Fig. 5.10 we show the radial profiles of B field strength (calculated from the thin projections of the magnetic field strength, described in Appendix D of Appendix III. We find that below z=1, the radial profiles do not show significant changes. However at $z = 2$, the magnetic field strength is 1.5–3 times higher than at lower redshifts within radial distances of less than 7 kpc. At larger radial distances the magnetic field strength is only half of what we see in low redshift galaxies. In the case of the vertical profiles, we find a slight increase of a factor of 1.15 at z=2 compared to z=0. We note that the magnetic field strength profiles are lower in magnitude than those from the observations of NGC6946 (Beck 2007), M101 (Berkhuijsen et al. 2016) and the CHANG-ES galaxies (Krause et al. 2018). This can be due to the limited resolution of IllustrisTNG, causing a missing turbulent field (similar to the Auriga simulations Pakmor et al. 2017).

Assuming a constant magnetic field with no field reversals, we can estimate the average line-of-sight magnetic field strength (a lower limit of the actual magnetic field strength), if both DM and RM are measured for the same FRB sightline: $\langle B_{||,\mathrm{LOS}} \rangle = 1.23 \frac{\mathrm{RM}}{\mathrm{DM}} \mu\mathrm{G}$. The distribution width of $\langle B_{||,\mathrm{LOS}} \rangle$ increases until $z = 1$ by a factor of 1.15, and then decreases by 20% from $z = 1$ to $z = 2$, becoming smaller

than at $z = 0$ (shown in panel c of Fig. 5.9). This is in agreement with the $w_{\rm RM,rf}$ increase mainly caused by the increase in n_e below $z = 1$, and at higher redshifts the magnetic field properties of the galaxies change. Since we estimated $\langle B_{||,\rm LOS}\rangle$ with the assumption of no field reversals, one possible explanation for the decrease in $\langle B_{||,\rm LOS}\rangle$ is the presence of more reversals or random field at $z > 1$ compared to $z < 1$.

Furthermore, we find that the strength of the different magnetic field components changes with redshift. In the top panel of Fig. 5.11 we show that the relative strength of the azimuthal field increases with time. At higher redshift, the azimuthal and radial components of the magnetic field have similar relative strengths, and are only twice as strong as the vertical field strength. As we go towards lower redshift, the relative strength of the azimuthal field increases, becoming 5-6 times larger than the other two components. The increase in the azimuthal field strength is caused by the ordering of the field by the differential rotation of the galaxy disks (Arshakian et al. 2009; Beck 2013). The total magnetic field is already amplified at higher redshifts to saturation, but the ordering of the field only happens at redshifts of $z = 1 - 2$ (similar to Pakmor et al. 2017). The presence of a strong large-scale ordered field can cause high |RM| values, which would increase $w_{\rm RM,rf}$. However, the mean-field dynamo would cause an increase in all magnetic field strength components (see e.g. Shukurov & Subramanian 2021, Section 13.5), in contradiction to the results from TNG50, suggesting the simulation does not contain the mean-field dynamo, which can be due to its limited physical resolution. Nevertheless, purely differential rotation would not cause a decrease in the radial and vertical magnetic field strength with time either, and these would stay constant. The decrease we see in these components could be explained by other processes, such as outflows (Chamandy & Taylor 2015), accretion (Moss et al. 2000), dissipation or reconnection.

Lastly, we use the magnetic field maps where we preserved the sign of the field (thin projections of the magnetic field components centered on the mid-plane) for each magnetic field component, to investigate the presence of 1) large-scale B fields, and 2) B field reversals or random fields in the galaxies. By calculating the average magnetic field strength of the face-on maps with preserved field signs (from here on called signed magnetic field strength), we can separate the two cases. If its absolute value is a few μG the galaxy has a large-scale field without reversal, and if this value is close to 0 μG the field is random or has a field reversal. The distribution of these signed magnetic field strengths is symmetric about 0 μG. In the case of the radial and vertical field, the width of this distribution is low ($< 1\,\mu$G) and does not change with redshift. This is due to their lower field strength compared to the azimuthal component, and that they are more likely to have random field. We find that the number of galaxies with reversals in the azimuthal field or with azimuthal fields dominated by random fields increases towards higher redshift. At $z = 0$ we find 26% (53%) of galaxies have a mean azimuthal field larger than 2 μG (1 μG), and at $z = 2$ we find 6% (22%) of galaxies have a mean azimuthal field larger than 2 μG (1 μG). In the bottom plot of Fig.5.11 we show how the width of the signed azimuthal magnetic field strength distribution ($w_{\rm B,signed}$) changes with redshift. At $z \geq 0.7$ it quickly decreases. As the changes in field direction along the line of sight can cancel each other, more field reversals and

random fields can also cause lower $w_{\rm RM,rf}$.

5.4.2.2 $w_{\rm RM,rf}$ changes versus star formation activity – the role of B fields

The width of the RM distribution ($w_{\rm RM,rf}$) of quenched galaxies is six times lower than that of star-forming galaxies (see Fig. 5.6). This is mainly caused by the decrease in n_e, but we find that the width of the distribution of $\langle B_{||,\rm LOS}\rangle$ along the line of sight in star-forming galaxies is 1.5 times larger than that of red galaxies. This suggests a difference in the magnetic field properties of quenched and star-forming galaxies, in addition to the differences in n_e. Marinacci et al. (2018) investigated the magnetic fields of galaxies in IllustrisTNG100 and IllustrisTNG300, and found that the highest values of field strength are at the highest density peaks. They found that early-type galaxies have an irregular gas distribution (due to the interaction of AGN feedback with the surrounding gas). The magnetic field traces the gas density closely and is therefore also irregular. We also see similar trends in our sample: quenched galaxies are often not well described by a double exponential radial magnetic field strength profile, with a maximum B field strength at larger radii instead of at the center of the galaxy. Their central magnetic field strengths are lower than those for star-forming galaxies. They also exhibit "wiggles" (magnetic field strength fluctuating with radius) in the radial profiles. Similar features can be seen in the gas density profiles, but the n_e profiles can still be described by double exponentials. This irregularity in the magnetic field can cause lower $w_{\rm RM,rf}$.

5.4.2.3 $w_{\rm RM,rf}$ changes versus stellar mass – the role of B fields

We find that the width of the RM distribution ($w_{\rm RM,rf}$) changes with stellar mass. For galaxies below $\log(M_*/{\rm M}_\odot) \sim 10.5$ $w_{\rm RM,rf}$ increases, and for galaxies above that stellar mass, $w_{\rm RM,rf}$ drops and decreases (see Fig. 5.7). As the quenching process usually starts at $\log(M_*/{\rm M}_\odot) \sim 10.5$ in the simulation (Weinberger et al. 2018), the galaxies start to have a different radial B field profile, with lower magnetic field strength at the center and a more irregular magnetic field. This, in combination with lower electron densities, causes a lower $w_{\rm RM,rf}$.

5.4.2.4 $w_{\rm RM,rf}$ changes versus galaxy inclination – the role of B fields

Galaxies with larger inclinations have a larger RM distribution width ($w_{\rm RM,rf}$, see Fig. 5.7) because the sightlines pass through more interstellar medium inside the galaxy, than in the case of face-on galaxies. Another reason is the azimuthal field dominating over the two other magnetic field components (at most redshifts, see Section 5.4.2.1); in the case of an edge-on galaxy, the azimuthal field can be parallel to the line of sight, causing a higher possible RM if there is no field reversal. In the case of a face-on galaxy, the vertical field (which is weaker than the azimuthal field) will contribute the most to the line-of-sight magnetic field, resulting in lower RMs. We note this contribution can be close to 0 in the case of symmetric vertical fields. We can see that at $z \geq 1$, $w_{\rm RM,rf}$ does not increase as much with inclination, compared to lower redshifts. This

is because the field was less ordered at higher redshift (see Section 5.4.2.1 and Fig. 5.11), and the azimuthal field does not dominate over the other components, causing a weaker inclination dependence.

5.4.2.5 $w_{\rm RM,rf}$ changes versus projected FRB offset – the role of B fields

Sightlines with larger $b_{\rm offset}$ have smaller RM distribution width ($w_{\rm RM,rf}$), on average, than sightlines with smaller $b_{\rm offset}$ (see Fig. 5.7). At the center of galaxies the magnetic field is the strongest (apart from quenched galaxies), and the radial profile often can be fitted by a decreasing double exponential (see Appendix D of Appendix III. RM decreases more rapidly than DM, because both n_e and B exponentially decrease with radius.

5.4.3 Comparison to previous works

5.4.3.1 DM

There have been multiple previous works in the past years that have estimated $\rm DM_{host}$. Here we compare our results to most of them.

Hackstein et al. (2019) investigated $\rm DM_{host}$ in a spiral similar to the MW (using the NE2001 electron density model of the Milky Way, Cordes & Lazio 2002). They found an observed mean DM contribution of ∼110 pc cm^{-3} at z=0, double our result, and this is also the case if we select galaxies with MW mass (10.69<log(M_*/M$_\odot$)<10.86, Licquia & Newman 2015). The differences could be due to the differences in the n_e profiles: NE2001 has a thick disk profile, where $n_e > 10^{-2}\,\rm cm^{-3}$ out to 15 kpc, whereas we have a double exponential decline that reaches n_e of $\sim 10^{-2}\,\rm cm^{-3}$ at ∼ 12 kpc on average. As Hackstein et al. (2019) did not take into account increasing n_e at higher redshift, they found that the observed DM decreases with increasing z to ∼35 pc cm^{-3} at z=2 (compared to ∼50 pc cm^{-3} from our results).

Xu & Han (2015) investigated the galaxy disk inclination dependence of the DM of FRB hosts, also using the NE2001 model. They find a similar exponential DM decrease with increasing inclination, similar to our result, but with a larger magnitude decrease. We find larger DMs for face-on galaxies by a factor of two and lower DMs for edge-on galaxies by a factor of two than Xu & Han (2015). This can be again explained by different n_e profiles: while the radial n_e profiles of our galaxies are lower on average than the one from NE2001, our vertical profiles have larger n_e out to larger vertical heights. In face-on view, the majority of the sightline passes through the halo providing us with a larger DM compared to Xu & Han (2015), and in edge-on view the sightline passes through the disk causing us to have a smaller DM.

Walker et al. (2020) calculated DM for a spiral and an elliptical galaxy n_e model with different starting positions corresponding to different progenitors (OB stars, young and old pulsars, millisecond pulsars). The DM of sources following stellar distributions in spiral galaxies have similar lognormal shaped DM distributions, with medians of 68 – 98 pc cm^{-3}, which is slightly higher than ours. They found DM can potentially be

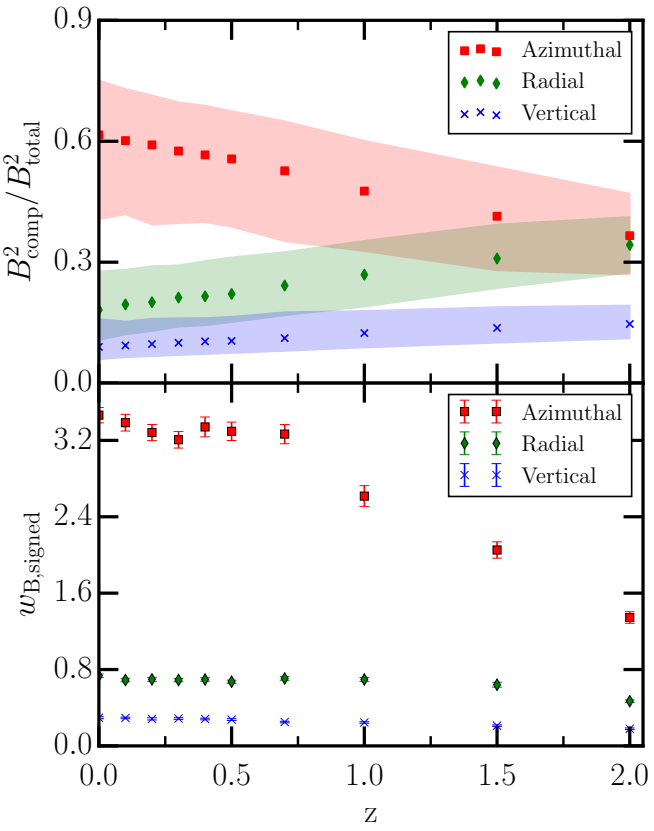

Figure 5.11: **Top:** The median of the different magnetic field components' ratios to the total magnetic field ($B^2_{\rm component}/B^2_{\rm total}$, where the components are azimuthal, radial, and vertical). The median ratio of azimuthal field increases with time, while the ratio of radial and vertical field decreases. This shows how the differential rotation orders the field, converting other magnetic field components to azimuthal field. **Bottom:** The distribution width of the average of the signed magnetic field strength maps. The distribution width of the azimuthal B field decreases with increasing redshift, showing that there are more reversals and random field at high redshift. The distribution widths of the radial and vertical B field are small at all redshift.

higher than 700 pc cm^{-3}, while our sample can produce DMs of several 1000 pc cm^{-3}. In summary, their results are consistent with ours.

Hackstein et al. (2020) used galaxy models from Lacey et al. (2016) produced by GALFORM, a semi-analytic galaxy formation model (SAM), to calculate DM. GALFORM includes effects of gas cooling, angular momentum conservation, star formation, and AGN as well as stellar feedback. The model provides the evolution of the global properties of galaxies, from which n_e can be calculated. Hackstein et al. (2020) give the likelihood function of observed host DMs for the full sample considering redshift distributions based on the capabilities of ASKAP, CHIME and Parkes radio telescope: possible values range from approximately 0.1 to 450 pc cm^{-3}. To compare, we also use our sightlines from every redshift, and convert them to the observer's frame. Considering 3 σ (99.7% of data points), DM ranges from 10^{-4} to 490 rad m^{-2}, which has a similar range. It is not surprising that in general the range of values are consistent, as previous works show that SAMs and hydrodynamical simulations are generally in good agreement, although there are differences due to the dissimilarity in the evolution of gas properties (see e.g. Mitchell et al. 2018's comparison between EAGLE and GALFORM).

As we showed in Fig. 5.3, Zhang et al. (2020) calculated the DM contribution of host galaxies using IllustrisTNG100-1, considering redshifts up to z=1.5. They selected (a) 200 galaxies similar to the host of FRB180916, (b) 200 similar to the hosts of non-repeating FRBs known at the time of Zhang et al. (2020)'s paper and (c) 1000 similar to the host of the repeating FRB121102. For each subhalo they selected 500 starting positions, and for each position they consider 10 random direction. Their DM$_{\rm median}$ results agree within the 1 σ width of our result from Section 5.3 (using every galaxy below z=2), despite the physical resolution of TNG100 being three times worse than TNG50's[5]. Based on the galaxy selection criteria, our selection should be similar to cases (a) and (b), as both have a similar stellar mass range: $9<\log(M_*/{\rm M}_\odot)<11$ and $9<\log(M_*/{\rm M}_\odot)<11.5$, respectively. Case (c) has galaxies with $\log(M_*/{\rm M}_\odot) < 8$, which our selection does not include. Zhang et al. (2020) reports that the difference between the (a) and (b) cases are due to the different FRB positions, as in case (b) the FRBs are at the edges of the galaxies. This is in agreement with the decreasing DM$_{\rm host,rf}$ trend we have found as a function of $b_{\rm offset}$. However, it does not explain why the median DM$_{\rm host,rf}$ in case (a) is larger than in our sample. One possible explanation is the difference in resolution between the two simulations. Alternatively, it may also be due to the longer integral path lengths they used to calculate DM, which can be larger than ours by a factor of $\sim$ 10, due to how they defined the integral to extend to each cell that is assigned to a subhalo.

We note that another key difference between the two cases is the SFR of the selected galaxies: (a) contains galaxies with $0.01<{\rm SFR}({\rm M}_\odot/{\rm yr})<10$, and (b) has ones with $0<{\rm SFR}({\rm M}_\odot/{\rm yr})<2$, meaning that group has a lower SFR on average. As we showed in Section 5.4.1.2, star formation increases with the electron densities, thus it is also

[5]The TNG model has systematics with resolution: galaxies with the same halo masses have larger stellar masses with increasing resolution. This can have an effect on the black hole masses, and on the gas fractions, thus n_e(Pillepich et al. 2018)

connected to DM_{host}, which could explain why DM is generally larger in case (a) than in case (b). Since we consider all galaxies with SFRs above 0, our result can be found in between the two cases from Zhang et al. (2020). Additionally, we also include galaxies with even larger stellar masses, which have lower DM on average, further lowering the median DM.

Jaroszyński (2020) used IllustrisTNG100-3 and IllustrisTNG100-1 subboxes to calculate the host galaxy contributions to DM, using galaxies with $7.5<\log(M_*/M_\odot)<11$ at $0 \leq z \leq 3$. They stack galaxies to determine n_e as a function of distance from the galaxy center out to 10 Mpc, and the free parameters for their DM calculation are the FRB distance from the host center and the angle between the ray and the direction to the center. They find that n_e and DM increase with stellar mass, up to $\log(M_*/M_\odot)<10.5$, and both are lower for massive galaxies with $\log(M_*/M_\odot)>10.5$, similarly to what we found. However, this changes after z=2, where $\log(M_*/M_\odot)>10.5$ galaxies have larger DMs than galaxies with lower stellar mass. For us this change already happens at z=1.5. This can be due to resolution affecting the black hole masses, which would cause the quenching mechanism to turn on earlier in TNG50. They also find that DM decreases with the distance of the line of sight from the center of the galaxy (so equivalent to our b_{offset}). While qualitatively the trends are similar to what we found, the host DM values are significantly higher than what we calculated, and even higher than the results of Zhang et al. (2020). At $z \leq$2 their DMs can be a factor of 2 – 3 higher than ours, and at z=2 these becomes 6 times higher. We noticed that the difference is larger for galaxies with stellar masses above $\log(M_*/M_\odot)>10$, for less massive galaxies our results are in a better agreement. The large magnitude in DM difference is probably due to differences in how Jaroszyński (2020) define the end of the integral (the galaxy's radius). They integrate up to $\sim$ 600 kpc as their n_e profiles fall to 0 cm^{-3} at that radius, while most of our galaxies have a radius of $\sim$ 20 kpc. Another reason for differences could be that they calculated the n_e profiles statistically from galaxies in IllustrisTNG100-3 and IllustrisTNG100-1 subboxes which have lower resolution. In contrast, we used TNG50 with higher resolution and directly integrated n_e in many sightlines. Jaroszyński (2020) also calculated the DM contribution of FRB190608, which we investigate in Section 5.6. We found the observed $DM_{host,median}$ to be 90 – 130 pc cm^{-3}, and they derived 144 $\pm$ 30 pc cm^{-3}, which are in agreement with each other within 1σ. The DM difference is not large for this case because of the galaxy's low redshift.

Using FRBs that have been localized to host galaxies, Macquart et al. (2020) fitted their DM_{excess} versus redshift relation, and found that the host DM contributions are best described by a lognormal distribution with median 100 pc cm^{-3} and σ =1. Our DM host distribution medians at $z = 0$ are half of that (but they reach 100 pc cm^{-3} at $z = 0.7$), and our σ is slightly larger ($\sim$1.3). However, the parameters of the lognormal from Macquart et al. (2020) and our results are on the same order of magnitude.

Walker et al. 2023 (in prep) have investigated the contribution of the Cosmic Web to the DM of FRBs based on TNG300, including intervening galaxies in the LOS. They found a similar trend of increasing restframe DM with increasing intervening galaxy redshift, but this increase is suppressed when the DM is converted to the observer's

frame. The median of their DM distributions is on an order of 1 $\mathrm{pc\,cm^{-3}}$, which is significantly lower than ours, but this is expected as the sightlines can go through at impact parameters of 100s or 1000s of kpc in the intervening galaxies (Walker et al. 2023, in prep).

5.4.3.2 RM

We compare our results to two studies about the RM contribution of FRB host galaxies, and also to a work about intervening galaxies in front of background quasars.

Basu et al. (2018) investigated the RM distribution of disk galaxies, using galaxies with a large-scale axisymmetric spiral magnetic field and a radially decreasing electron density (while neither the B field geometry nor n_e changes with distance from the midplane). They studied the RM of background sources, thus their sightlines go through the entire galaxy, unlike in our case. In spite of these differences, they found a similar distribution shape as we did for the RM of FRBs in Section 5.3: they modelled these distribution as the sum of a Lorenztian and two Gaussians, and found that the width of the Lorentzian was proportional to the mean axisymmetric field strength. Our distributions can also be fitted by the same function. The width of their Lorentzian ranges from 15 – 60 rad $\mathrm{m^{-2}}$ for different B field strengths. We find that at z=0 the width of the Lorentzian for our sample is 60 rad $\mathrm{m^{-2}}$, which is close to their results. However, the width of our Lorentzian increases with redshift with the largest value of 150 rad $\mathrm{m^{-2}}$ at z=1.5, more than two times larger than Basu et al. (2018)'s results, while the total magnetic field strengths of our sample does not increase with redshift. The increase in width is probably caused by the increase in n_e. Nevertheless, there is a number of differences between the two experiments: in Basu et al. (2018) there is only a large-scale magnetic field, with no vertical magnetic field component, and the sightlines go through the whole galaxy. In our simulation, while the total magnetic field strength does not change with redshift, the strength of the different magnetic field components do, and we also find more reversals as redshift increases.

Hackstein et al. (2019) calculated the RM contribution of a possible MW-like spiral host galaxy (using NE2001 and a model of the MW galactic-scale magnetic field – Jansson & Farrar 2012), and found the mean |RM| is $\sim$ 65 rad $\mathrm{m^{-2}}$ at z=0. To compare our results, we also calculate the mean |RM| at z=0, and we derive $\sim$ 100 rad $\mathrm{m^{-2}}$, which is almost twice as large. Since the n_e and B models they used were for the Milky Way, we selected galaxies at $z = 0$ with similar stellar masses as the Milky Way ($10.69<\log(M_*/\mathrm{M_\odot})<10.86$, Licquia & Newman 2015), and recalculated |RM|. We found it to be 63 rad $\mathrm{m^{-2}}$, which is very close to what Hackstein et al. (2019) found. This is surprising as the DM distributions we find are different compared to the NE2001 model, but might show that for MW-like galaxies, their model gives the same result as TNG50. As Hackstein et al. (2019) did not consider that n_e or B change with redshift, they predicted that the observed RM would fall to |RM| $\sim$ 7 rad $\mathrm{m^{-2}}$ at z=2. We find the observed |RM| would be $\sim$ 50 rad $\mathrm{m^{-2}}$ at $z = 2$ from our sample: it would still be smaller compared to z=0, but by only a factor of two.

Hackstein et al. (2020) used galaxy models from Rodrigues et al. (2019), who studied the evolution of magnetic fields of galaxies from Lacey et al. (2016) produced by GALFORM, a semi-analytic galaxy formation model, by using the MAGNETIZER code on them (Rodrigues & Chamandy 2020). This code numerically solves the non-linear turbulent mean-field dynamo equation, which provides them with the radial profiles of the strength of the radial and toroidal components of the coherent magnetic field, and both the B field strength and the density declines exponentially with the distance from the plane. When calculating RM they do not include the small-scale field. They use a few million galaxies with stellar masses of $7<\log(M_*/\mathrm{M}_\odot)<12$, including spiral, lenticular and elliptical galaxies, but do not include irregular galaxies. A large fraction of this galaxy sample have a very weak B field strength (<0.05 μG). They give the likelihood function of observed host |RM|s for the full sample (the same way as for DM): possible values range approximately from 0.01 to 320 rad m^{-2}. To compare our results to theirs, we also use all of our sightlines from every redshift, and convert them to the observer's frame and use the absolute values of RM. Considering 2 σ (95% of our data), we get a range of 0.2 to 490 rad m^{-2}, which shows slightly larger possible |RM|s than those from Hackstein et al. (2020) but is consistent with their results. As the magnetic fields in Hackstein et al. (2020) are based on the mean-field dynamo theory and only includes large-scale field, it surprising their results agree so well with our RMs from the TNG50 MHD simulation, where we do not see the amplification from the mean-field dynamo. However, if we consider 3 σ (99.7%), we get a range of 10^{-8} to 2650 rad m^{-2}, which includes significantly higher |RM| values. This could be because the magnetic field of many galaxies in their sample are very weak, and they only include the large-scale coherent magnetic field and not the small-scale or random field. Rodrigues et al. (2019) found that only 40% of galaxies with $\log(M_*/\mathrm{M}_\odot)=9$ have significant B field, and they found a clear bimodality in the distribution of B field strengths, one of the parameters they used to characterize B field is the maximum B field strength in the radial profile. We find a small bimodality in the distribution of the B field strengths at the center of galaxies (for us the maximum magnetic field strength is usually at the center of the galaxy), but only $\sim$15% of our galaxies are in the group of weak magnetic fields.

Overall, we found that our results are consistent with previous results, even though they were derived with different methods. This can be due to the fact that all of these methods mainly resolve the large-scale magnetic field of galaxies. We might find differences if we can resolve the small-scale field, for example if we use a simulation with even higher spatial resolution than IllustrisTNG50.

5.5 Implication on future studies of the magnetic field of the IGM

5.5.1 $\mathrm{DM_{host}}$ and $\mathrm{RM_{host}}$ in the observer's frame

Zhou et al. (2014) has pointed out that if $\mathrm{DM_{host,rf}}$ does not increase as fast as the $1+z$ factor from the redshift dilution decreases it, FRBs can be easily used as cos-

mological probes without much contamination from the host galaxy DMs. Because of this, we investigate how the DM and RM contributions of the host galaxies change with redshift in the observer's frame ($\mathrm{DM_{host,obs}}$ and $\mathrm{RM_{host,obs}}$). We calculated $\mathrm{DM_{host,obs}}$

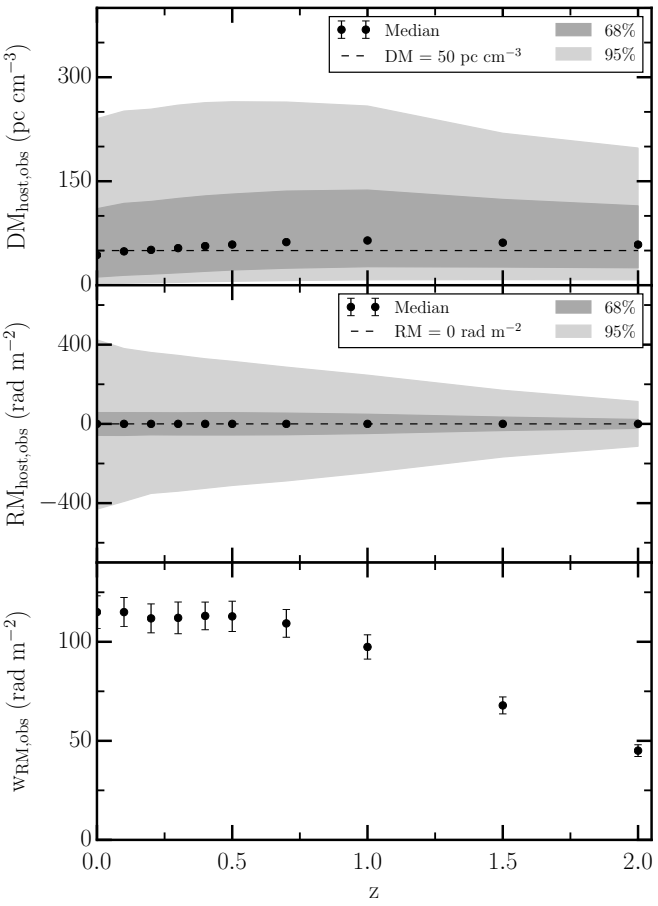

Figure 5.12: **Top**: The possible observed DM contribution of host galaxies based on 68% and 95% of our sightlines. The black points are the medians of DM at each redshift. The contribution decreases slightly at higher redshifts. **Middle:** The same as top, but for the possible observed RM contribution of host galaxies. This contribution decreases significantly with redshift. **Bottom:** The width of the observed RM distribution as a function of redshift. It decreases significantly as a function of redshift.

and $\mathrm{RM_{host,obs}}$ by correcting $\mathrm{DM_{host,rf}}$ and $\mathrm{RM_{host,rf}}$ calculated from the simulation with the redshift of the galaxies:

$$\mathrm{DM_{host,obs}} = \frac{\mathrm{DM_{host,rf}}}{(1+z_{\mathrm{host}})} \tag{5.21}$$

and

$$\mathrm{RM_{host,obs}} = \frac{\mathrm{RM_{host,rf}}}{1+(z_{\mathrm{host}})^2}. \tag{5.22}$$

In Fig. 5.12, we show the 68% and 95% of DM and RM for each redshift. Considering all sightlines at all redshifts 95% of $\mathrm{DM_{host,obs}}$ is between 4 and 250 pc $\mathrm{cm^{-3}}$, and 95% of $|\mathrm{RM_{host,obs}}|$ is less than 310 rad $\mathrm{m^{-2}}$. These ranges decrease at higher redshift: only slightly in the case of $\mathrm{DM_{host,obs}}$, but significantly in the case of $\mathrm{RM_{host,obs}}$.

The differences in the $\mathrm{DM_{host,obs}}$ at different redshifts is smaller than what we have seen in the rest frame DMs. The median of $\mathrm{DM_{host,obs}}$ is between 46 and 69 pc $\mathrm{cm^{-3}}$, it first increases slightly, then decreases after $z = 1$. Thus, the median $\mathrm{DM_{host,obs}}$ is similar at every redshift. The $w_{\mathrm{DM,obs}}$ also does not change significantly (1σ width: 92−115 pc $\mathrm{cm^{-3}}$, and 2σ width: 202−278 pc $\mathrm{cm^{-3}}$). This means if we have no information about the host galaxy, we can subtract the same host DM contribution from each FRB's total observed DM, independently from the host's redshift. This is in contrast to the results of Jaroszyński (2020), who found even the observed DM increases with redshift (probably due to their longer integral path lengths).

We show in the middle panel of Fig. 5.12 that the median of $\mathrm{RM_{host,obs}}$ is 0 rad $\mathrm{m^{-2}}$ at every redshift. The 2 σ width of the $\mathrm{RM_{host,obs}}$ distribution linearly decreases with redshift: it drops from 800 rad $\mathrm{m^{-2}}$ at $z = 0$ to 200 rad $\mathrm{m^{-2}}$ at $z = 2$. In the bottom panel of 5.12 we show the changes of $w_{\mathrm{RM,obs}}$: at $z \leq 0.5$ it does not change significantly ($w_{\mathrm{RM,obs}} = 111 - 119$ rad $\mathrm{m^{-2}}$), but it starts to decrease after $z = 0.7$.

We find that the increase in $\mathrm{DM_{host,rf}}$ and $\mathrm{RM_{host,rf}}$ with increasing redshift is weaker, than the decrease due to redshift dilution. As both $\mathrm{DM_{IGM}}$ and $\mathrm{RM_{IGM}}$ should increase towards higher redshift, if we observe FRBs at high redshift, we can get better constraints on cosmological parameters and the IGMF.

5.5.2 Number of FRBs needed for IGM studies

FRBs can be used as a promising probe of the IGMF (Zheng et al. 2014; Akahori et al. 2016). However, since the RMs measured towards a sample of FRBs contains contribution from the FRB host galaxy and the IGMF, we investigate the minimum number of polarized FRBs required to statistically infer the IGMF. We note that in the past most surveys have not recorded the polarization data of FRBs, however, the current and future surveys are going to also observe polarization, which will result in an increase in the number of FRBs with measured RMs.

We perform a two-sample Kolmogorov-Smirnov (KS) test on the distributions of RM, with and without the contribution from IGMF, in order to estimate the number of polarized FRBs needed to constrain the IGMF. We assume that the RM contributed by the Milky Way has been robustly subtracted, the RM contributed by the FRB host galaxies at a particular redshift follows the distribution shown in the bottom panel of Fig. 5.3, and the RM from the local environment is negligible. We model the statistical distribution of RM arising in the IGMF ($\mathrm{RM_{IGM}}$) as Gaussian distribution with mean zero, and standard deviation $\sigma_{\mathrm{RM,IGM}}$.

For the purpose of this work, we consider $\sigma_{\mathrm{RM,IGM}} = 2$, 10, 20, and 40 rad $\mathrm{m^{-2}}$, following the findings of (Akahori et al. 2016). They found that $\sigma_{\mathrm{RM,IGM}}$ increases from $z = 2$ to $z = 7$, from 16 to 45 rad $\mathrm{m^{-2}}$ considering all IGM (including hot gas in clusters), and from 1.3 to 9 rad $\mathrm{m^{-2}}$ for only filaments. In order to estimate the

Table 5.2: The parameters of the fit (Eq. 5.23) for $N_{\rm FRB}$ as a function of $\sigma_{\rm RM,IGM}$ at $z = 0.5$ and $z = 2$.

z	$a_{\rm IGM}$	$b_{\rm IGM}$	$c_{\rm IGM}$
0.5	3706.0 ± 413.6	-7.0 ± 0.2	-4118.0 ± 547.7
2.0	1759.0 ± 202.9	-4.0 ± 0.2	-1825.0 ± 227.4

statistical difference in the distributions of RM for $N_{\rm FRB}$ FRBs, with and without the contribution of IGMF, we randomly draw $N_{\rm FRB}$ values of $\rm RM_{host,obs} + RM_{IGM}$ and $\rm RM_{host,obs}$, and determine the p-value by applying KS test. We performed 1000 Monte-Carlo simulations for a given $N_{\rm FRB}$, where $N_{\rm FRB}$ ranges between 10 and 10^6. For a given $\sigma_{\rm RM,IGM}$, the $N_{\rm FRB}$, for which at least 95% of the Monte-Carlo samples has $p < 0.05$, is considered as the minimum number of FRBs needed to discern the contribution of IGMF at 95% confidence level. We did these tests for sightlines at $z = 0.5$ and $z = 2$.

In Fig. 5.13 we show how many FRBs we need to detect an IGMF with a given $\sigma_{\rm RM,IGM}$ at these redshifts. To detect a $\sigma_{\rm RM,IGM}$ of 40 rad m^{-2}, we need at least 350 FRBs at $z = 0.5$ or 150 FRBs at $z = 2$. For a small $\sigma_{\rm RM,IGM}$ of 2 rad m^{-2} we need at least 95 000 FRBs at $z = 0.5$ or 9 500 FRBs at $z = 2$. We need fewer high redshift FRBs than low redshift FRBs to detect the same $\sigma_{\rm RM,IGM}$ due to the width of the distribution of the observed $\rm RM_{host}$ decreasing with redshift. We find that $N_{\rm FRB}$ as a function of $\sigma_{\rm RM,IGM}$ can be fitted by a function in the following form:

$$N_{\rm FRB} = a_{\rm IGM} \exp(-b_{\rm IGM}/\sigma_{\rm RM,IGM}) + c_{\rm IGM}, \tag{5.23}$$

where the $a_{\rm IGM}$, $b_{\rm IGM}$ and $c_{\rm IGM}$ parameters are listed in 5.2 for $z = 0.5$ and $z = 2$.

We also investigate how adding measurement uncertainty to the observed RM would affect the number of FRBs needed. We added a Gaussian noise with σ = 1, 5, 10, 20, and 50 rad m^{-2} to our RMs. We found that the number of FRBs needed to detect the IGMF exponentially increases with the error of RM. An error of 1 to 10 rad m^{-2} would increase the number of FRBs by 1.5 to 5 times (depending on $\sigma_{\rm IGM}$). In the case of $\sigma_{\rm IGM}>$ 10 rad m^{-2} higher errors also increase the required number of FRBs by a similar magnitude. For $\sigma_{\rm IGM}$ = 2 rad m^{-2}, an $\rm RM_{error}$ = 20 rad m^{-2} and $\rm RM_{error}$ = 50 rad m^{-2} increases the required number of FRBs by 20 and 300 times, respectively. This additional uncertainty can also be considered the contribution of the immediate environment if it is on an order of $1 - 50$ rad m^{-2}. Thus the increase in the required number of FRBs is true as well as in the case of RM from the source environment.

We conclude that in the case of a $\sigma_{\rm RM,IGM}$ = 40 rad m^{-2} we will be able to constrain the IGMF with a few hundred - thousand FRBs (even if we take into account the measurement error of RM), which will be realistically achieved in the next years. In the case of $\sigma_{\rm RM,IGM}$ = 2 rad m^{-2}, we will need significantly more FRBs.

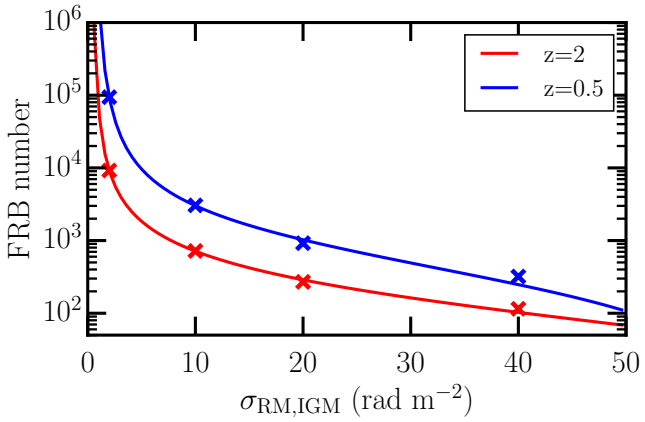

Figure 5.13: The number of FRBs needed to detect a given $\sigma_{\rm RM,IGM}$ at two redshifts ($z = 0.5$ and $z = 2$). We consider the IGMF possible to detect if the KS test returns a p-value below 0.05 for 95% of Monte Carlo tests (for details see Section 5.5.2). The data points show the FRB number needed for significant detection for a given $\sigma_{\rm RM,IGM}$, and the solid line is the reciprocal exponential fit.

5.6 Application to localized FRBs: FRB190608 as a case study

In this section, we show how we can constrain the $\rm DM_{host,rf}$ and $\rm RM_{host,rf}$ contribution of localized FRBs with identified host galaxies (with detailed information about the galaxy properties and the FRB position within the host) using TNG50 of the IllustrisTNG simulation. First, we calculate $\rm DM_{host,rf}$ and $\rm RM_{host,rf}$ by placing FRBs in galaxies with similar properties to the host at specific locations. Then we use our sightlines calculated in Section 5.3 (referred to as 'database' from here on), and select sightlines that match the host galaxy properties, i and $b_{\rm offset}$. We compare these methods to see how well our database of sightlines can be used. We also show that our estimates are consistent with observations.

The host galaxy of FRB190608 is well known, thus it provides numerous constraints on both the selection of analog galaxies from the simulation and the location of the FRBs in them. The FRB was detected by Macquart et al. (2020) with the ASKAP-ICS. The host is a spiral galaxy at $z = 0.12$ with $\log(M_*/\rm M_\odot) = 10.06^{+0.09}_{-0.12}$ and an SFR of $0.69 \pm 0.21\, M_\odot\, \rm yr^{-1}$ (Heintz et al. 2020). It has an inclination of 43° and a position angle (PA) of 54° based on the HST NIR image of the host galaxy, and the FRB is along the minor axis of the galaxy at a projected offset of 6.52 ± 0.82 kpc from the center, in a spiral arm (Mannings et al. 2021). The DM and RM of the FRB were measured as well: $\rm DM_{obs} = 338.7 \pm 0.5\, pc\, cm^{-3}$ (Macquart et al. 2020) and $\rm RM_{obs} = +353 \pm 2\, rad\, m^{-2}$ (Day et al. 2020). These contain all the different components along the line of sight; the immediate source environment, the host galaxy, the IGM and the Milky Way.

We select analogs of the host galaxy of FRB190608 from the TNG50 simulation based on their stellar mass, SFR and $r_{\rm SF,99}$ from the snapshot at $z = 0.1$. We found

Table 5.3: The median and 1σ range of FRB190806's $\mathrm{DM_{host,rf}}$ and $\mathrm{RM_{host,rf}}$ from different sightlines.

Subset of sightlines	N_{sl}	median $\mathrm{DM_{host,rf}}$ ($\mathrm{pc\,cm^{-3}}$)	1σ DM ($\mathrm{pc\,cm^{-3}}$)	median $\mathrm{RM_{host,rf}}$ ($\mathrm{rad\,m^{-2}}$)	1σ RM ($\mathrm{rad\,m^{-2}}$)
Spec. loc.	3000	118	60 – 190	+7	−74 – +99
DB. all	3000	103	47 – 207	+3	−192 – +231
DB. b_{offset}	257	107	49 – 207	+3	−222 – +226
DB. i	61	87	50 – 146	−17	−186 – +89
DB. $b_{\mathrm{offset}}+i$	7	93	75 – 144	+24	−143 – +262

Notes: First line lists the results from placing the FRBs at the minor axis of the host galaxy analogs, and the rest of the table shows the results using our 'database' of sightlines from Section 5.3.1. We show the results using all sightlines from the analog galaxies in the database, sightlines selected based on their galaxy inclination, b_{offset}, and both. We show how the number of appropriate sightlines decreases when we apply stricter selection rules.

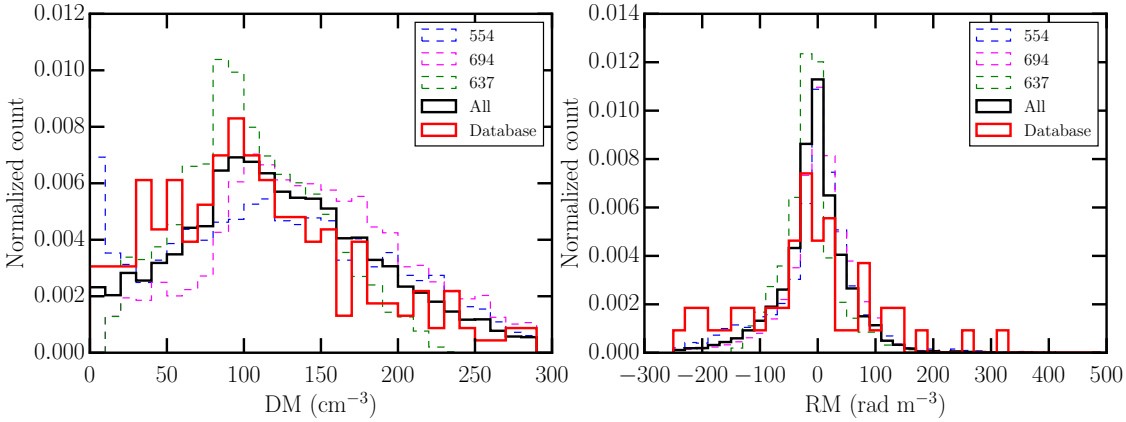

Figure 5.14: **Left:** The $\mathrm{DM_{host,rf}}$ distribution of FRBs placed in the analogs of the host galaxy of FRB190608. **Right:** The $\mathrm{RM_{host,rf}}$ distribution of FRBs placed in the in the analogs of the host galaxy of FRB190608.

three galaxies that had the same stellar mass as the host within the error of the stellar mass, the same SFR_{MS}-SFR difference, and an $r_{SF,99}$ larger than the offset of the FRB. We calculate the host's difference from the MS of star-forming galaxies using the relation from Zahid et al. (2012), then we use the same difference from the simulation derived MS to constrain the SFR of the host galaxy analogs. The halo IDs are 554, 637 and 694, and all of the selected galaxies are the first (most massive) subhalos of their parent halo. We rotate the galaxies to the same inclination as the one measured for the host galaxy. Considering the PA of the host and the position of the FRB in the HST image, we place the FRBs along the minor axis of the galaxy. We then calculate the DM and RM in the same way as we calculated for the other FRBs in this paper (see Section 5.2).

The DM distributions of the three host galaxy analogs of FRB190608 are shown in Fig. 5.14. The median of the DM distributions for each galaxy is between 101 and 146 pc cm^{-3} (118 pc cm^{-3} for all sightlines), and the 1σ range of possible values is 60 – 190 pc cm^{-3}. We convert this to the observed DM: median $DM_{host,obs}$ = 83 – 121 pc cm^{-3}, and the range of values is 50 – 157 pc cm^{-3}. This is consistent with the observation, as it is smaller than the observed DM of the FRB. Even if we consider the 2 sigma range of possible values, we get 286 pc cm^{-3} as the upper bound. If we subtract the DM contributed by MW (DM_{MW} = 38 pc cm^{-3} along this sightline Cordes & Lazio 2002) from the observed DM we derive 300.7 pc cm^{-3}, which is still above our upper limit.

Chittidi et al. (2021) derived the host DM from the Hα emission measure: the DM of the host ISM is 94 ± 38 pc cm^{-3} (range of 56 – 132 pc cm^{-3}) and the DM of the host halo is 55 ± 25 pc cm^{-3} (range of 30 – 80 pc cm^{-3}). Including both the ISM and the halo of the host they derived a range of 100 – 190 pc cm^{-3}. Their range of host ISM DM is very close to the host DMs we derived, although in our case larger values are also possible, which could mean we have some DM contribution from the halos of the galaxies. Thus we conclude that our results are consistent with observations.

We constrain the IGM's DM contribution by subtracting our host contribution estimate and the contribution of the Milky Way from the observed DM, including the ISM and the halo – the latter is 39 pc cm^{-3} according to Prochaska & Zheng 2019. We obtain a residual DM_{res} = 105 – 212 pc cm^{-3}. This DM can arise from the IGM and the immediate source environment, making this estimate an upper limit on DM_{IGM}. In comparison, Simha et al. 2020 derived a DM_{IGM} (also including intervening halos) of 98 – 154 pc cm^{-3} using the Monte Carlo Physarum Machine (Elek et al. 2022), which has a very similar range to our result. We may have some larger possible DM values because we did not take into account the immediate environment of the source.

We calculate a median $RM_{host,rf}$ of +7 rad m^{-2} with 1σ range of −74 – +99 rad m^{-2}. If we convert this to the observer's frame, we derive a median $RM_{host,obs}$ = +5.6 rad m^{-2} and a 1σ range of −59 – +79 rad m^{-2}. We note that median $RM_{host,rf}$ might be further from 0 rad m^{-2} as we have multiple restrictions on the position of the FRB, which can skew the distribution. Based on the all-sky RM map of Hutschenreuter et al. (2022), the contribution of the Milky Way towards FRB190608 is RM_{MW} = −24 ± 13 rad m^{-2}. If we subtract these contributions, we derive a range of residual RM_{res} = +283 – +451 rad m^{-2}, which includes the contributions of the IGM and the

immediate source environment. In the case of RM, the contributions along the line of sight can be negative or positive, hence it is difficult to determine if $\mathrm{RM_{IGM}}$ is lower or higher than this estimate.

We can also provide DM and RM estimates using our database of 16.5 million sightlines calculated in Section 5.3, however, there will be fewer sightlines that fulfill all the placing criteria we used above. In table 5.3, we show the median and 1σ ranges of DM and RM of all sightlines that belong to the three analog galaxies regardless of inclination and b_{offset}, of sightlines that have $b_{\mathrm{offset}} = 6.52 \pm 0.82$, of sightlines with $42.27 < i < 43.95$, and of sightlines that fulfill both the b_{offset} and i criteria. The medians and ranges of the different sightline selections are of the same magnitude. We find that constraining the inclination of selected sightlines had a bigger effect on the ranges of DM and RM than constraining b_{offset} (which gives almost the same DM and RM range compared to the full sample of sightlines). We find this to be the case even if we increase the uncertainty of the inclination ($32.27 < i < 53.95$), so it is not only caused by the lower relative uncertainty of the inclination compared to that of the offset.

We can see that in the case of host DM we get a similar range of values from our database of sightlines (even without strict selection criteria) and from placing FRBs at a more specified location, but for host RM the possible range is much larger in the case of sightlines from our database. This could be because RM is more sensitive to the exact place in the galaxy, as in our previous test we placed FRBs specifically on the minor axis. The DM histogram of the offset-selected sightlines, and the inclination-selected RM sightlines match the histogram of our previous test the most. Therefore we suggest, if possible, selecting sightlines based on their inclination when one wants to constrain the RM contribution of a host galaxy from our database of sightlines.

In summary, we showed that IllustrisTNG gives reasonable estimates on the DM and RM of host galaxies as they are consistent with observations. We demonstrated that our database of sightlines can be used to constrain the DM and RM contributions of host galaxies.

5.7 Conclusions

We have calculated the DM and RM contribution of FRB host galaxies ($\mathrm{DM_{host,rf}}$ and $\mathrm{RM_{host,rf}}$) using the state-of-the-art MHD simulation TNG50 of IllustrisTNG project for a large sample of galaxies ($\sim$16 500). We investigated how the median $\mathrm{DM_{host,rf}}$ and the width of the $\mathrm{RM_{host,rf}}$ distribution ($w_{\mathrm{RM,rf}}$) change with redshift, stellar mass, inclination, and FRB projected offsets from the center of galaxies (b_{offset}).

Our main findings are:

- The distributions of $\mathrm{DM_{host,rf}}$ can be fitted by a lognormal function, and the shape of the distributions of $\mathrm{RM_{host,rf}}$ can be fitted by a combination of one Lorentzian and two Gaussian functions. The shape of the distributions does not change with the host galaxy's redshift, stellar mass, star formation, inclination,

or $b_{\rm offset}$. However, we find that the parameters of these distributions change with the properties listed above (see Tables A.2 and A.3 of Appendix III).

- We find that the median of $\rm DM_{host,rf}$ increases as a function of redshift. This can be explained by galaxies at higher redshifts having higher SFRs and therefore higher electron densities. This can be seen as an increase in the electron density profiles of galaxies in the simulation at higher redshifts.

- The median of $\rm RM_{host,rf}$ is always 0 rad $\rm m^{-2}$, and $w_{\rm RM,rf}$ increases with redshift up to $z = 1.5$. After that, it quickly decreases. This is caused by a change in the magnetic field properties: the average of the total magnetic field strength in the disk increases by a factor of 1.2 up to z = 1, and at z=2 it drops to the same value as at z=0. At $z = 2$ the azimuthal and radial components have similar relative strengths, but at $z = 0$ the relative strength of the azimuthal field is 5-6 times larger than the other two components. We also find the presence of more azimuthal reversals or random fields at $z > 1$ compared to $z < 1$, showing the B field becomes ordered as redshift decreases.

- The median of $\rm DM_{host,rf}$ increases with stellar mass, up to $\log(M_*/\rm M_\odot)$>10.5), beyond which it drops. The same trend can be seen for $w_{\rm RM,rf}$. This is caused by the increase in n_e due to increasing SFR with stellar mass, and the quenching process beginning in galaxies with $\log(M_*/\rm M_\odot) \sim 10.5$, which also causes B fields with irregularities and lower central B field.

- We show that the median $\rm DM_{host,obs}$ of our entire sample of galaxies from the simulation does not change significantly with redshift, remaining between 46 and 69 pc $\rm cm^{-3}$, in spite of $\rm DM_{host,rf}$ increasing with redshift. This can be useful in cases where we do not know the redshift of the FRB's galaxy, as we can assume the same range of $\rm DM_{host,obs}$ at all redshifts.

- We find that $w_{\rm RM,rf}$ is decreasing with redshift, which means we can constrain the host's contribution more precisely at high redshift. We find that we would need more than 95 000 polarized FRBs at $z = 0.5$ to measure an $\sigma_{\rm RM,IGM}$ ~2 rad $\rm m^{-2}$ with a confidence level of 95%, but we would only need 9 500 FRBs at $z = 2$ for the same precision. As more surveys are carried out recording polarization data of FRBs, the number of FRBs with measured RM is expected to increase significantly.

- The fitted DM and RM PDFs can be used in the frameworks of Walker et al. (2020) and Hackstein et al. (2020) to estimate the redshift of FRBs and to constrain the IGMF, providing additional choices for the host galaxy DM and RM PDFs.

- We apply our method to estimate the host DM and RM contribution for the well localized FRB190806. We found our DM and RM estimates are consistent with observations, thus our database of sightlines can be used to constrain the DM and RM contributions of host galaxies.

We note that the TNG50 model probably does not model the action of the mean-field dynamo, due to the limited spatial resolution. A future (improved) MHD simulation may be able to include the mean-field dynamo, which might affect our RM results. However, observations show that the large-scale field is generally weaker than the field at small scales (Beck et al. 2019), so these effects might be low but would warrant further investigations.

We provide an estimate of the host galaxies' DM and RM contribution which will allow future studies to separate the DM and RM of the IGM from the observed DM and RM of the FRBs. These results will help studies of the magnetic field of the IGM and the cosmic baryon density. We will publish the list of 16.5 million DM and RM values, together with the galaxy IDs in TNG50, positions of the FRBs and galaxy inclinations on github and provide a python package that can be used to get the PDFs fitted in this work. This will allow future works to use their own subset of FRBs, with different assumptions on host galaxy properties (stellar mass and star formation rate) and FRB redshift distributions to fit their own distributions.

Chapter 6

The rotation measure of intervening galaxies based on the IllustrisTNG50 simulation

Contents

6.1 Introduction

The magnetic field of distant galaxies (e.g. $0.3 \leq z \leq 2.2$ for Mg II absorbers, Churchill et al. 2005) can be statistically derived by measuring the rotation measure (RM) of polarized radio quasars with intervening galaxies (target sample) and quasars without intervening galaxies (control sample or 'clean' sightlines), as I described in Chapter 1. This technique has been used by Kronberg et al. (2008); Bernet et al. (2008, 2013) and Farnes et al. (2014, 2017), and an earlier attempt was made by Kronberg et al. (1992) using only one polarized quasar. One method used to separate these quasars is by the presence of absorption lines in their spectra; for example: quasars

with absorption lines can be assumed to have intervening galaxy in the line-of-sight, and quasars without absorption lines can be assumed to not have an intervening galaxy. We note that this is not completely correct in all cases, as some galaxies might not cause absorption lines. In the case of HI absorption, without an optical spectrum, it is difficult to decide if absorption lines are caused by an intervening galaxy or the interstellar medium associated with the quasar. Recently, a new machine-learning algorithm has been used to separate systems with intervening galaxies and systems with associated absorption without requiring optical data (Curran 2021).

The observed RM towards a quasar with an intervening galaxy is the sum of different components in the target sample:

$$\mathrm{RM_{obs,target}} = \mathrm{RM_{MW}} + \mathrm{RM_{IGM}} + \frac{\mathrm{RM_{gal}}}{(1+z_{\mathrm{gal}})^2} + \frac{\mathrm{RM_{QSO}}}{(1+z_{\mathrm{QSO}})^2}, \tag{6.1}$$

where $\mathrm{RM_{gal}}$ is the rest frame RM of the intervening galaxies. By observing a control sample of quasars without an intervening galaxy, we can get an estimate on the RM contributors ($\mathrm{RM_{MW}}$, $\mathrm{RM_{IGM}}$, $\mathrm{RM_{QSO}}$):

$$\mathrm{RM_{obs,control}} = \mathrm{RM_{MW}} + \mathrm{RM_{IGM}} + \frac{\mathrm{RM_{QSO}}}{(1+z_{\mathrm{QSO}})^2}, \tag{6.2}$$

assuming that the distribution of the RM of the quasars, IGM, and the Milky Way have the same statistical properties for the two samples. As pointed out by Basu et al. (2018), for this experiment, it is important to use background sources with the same redshift distribution in both samples because even if the background sources have the same $\mathrm{RM_{QSO}}$ in their rest frame, the $(1+z)^2$ will lead to a systematic bias in the observed RMs. The $\mathrm{RM_{IGM}}$.would also be different for two samples with different redshift distributions (Akahori et al. 2016).

We calculate the RM contribution of galaxies from the TNG50 simulation (Pillepich et al. 2018; Nelson et al. 2019a; Pillepich et al. 2019; Nelson et al. 2019b) to explore how $\mathrm{RM_{gal}}$ changes with redshift, galaxy properties, and the impact parameter. We also investigate if the magnetic field properties can be recovered from the probability distribution function of $\mathrm{RM_{gal}}$. If $\mathrm{RM_{gal}}$ can be isolated from the total observed RM in observations of polarized quasars, we can compare that to our calculated $\mathrm{RM_{gal}}$ from the simulation and derive the magnetic field properties of the intervening galaxies. This can provide us with a relation that can be used to recover the magnetic field properties of the intervening galaxies from observed RM PDFs in future works, similar to the relation between the width of a Lorentzian fitted to the RM PDF and the mean coherent field strength at the center of a sample of galaxies provided by Basu et al. (2018). One improvement of our work is the wide range of different magnetic field configurations (magnetic field reversals in the magnetic field, presence of vertical fields in the halo) and galaxies with a wide range of properties (e.g. stellar mass, SFR) compared to the simple axisymmetric disk magnetic field model of Basu et al. (2018).

6.2 Methods

6.2.1 Galaxy selection

The TNG50 simulation includes a large number of galaxies (also called 'subhalos'[1]) from $z = 0$ to $z = 12$, including spiral and early-type galaxies. We assume that different types of galaxies with different properties could be intervening in front of background quasars. However, we also need to restrict the number of galaxies in our study due to computational limitations, as the time required to calculate RM in all galaxies in the simulation would be too long, as, for example, there are $\sim 150\,000$ galaxies at $z \leq 2$ with $\log(M_*/\mathrm{M}_\odot) > 7$. We aim to investigate a general case using "normal" galaxies.

We select galaxies from $z = 0$ out to $z = 2$, with $\log(M_*/\mathrm{M}_\odot)$ in the range of 9 – 12, resulting in a total of 16 500 galaxies. We define $z = 2$ as the upper limit, as starting from the following snapshot ($z = 3$), the number of galaxies in this mass range is only ~ 700 and rapidly decreases at higher redshifts, making statistics difficult. This redshift range of $0 \leq z \leq 2$ also overlaps with that of Mg II absorbers (Churchill et al. 2005, which is one way to find intervening galaxies). We excluded satellite galaxies[2], subhalos which are flagged by the simulation as unsuitable for most analysis[3] (Nelson et al. 2019a), and galaxies labeled with star formation rate (SFR) = 0[4] in the simulation output.

In this Chapter, we are investigating a general case with a wide range of galaxy types. However, it would be interesting for future work to look at different systems with more specific galaxy properties.

6.2.2 Calculating RM of intervening galaxies

The conversion of simulation units to physical units was done following the recommended procedures for the TNG data (Nelson et al. 2019a). First, we converted the comoving units in the simulation (coordinates of cells, gas density, magnetic field strength, masses) to physical units, then converted the density and magnetic field to CGS units. The calculation of electron density (n_e) was done according to Springel & Hernquist (2003) (see also e.g. Pakmor et al. 2018, Zhang et al. 2020). The conversions and n_e calculations can be found in more detail in Chapter 5, in Section 5.2.5 and Section 5.2.6.

The RM is the line-of-sight integral of n_e and the line-of-sight magnetic field ($B_{||}$). We define a radius for each galaxy that encloses 99% of the star-forming gas of the subhalo ($r_{\mathrm{SF},99}$). We assume that galaxies are randomly oriented with respect to the line-of-sight. This is already satisfied in the IllustrisTNG simulation, so we keep the original inclination of the galaxies. For more details about the inclination distribution

[1] The friends-of-friends algorithm organizes the dark matter particles into halos, and the subfind algorithm separates the halos into subhalos.

[2] Galaxies that are not the most massive subhalos of their parent halo.

[3] Galaxies that form within the virial radius of their parent halo, and are dominated by dark matter.

[4] In reality, their SFR is below the SFR resolution limit of 10^{-5} M_*/yr

and rotation of galaxies, see Appendix II.1. We generate one RM map for each galaxy with one inclination. The integration is done in a cube, where the far side of the cube is $-r_{\rm SF,99}$ and the near side of the cube is $+r_{\rm SF,99}$. We use N steps with dl=20 pc as the stepsize, and the integration takes the closest cell to the position on the sightline in every step, which has $n_{e,i}$ and $B_{||,i}$. The RM in one pixel is:

$$\mathrm{RM} = k \sum_{i=0}^{N} B_{||,i} n_{e,i} \mathrm{d}l, \tag{6.3}$$

where $k = 0.81\ \mu\mathrm{G}^{-1}$. For the analysis and the construction of the probability density functions (PDFs) of galaxy RMs, we pick 100 sightlines from each map (tested with 1 - 1000 sightlines per map in Section 6.2.3), which are uniformly distributed in a circle with a radius of $r_{\rm SF,99}$ for each galaxy.

One inclination per galaxy should already give us a representative sample of RMs because of the large number of galaxies ($\sim$ 1000 - 2000 at each redshift). However, we might encounter bias in the resulting RM PDFs if we want to define small subsets of galaxies, for example, with a specific inclination and stellar mass, due to each galaxy having only one inclination for all of its sightlines. For the analysis in this chapter, one inclination per galaxy is adequate.

6.2.3 Effects of different parameter choices for RM calculation

We investigated how many sightlines we need per galaxy and when the resulting RM PDFs (containing all RMs from all galaxies) converge to the same PDF. We calculated 1, 10, 100, and 1000 sightlines per galaxy for galaxies at $z = 0$ and did this test five times. We show the RM PDFs in the left panel of Fig. 6.1. The PDFs have the same 16th and 84th percentile. However, the widths of the PDFs between the 2.5th and 97.5th percentile are different (right panel of Fig. 6.1), and change by 20% from 1 to 1000 sightlines. It starts to converge and only changes by 0.7% for 100 or more line-of-sight per galaxy. The 97.5% RM width in Fig. 6.1 was calculated as the median of the 97.5% RM width of the five tests and its uncertainty as the standard deviation of the five tests.

6.3 Results

In this section, we calculate the PDFs of the RM of galaxies and separate the galaxies into groups based on observable quantities (e.g. redshift, impact parameter, red - blue) to investigate if the PDFs change. We fit the PDFs and also fit how the characteristics of the PDFs change with the galaxy properties (e.g. with redshift).

6.3.1 RM PDFs at $z = 0$

In Fig. 6.2, we show the RM PDF of galaxies at $z = 0$. It is symmetric around 0 rad m^{-2}, with both a long positive and negative tail. The RM PDF can be fitted by

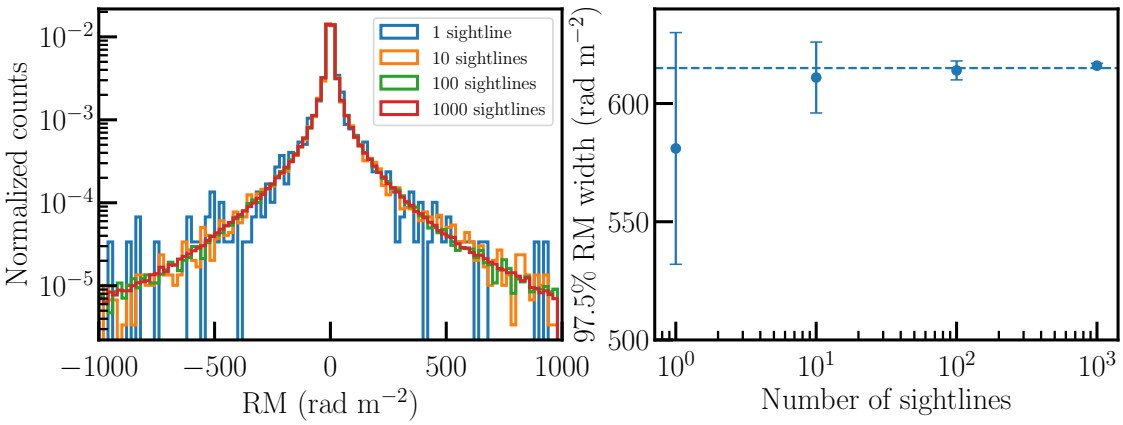

Figure 6.1: Left: The RM PDF of galaxies at $z = 0$ with a different number of sightlines per galaxy. Right: The width of the RM PDFs containing 97.5% of the data.

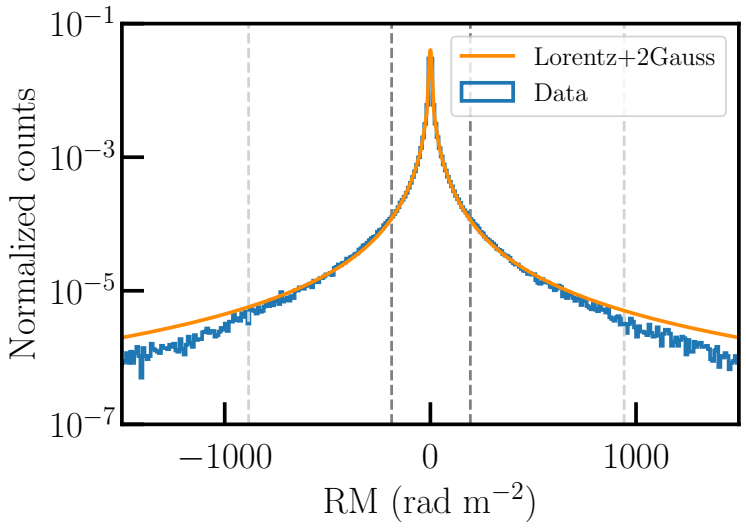

Figure 6.2: The RM PDF of galaxies at $z = 0$, and the fit of a Lorentzian and two Gaussians. The dark grey dashed line shows 95% of the data, and the light grey dashed line shows 99.7% of the data. The fit follows the data up to the tails of the distribution, only deviating for the wings containing 0.3% of the data.

the sum of a Lorentzian and two Gaussians, similar to Basu et al. (2018). We define this function as:

$$f_{\mathrm{RM,gal}}(x) = a_1 \cdot \left[\frac{\gamma^2}{\pi\gamma(\gamma^2+x^2)}\right] + a_2 \cdot \exp\left[-\frac{1}{2}\left(\frac{x}{\sigma_1}\right)^2\right] + a_3 \cdot \exp\left[-\frac{1}{2}\left(\frac{x}{\sigma_2}\right)^2\right], \tag{6.4}$$

where a_1, a_2 and a_3 are normalization factors, γ is the parameter of the Lorentzian function, and σ_1 and σ_2 are parameters of the Gaussian functions. The parameters γ, σ_1, σ_2, a_2, and a_3 are in units of rad m^{-2}, and a_1 is in units of (rad m^{-2})^2. This is different from the definition of Basu et al. (2018), as we assumed the mean to be 0 rad m^{-2}, while they left them as free parameters for each function (although they found the means are close to 0 rad m^{-2}). We fixed it as 0 rad m^{-2} because the PDFs are symmetric around $\sim$ 0 rad m^{-2}: the mean of the RMs at different redshifts are between -2 and $+1$ rad m^{-2} (with an uncertainty of $\pm$ 2 rad m^{-2}). The fit follows the data well and only deviates for the wings containing 0.3% of the data, which is insignificant.

We define the width of the RM PDF (w_{RM}) as the difference between the 84th and 16th percentile, containing 68% of the data.

6.3.2 RM width versus z

We fit the RM PDFs with the function Eq. 6.4 at every redshift from $z = 0$ to $z = 2$ available in the simulation with full magnetic field information (ten snapshots in total, for details see Table 5.1). We find that the width of the RM PDF increases with redshift until $z = 1$ and starts to decrease at $z = 1.5$. The increase is caused by increasing n_e with redshift (as shown in Fig. 5.9), which is the result of the increasing star formation rate at higher redshift, while the average total B strength is constant over redshift (shown in the bottom of Fig. E.1 and discussed in Appendix E of Appendix III. The decrease is due to the presence of more turbulent magnetic fields at $z > 1$.

In Fig. 6.4, we show the variation of the 68% width of the RM PDF (w_{RM}) versus redshift. This curve and the evolution of the parameters of the Lorentzian-Gaussian fitted PDFs as a function of redshift can be described by a curved power law:

$$w_{\mathrm{RM,rf}}(z) = A_{\mathrm{RM}} \cdot z^{D_{\mathrm{RM}}+B_{\mathrm{RM}}\cdot z} + C_{\mathrm{RM}}, \tag{6.5}$$

where A_{RM}, B_{RM}, C_{RM} and D_{RM} are the fitted parameters, listed in Table 6.1. The γ parameter of the Lorentzian function and the σ parameters of the Gaussian functions change as the width of the PDF (increase from $z = 0$ to $z = 1$, then decrease from $z = 1.5$). The normalization factor of the Lorentzian function (a_1) changes slightly differently as it increases from $z = 0$ to $z = 2$. However, the normalization factors of the Gaussian functions (a_2 and a_3) decrease from $z = 0$ to $z = 2$. These fits are useful to provide an RM estimate between the fixed redshifts of the snapshots of the simulation. For example, the parameters of the RM PDFs can be calculated from Eq. 6.5 using Table 6.1 for a given z, to match the redshift range of an observed sample.

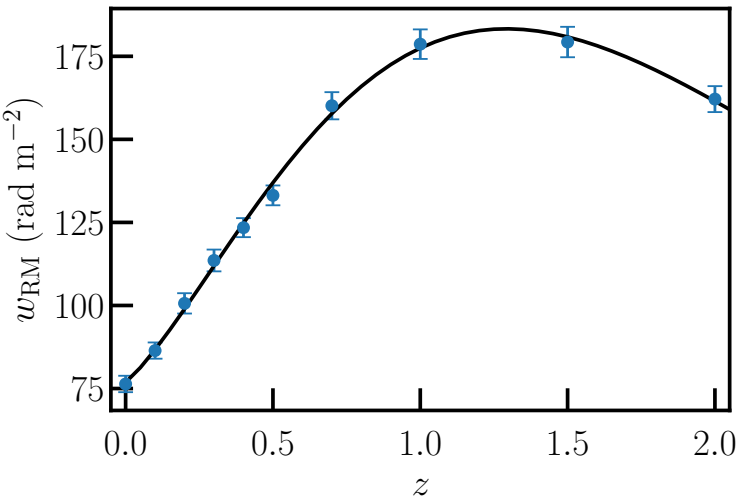

Figure 6.3: The width of the RM PDF as a function of redshift. It changes as a curved power law.

Without the fits, we could only give an RM PDF at 10 fixed redshifts between $z = 0$ and $z = 2$. We note that the fits should be used at $z > 2$ with caution, as data from higher redshift was not considered in the fits.

6.3.3 RM width versus impact parameter

The impact parameter is the projected distance between the center of the intervening galaxy and the position of the sightline (i.e. the background quasar). In the top panel of Fig. 6.5, we show the RM PDFs of sightlines with different impact parameters. As the impact parameter increases, the PDFs become narrower. This is due to the double exponential decrease of both n_e and B with radius and vertical distance from the midplane of galaxies. In the bottom panel of Fig. 6.5, we show the exponential decrease of $w_{\rm RM}$. As we show that there can be a difference of a factor of ~ 10 between sightlines at 20 kpc impact parameter compared to 1 kpc impact parameter, it is crucial to make sure there are no impact parameters that are over-represented when deriving the magnetic field of intervening galaxies. This difference is even more significant than the change we see with redshift, which is only a factor of $\sim$2.

6.4 Discussion

6.4.1 σ_{RM} from the projected spatial extent of the background source

So far, our calculations have been done in pencil beams, but real observations have a finite beam size and could have RM variations within the beam, and cause a different observed RM. Depending on the projected spatial size of the background source at the redshift of the absorber, an RM dispersion ($\sigma_{\rm RM}$) could arise from the turbulent

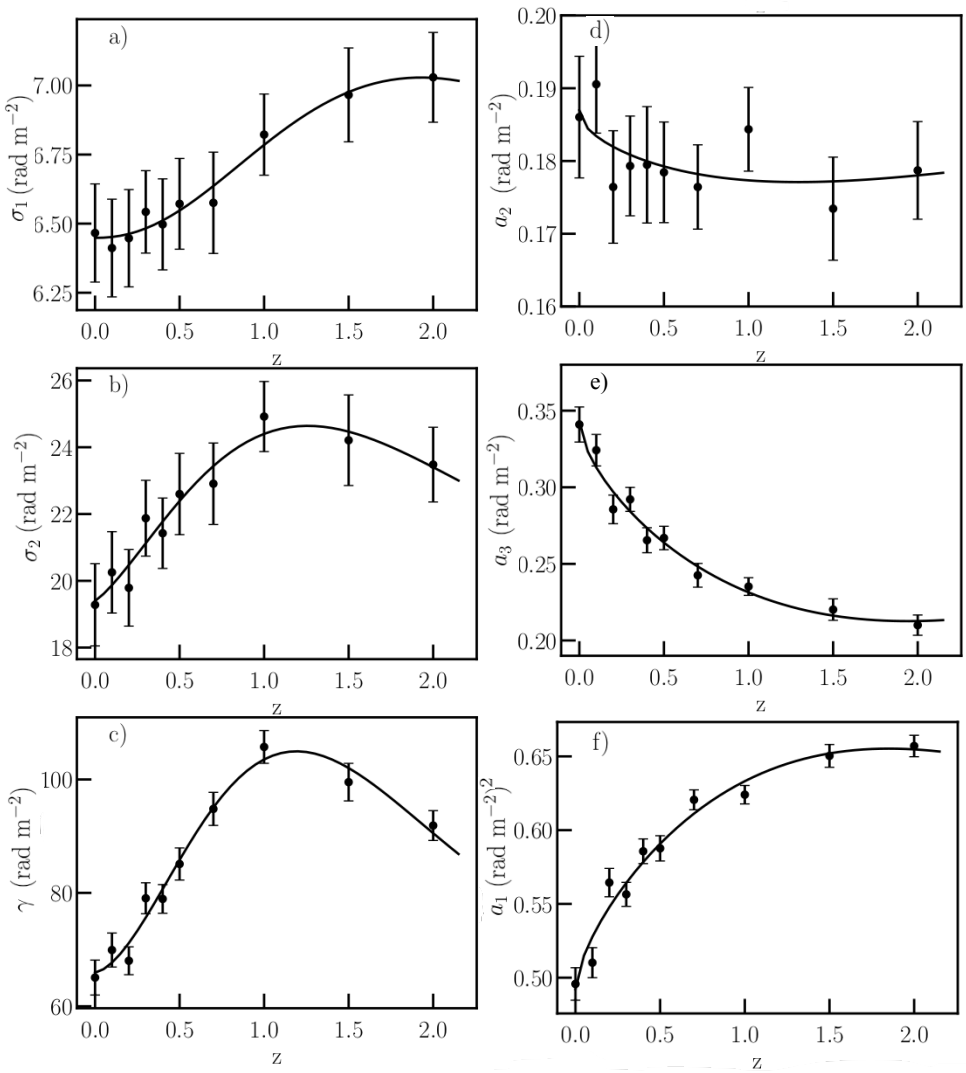

Figure 6.4: The parameters of the fitted RM PDF change as a function of redshift. They can all be fitted as curved power laws.

Parameter	$A_{\rm RM}$	$B_{\rm RM}$	$C_{\rm RM}$	$D_{\rm RM}$
$w_{\rm RM}$ (rad m^{-2})	101 ± 2	-0.66 ± 0.05	77 ± 2	1.1 ± 0.1
σ_1 (rad m^{-2})	0.33 ± 0.05	-0.9 ± 0.4	6.45 ± 0.03	2.4 ± 0.8
σ_2 (rad m^{-2})	5.1 ± 0.3	-0.8 ± 0.1	19.3 ± 0.2	1.1 ± 0.1
γ (rad m^{-2})	37.2 ± 1.4	-1.0 ± 0.1	65.8 ± 1.1	1.4 ± 0.1
a_1 ((rad m^{-2})^2)	0.12 ± 0.01	-0.15 ± 0.09	0.49 ± 0.01	0.6 ± 0.1
a_2 (rad m^{-2})	-0.011 ± 0.003	-0.21 ± 0.25	0.184 ± 0.002	0.53 ± 0.28
a_3 (rad m^{-2})	-0.12 ± 0.01	-0.21 ± 0.08	0.34 ± 0.01	0.6 ± 0.1

Table 6.1: The fit parameters of the redshift evolution (described as curved power laws) of the RM PDF's width ($w_{\rm RM}$) and the parameters of the fitted PDF. While $A_{\rm RM}$ and $C_{\rm RM}$ have the same units as the fitted parameter (e.g. rad m^{-2} in case of $w_{\rm RM}$), $B_{\rm RM}$ and $D_{\rm RM}$ are unitless.

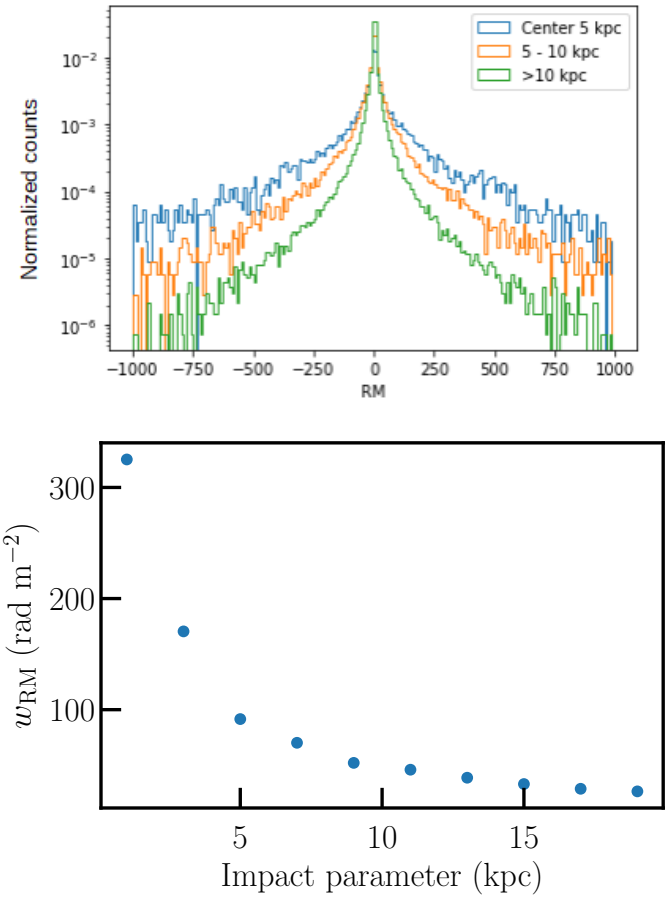

Figure 6.5: Top: The RM PDFs of sightlines with different impact parameters. The PDFs become narrower for larger impact parameters. Bottom: The exponential decrease of the width of the RM PDF as a function of the impact parameter.

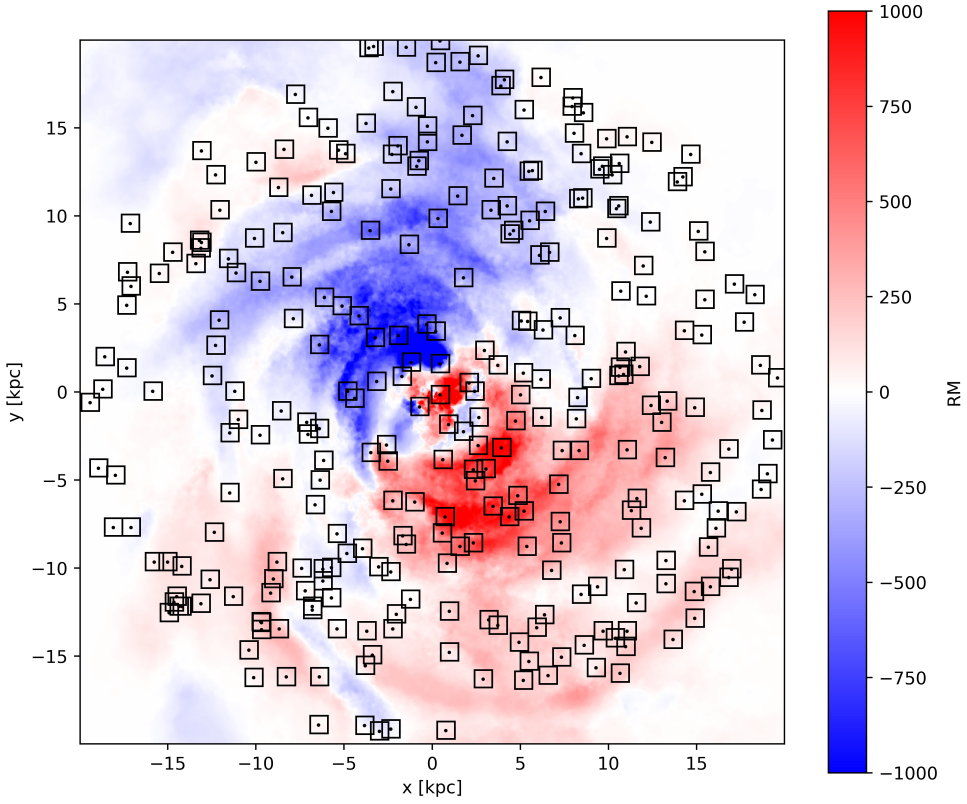

Figure 6.6: An example RM map of a galaxy. The randomly chosen positions are overplotted on the map along with the areas of averaging.

magnetic field in the intervening galaxy, and even result in a different average RM. Because of this, we investigate if we find a difference in RMs calculated in two different ways: in a pencil-beam integral or an area-averaged integral.

For this test, we calculated the RM for 100 random pencil-beam sightlines (i.e. in one pixel) and in an area (i.e. in a square) around the pixel for each of our selected galaxies at $z = 0$. Even though real telescopes have a more complex beam shape than a square, our simplification of choosing a square does not affect the results. To see an example of positions and averaging areas, see Fig. 6.6. We tried different sizes of areas for averaging (50 pc to 1 kpc), and even with a 1 kpc x 1 kpc square, we do not find a difference between the two methods: the RM from pencil beams and area average do not differ significantly The comparison is shown in Fig. 6.7. The resulting PDFs from all sightlines are also essentially the same: the width of the PDF between the 16th and 84th percentile is the same (31 $\mathrm{rad\,m^{-2}}$ in this case), and the width between the 2.5th and 97.5th percentile only differs by a small amount (309 vs. 315 $\mathrm{rad\,m^{-2}}$). We calculate σ_{RM} as the standard deviation of the RM of each pixel in the averaging areas. We found that the σ_{RM} in these regions is very low, below $10\,\mathrm{rad\,m^{-2}}$ in 80% of the galaxies. In contrast, only 20% of the sightlines of galaxies at $z = 2$ have $\sigma_{\mathrm{RM}} < 10\,\mathrm{rad\,m^{-2}}$, and 80% of them have $\sigma_{\mathrm{RM}} < 150\,\mathrm{rad\,m^{-2}}$. In Fig. 6.9, we show the PDF of σ_{RM} for an averaging area of 1 kpc x 1 kpc for $z = 0$ and $z = 2$.

We found the two methods do not differ significantly (the width between the 2.5th and 97.5th percentile only differs by 2% for PDFs at $z = 0$ and by 14% at $z = 2$), which could mean much of the turbulent field is missing on scales of < 1 kpc in the TNG50 simulation. We explore this possibility in more detail in the next subsection. We conclude that we do not need to take into account the apparent size of the background source in our analysis, as it would not lead to a different RM compared to the RM from pencil-beams, and thus the RM PDFs would be the same. We note this does not mean the size would not affect the RMs in the case of observations, as this is only true for the synthetic observations generated from the simulation because it lacks some of the turbulent field, which we will explore in the next section.

6.4.2 Ratio of the turbulent magnetic field in the simulation

The total magnetic field can be written as the sum of the large-scale ($\overline{B}$) and the turbulent (b) field:

$$B_{\mathrm{total}} = \overline{B} + b, \tag{6.6}$$

and the average of the turbulent magnetic field:

$$\overline{b} = 0. \tag{6.7}$$

When we average the square of the total magnetic field strength, the result will contain both the large-scale and the turbulent field:

$$\overline{B^2_{\mathrm{total}}} = \overline{(\overline{B} + b)^2} = \overline{\overline{B^2} + 2\overline{B}b + b^2} = \overline{B^2} + \overline{b^2}, \tag{6.8}$$

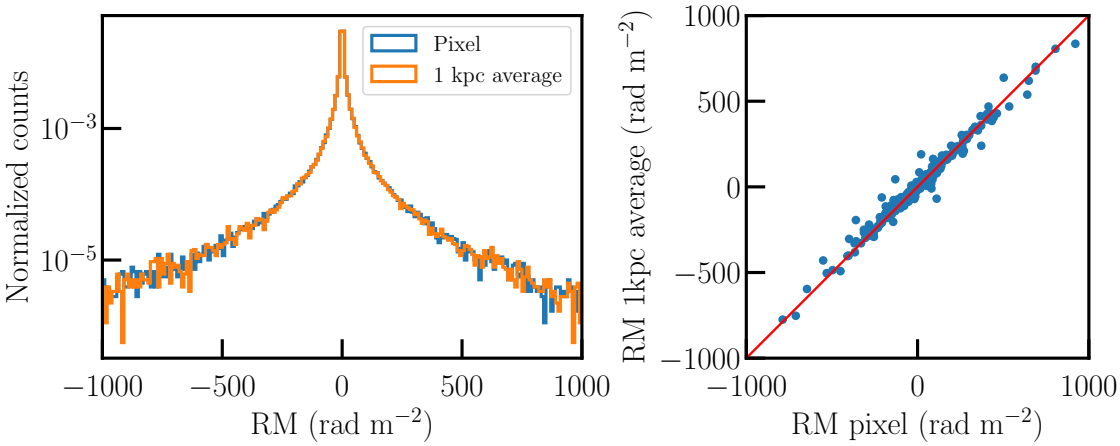

Figure 6.7: Left: Comparison between the PDF of RMs taken from pixels, and the PDF of RMs calculated as an average around the pixels in a 1 kpc x 1 kpc region. Right: Comparison of the RMs from the two methods, and a line showing the 1 to 1 ratio. The difference between the two methods is insignificant.

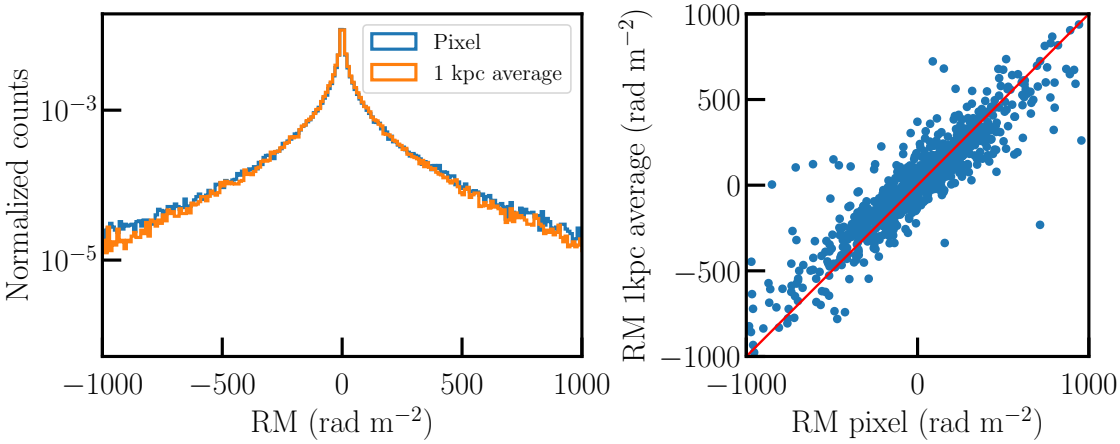

Figure 6.8: The same as Fig. 6.7, but for galaxies at $z = 2$. There is a slight difference between the two methods, suggesting a larger prevalence of turbulent fields.

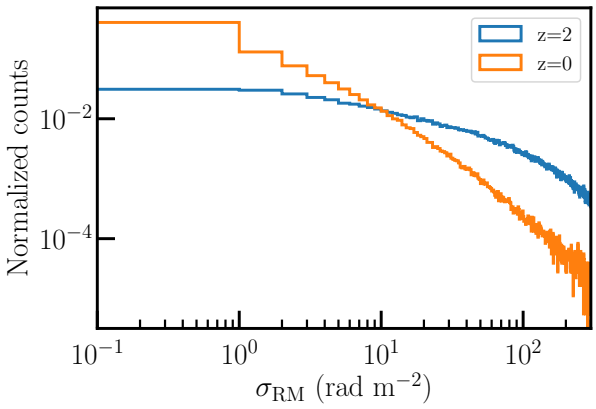

Figure 6.9: The RM dispersion ($\sigma_{\rm RM}$) in the 1 kpc x 1 kpc regions around the pencil-beam sightlines (pixels), using sightlines of galaxies at $z = 0$ and $z = 2$. At $z = 0$, most ($\sim 80\%$) of the regions have a very low $\sigma_{\rm RM} < 10\,{\rm rad\,m^{-2}}$. In contrast, only 20% of the sightlines of galaxies at $z = 2$ have $\sigma_{\rm RM} < 10\,{\rm rad\,m^{-2}}$, and 80% of them have $\sigma_{\rm RM} < 150\,{\rm rad\,m^{-2}}$.

where we applied the Reynolds rules: $\langle\langle f\rangle\rangle = \langle f\rangle$ and $\langle\langle f\rangle g\rangle = \langle f\rangle\langle g\rangle$.

However, if we average the magnetic field strength without raising it to the second power, we average out the turbulent magnetic field:

$$\overline{B_{\rm total}} = \overline{B} + \overline{b} = \overline{B} \tag{6.9}$$

We calculated the magnetic field strength maps of each galaxy in a face-on view, where each pixel is the integral of the square of the total magnetic field strength from -1 kpc to +1 kpc below and above the midplane of the galaxy. We also calculated maps for the azimuthal, radial, and vertical magnetic fields without raising them to the second power (a detailed description can be found in Appendix D of Appendix III. We calculated the average magnetic field strengths from these face-on maps of the total magnetic field and the magnetic field components. In the case of only coherent fields, the following equation should be true:

$$B^2_{\rm total} = B^2_{\rm azm} + B^2_{\rm rad} + B^2_{\rm vert} = \overline{B^2}. \tag{6.10}$$

However, we found that the ratio of $\frac{\sum_{i=0}^{3}(B_{\rm comp,i})^2}{B^2_{\rm total}}$ is below 1 (where $B_{\rm comp,i}$ is the magnetic field of the different components) at all redshift. We show this in Fig. 6.10, we found $\frac{\sum_{i=0}^{3}(B_{\rm comp,i})^2}{B^2_{\rm total}}$ slightly decreases with redshift from $z = 0$ to $z = 2$, from 90% to 87%. This suggests the presence of turbulent magnetic field in the galaxies, ranging from 10% to 13%, corresponding to only ~ 3 μG. Based on observations of nearby galaxies (Beck et al. 1996), we expect the turbulent field to be larger than the large-scale field: $b/\overline{B} = 1 - 3$. Beck et al. (2019), based on a summary of newer observations, notes that the isotropic turbulent field can make up 75 - 97% of the total field strength.

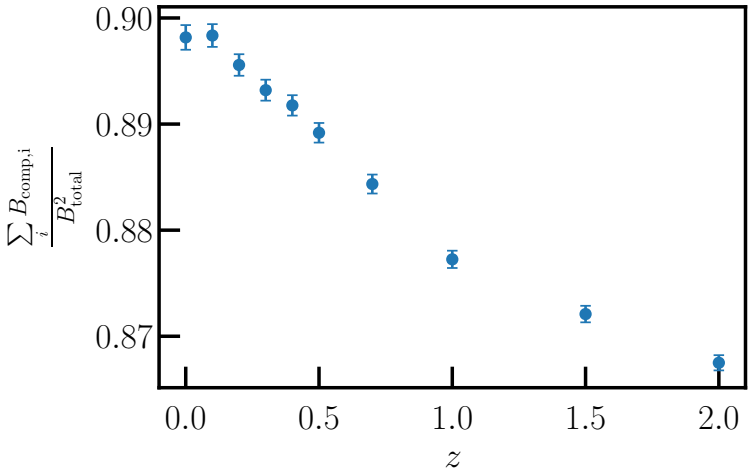

Figure 6.10: The median of the ratio of the B field components and the total magnetic field, which indicates the presence of turbulent fields, for galaxies at different redshifts. It slightly decreases from $z = 0$ to $z = 2$ by a few %, due to the higher prevalence of turbulent fields at higher redshift. The error bars correspond to the standard errors of the median ($1.253\,\sigma/\sqrt{N}$).

The slight decrease towards higher redshift (e.g. $z = 2$) could mean the field is more turbulent compared to $z = 0$. Although this is just a few %, based on this, the turbulent field at $z = 2$ is 1.3 times larger compared to $z = 0$. This could also explain why the RMs from area averaging and from pencil-beams have a larger difference in galaxies at $z = 2$ compared to $z = 0$ (see Section 6.4.1).

6.4.3 Recovering B field properties

We explore if we can recover the properties of the B field from the RM PDFs by measuring the RM PDF width.

In Fig. 6.11, we show the width of the RM PDFs of individual galaxies at $z = 0$ as a function of their average total magnetic field strength. We binned the galaxies into groups by their magnetic field strength, from 0 to 16 μG, in 4 μG bins. The number of galaxies in each bin is different: we have the majority of galaxies (~ 1100) in the first bin ($B < 4\,\mu$G), but only ~ 10 in the last two bins ($B > 8\,\mu$G). We found an increasing trend of RM width for galaxies with larger B field strengths. This is a linear relation between the logarithm of the PDF width and the magnetic field strength:

$$\log w_{\mathrm{RM}} = m \cdot \log B + C, \tag{6.11}$$

where $m = 1.2 \pm 0.2$ and $C = 1.4 \pm 0.2$ are the fit parameters. We can recover the same relation using only a fraction of all sightlines: ~ 5000.

Although the average of w_{RM} follows a relation with B, its spread is large: galaxies with the same magnetic field strength can have w_{RM} of ~ 10 rad m^{-2} and ~ 500 rad m^{-2}. A difference in electron densities could cause a difference in the resulting

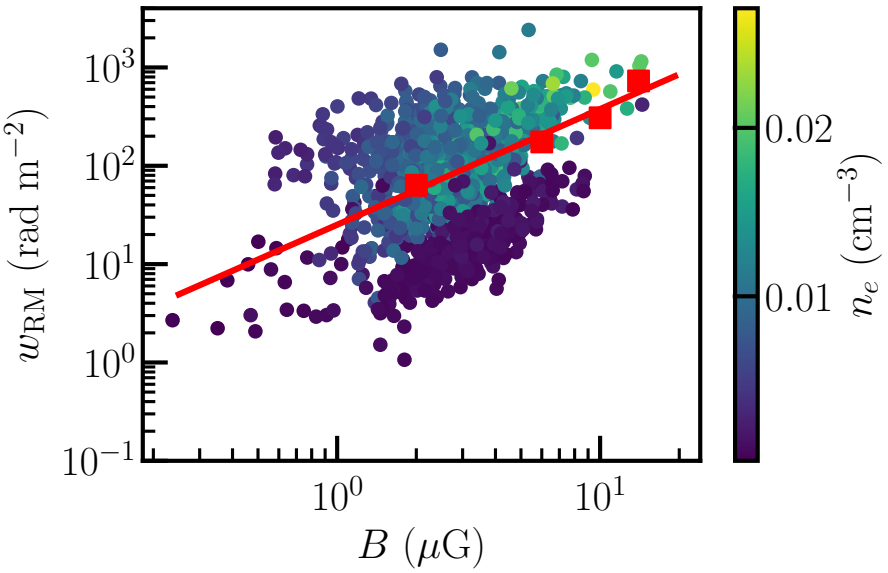

Figure 6.11: The width of the RM PDF of individual galaxies at $z = 0$ as a function of their average total magnetic field strength. The points are colored according to the mean electron density of the galaxies. We bin the galaxies by their magnetic field strength from 0 to 16 μG in 4 μG bins (red squares), and we can see an increase in w_{RM} with magnetic field strength, which can be fitted linearly (shown by the red line).

RM, even if the magnetic field properties are the same. In Fig. 6.11, we see that galaxies with an average electron density (n_e) below 0.003 cm^{-3} form a distinct group with consistently lower w_{RM}.

This relation can be used to infer the average magnetic field of intervening galaxies from observations if we can measure the width of their RM PDF.

6.4.4 Comparison to Basu et al. (2018)

We compare our RM PDFs to the RM PDF of Basu et al. (2018), who used a large-scale axisymmetric spiral magnetic field model (with a distribution of magnetic field strengths with a sample mean of B_0 and standard deviation of σ_{B_0}) and radially decreasing n_e to calculate the RM of intervening galaxies. However, neither the B field geometry nor n_e changes with distance from the midplane of the galaxies. In contrast, the magnetic field and n_e of galaxies in the TNG simulation also have a dependence on the vertical distance from the midplane, there is evidence of turbulent field, and not all galaxies have axisymmetric large-scale magnetic fields, as some show reversals in the direction of the large-scale magnetic field (for more details about the magnetic field profiles and maps see Appendix D of Appendix III.

Our RM PDFs of individual galaxies and those of Basu et al. (2018) show a significant difference. The RM PDFs of individual galaxies Basu et al. (2018) show two symmetric peaks around 0 rad m^{-2}, but our PDFs have one peak at 0 rad m^{-2}. Tur-

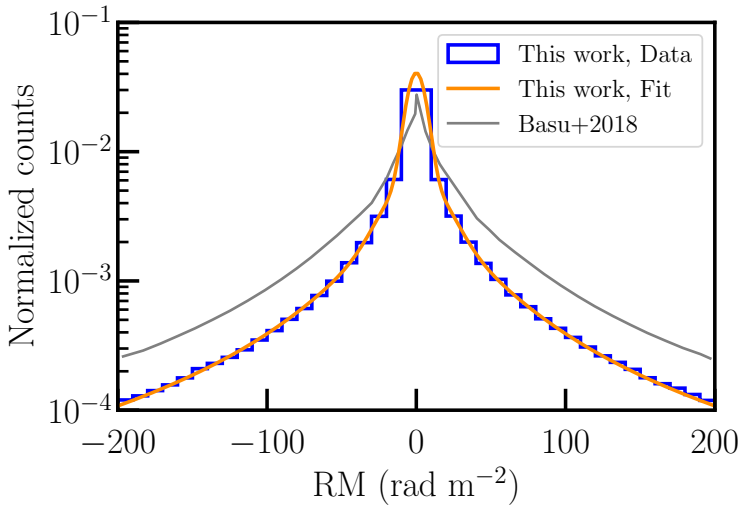

Figure 6.12: The RM PDF of galaxies at $z = 0$ from the TNG50 simulation, with our fit overlayed on it. The fit from Basu et al. (2018) is also shown for comparison. It predicts fewer sightlines with a low RM near $0\,\mathrm{rad\,m^{-2}}$, and a larger RM tail.

bulent fields (as there is still some turbulent field present in TGN50 compared to no turbulent fields in Basu et al. (2018)) or field reversals could broaden the two peaks to result in only one peak in the center, as more sightlines would experience similar amounts of positive and negative RM, resulting in RMs close to 0 $\mathrm{rad\,m^{-2}}$.

In Fig. 6.12, we show a comparison of our RM PDF (using all galaxies) at $z = 0$ and the RM PDF of Basu et al. (2018). We find the shape of the histogram of the intervening galaxy RMs using many different galaxies from TNG50 to be similar to the shape that Basu et al. (2018) found, which is surprising considering that TNG50 is more complicated, a cosmological MHD simulation. Even so, we showed that TNG50 lacks much of the turbulent field, which could explain the similarities between the two results. It could be that the overall shape is similar due to a sharp peak arising at RM = 0 $\mathrm{rad\,m^{-2}}$ in the results of Basu et al. (2018) due to the uniform distribution of i (from 0 to π). However, the two PDFs are not entirely the same, and we predict more sightlines with low RMs around 0 $\mathrm{rad\,m^{-2}}$, and fewer sightlines with larger RMs (i.e. our PDF is narrower), which is not surprising based on the RM PDFs of individual galaxies. This could be due to the differences in the model of Basu et al. (2018) and TNG50: the presence of turbulent fields (even though it is only a fraction of how strong it should be) and reversals in the large-scale field, as both can cause low RM because of the changes in the field direction in the line-of-sight.

6.4.5 Comparison to Chapter 5

We compare our RM PDFs to those we present in Chapter 5. In Chapter 5, we calculate the RM of FRB host galaxies, where the main difference to this Chapter is that the integral starts within the galaxy. The shape of the PDFs can be fitted by

the sum of a Lorentzian and two Gaussians in both cases (the RM PDF of FRB host galaxies is shown in the bottom panel of Fig. 5.3). However, the $w_{\rm RM}$ of the FRB host galaxy RM PDFs are larger than those of intervening galaxies at every redshift by a factor of 1.5 to 2.5. Nevertheless, the $w_{\rm RM}$ from both cases follow a curved power law as a function of redshift (with different parameters), shown in the bottom panel of Fig. 5.4 for the FRB case. In summary, on average, the |RM| from FRB host galaxies is larger than the |RM| from intervening galaxies. One explanation for this is the presence of reversals in the azimuthal field (see Fig. D.4 of Appendix III), and a symmetric halo field (where $B_{\rm vert}$ changes its sign below and above the disk), as these could lead to the positive RM and the negative RM canceling out in the observed RM if the sightline goes through the whole galaxy. We explain these through a simplified example of a face-on galaxy with symmetric halo magnetic fields. In this case, RM from the magneto-ionic medium from the far side of the halo and disk results in a negative RM (the direction of $B_{\rm vert}$ is directed away from the observer), but the near side results in a negative RM of similar magnitude (the direction of $B_{\rm vert}$ is directed towards the observer), and the whole line of sight will result in an RM of near 0 rad m^{-2}. In the case of a face-on FRB host galaxy with an FRB in the midplane, the line of sight would only go through the near side of a galaxy, resulting in a positive RM.

Additionally, we note that the location of the sightlines can also cause a difference in the RMs. In the FRB case, sightlines start in denser regions of the galaxy (e.g. more sightlines start in the disks of the galaxies than sightlines that start in their halos). However, in the case of this Chapter, the sightlines are distributed uniformly (i.e. we have the same chance of probing the halo and the disk). Both n_e and B are higher in the disk than in the halo, resulting in higher RMs in the FRB case.

6.5 Conclusions

We calculated the RM of intervening galaxies using 16 500 galaxies in the cosmological MHD simulation IllustrisTNG50. The PDFs can be fitted by the sum of a Lorentzian and two Gaussians, similar to Basu et al. (2018). We also found that the width of the RM PDFs of individual galaxies ($w_{\rm RM}$) shows a correlation with their average total magnetic field strength: galaxies with stronger B fields have wider RM PDFs. Equation 6.11 can be used in future works to derive the magnetic field strength of observed intervening galaxies (assuming galaxies in the TNG50 simulation are similar to observed galaxies).

Our results are in broad agreement with the results of Basu et al. (2018), as they can be fitted by the same function, but we predict less sightlines with large RMs and more sightlines with RMs near 0 rad m^{-2}. The presence of turbulent fields in the simulation (even if it is only a 10% of the total field) and the presence of magnetic field reversals could cause smaller RMs, as the positive and negative RM would cancel out in more sightlines than in a strictly axisymmetric large-scale field, where the field with a preferred direction can cause a larger |RM|. We found that $w_{\rm RM}$ follows a power law as the function of redshift, increasing from $z = 0$ to $z = 1$, and decreasing from

$z = 1.5$ to $z = 2$. The increase is due to the increase in n_e, and the decrease is due to the presence of more turbulent and random fields at higher redshifts ($z > 1$). The parameters of the fitted PDF also change as a power law. The $w_{\rm RM}$ decreases with the impact parameter due to the double exponential radial and vertical profiles of n_e and B.

The calculated |RM|s in this Chapter are lower on average compared to Chapter 5, which is partly due to the placing of the FRBs in dense regions (i.e. disk) compared to a uniform distribution of sightlines (i.e. disk and halo) in this Chapter, and partly due to the fact that the sightline is only going through some part of the galaxies, not through the whole galaxy: because of the presence of reversals in the direction of the magnetic field a sightline that goes through the entire galaxy could experience a similar negative and positive RM, resulting in an RM ~ 0 rad m^{-2}.

Chapter 7

Conclusions and outlook

Contents

7.1 Summary of science chapters

In this thesis, I examined the redshift evolution of large-scale magnetic fields using both observations and simulations. Obtaining observations of the magnetic fields of distant galaxies is crucial to constrain the dynamo theory at high redshift, which is well supported by evidence in nearby galaxies, but currently lacks measurements at high redshift. Obtaining measurements of coherent, galactic-scale magnetic fields is even more important, and can be used to derive the amplification time-scale of the large-scale dynamo. By using simulations we can predict how the observables of magnetic fields change with redshift, which can be used to plan future observations and to help retrieve magnetic field properties in observations assuming the simulation is representative of reality. In my thesis, I directly measured the magnetic field strength in two intermediate redshift galaxies (0.414 and 0.685, which corresponds to galaxies 4.4 and 6.3 Gyr ago, respectively), using observations from the Very Large Array (VLA) in Chapters 3 and 4, and predicted the redshift evolution of the rotation measure (RM) of intervening galaxies in front of polarized synchrotron emitting background quasars using the TNG50 simulation in Chapter 6. The RM estimates from the simulation can in turn be used by future observations of a large sample of quasars with intervening galaxies to measure the magnetic field in the intervening galaxies. Apart from

investigating the magnetic field of galaxies, I also examined the observability of the intergalactic magnetic field (IGMF) in Chapter 5: by observing the dispersion measure and rotation measure of a large sample of FRBs, we can measure the IGMF. For this, we need to account for the RM and the dispersion measure (DM) contribution of FRB host galaxies, however, this is very difficult to observe. For this reason, I calculated the RM and DM of FRB host galaxies from a simulation. These predictions will allow us to measure the IGMF in the near future, hopefully in the next few years (for future surveys see Section 7.2.2).

7.1.1 Measuring the magnetic field in intermediate redshift galaxies using lensing systems

In Chapters 3 and 4 I analysed the broadband radio polarization observations of two lensing systems to derive the magnetic field strength and structure of the lensing galaxies at $z \sim 0.4$ and $z \sim 0.7$. This kind of back-lit experiment is uniquely capable of directly measuring the coherent large-scale magnetic field strength in intermediate redshift galaxies, demonstrated by Mao et al. (2017). The direct measurement can be achieved as the sightlines of the lensed images have approximately the same RM contribution from the Milky Way, the IGM and the background source, leaving the RM difference between the lensed images to be caused by the magneto-ionic medium of the intervening lensing galaxy. This thesis expands the number of magnetic field measurements with this method from one to three galaxies, probes the disk field to a higher redshift ($z = 0.685$), and measures the halo field of a galaxy (at $z = 0.414$), compared to the previous detection of a disk field at $z = 0.4$.

The observations were taken with the VLA in A configuration, which results in the highest angular resolution images that are possible with the VLA. We obtained measurements in L-, S-, and C-band, which provides us with a wide wavelength coverage, essential for the accurate derivation of the polarization properties of the lensed images with the methods of RM synthesis and Stokes QU fitting.

In the lensing system B1600+434, the lensing galaxy is an edge-on spiral galaxy at $z = 0.414$, and the lensed images probe its halo. We measured the magnetic field of the halo at $z = 0.414$: we find the coherent vertical magnetic field strength to be 1.2–1.8 μG at a vertical distance of 0.7 kpc from the plane of the galaxy, and 0.2–0.9 μG at 6.2 kpc (assuming Milky-Way-like galaxy properties and an exponential model). This is the first time the halo magnetic field was measured in a distant spiral galaxy.

In the lensing system B0218+357, the lensing galaxy is a face-on spiral at $z = 0.685$, and the sightlines of the two lensed images go through the disk at 0.26 and 2 kpc from the center of the galaxy. Depending on whether the RM difference between the images is due to the large-scale field of the lensing galaxy, or an HII region inside the lensing galaxy, we either provide the highest redshift direct measurement of the coherent large-scale magnetic field in a galaxy to date, or we measure the B field of an HII region at $z = 0.685$. We explore the possible magnetic field strengths using different large-scale magnetic field geometry models. The most likely scenario is that the RM is due to an axysimmetric disk field of $2 - 20$ μG. If the RM difference is due to the magneto-ionic

medium of the HII region, its line-of sight magnetic field strengths also falls into a similar range (0.4 – 9.6 μG).

The strength of the halo field in the lensing galaxy of B1600+434 and the strength of the disk field in the lensing galaxy of B0218+357 are consistent with the halo field and the disk field of nearby galaxies (Beck 2015a, Beck & Wielebinski 2013, CHANG-ES - Irwin et al. 2012) and the Milky Way, even at $0.4 < z < 0.7$. In the case the RM difference in the B0218+357 system is caused by an HII region, the derived magnetic field strengths are also in broad agreement with the magnetic field strength of Galactic HII regions.

We investigated if our results are compatible with the dynamo theory. The mechanism generating the large-scale coherent magnetic field has already built up the field strength and structure to what we see in present-day galaxies, at redshifts of 0.4 and 0.7. Based on the B1600+434 system we derive a dynamo e-folding time of $< 2.9 \cdot 10^{8}$ yr, which is in agreement with the theory, however for the system B0218+357 we derive a shorter e-folding time than expected ($\tau_{\rm dynamo} < 2 \cdot 10^8$ yr). This is easily resolved if we assume the disk settled into equilibrium sooner, at $z \sim 3.5$. This would not be surprising in the light of recent JWST detections of disk galaxies at high redshift ($z \sim 3 - 6$, Ferreira et al. 2022). Furthermore, we find that the halo magnetic field strength is lower compared to the disk field of a similar galaxy at $z \simeq 0.4$ (Mao et al. 2017), which is what the dynamo theory predicts.

7.1.2 Predicting the observables of magnetic fields using the TNG50 simulation

In Chapters 5 and 6 we used the state-of-the-art cosmological magnetohydrodynamic (MHD) simulation IllustrisTNG50 (Pillepich et al. 2019; Nelson et al. 2019b), which includes magnetic fields and has the highest currently available spatial resolution. We used the same selection of galaxies in the two projects: 16 500 galaxies in total, at $0 < z < 2$ with $9 < \log(M_*/\mathrm{M}_\odot) < 12$.

7.1.2.1 Rotation measure of intervening galaxies

In Chapter 6 we provided statistics on the RM contribution of a large sample of intervening galaxies and how their probability density distribution (PDF) is related to their average total magnetic field strength (Equation 6.11). This can be used to derive the magnetic field in distant galaxies, when combined together with observations of a large sample of quasars with intervening galaxies. Our results are in broad agreement with the results of Basu et al. (2018), as they can be both fitted by the the sum of Lorentzian and two Gaussian functions, but we predict less sightlines with large RMs and more sightlines with RMs near 0 rad m^{-2}. This difference can be attributed to the presence of turbulent fields and magnetic field reversals in the TNG simulation, compared to the axisymmetric large-scale field model Basu et al. (2018).

We found that the width of the RM PDF ($w_{\rm RM}$) follows a power law as the function of redshift, increasing from $z = 0$ to $z = 1$, and decreasing from $z = 1.5$ to $z = 2$. The

increase is due to the increase in electron densities (n_e) due to increasing star formation rate (SFR), and the decrease is due to the presence of more turbulent, random fields and field reversals at higher redshifts ($z > 1$). The parameters of the fitted PDF also change as a function of a power law. These fits can be used to reproduce the RM PDFs for intervening galaxies at all redshifts between $z = 0$ and $z = 2$, apart from the few redshift snapshots in the simulation.

7.1.2.2 Dispersion measure and rotation measure of FRB host galaxies

In Chapter 5 we provided statistics on on the RM and DM contribution of a large sample of FRB host galaxies, which will aid us in constraining the IGM magnetic field once large samples of FRBs with observed DM and RM become available. For example, our results can be used in the frameworks of Walker et al. (2020) and Hackstein et al. (2020) to estimate the redshift of FRBs and to constrain the IGMF, providing additional choices for the host galaxy DM and RM PDFs.

We have calculated the DM and RM contribution of FRB host galaxies ($\mathrm{DM_{host,rf}}$ and $\mathrm{RM_{host,rf}}$). The distributions of $\mathrm{DM_{host,rf}}$ can be fitted by a lognormal function, and those of $\mathrm{RM_{host,rf}}$ can be fitted by a combination of one Lorentzian and two Gaussian functions (same as Chapter 6). We investigated how the median $\mathrm{DM_{host,rf}}$ and the width of the $\mathrm{RM_{host,rf}}$ distribution ($w_{\mathrm{RM,rf}}$) change with redshift, stellar mass, inclination, and FRB projected offsets from the center of galaxies (b_{offset}).

We found that $w_{\mathrm{RM,rf}}$ decreases with redshift, which means we can constrain the host's contribution more precisely at higher redshift. We find that we would need more than 95 000 polarized FRBs at $z = 0.5$ to measure a $\sigma_{\mathrm{RM,IGM}}$ $\sim$2 rad m^{-2} with a confidence level of 95%. At $z = 2$ we would only need 9 500 FRBs for the same precision. As more FRB surveys in are carried out recording polarization data of FRBs, the number of FRBs with measured RM is expected to increase significantly (e.g. CHIME and DSA-2000, see Section 7.2.2).

7.1.2.3 Differences between the RMs of FRB hosts and intervening galaxies

The calculated |RM|s in the case of intervening galaxies (Chapter 6) are lower on average compared to FRB host galaxies (Chapter 5), which is partly due to the placing of the FRBs in dense regions (i.e. disk) compared to a uniform distribution of sightlines (i.e. disk and halo) in Chapter 6, and partly due to the fact that the sightline is only going through some part of the galaxies, not through the whole galaxy: because of the presence of reversals in the direction of the magnetic field a sightline that goes through the entire galaxy could experience a similar negative and positive RM, resulting in an RM $\sim$ 0 rad m^{-2}.

7.1.2.4 Limitations of the TNG50 simulation

TNG50 does not include all sources of turbulence on small scales ($\lesssim$ 100 pc) due to its limited spatial resolution, thus it underestimates the small-scale turbulent field. The turbulent field in the simulation is only 3μG, about 10% of the large-scale field,

in contrast to observations, where the turbulent is field is on the same order of magnitude or even stronger than the large-scale field. As the small-scale turbulent field is transformed and amplified into the large-scale regular field by the dynamo theory, this means the simulation might not model the action of the mean-field dynamo completely, and subsequently underestimate the large-scale coherent field strength. A future (improved) MHD simulation may be able to include the mean-field dynamo if it can reach higher spatial resolution, which might affect our RM results, which could have a larger distribution width. It would be useful if simulations would be able to include turbulence on a smaller scale (on the order of a few pc), or if a random magnetic field could be added by postprocessing (similarly to how stellar clusters were added by Pellegrini et al. 2020 in postprocessing, and accounts for e.g. stellar wind and supernovae, which alters the electron densities in the simulation). Currently the turbulent magnetic field in the simulation is only 10% of the total magnetic field strength, which is significantly lower than what is expected from observations (75 - 97%, Beck et al. 2019). However, observations show that the large-scale field is generally weaker than the field at small scales (Beck et al. 2019), so it might have insignificant effect on our derived RMs, but would warrant further investigations when such a simulation becomes available. Until then, it is possible to apply the method of Pellegrini et al. (2020) on a few galaxies in TNG50, to look into if the results are consistent with our work.

It is also important to note that IllustrisTNG is based on the ΛCDM cosmological model. Our results are only appropriate if we assume the Universe is well described by this model, and our analyses presented in this work can be repeated with simulations using a different model (e.g. MOND).

7.2 Future prospects

7.2.1 Deriving a more accurate magnetic field strength from lensing systems

Based on the results of this thesis, in future magnetic field measurements using lensing systems we will need to be careful about the possible RM variability of the background quasar and will need to characterize the lensing galaxies, in order to derive higher precision magnetic field strengths with less assumptions.

First of all, it is important to rule out any RM variation of the background source, as in combination with the time delay of the lensing system, it could alter the observed RM difference of the lensed images: if for example in one point in time the intrinsic RM of the background source increased, in one lensed image it could still show the previous RM, while in the leading lensed image we would measure the new higher RM. This would lead to an RM difference that is unrelated to the magneto-ionic medium of the lensing galaxy. So far, the three lensing systems that have been studied do not show a significant variability in RM (only on the order of a few $\mathrm{rad\,m^{-2}}$, e.g. Biggs & Browne 2018), even if there is evidence of variation in their other polarization properties. However, it will be important in the future to conduct follow-up observations similar to the VLA broadband polarization follow-up we did for B1600+434 in Chapter 3, which

showed consistent RMs to our previous observations. Re-observing the systems once might be enough to rule out any significant RM variation, but for the proper characterization of changes in polarization properties we can conduct polarization monitoring with multi epoch observations during a time period of the time delay of the lensing system.

The lensing galaxies would need to be characterized better, as many galaxy properties (inclination, electron densities - thus SFR) can affect the derived magnetic field strength and the interpretation of the magnetic field structure, and if we do not have good constraints on them, we need to make assumptions or have results with large uncertainties. This characterization is difficult to achieve, as we would need high angular resolution imaging to be able to separate the emission from the lensing galaxy and the lensed images because of the small angular separation ($\sim$ arcseconds) between them. The most important parameters to obtain would be the electron density and the inclination of the lensing galaxy, as these introduce the highest uncertainties. The electron densities could be measured with spectroscopy of the ionized gas (e.g. Hα, Hβ, or OII doublet line, Osterbrock 1974; Ashkenazy et al. 1991; Mijatović et al. 2020), or obtained from measurements of the SFR (as recent works show a strong correlation between n_e and SFR, see e.g. Kaasinen et al. 2017; Reddy et al. 2023), even though it might be difficult for lensing sytems with small image separations and faint lensing galaxies. The current method of only using the differential X-ray Hydrogen absorption between the images (also used in this thesis) to estimate the electron column densities has the drawback of needing to assume an ionization fraction, and an electron density for one of the sightlines. If we knew the electron densities in the lensing galaxy, we would need to make less assumptions, and hence arrive at more accurate magnetic field strengths. One possibility to counter this is to additionally obtain optical spectra with high angular resolution (that can reach 0.042") with the Multi-Unit Spectroscopic Explorer (MUSE) of the European Southern Observatory (ESO), and to measure the electron densities in the lensing galaxies. However, with MUSE we can only observe sources in the Southern sky. In the Northern sky, the Keck telescope with a resolution of 0.04" could be utilized (Darvish et al. 2015). Another possibility would be the James Webb Space telescope (JWST), as with its high angular resolution ($\sim$ 0.1") IR imaging and spectra we can measure the galaxy's SFR, stellar mass, and inclination (Shipley et al. 2016). As we showed in Chapters 3 and 4, the inclination can have a large effect on the derived magnetic field strength and the interpretation of the magnetic field structure. Therefore it is important to measure the galaxy inclinations as precisely as possible. If we can acquire the stellar mass and the SFR of the lensing galaxy, we will be able to see how the magnetic field changes with stellar mass and SFR.

7.2.2 Future radio surveys and telescopes

There are multiple on-going and future radio surveys that will significantly increase the available radio observations of lensing systems, quasars with intervening galaxies, and FRBs, thus will help further our understanding of the evolution of galactic and intergalactic magnetic fields. In the rest of this subsection I describe all the different

on-going and planned surveys and telescopes.

The Very Large Array Sky Survey (VLASS) will map the Northern radio sky with the VLA with a total $\sim$ 5500 hours over seven years (from 2017 to 2024), and is expected to observe 10 million radio sources (Lacy et al. 2020). Data are being taken in total intensity (Stokes I) and polarization (Stokes Q, U, and V) in the frequency range of 2–4 GHz with an angular resolution of 2.5 arcsecond. The survey is eventually planned to reach a sensitivity of 69 μJy. This survey will provide $\sim$ 10 new resolved lensing systems, and a new catalog of polarized quasars with possibly intervening galaxies (improved from the current number of <100 systems), which can be used in the future to study the magnetic field strengths in galaxies at $z \geq 0.1$.

The Polarization Sky Survey of the Universe's Magnetism (POSSUM) is on-going, and uses the Australian Square Kilometre Array Pathfinder (ASKAP) radio telescope to map the Southern sky (Gaensler et al. 2010; Anderson et al. 2021). The survey has a frequency range of 800 – 1440 MHz, and an angular resolution of $\sim$ 20". They will publish data products of Stokes I, Q, U frequency spectra, and catalogs and 2D maps of polarization properties, with an expected polarized source count of one million sources. While this survey will also increase the number of known polarized background quasars with intervening galaxies with measured RMs, it will not provide us with additional lensing systems, as the survey's angular resolution is too low compared to typical arcsec scale lensing systems lensed by galaxies.

In the near future, a large number of FRBs with their polarization properties are expected to be observed by the Canadian Hydrogen Intensity Mapping Experiment (CHIME, CHIME Collaboration et al. 2022) radio telescope. They already published a catalog of $\sim$500 new FRBs (CHIME/FRB Collaboration et al. 2021; Chime/Frb Collaboration et al. 2023), and the results of the polarization analysis are expected to become available later, with some early results already published (Mckinven et al. 2023). This will increase the number of FRBs with known RM dramatically, as in many previous observations the polarization was not recorded. However, this telescope will measure both the DM and RM of FRBs (Mckinven et al. 2021), which can be used to statistically derive the strength of the IGMF by subtracting the DM and RM contributions of the Milky Way, the immediate environment of the FRB, and the FRB host galaxies (I have constrained this in Chapter 5). Another telescope is under development: the Deep Synoptic Array (DSA) 2000 will consist of 2000 telescopes, each with a five meter dish, expected to have first light in 2026 (Hallinan et al. 2019). It is predicted that DSA-2000 will detect and pinpoint the location of more than 10 000 FRBs per year, observing in full polarization. Together with other FRB surveys, we should be able to measure a $\sigma_{\rm RM,IGM}$ $\sim$2 rad m^{-2} with a confidence level of 95% in under 10 years, but the exact number of FRBs needed (and thus time) depends on the redshift distribution of the observed FRBs. If the $\sigma_{\rm RM,IGM}$ is larger than $\sim$2 rad m^{-2}, we can reach a confidence level of 95% with a fewer number of FRBs.

The Square Kilometer Array (SKA) will be an immense improvement on the sensitivity and angular resolution of current telescopes (Braun et al. 2019), and will revolutionize every field in radio astronomy, including cosmic magnetism (Braun et al. 2015; Heald et al. 2020). Apart from possibly providing us with $\sim$ 100 000 new lensing

systems (Koopmans et al. 2004; McKean et al. 2015), $\sim$ 50 000 background quasars with intervening foreground galaxies (Gaensler et al. 2015), and FRBs, the SKA will even allow us to detect the polarized synchrotron emission of galaxies up to $z = 0.5$ (Beck 2013, assuming a polarization fraction of 10%), making it possible to use the same method that before could only be used in nearby galaxies.

7.2.3 Further characterization of the magnetic fields of galaxies in the TNG50 simulation

In this thesis, to categorize the structure of magnetic fields, I separated galaxies that have a magnetic field structure without reversal, and the ones that have either reversals or turbulent random fields. Telling the difference between galaxies that have reversals and ones that have mostly random fields is not straight-forward in an automatic way (and going one-by-one is difficult for our large sample of 16 000 galaxies), even though the cases are very different physically - in one case we have a galaxy-scale field but its sign reverses in the disk, and in the other case only a turbulent small-scale field. I propose a possible method that could be used to achieve this separation: Connected Component Analysis (CCA, a basic algorithm in image processing, see e.g. Lacassagne & Zavidovique 2011), which can find connected regions in an image. Examples of how this classification could work are shown in Fig. 7.1: 1. shows a field with no reversal (one region found by the algorithm), 2. field with reversal (two regions), 3. a chaotic field, that has some features of a large-scale field with reversal (no region), and 4. a fully chaotic field (no region). The exact parameters for the algorithm still need to be fine-tuned, but the preliminary results show this is a promising way to separate large-scale fields from turbulent ones in galaxy maps. Once these are classified, we can start to understand what are the differences between galaxies with and without large-scale field reversals, which is interesting as most nearby galaxies have a large-scale field without reversal (Beck 2015a), but the Milky Way has a large-scale field reversal (Haverkorn 2015; Ma et al. 2020), similar to the second panel in Fig. 7.1. It would be interesting to further explore the merger histories of galaxies and to investigate how merging affects the magnetic field structure and strength of galaxies, for example if galaxies develop reversals after merger events. In turn, there is evidence based on simulations that magnetic fields also affect the merging process (e.g. modify the transfer of angular momentum and quicken the merging process, Whittingham et al. 2023). These merger histories are readily available in the simulation (see e.g. Sotillo-Ramos et al. 2022).

7.2.4 Planning observations based on TNG50

Based on what we find in the simulation, we can plan observations to verify if the same trends exist in reality. Most of these tests would be best carried out on nearby galaxies. . For example, from my preliminary results I found that in the simulation, the galaxy quenching caused by active galactic nuclei (AGN) feedback seems to have an effect on the magnetic field structure of galaxies: galaxies with larger stellar masses have a different radial B field profile compared to galaxies with lower stellar masses. In

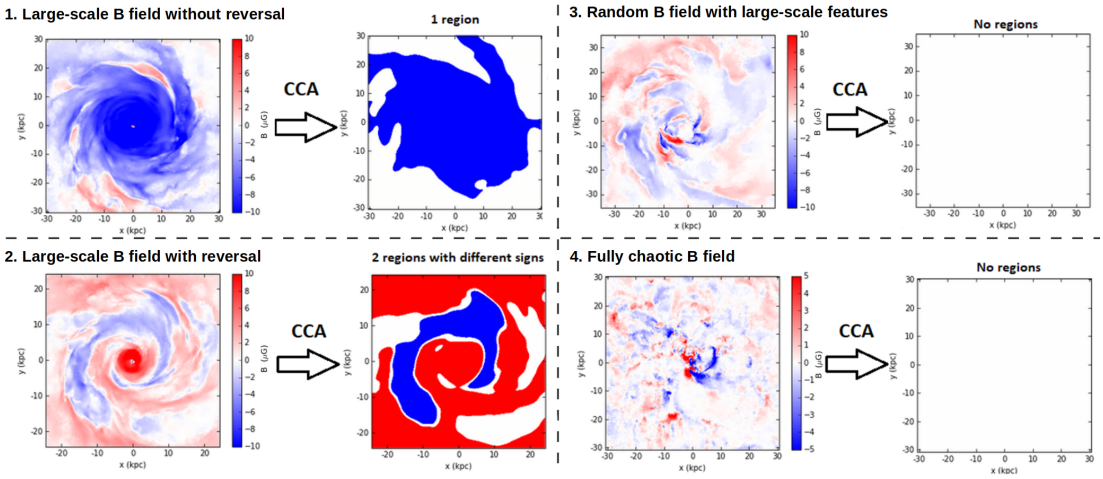

Figure 7.1: The face-on projections of the azimuthal magnetic field in a 2 kpc slice centered at the plane of four galaxies in the simulation (similarly to Pakmor et al. 2018, for more details see Appendix D of Appendix III. This illustration shows how we can characterize the B field structure of galaxies, by automatically finding large regions of the same sign in their maps. This can be achieved with Connected Component Analysis (CCA): 1 region − large-scale B field without reversal, 2 regions − large-scale B field with reversal, 0 regions − chaotic B field.

galaxies with strong AGN feedback, the magnetic field strength in the central regions of the galaxies is lower than in the outer parts, opposite of what we see in "normal" galaxies. We would need to map the magnetic field profiles for galaxies with different stellar masses, especially ones hosting AGNs (e.g. M81, see Devereux et al. 2003; Krause et al. 1989). Another interesting prediction from the simulation is that there can be magnetic fields out to a large vertical distance from the plane of the galaxy disk ($\sim$ 20 kpc).

The observations of nearby galaxies can be compared to the simulation by generating synchrotron maps from TNG50 (by e.g. following the method described in Marinacci et al. 2018). It would be also interesting to compare the atomic gas and magnetic field properties and structure in the simulated galaxies to the observations, to get a full understanding on the multi-phase ISM. While the atomic gas is not available by default in IllustrisTNG, the phases of the gas can be separated by post-processing (Diemer et al. 2018). We could see if the simulation is in agreement with the observations, and what processes might still be missing or would need improving: we could gain insights on the sources of turbulence (e.g. from supernovae), and even on AGN feedback.

7.3 Final remarks

In my thesis I measured the regular large-scale magnetic field strength in the halo of a spiral galaxy at $z = 0.414$, and in the disk of a spiral galaxy at $z = 0.685$, finding

that the mean-field dynamo is possibly already operating at $z = 0.685$. Furthermore, I constrained the rotation measure contribution of intervening galaxies and FRB host galaxies using the TNG50 simulation, which calculations will be essential in deriving the magnetic field strength of distant galaxies and detecting the intergalactic magnetic field. In the coming years, there will be a number of future radio surveys (VLASS, POSSUM) and new radio telescopes (SKA, DSA-2000) that will dramatically increase the number of polarized radio sources (including more than 100 00 new lensing systems – McKean et al. 2015, 50 000 polarized quasars with foreground galaxies – Gaensler et al. 2015, and tens of thousands of FRBs – Hallinan et al. 2019), increase the sensitivity and resolution of our measurements, and will help us to characterize the magnetic field of galaxies and to constrain the mean-field dynamo theory to even higher redshifts.

Bibliography

Acciari V. A., et al., 2022, MNRAS, 510, 2344 (Cited on page 64.)

Ahnen M. L., et al., 2016, A&A, 595, A98 (Cited on page 64.)

Akahori T., Ryu D., Gaensler B. M., 2016, ApJ, 824, 105 (Cited on pages 16, 72, 74, 75, 76, 110 and 120.)

Anderson C. S., et al., 2021, PASA, 38, e020 (Cited on pages 75 and 143.)

Andersson B. G., Lazarian A., Vaillancourt J. E., 2015, ARA&A, 53, 501 (Cited on page 6.)

Arshakian T. G., Beck R., Krause M., Sokoloff D., 2009, A&A, 494, 21 (Cited on pages 8, 9, 37, 52, 53, 66 and 101.)

Arvo J., 1992, in KIRK D., ed., , Graphics Gems III (IBM Version). Morgan Kaufmann, San Francisco, pp 117–120, doi:10.1016/B978-0-08-050755-2.50034-8, https://www.sciencedirect.com/science/article/pii/B9780080507552500348 (Cited on page 81.)

Ashkenazy J., Kipper R., Caner M., 1991, Phys. Rev. A, 43, 5568 (Cited on page 142.)

Azimlu M., Marciniak R., Barmby P., 2011, AJ, 142, 139 (Cited on page 57.)

Badole S., et al., 2022, A&A, 658, A7 (Cited on page 48.)

Bannister K. W., et al., 2019, Science, 365, 565 (Cited on page 74.)

Basu A., Mao S. A., Fletcher A., Kanekar N., Shukurov A., Schnitzeler D., Vacca V., Junklewitz H., 2018, MNRAS, 477, 2528 (Cited on pages iii, vii, 11, 37, 86, 107, 119, 120, 124, 133, 134, 135, 139 and 169.)

Baugh C. M., 2006, Reports on Progress in Physics, 69, 3101 (Cited on page 13.)

Baym G., Bödeker D., McLerran L., 1996, Phys. Rev. D, 53, 662 (Cited on page 73.)

Beck R., 1982, A&A, 106, 121 (Cited on page 5.)

Beck R., 2007, A&A, 470, 539 (Cited on pages 91, 95 and 100.)

Beck R., 2012, Space Sci. Rev., 166, 215 (Cited on page 87.)

Beck R., 2013, in Beck R., Balogh A., Bykov A., Treumann R. A., Widrow L., eds, , Vol. 39, Large-Scale Magnetic Fields in the Universe. pp 215–230, doi:10.1007/978-1-4614-5728-2$_8$ (Cited on pages 5, 27, 36, 101 and 144.)

Beck R., 2015a, A&A Rev., 24, 4 (Cited on pages 4, 7, 8, 54, 67, 139 and 144.)

Beck R., 2015b, A&A, 578, A93 (Cited on pages 7 and 67.)

Beck R., Wielebinski R., 2013, in Oswalt T. D., Gilmore G., eds, , Vol. 5, Planets, Stars and Stellar Systems. Volume 5: Galactic Structure and Stellar Populations. p. 641, doi:10.1007/978-94-007-5612-0$_1$3 (Cited on pages 7, 36, 54, 67 and 139.)

Beck R., Brandenburg A., Moss D., Shukurov A., Sokoloff D., 1996, ARA&A, 34, 155 (Cited on page 131.)

Beck A. M., Lesch H., Dolag K., Kotarba H., Geng A., Stasyszyn F. A., 2012, MNRAS, 422, 2152 (Cited on page 8.)

Beck R., Chamandy L., Elson E., Blackman E. G., 2019, Galaxies, 8, 4 (Cited on pages 4, 5, 7, 9, 36, 50, 51, 52, 117, 131 and 141.)

Beck R., Berkhuijsen E. M., Gießübel R., Mulcahy D. D., 2020, A&A, 633, A5 (Cited on page 7.)

Bell E. F., et al., 2004, ApJ, 608, 752 (Cited on page 87.)

Berkhuijsen E. M., Urbanik M., Beck R., Han J. L., 2016, A&A, 588, A114 (Cited on pages 95 and 100.)

Bernet M. L., Miniati F., Lilly S. J., Kronberg P. P., Dessauges-Zavadsky M., 2008, Nature, 454, 302 (Cited on pages 9, 10, 11, 13, 36 and 119.)

Bernet M. L., Miniati F., Lilly S. J., 2013, ApJ, 772, L28 (Cited on pages 9, 11, 36 and 119.)

Bertone S., Vogt C., Enßlin T., 2006, MNRAS, 370, 319 (Cited on pages 4 and 16.)

Bhandari S., et al., 2018, MNRAS, 475, 1427 (Cited on page 74.)

Bhandari S., et al., 2022, AJ, 163, 69 (Cited on page 80.)

Biggs A. D., 2021, MNRAS, 505, 2610 (Cited on pages 42 and 44.)

Biggs A. D., Browne I. W. A., 2018, MNRAS, 476, 5393 (Cited on pages 60, 63 and 141.)

Biggs A. D., Wucknitz O., Porcas R. W., Browne I. W. A., Jackson N. J., Mao S., Wilkinson P. N., 2003, MNRAS, 338, 599 (Cited on page 60.)

Birnboim Y., Balberg S., Teyssier R., 2015, MNRAS, 447, 3678 (Cited on pages 4 and 36.)

Bochenek C. D., Ravi V., Dong D., 2021, ApJ, 907, L31 (Cited on page 80.)

Borlaff A. S., et al., 2023, ApJ, 952, 4 (Cited on page 7.)

Boulares A., Cox D. P., 1990, ApJ, 365, 544 (Cited on page 4.)

Brandenburg A., Subramanian K., 2005, Phys. Rep., 417, 1 (Cited on page 73.)

Braun R., Bourke T., Green J. A., Keane E., Wagg J., 2015, in Advancing Astrophysics with the Square Kilometre Array (AASKA14). p. 174, doi:10.22323/1.215.0174 (Cited on page 143.)

Braun R., Bonaldi A., Bourke T., Keane E., Wagg J., 2019, arXiv e-prints, p. arXiv:1912.12699 (Cited on page 143.)

Brentjens M. A., de Bruyn A. G., 2005, A&A, 441, 1217 (Cited on pages 28, 29 and 41.)

Briggs D. S., 1995a, PhD thesis, New Mexico Institute of Mining and Technology (Cited on page 25.)

Briggs D. S., 1995b, in American Astronomical Society Meeting Abstracts. p. 112.02 (Cited on page 40.)

Brown J. C., Haverkorn M., Gaensler B. M., Taylor A. R., Bizunok N. S., McClure-Griffiths N. M., Dickey J. M., Green A. J., 2007, ApJ, 663, 258 (Cited on page 7.)

Browne I. W. A., Patnaik A. R., Walsh D., Wilkinson P. N., 1993, MNRAS, 263, L32 (Cited on page 56.)

Burn B. J., 1966, MNRAS, 133, 67 (Cited on pages 28, 30 and 42.)

Burud I., et al., 2000, ApJ, 544, 117 (Cited on page 45.)

CASA Team et al., 2022, PASP, 134, 114501 (Cited on page 22.)

CHIME Collaboration et al., 2022, ApJS, 261, 29 (Cited on pages 72 and 143.)

CHIME/FRB Collaboration et al., 2020, Nature, 587, 54 (Cited on page 80.)

CHIME/FRB Collaboration et al., 2021, ApJS, 257, 59 (Cited on pages 74 and 143.)

Carretti E., O'Sullivan S. P., Vacca V., Vazza F., Gheller C., Vernstrom T., Bonafede A., 2023, MNRAS, 518, 2273 (Cited on pages 16 and 73.)

Cen R., Ostriker J. P., 1999, ApJ, 514, 1 (Cited on page 75.)

Chamandy L., Taylor A. R., 2015, ApJ, 808, 28 (Cited on page 101.)

Chamandy L., Shukurov A., Taylor A. R., 2016, ApJ, 833, 43 (Cited on page 37.)

Chatterjee S., et al., 2017, Nature, 541, 58 (Cited on page 74.)

Chime/Frb Collaboration et al., 2023, ApJ, 947, 83 (Cited on page 143.)

Chittidi J. S., et al., 2021, ApJ, 922, 173 (Cited on page 114.)

Churchill C., Steidel C., Kacprzak G., 2005, in Braun R., ed., Astronomical Society of the Pacific Conference Series Vol. 331, Extra-Planar Gas. p. 387 (arXiv:astro-ph/0411269), doi:10.48550/arXiv.astro-ph/0411269 (Cited on pages 119 and 121.)

Clemens D. P., El-Batal A. M., Cerny C., Kressy S., Schroeder G., Pillai T., 2018, ApJ, 867, 79 (Cited on page 67.)

Cohen J. G., Lawrence C. R., Blandford R. D., 2003, ApJ, 583, 67 (Cited on page 56.)

Combes F., 2017, Frontiers in Astronomy and Space Sciences, 4, 10 (Cited on page 98.)

Condon J. J., Ransom S. M., 2016, Essential Radio Astronomy (Cited on page 20.)

Condon J. J., Cotton W. D., Broderick J. J., 2002, AJ, 124, 675 (Cited on page 20.)

Conselice C. J., 2014, ARA&A, 52, 291 (Cited on page 87.)

Contopoulos G., Jappel A., 1974, Transactions of the International Astronomical Union, Volume_XVB: Proceedings of the Fifteenth General Assembly, Sydney 1973 and Extraordinary Assembly, Poland 1973. (Cited on page 25.)

Cordes J. M., Chatterjee S., 2019, ARA&A, 57, 417 (Cited on page 74.)

Cordes J. M., Lazio T. J. W., 2002, arXiv e-prints, pp astro–ph/0207156 (Cited on pages 64, 75, 103 and 114.)

Costa A. H., Spangler S. R., Sink J. R., Brown S., Mao S. A., 2016, ApJ, 821, 92 (Cited on pages 67 and 68.)

Curran S. J., 2021, MNRAS, 506, 1548 (Cited on page 120.)

Dai X., Kochanek C. S., 2005, ApJ, 625, 633 (Cited on page 47.)

Darvish B., Mobasher B., Sobral D., Hemmati S., Nayyeri H., Shivaei I., 2015, ApJ, 814, 84 (Cited on page 142.)

Davies R. D., 2007, Astronomische Nachrichten, 328, 436 (Cited on page 6.)

Davis M., Efstathiou G., Frenk C. S., White S. D. M., 1985, ApJ, 292, 371 (Cited on page 31.)

Day C. K., et al., 2020, MNRAS, 497, 3335 (Cited on page 112.)

Devaraj R., Clemens D. P., Dewangan L. K., Luna A., Ray T. P., Mackey J., 2021, ApJ, 911, 81 (Cited on page 67.)

Devereux N., Ford H., Tsvetanov Z., Jacoby G., 2003, AJ, 125, 1226 (Cited on page 145.)

Diemer B., et al., 2018, ApJS, 238, 33 (Cited on page 145.)

Dolag K., Gaensler B. M., Beck A. M., Beck M. C., 2015, MNRAS, 451, 4277 (Cited on page 75.)

Donnari M., et al., 2019, MNRAS, 485, 4817 (Cited on page 87.)

Drzazga R. T., Chyży K. T., Jurusik W., Wiórkiewicz K., 2011, A&A, 533, A22 (Cited on page 4.)

Durrer R., Neronov A., 2013, A&A Rev., 21, 62 (Cited on pages 8 and 16.)

Dyer C. C., Shaver E. G., 1992, ApJ, 390, L5 (Cited on pages 12, 37 and 44.)

Eckert D., et al., 2015, Nature, 528, 105 (Cited on page 75.)

Elek O., Burchett J. N., Prochaska J. X., Forbes A. G., 2022, arXiv e-prints, p. arXiv:2204.01256 (Cited on page 114.)

Elmegreen B. G., 1982, ApJ, 253, 655 (Cited on page 4.)

Emonts B., et al., 2020, in Pizzo R., Deul E. R., Mol J. D., de Plaa J., Verkouter H., eds, Astronomical Society of the Pacific Conference Series Vol. 527, Astronomical Data Analysis Software and Systems XXIX. p. 267 (arXiv:1912.09437), doi:10.48550/arXiv.1912.09437 (Cited on page 40.)

Falco E. E., et al., 1999, ApJ, 523, 617 (Cited on page 57.)

Falomo R., Treves A., Scarpa R., Paiano S., Landoni M., 2017, MNRAS, 470, 2814 (Cited on page 56.)

Farnes J. S., O'Sullivan S. P., Corrigan M. E., Gaensler B. M., 2014, ApJ, 795, 63 (Cited on pages 9, 11, 36 and 119.)

Farnes J. S., Rudnick L., Gaensler B. M., Haverkorn M., O'Sullivan S. P., Curran S. J., 2017, ApJ, 841, 67 (Cited on pages 9, 11, 36 and 119.)

Farnsworth D., Rudnick L., Brown S., 2011, AJ, 141, 191 (Cited on pages 29, 42, 58 and 60.)

Fassnacht C. D., Cohen J. G., 1998, AJ, 115, 377 (Cited on pages 38 and 51.)

Ferreira R. J. Z., Jain R. K., Sloth M. S., 2013, J. Cosmology Astropart. Phys., 2013, 004 (Cited on page 73.)

Ferreira L., et al., 2022, ApJ, 938, L2 (Cited on pages 15, 66, 69, 79 and 139.)

Ferriere K., 1996, A&A, 310, 438 (Cited on page 8.)

Ferrière K. M., 2001, Reviews of Modern Physics, 73, 1031 (Cited on page 4.)

Ferrière K., West J. L., Jaffe T. R., 2021, MNRAS, 507, 4968 (Cited on page 28.)

Fletcher A., Berkhuijsen E. M., Beck R., Shukurov A., 2004, A&A, 414, 53 (Cited on pages 5, 7 and 67.)

Fletcher A., Beck R., Shukurov A., Berkhuijsen E. M., Horellou C., 2011, MNRAS, 412, 2396 (Cited on pages 5 and 7.)

Gaensler B. M., Madsen G. J., Chatterjee S., Mao S. A., 2008, PASA, 25, 184 (Cited on pages 48 and 51.)

Gaensler B. M., Landecker T. L., Taylor A. R., POSSUM Collaboration 2010, in American Astronomical Society Meeting Abstracts #215. p. 470.13 (Cited on page 143.)

Gaensler B., et al., 2015, in Advancing Astrophysics with the Square Kilometre Array (AASKA14). p. 103 (arXiv:1501.00626), doi:10.22323/1.215.0103 (Cited on pages 144 and 146.)

Gao H., Li Z., Zhang B., 2014, ApJ, 788, 189 (Cited on page 74.)

Gardenier D. W., 2019, frbpoppy: Fast radio burst population synthesis in Python, Astrophysics Source Code Library, record ascl:1911.009 (ascl:1911.009) (Cited on page 79.)

Geach J. E., Lopez-Rodriguez E., Doherty M. J., Chen J., Ivison R. J., Bendo G. J., Dye S., Coppin K. E. K., 2023, Nature, p. arXiv:2309.02034 (Cited on pages 9 and 10.)

Genzel R., et al., 2006, Nature, 442, 786 (Cited on pages 9 and 37.)

Gießübel R., Heald G., Beck R., Arshakian T. G., 2013, A&A, 559, A27 (Cited on page 6.)

Girelli G., Pozzetti L., Bolzonella M., Giocoli C., Marulli F., Baldi M., 2020, A&A, 634, A135 (Cited on page 51.)

Govoni F., Feretti L., 2004, International Journal of Modern Physics D, 13, 1549 (Cited on page 19.)

Grand R. J. J., et al., 2017, MNRAS, 467, 179 (Cited on pages 13, 14 and 78.)

Gray D. F., 1992, The observation and analysis of stellar photospheres.. Vol. 20 (Cited on page 169.)

Greaves J. S., Holland W. S., Jenness T., Hawarden T. G., 2000, Nature, 404, 732 (Cited on page 4.)

Grundahl F., Hjorth J., 1995, MNRAS, 275, L67 (Cited on page 57.)

Hackstein S., Vazza F., Brüggen M., Sigl G., Dundovic A., 2016, MNRAS, 462, 3660 (Cited on page 73.)

Hackstein S., Brüggen M., Vazza F., Gaensler B. M., Heesen V., 2019, MNRAS, 488, 4220 (Cited on pages 76, 103 and 107.)

Hackstein S., Brüggen M., Vazza F., Rodrigues L. F. S., 2020, MNRAS, 498, 4811 (Cited on pages 76, 79, 105, 107, 108, 116 and 140.)

Hada K., Niinuma K., Sitarek J., Spingola C., Hirano A., 2020, ApJ, 901, 2 (Cited on pages 57 and 60.)

Hakobyan A. A., Adibekyan V. Z., Aramyan L. S., Petrosian A. R., Gomes J. M., Mamon G. A., Kunth D., Turatto M., 2012, A&A, 544, A81 (Cited on page 169.)

Hallinan G., et al., 2019, in Bulletin of the American Astronomical Society. p. 255 (arXiv:1907.07648), doi:10.48550/arXiv.1907.07648 (Cited on pages 72, 143 and 146.)

Hamaker J. P., Bregman J. D., 1996, A&AS, 117, 161 (Cited on page 25.)

Hanasz M., Lesch H., Naab T., Gawryszczak A., Kowalik K., Wóltański D., 2013, ApJ, 777, L38 (Cited on pages 4 and 36.)

Hanayama H., Takahashi K., Kotake K., Oguri M., Ichiki K., Ohno H., 2005, ApJ, 633, 941 (Cited on page 8.)

Harvey-Smith L., Madsen G. J., Gaensler B. M., 2011, ApJ, 736, 83 (Cited on pages 67 and 68.)

Hashimoto T., et al., 2020, MNRAS, 497, 4107 (Cited on page 92.)

Haverkorn M., 2015, in Lazarian A., de Gouveia Dal Pino E. M., Melioli C., eds, Astrophysics and Space Science Library Vol. 407, Magnetic Fields in Diffuse Media. p. 483 (arXiv:1406.0283), doi:10.1007/978-3-662-44625-6$_1$7 (Cited on page 144.)

Haverkorn M., Heesen V., 2012, Space Sci. Rev., 166, 133 (Cited on page 8.)

Haverkorn M., Brown J. C., Gaensler B. M., McClure-Griffiths N. M., 2008, ApJ, 680, 362 (Cited on pages 15 and 77.)

He C., Ng C. Y., Kaspi V. M., 2013, ApJ, 768, 64 (Cited on pages 48 and 64.)

Heald G., 2009, in Strassmeier K. G., Kosovichev A. G., Beckman J. E., eds, Vol. 259, Cosmic Magnetic Fields: From Planets, to Stars and Galaxies. pp 591–602, doi:10.1017/S1743921309031421 (Cited on page 28.)

Heald G., et al., 2020, Galaxies, 8, 53 (Cited on page 143.)

Heesen V., Krause M., Beck R., Dettmar R. J., 2009, A&A, 506, 1123 (Cited on pages 7 and 67.)

Heiles C., Haverkorn M., 2012, Space Sci. Rev., 166, 293 (Cited on page 4.)

Heintz K. E., et al., 2020, ApJ, 903, 152 (Cited on pages 78, 80 and 112.)

Högbom J. A., 1974, A&AS, 15, 417 (Cited on page 24.)

Hou L. G., Han J. L., Shi W. B., 2009, A&A, 499, 473 (Cited on page 57.)

Hovatta T., O'Sullivan S., Martí-Vidal I., Savolainen T., Tchekhovskoy A., 2019, A&A, 623, A111 (Cited on page 42.)

Hutschenreuter S., et al., 2022, A&A, 657, A43 (Cited on pages 16, 38, 76 and 114.)

Irwin J., et al., 2012, AJ, 144, 43 (Cited on pages 53, 54 and 139.)

Jackson N., et al., 1995, MNRAS, 274, L25 (Cited on page 38.)

Jackson N., Xanthopoulos E., Browne I. W. A., 2000, MNRAS, 311, 389 (Cited on page 57.)

Jaffe T. R., Leahy J. P., Banday A. J., Leach S. M., Lowe S. R., Wilkinson A., 2010, MNRAS, 401, 1013 (Cited on pages v and 6.)

James C. W., et al., 2022, MNRAS, 516, 4862 (Cited on page 74.)

Jansson R., Farrar G. R., 2012, ApJ, 757, 14 (Cited on page 107.)

Jaroszyński M., 2020, Acta Astron., 70, 87 (Cited on pages 106 and 110.)

Jaunsen A. O., Hjorth J., 1997, A&A, 317, L39 (Cited on pages 38 and 51.)

Kaasinen M., Bian F., Groves B., Kewley L. J., Gupta A., 2017, MNRAS, 465, 3220 (Cited on pages 97 and 142.)

Kahniashvili T., Brandenburg A., Campanelli L., Ratra B., Tevzadze A. G., 2012, Phys. Rev. D, 86, 103005 (Cited on page 73.)

Kahniashvili T., Tevzadze A. G., Brandenburg A., Neronov A., 2013, Phys. Rev. D, 87, 083007 (Cited on page 73.)

Keating L. C., Pen U.-L., 2020, MNRAS, 496, L106 (Cited on page 75.)

Kierdorf M., et al., 2020, A&A, 642, A118 (Cited on page 5.)

Kim C.-G., Kim W.-T., Ostriker E. C., 2006, ApJ, 649, L13 (Cited on page 8.)

Kochanek C. S., Falco E. E., Impey C. D., Lehár J., McLeod B. A., Rix H. W., 1999, in Holt S., Smith E., eds, American Institute of Physics Conference Series Vol. 470, After the Dark Ages: When Galaxies were Young (the Universe at 2 Z 5). pp 163–175 (arXiv:astro-ph/9811111), doi:10.1063/1.58598 (Cited on pages 38 and 39.)

Koopmans L. V. E., de Bruyn A. G., Jackson N., 1998, MNRAS, 295, 534 (Cited on page 51.)

Koopmans L. V. E., de Bruyn A. G., Xanthopoulos E., Fassnacht C. D., 2000, A&A, 356, 391 (Cited on page 45.)

Koopmans L. V. E., Browne I. W. A., Jackson N. J., 2004, New A Rev., 48, 1085 (Cited on page 144.)

Kourkchi E., et al., 2020, ApJ, 902, 145 (Cited on page 165.)

Kovács O. E., Bogdán Á., Smith R. K., Kraft R. P., Forman W. R., 2019, ApJ, 872, 83 (Cited on page 75.)

Krause M., 1990, in Beck R., Kronberg P. P., Wielebinski R., eds, Vol. 140, Galactic and Intergalactic Magnetic Fields. p. 187 (Cited on pages v and 7.)

Krause M., 2009, in Revista Mexicana de Astronomia y Astrofisica Conference Series. pp 25–29 (arXiv:0806.2060), doi:10.48550/arXiv.0806.2060 (Cited on page 7.)

Krause M., Beck R., Hummel E., 1989, A&A, 217, 17 (Cited on pages 5, 7 and 145.)

Krause M., et al., 2018, A&A, 611, A72 (Cited on pages 95 and 100.)

Kronberg P. P., Perry J. J., Zukowski E. L. H., 1992, ApJ, 387, 528 (Cited on pages 9, 36 and 119.)

Kronberg P. P., Bernet M. L., Miniati F., Lilly S. J., Short M. B., Higdon D. M., 2008, ApJ, 676, 70 (Cited on pages 9 and 119.)

Kroupa P., 2015, Canadian Journal of Physics, 93, 169 (Cited on page 15.)

Kroupa P., et al., 2023, arXiv e-prints, p. arXiv:2309.11552 (Cited on page 15.)

Krumholz M. R., Federrath C., 2019, Frontiers in Astronomy and Space Sciences, 6, 7 (Cited on pages 4 and 36.)

Krumholz M. R., Matzner C. D., 2009, ApJ, 703, 1352 (Cited on page 57.)

Kulkarni S. R., Heiles C., 1987, in Hollenbach D. J., Thronson Harley A. J., eds, Vol. 134, Interstellar Processes. p. 87, doi:10.1007/978-94-009-3861-8$_5$ (Cited on page 4.)

Labbé I., et al., 2023, Nature, 616, 266 (Cited on pages 15, 66 and 79.)

Lacassagne L., Zavidovique B., 2011, J. Real-Time Image Process., 6, 117â135 (Cited on page 144.)

Lacey C. G., et al., 2016, MNRAS, 462, 3854 (Cited on pages 105 and 108.)

Lacy M., et al., 2020, PASP, 132, 035001 (Cited on page 143.)

Lazar M., Schlickeiser R., Wielebinski R., Poedts S., 2009, ApJ, 693, 1133 (Cited on page 8.)

Lehár J., et al., 2000, ApJ, 536, 584 (Cited on page 57.)

Leslie S. K., et al., 2018, A&A, 615, A7 (Cited on page 169.)

Li H.-B., Henning T., 2011, Nature, 479, 499 (Cited on page 6.)

Li H. B., Goodman A., Sridharan T. K., Houde M., Li Z. Y., Novak G., Tang K. S., 2014, in Beuther H., Klessen R. S., Dullemond C. P., Henning T., eds, Protostars and Planets VI. pp 101–123 (arXiv:1404.2024), doi:10.2458/azu$_u$*apress*$_9$780816531240 – *ch*005 (Cited on page 67.)

Li D., et al., 2021, Nature, 598, 267 (Cited on page 74.)

Licquia T. C., Newman J. A., 2015, ApJ, 806, 96 (Cited on pages 103 and 107.)

Lopez-Rodriguez E., et al., 2022, ApJ, 936, 92 (Cited on page 6.)

Lorimer D. R., Kramer M., 2004, Handbook of Pulsar Astronomy. Vol. 4 (Cited on page 26.)

Lorimer D. R., Bailes M., McLaughlin M. A., Narkevic D. J., Crawford F., 2007, Science, 318, 777 (Cited on pages 16 and 74.)

Lüghausen F., Famaey B., Kroupa P., 2015, Canadian Journal of Physics, 93, 232 (Cited on page 15.)

Lyutikov M., 2022, ApJ, 933, L6 (Cited on pages 75 and 76.)

Ma Y. K., Mao S. A., Stil J., Basu A., West J., Heiles C., Hill A. S., Betti S. K., 2019, MNRAS, 487, 3432 (Cited on page 42.)

Ma Y. K., Mao S. A., Ordog A., Brown J. C., 2020, MNRAS, 497, 3097 (Cited on page 144.)

Macquart J. P., et al., 2015, in Advancing Astrophysics with the Square Kilometre Array (AASKA14). p. 55 (arXiv:1501.07535), doi:10.22323/1.215.0055 (Cited on pages 74 and 79.)

Macquart J. P., et al., 2020, Nature, 581, 391 (Cited on pages 72, 75, 106 and 112.)

Maller A. H., Flores R. A., Primack J. R., 1997, ApJ, 486, 681 (Cited on page 38.)

Maller A. H., Simard L., Guhathakurta P., Hjorth J., Jaunsen A. O., Flores R. A., Primack J. R., 2000, ApJ, 533, 194 (Cited on pages 48 and 165.)

Mannings A. G., et al., 2021, ApJ, 917, 75 (Cited on page 112.)

Mannings A. G., et al., 2022, arXiv e-prints, p. arXiv:2209.15113 (Cited on page 74.)

Mao S. A., Gaensler B. M., Haverkorn M., Zweibel E. G., Madsen G. J., McClure-Griffiths N. M., Shukurov A., Kronberg P. P., 2010, ApJ, 714, 1170 (Cited on page 53.)

Mao S. A., et al., 2012a, ApJ, 755, 21 (Cited on page 53.)

Mao S. A., et al., 2012b, ApJ, 759, 25 (Cited on page 6.)

Mao S. A., Zweibel E., Fletcher A., Ott J., Tabatabaei F., 2015, ApJ, 800, 92 (Cited on page 5.)

Mao S. A., et al., 2017, Nature Astronomy, 1, 621 (Cited on pages 9, 11, 12, 36, 37, 38, 52, 53, 54, 65, 66, 67, 138 and 139.)

Marcote B., Kirsten F., Hessels J., Nimmo K., Paragi Z., Project P., 2022, in European VLBI Network Mini-Symposium and Users' Meeting 2021. p. 35 (arXiv:2202.11644), doi:10.22323/1.399.0035 (Cited on page 74.)

Marinacci F., et al., 2018, MNRAS, 480, 5113 (Cited on pages 102 and 145.)

Masui K., et al., 2015, Nature, 528, 523 (Cited on page 74.)

McKean J., et al., 2015, in Advancing Astrophysics with the Square Kilometre Array (AASKA14). p. 84 (arXiv:1502.03362), doi:10.22323/1.215.0084 (Cited on pages 144 and 146.)

McMullin J. P., Waters B., Schiebel D., Young W., Golap K., 2007, in Shaw R. A., Hill F., Bell D. J., eds, Astronomical Society of the Pacific Conference Series Vol. 376, Astronomical Data Analysis Software and Systems XVI. p. 127 (Cited on pages 22 and 40.)

McQuinn M., 2014, ApJ, 780, L33 (Cited on pages 74 and 75.)

Mckinven R., et al., 2021, ApJ, 920, 138 (Cited on pages 74 and 143.)

Mckinven R., et al., 2023, ApJ, 951, 82 (Cited on page 143.)

Menten K. M., Reid M. J., 1996, ApJ, 465, L99 (Cited on page 57.)

Michilli D., et al., 2018, Nature, 553, 182 (Cited on page 74.)

Mijatović Z., Djurović S., Gavanski L., Gajo T., Favre A., Morel V., Bultel A., 2020, Spectrochimica Acta, 166, 105821 (Cited on page 142.)

Milgrom M., 1983, ApJ, 270, 365 (Cited on page 15.)

Mitchell P. D., et al., 2018, MNRAS, 474, 492 (Cited on page 105.)

Mittal R., Porcas R., Wucknitz O., 2007, A&A, 465, 405 (Cited on pages 57, 67 and 68.)

Mo J.-F., Zhu W., Wang Y., Tang L., Feng L.-L., 2023, MNRAS, 518, 539 (Cited on page 80.)

Moon S., Kim W.-T., Kim C.-G., Ostriker E. C., 2023, ApJ, 946, 114 (Cited on page 36.)

Mora-Partiarroyo S. C., et al., 2019, A&A, 632, A11 (Cited on pages 7 and 53.)

Moss D., Shukurov A., Sokoloff D., 2000, A&A, 358, 1142 (Cited on page 101.)

Nagesh S. T., Banik I., Thies I., Kroupa P., Famaey B., Wittenburg N., Parziale R., Haslbauer M., 2021, Canadian Journal of Physics, 99, 607 (Cited on page 15.)

Narasimha D., Chitre S. M., 2004, Journal of Korean Astronomical Society, 37, 355 (Cited on pages 11 and 38.)

Nelson D., et al., 2019a, Computational Astrophysics and Cosmology, 6, 2 (Cited on pages 14, 31, 32, 72, 76, 77, 78, 79, 81, 120 and 121.)

Nelson D., et al., 2019b, MNRAS, 490, 3234 (Cited on pages 14, 77, 120 and 139.)

Neronov A., Vovk I., 2010, Science, 328, 73 (Cited on pages 52 and 66.)

Nicastro F., et al., 2018, Nature, 558, 406 (Cited on page 75.)

Nielsen N. M., Churchill C. W., Kacprzak G. G., 2013, ApJ, 776, 115 (Cited on page 10.)

Noeske K. G., et al., 2007, ApJ, 660, L43 (Cited on page 87.)

Ntormousi E., Tassis K., Del Sordo F., Fragkoudi F., Pakmor R., 2020, A&A, 641, A165 (Cited on pages 14 and 15.)

O'Sullivan S. P., et al., 2012, MNRAS, 421, 3300 (Cited on pages 29 and 42.)

O'Sullivan S. P., et al., 2020, MNRAS, 495, 2607 (Cited on page 73.)

Ogbodo C. S., Green J. A., Dawson J. R., Breen S. L., Mao S. A., McClure-Griffiths N. M., Robishaw T., Harvey-Smith L., 2020, MNRAS, 493, 199 (Cited on page 6.)

Oppermann N., et al., 2012, A&A, 542, A93 (Cited on pages 38 and 76.)

Osterbrock D. E., 1974, Astrophysics of gaseous nebulae (Cited on page 142.)

Pakmor R., Springel V., 2013, MNRAS, 432, 176 (Cited on page 13.)

Pakmor R., et al., 2017, MNRAS, 469, 3185 (Cited on pages 14, 93, 100 and 101.)

Pakmor R., Guillet T., Pfrommer C., Gómez F. A., Grand R. J. J., Marinacci F., Simpson C. M., Springel V., 2018, MNRAS, 481, 4410 (Cited on pages 14, 37, 82, 93, 121 and 145.)

Parker E. N., 1966, ApJ, 145, 811 (Cited on page 4.)

Patnaik A. R., Browne I. W. A., Wilkinson P. N., Wrobel J. M., 1992, MNRAS, 254, 655 (Cited on page 55.)

Patnaik A. R., Browne I. W. A., King L. J., Muxlow T. W. B., Walsh D., Wilkinson P. N., 1993, MNRAS, 261, 435 (Cited on pages 55, 56 and 60.)

Patnaik A. R., Porcas R. W., Browne I. W. A., 1995, MNRAS, 274, L5 (Cited on page 60.)

Patnaik A. R., Menten K. M., Porcas R. W., Kemball A. J., 2001, in Brainerd T. G., Kochanek C. S., eds, Astronomical Society of the Pacific Conference Series Vol. 237, Gravitational Lensing: Recent Progress and Future Go. p. 99 (arXiv:astro-ph/9909329), doi:10.48550/arXiv.astro-ph/9909329 (Cited on page 60.)

Pellegrini E. W., Reissl S., Rahner D., Klessen R. S., Glover S. C. O., Pakmor R., Herrera-Camus R., Grand R. J. J., 2020, MNRAS, 498, 3193 (Cited on pages 82 and 141.)

Perley R. A., Butler B. J., 2013a, ApJS, 204, 19 (Cited on page 40.)

Perley R. A., Butler B. J., 2013b, ApJS, 206, 16 (Cited on pages 40 and 41.)

Petroff E., et al., 2015, MNRAS, 447, 246 (Cited on page 16.)

Petroff E., et al., 2016, PASA, 33, e045 (Cited on page 74.)

Petroff E., Hessels J. W. T., Lorimer D. R., 2019, A&A Rev., 27, 4 (Cited on page 74.)

Petroff E., Hessels J. W. T., Lorimer D. R., 2022, A&A Rev., 30, 2 (Cited on page 16.)

Pettini M., 2011, Proceedings of the Royal Society of London Series A, 467, 2735 (Cited on page 11.)

Pfrommer C., Werhahn M., Pakmor R., Girichidis P., Simpson C. M., 2022, MNRAS, 515, 4229 (Cited on pages 37 and 53.)

Pillepich A., et al., 2018, MNRAS, 473, 4077 (Cited on pages 14, 72, 76, 77, 82, 105 and 120.)

Pillepich A., et al., 2019, MNRAS, 490, 3196 (Cited on pages 14, 77, 120 and 139.)

Piro A. L., Gaensler B. M., 2018, ApJ, 861, 150 (Cited on pages 75 and 76.)

Planck Collaboration et al., 2016a, A&A, 586, A138 (Cited on page 4.)

Planck Collaboration et al., 2016b, A&A, 594, A13 (Cited on page 31.)

Planck Collaboration et al., 2016c, A&A, 594, A19 (Cited on pages 16 and 73.)

Platts E., Weltman A., Walters A., Tendulkar S. P., Gordin J. E. B., Kandhai S., 2019, Phys. Rep., 821, 1 (Cited on page 75.)

Prochaska J. X., Zheng Y., 2019, MNRAS, 485, 648 (Cited on page 114.)

Purcell C. R., Van Eck C. L., West J., Sun X. H., Gaensler B. M., 2020, RM-Tools: Rotation measure (RM) synthesis and Stokes QU-fitting, Astrophysics Source Code Library, record ascl:2005.003 (ascl:2005.003) (Cited on pages 29, 41 and 58.)

Ravi V., et al., 2019, Nature, 572, 352 (Cited on page 79.)

Raycheva N. C., et al., 2022, A&A, 663, A170 (Cited on page 68.)

Reddy N. A., et al., 2023, ApJ, 951, 56 (Cited on page 142.)

Rees M. J., 1987, QJRAS, 28, 197 (Cited on pages 4 and 36.)

Robishaw T., Quataert E., Heiles C., 2008, ApJ, 680, 981 (Cited on page 6.)

Rodrigues L. F. S., Chamandy L., 2020, Magnetizer: Computing magnetic fields of evolving galaxies, Astrophysics Source Code Library, record ascl:2008.011 (ascl:2008.011) (Cited on page 108.)

Rodrigues L. F. S., Chamandy L., Shukurov A., Baugh C. M., Taylor A. R., 2019, MNRAS, 483, 2424 (Cited on pages 14, 76 and 108.)

Rodríguez L. F., Gómez Y., Tafoya D., 2012, MNRAS, 420, 279 (Cited on pages 67 and 68.)

Ruzmaikin A. A., Sokolov D. D., Shukurov A. M., 1988, Magnetic Fields of Galaxies. Vol. 133, doi:10.1007/978-94-009-2835-0, (Cited on pages 8, 52 and 66.)

Rybicki G. B., Lightman A. P., 1979, Radiative processes in astrophysics (Cited on page 19.)

Schlickeiser R., 2012, Phys. Rev. Lett., 109, 261101 (Cited on page 8.)

Schneider P., Ehlers J., Falco E. E., 1992, Gravitational Lenses, doi:10.1007/978-3-662-03758-4. (Cited on page 37.)

Seta A., Rodrigues L. F. S., Federrath C., Hales C. A., 2021, ApJ, 907, 2 (Cited on pages 9 and 10.)

Shah H., Seta A., 2021, MNRAS, 508, 1371 (Cited on pages 9 and 10.)

Sharda P., Federrath C., Krumholz M. R., 2020, MNRAS, 497, 336 (Cited on page 4.)

Shimakawa R., et al., 2015, MNRAS, 451, 1284 (Cited on page 97.)

Shipley H. V., Papovich C., Rieke G. H., Brown M. J. I., Moustakas J., 2016, ApJ, 818, 60 (Cited on page 142.)

Shukurov A., 2005, in Wielebinski R., Beck R., eds, , Vol. 664, Cosmic Magnetic Fields. p. 113, doi:10.1007/3540313966$_6$ (Cited on pages 8, 9 and 53.)

Shukurov A., Subramanian K., 2021, Astrophysical Magnetic Fields: From Galaxies to the Early Universe. Cambridge Astrophysics, Cambridge University Press, doi:10.1017/9781139046657 (Cited on page 101.)

Sigl G., Miniati F., Ensslin T. A., 2003, Phys. Rev. D, 68, 043002 (Cited on page 73.)

Sigut T. A. A., Mahjour A. K., Tycner C., 2020, ApJ, 894, 18 (Cited on page 169.)

Simha S., et al., 2020, ApJ, 901, 134 (Cited on page 114.)

Slavin J. D., Cox D. P., 1992, ApJ, 392, 131 (Cited on page 4.)

Sokoloff D. D., Bykov A. A., Shukurov A., Berkhuijsen E. M., Beck R., Poezd A. D., 1998, MNRAS, 299, 189 (Cited on page 5.)

Sotillo-Ramos D., et al., 2022, MNRAS, 516, 5404 (Cited on page 144.)

Spitler L. G., et al., 2016, Nature, 531, 202 (Cited on page 74.)

Spitzer L. J., 1958, in Lehnert B., ed., Vol. 6, Electromagnetic Phenomena in Cosmical Physics. p. 169 (Cited on page 4.)

Springel V., Hernquist L., 2003, MNRAS, 339, 289 (Cited on pages 82, 97 and 121.)

Springel V., White S. D. M., Tormen G., Kauffmann G., 2001, MNRAS, 328, 726 (Cited on page 32.)

Springel V., et al., 2005, Nature, 435, 629 (Cited on page 17.)

Springel V., Pakmor R., Weinberger R., 2019, AREPO: Cosmological magnetohydrodynamical moving-mesh simulation code, Astrophysics Source Code Library, record ascl:1909.010 (ascl:1909.010) (Cited on page 32.)

Stein Y., et al., 2019, A&A, 623, A33 (Cited on page 7.)

Stil J. M., Taylor A. R., Sunstrum C., 2011, ApJ, 726, 4 (Cited on page 38.)

Stokes G. G., 1851, Transactions of the Cambridge Philosophical Society, 9, 399 (Cited on page 25.)

Sun X. H., Han J. L., Reich W., Reich P., Shi W. B., Wielebinski R., Fürst E., 2007, A&A, 463, 993 (Cited on page 68.)

Tabatabaei F. S., Krause M., Fletcher A., Beck R., 2008, A&A, 490, 1005 (Cited on page 4.)

Tabatabaei F. S., et al., 2017, ApJ, 836, 185 (Cited on pages 4 and 36.)

Tang Y.-W., Ho P. T. P., Koch P. M., Girart J. M., Lai S.-P., Rao R., 2009, ApJ, 700, 251 (Cited on page 6.)

Taylor G. B., Carilli C. L., Perley R. A., 1999, Synthesis Imaging in Radio Astronomy II. Astronomical Society of the Pacific Conference Series Vol. 180 (Cited on page 21.)

Taylor A. R., Stil J. M., Sunstrum C., 2009, ApJ, 702, 1230 (Cited on page 53.)

Teyssier R., 2002, A&A, 385, 337 (Cited on page 15.)

Thompson A. R., Moran J. M., Swenson George W. J., 2017, Interferometry and Synthesis in Radio Astronomy, 3rd Edition, doi:10.1007/978-3-319-44431-4. (Cited on pages 21 and 22.)

Thornton D., et al., 2013, Science, 341, 53 (Cited on page 74.)

Tombesi F., Cappi M., Reeves J. N., Palumbo G. G. C., Yaqoob T., Braito V., Dadina M., 2010, A&A, 521, A57 (Cited on page 98.)

Tsukui T., Iguchi S., 2021, Science, 372, 1201 (Cited on page 37.)

Vazza F., et al., 2021, Galaxies, 9, 109 (Cited on pages 16 and 73.)

Vernstrom T., Gaensler B. M., Rudnick L., Andernach H., 2019, ApJ, 878, 92 (Cited on page 38.)

Verschuur G. L., 1968, Phys. Rev. Lett., 21, 775 (Cited on page 6.)

Vogelsberger M., et al., 2014, Nature, 509, 177 (Cited on page 13.)

Vogelsberger M., Marinacci F., Torrey P., Puchwein E., 2020, Nature Reviews Physics, 2, 42 (Cited on page 13.)

Walker C. R. H., Ma Y.-Z., Breton R. P., 2020, A&A, 638, A37 (Cited on pages 75, 79, 80, 103, 116 and 140.)

Wang P., Abel T., 2009, ApJ, 696, 96 (Cited on page 13.)

Wang X.-G., Li L., Yang Y.-P., Luo J.-W., Zhang B., Lin D.-B., Liang E.-W., Qin S.-M., 2020, ApJ, 894, L22 (Cited on page 80.)

Weinberger R., et al., 2017, MNRAS, 465, 3291 (Cited on page 98.)

Weinberger R., et al., 2018, MNRAS, 479, 4056 (Cited on pages 98 and 102.)

Whittingham J., Sparre M., Pfrommer C., Pakmor R., 2023, MNRAS, (Cited on page 144.)

Wiener J., Zweibel E. G., Oh S. P., 2013, ApJ, 767, 87 (Cited on pages 4 and 36.)

Wiklind T., Combes F., 1995, A&A, 299, 382 (Cited on pages 63 and 66.)

Wittenburg N., Kroupa P., Banik I., Candlish G., Samaras N., 2023, MNRAS, 523, 453 (Cited on page 15.)

Wolfe A. M., Jorgenson R. A., Robishaw T., Heiles C., Prochaska J. X., 2011, ApJ, 733, 24 (Cited on pages 9, 10 and 36.)

Wucknitz O., Biggs A. D., Browne I. W. A., 2004, MNRAS, 349, 14 (Cited on page 64.)

Xu J., Han J. L., 2015, Research in Astronomy and Astrophysics, 15, 1629 (Cited on pages 64 and 103.)

Yao J. M., Manchester R. N., Wang N., 2017, ApJ, 835, 29 (Cited on pages 75 and 95.)

Yaron O., Ofek E., Gal-Yam A., Sass A., 2020, Transient Name Server AstroNote, 70, 1 (Cited on page 74.)

York T., Jackson N., Browne I. W. A., Wucknitz O., Skelton J. E., 2005, MNRAS, 357, 124 (Cited on page 56.)

Zahid H. J., Dima G. I., Kewley L. J., Erb D. K., Davé R., 2012, ApJ, 757, 54 (Cited on page 114.)

Zanazzi J. J., Lai D., 2020, ApJ, 892, L15 (Cited on page 80.)

Zhang G. Q., Yu H., He J. H., Wang F. Y., 2020, ApJ, 900, 170 (Cited on pages 75, 82, 85, 105, 106 and 121.)

Zheng Z., Ofek E. O., Kulkarni S. R., Neill J. D., Juric M., 2014, ApJ, 797, 71 (Cited on pages 16, 74 and 110.)

Zhou B., Li X., Wang T., Fan Y.-Z., Wei D.-M., 2014, Phys. Rev. D, 89, 107303 (Cited on pages 74, 75 and 108.)

Zuckerman B., 1973, ApJ, 183, 863 (Cited on page 57.)

Zweibel E. G., Heiles C., 1997, Nature, 385, 131 (Cited on page 5.)

de Graaff A., Cai Y.-C., Heymans C., Peacock J. A., 2019, A&A, 624, A48 (Cited on page 75.)

van den Bergh S., 1988, PASP, 100, 344 (Cited on page 169.)

Appendix I

Appendix for Chapter 3

I.1 The effects of the range of assumptions on magnetic field strength

We investigate how the different assumptions affect our derived B field strength and Which parameters affect it the most. We do this by assuming Milky Way like galaxy parameters and allowing one parameter to change in its full range. The ranges of these parameters can be found in Table I.1. Apart from these parameters, we also investigated a larger range of inclinations. Even though we used the inclination from Maller et al. (2000) ($81.7^{\circ}{}^{+0.4^{\circ}}_{-0.5^{\circ}}$) in our calculation in the main text of the paper, we also obtained $i = 70^{\circ} \pm 3^{\circ}$ using the `Smart Inclination Evaluation with Neural Network` (Kourkchi et al. 2020)[1] on CASTLES images from the NICMOS instrument of the Hubble Space Telescope (HST), which is not consistent with Maller et al. (2000). To investigate how the inclination affects our magnetic field strengths, we explore a wider range of $65^{\circ} < i < 85^{\circ}$. The range of magnetic field strengths reported in Chapter 3 at the position of lensed image B (-0.7 kpc away from the midplane of the galaxy) is 0.2 – 3 μG in the full parameter range, and 1.2 – 1.8 μG in the MW parameter range.

Below, we list the details of testing different ionization fractions, electron column densities at the position of image A, scale heights, and inclinations. In the first three subsections, the inclination is kept as Maller et al. (2000) ($81.7^{\circ}{}^{+0.4^{\circ}}_{-0.5^{\circ}}$), and in the last point it is $65^{\circ} < i < 85^{\circ}$. In subsections I.1.1, I.1.2, and I.1.4, we consider all geometry models, and in subsection I.1.3, we only consider the exponential models, as only those have exponential scale height in their definition.

[1] https://edd.ifa.hawaii.edu/inclinet/

Table I.1: The assumed ranges of the parameters, in a general case (full parameter range) and in the case of Milky Way like galaxy properties (MW parameter range).

Parameter	Full parameter range	MW parameter range
$f_{\rm ion}$	0.05 – 0.5	0.07 – 0.14
$\Delta\ N_e$ (pc cm^{-3})	48.6 – 486.1	78 – 103
$N_{\rm e,A}$ (pc cm^{-3})	1 – 100	2 – 5
$N_{\rm e,B}$ (pc cm^{-3})	49.6 – 586.1	83 – 105
$N_{\rm e,A} + N_{\rm e,B}$ (pc cm^{-3})	50.6 – 686.1	85 – 110
$h_{\rm B,scale}$ (kpc)	2 – 20	2 – 8

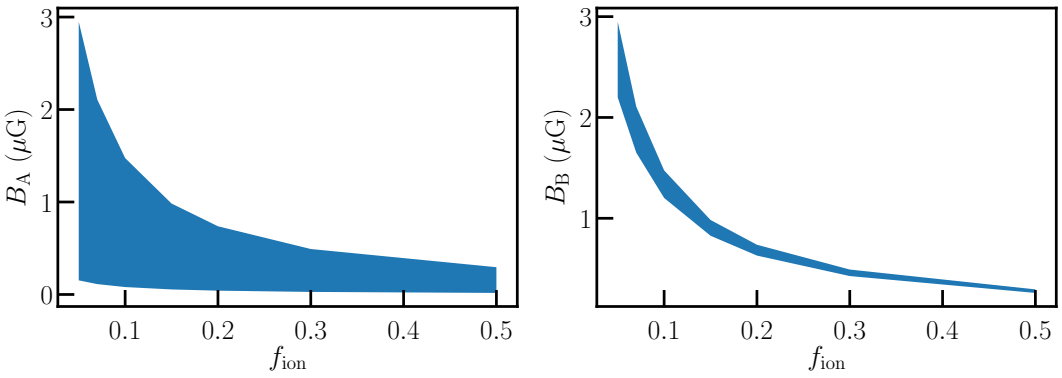

Figure I.1: The range of magnetic field strengths in the sightline of image A and image B calculated with different ionization fractions.

I.1.1 Ionization fraction

We change the ionization fraction ($f_{\rm ion}$) from 0.05 to 0.5 while keeping the other parameters in the MW parameter range. We find the magnetic field strength decreases exponentially with increasing ionization fraction (as in the case of higher $f_{\rm ion}$ more of the observed RM difference can be explained by high electron density instead of strong magnetic field). If we assume $f_{\rm ion} = 0.05$, the derived magnetic field strength can be ~ 10 times larger than with $f_{\rm ion} = 0.5$. We can see this effect even in our MW parameter range; the lowest value of $f_{\rm ion}$ (0.07) can result in B field strength ~ 2 times of the one calculated with its highest value ($f_{\rm ion} = 0.014$).

I.1.2 Electron column density at the position of image A

We change the electron column density at the position of image A ($N_{\rm e,A}$) from 1 – 100 $\rm pc\,cm^{-3}$, while keeping the other parameters in the MW parameter range. We set $f_{\rm ion}$ as 10 %, to exclude changes due to changes in the ionization fraction, as we saw in the previous point that a change in the ionization fraction can significantly affect our derived magnetic field strength. We find the lower range of magnetic field strengths at the position of image B decreases with higher $N_{\rm e,A}$: the B field strength can be three times lower in the case of $N_{\rm e,A} = 100\,\rm pc\,cm^{-3}$ compared to $N_{\rm e,A} = 1\,\rm pc\,cm^{-3}$. In the case of the B field strength at the position of image A, we do not find a strong dependence on $N_{\rm e,A}$, here the wide range is due to the different geometry models that give very different B field strengths.

I.1.3 Scale height

We change the scale height ($h_{\rm B,scale}$) from 2 to 20 kpc, while we have the MW parameter range for the other parameters, and set $f_{\rm ion}$ to 10 %. At the position of image B (0.7 kpc from the midplane), the scale height does not significantly affect the derived magnetic field strength, it only increases by a few (1 – 3) % from $h_{\rm B,scale} = 2$ kpc to 20 kpc. In the case of the location probed by image A (6.2 kpc away from the midplane),

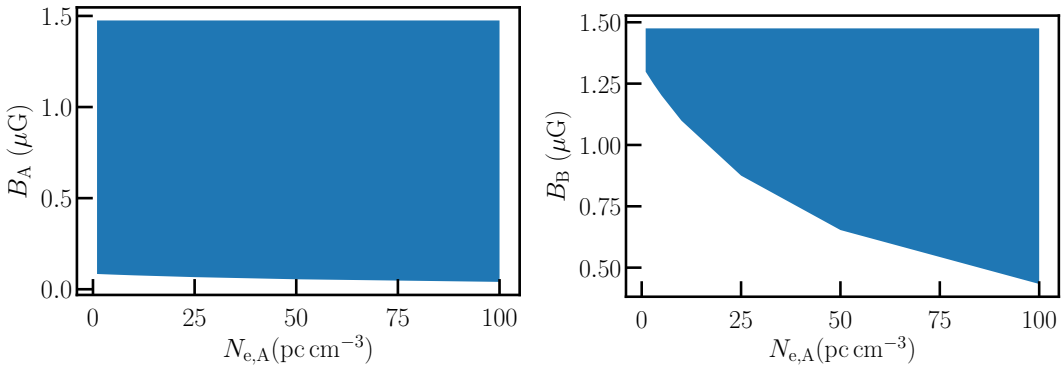

Figure I.2: The range of magnetic field strengths in the sightline of image A and image B calculated with different electron column densities assumed at the position of image A.

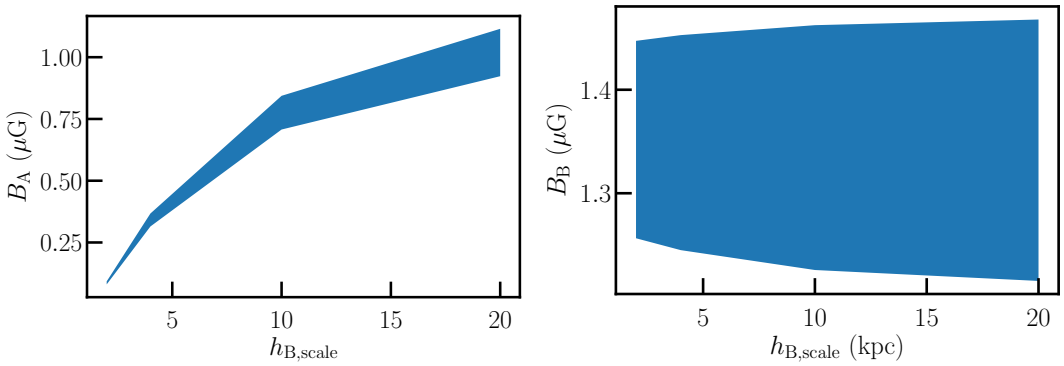

Figure I.3: The range of magnetic field strengths in the sightline of image A and image B calculated with different magnetic scale heights.

the effect is obviously larger: the magnetic field strength increases by a factor of ~ 10 from a $h_{\rm B,scale} = 2$ kpc to 20 kpc.

I.1.4 Inclination

We change the inclination (i) between 65° and 85°, while keeping other parameters in MW parameter range and setting $f_{\rm ion}$ to 10 %. We find that the derived magnetic field strengths increase with increasing inclination by a factor of ~ 5 from $i = 65°$ to $i = 85°$.

I.1.5 Summary of parameter effects

In summary, the assumed ionization fraction (by a factor of ~ 10) and the inclination of the galaxy (by a factor ~ 5) affect the derived magnetic field strengths the most. In the case of the position probed by image A, at 6.2 kpc from the midplane of the galaxy, the effect of the scale height is also significant (a factor of ~ 10).

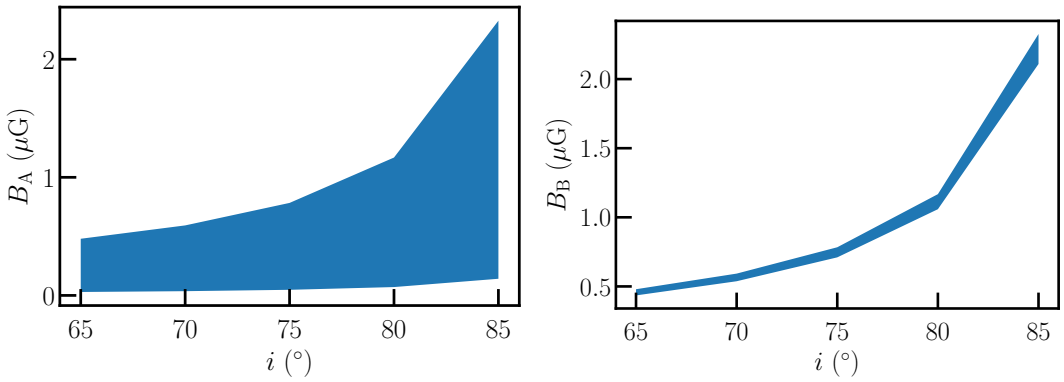

Figure I.4: The range of magnetic field strengths in the sightline of image A and image B calculated with different inclinations.

I.2 Choice of magnetic field geometry model

Considering our restricted parameter range of Milky Way like parameters, we see that the different models result in different magnetic field strengths (for the summary of the values, see Table 3.3).

The constant fields (both symmetric and antisymmetric) result in (absolute) magnetic field strengths of 1.2 – 1.8 μG at the positions probed by both images. The exponential models result in a field strength of 1.2 – 1.8 μG at the location of image B (0.7 kpc away from the midplane) and 0.1 – 0.9 μG at the location of image A (6.2 kpc away from midplane). The models with simple $1/h$ scaling also lead to 1.2 – 1.8 μG at the position probed by image B, but to a low 0.1 – 0.2 μG at the position probed by image A.

We conclude that all the models give consistent results in the case of the location probed by image B. In the case of the location probed by image A, the models give different results, which can be different by a factor of ~ 10. This difference is similar in magnitude to the variation that different parameter assumptions can cause. All derived magnetic field strengths are of a reasonable magnitude, thus it is not possible to exclude any of the models based on our data.

Appendix II

Appendix for Chapters 5 and 6

II.1 Inclination distribution of randomly oriented galaxies

The inclination distribution of randomly oriented galaxies is not uniform but $\sin(i)$ shaped. Even though some papers assume a uniform inclination distribution (e.g. Basu et al. 2018), this is incorrect in the case of a 3D galaxy, as we show in the following points:

1. Observational results of galaxies: Nearby spiral galaxies van den Bergh (1988) and galaxies in the Sloan Digital Sky Survey Hakobyan et al. (2012) follow a close to $\sin(i)$ distribution. Leslie et al. (2018) found a flat $\cos(i)$ distribution in the COSMOS survey.

2. Stellar inclinations: This distribution is also used for the inclination of stars (inclination here is the angle between the rotation axis and line-of-sight), as they assume the directional distribution of the rotational axes are random (Gray 1992; Sigut et al. 2020), similarly to our case with galaxies.

3. Inclination distribution of galaxies in IllustrisTNG50: If we calculate the inclination of galaxies in the simulation as the angle between the angular momentum vector and the line-of-sight, we find a $\sin(i)$ distribution.

4. Testing with the random rotation of a vector: If we generate a number of randomly oriented angular momentum vectors and place them in a box, the inclination distribution is the same independently of where we look at the galaxies (e.g. from inside the box). This gives the same distribution compared to the case of the inclination distribution of one galaxy rotated randomly many times, with the same line-of-sight ($\sin(i)$ distribution).

We rotate the galaxies in the simulation the following way (which results in a $\sin(i)$ distribution):

1. I define the inclination as the angle between the total angular momentum vector of the galaxy's stars and the line-of-sight. This angular momentum vector is perpendicular to the plane of the disk.

2. If the galaxy has a random orientation, this vector has an equal probability to point anywhere on a sphere surrounding this galaxy (imagining a sphere for every galaxy separately).

3. The probability of the inclination to be in a given range is proportional to the area of the sphere corresponding to the range of the angles (so for angles between i and i+di the area would be $2\pi * \sin(i) * \mathrm{d}i$).

4. This can be written as a PDF with sin(i) distribution of inclinations, which can be transformed into a uniform distribution in cos(i).

Appendix III

Paper: The dispersion measure and rotation measure from fast radio burst host galaxies based on the IllustrisTNG50 simulation

---

The paper Kovacs et al. (2023) that was submitted to A&A on the 13th of July is reproduced below in its original form.

Astronomy & Astrophysics manuscript no. output
July 13, 2023

The dispersion measure and rotation measure from fast radio burst host galaxies based on the IllustrisTNG50 simulation

Timea Kovacs[1], Sui Ann Mao[1], Aritra Basu[2,1], Yik Ki Ma[1,3], Ruediger Pakmor[4], Laura Spitler[1] and Charles R. H. Walker[1]

[1] Max-Planck-Institut für Radioastronomie, Auf dem Hügel 69, D-53121 Bonn, Germany
[2] Thüringer Landessternwarte, Sternwarte 5, D-07778 Tautenburg, Germany
[3] Research School of Astronomy & Astrophysics, Australian National University, Canberra, ACT 2611, Australia
[4] Max-Planck-Institut für Astrophysik, Karl-Schwarzschild-Str. 1, D-85748 Garching, Germany

Received XXX / Accepted YYY

ABSTRACT

Context. Fast radio bursts (FRB) will become important cosmological tools in the near future, as the number of observed FRBs is increasing rapidly with more surveys being carried out. Soon a large sample of FRBs will have available dispersion measures (DM) and rotation measures (RM), which can be used to study the cosmic baryon density and the intergalactic magnetic field (IGMF). However, the observed DM and RM of FRBs consists of multiple contributions which must be quantified to estimate the DM and RM of the intergalactic medium (IGM).
Aims. In this paper, we estimate one such contribution to DM and RM: that of FRB host galaxies. We show how this contribution changes with redshift, galaxy type, and the stellar mass of the galaxies. We also investigate its dependence on galaxy inclination, and on an FRB's offset from the center of the galaxy.
Methods. Using the IllustriusTNG50 simulations, we selected 16 500 galaxies at redshifts of $0 \leq z \leq 2$, with stellar masses in the range $9 \leq \log(M_*/\mathrm{M}_\odot) \leq 12$. In each galaxy, we calculate the DM and RM contributions of 1000 sightlines, and from these, construct DM and RM probability density functions.
Results. We find that the rest frame DM distributions of all galaxies at a given redshift can be fitted by a lognormal function, and its median and width increases as a function of redshift.The rest frame RM distribution is symmetric, with median $\mathrm{RM_{host,rf}}$=0 rad m^{-2}, and it can be fitted by the combination of a Lorentzian and two Gaussians. The redshift evolution of the distribution width can be fitted by a curved power law. The parameters of these functions change for different subsets of galaxies with different stellar mass, inclination, and FRB offset. These changes are due to an increasing n_e with redshift, SFR, and stellar mass, and we find a more ordered B field at lower z compared to higher z, suggested by more galaxies with B field reversals and B fields dominated by random B field at higher z.
Conclusions. We estimate the FRB host DM and RM contributions, which can be used in the future to isolate the IGM's contribution from the observed DM and RM of FRBs. We predict that to constrain an $\sigma_{\mathrm{RM,IGM}}$ of 2 rad m^{-2} to 95% confidence level we need to observe 95 000 FRBs at $z = 0.5$, but only 9 500 FRBs at $z = 2$.

Key words. magnetic fields– intergalactic medium – galaxies:ISM – ISM:general

1. Introduction

The seeds of intergalactic magnetic fields (IGMF) are an open question in astrophysics (Baym et al. 1996; Brandenburg & Subramanian 2005; Kahniashvili et al. 2012, 2013). They could be primordial (magnetic fields that already existed soon after the Big Bang), astrophysical (magnetic fields that were caused by galaxy evolution, e.g. feedback processes, star formation, active galactic nuclei), or both. The true scenario could also have implications on the dynamics of inflation (due to inflationary magnetogenesis, e.g. Ferreira et al. 2013; Vazza et al. 2021) and the physics of the early Universe. Recent measurements exclude purely astrophysical and purely primordial origins, and find an upper limit of ~ 4 nG on the co-moving magnetic field strength based on Cosmic Microwave Background (CMB) anisotropies (Planck Collaboration et al. 2016) and low-frequency radio observations with the Low-Frequency Array (LOFAR) of close pairs of extragalactic radio sources (O'Sullivan et al. 2020). Hackstein et al. (2016) found 0.1 nG magnetic field in voids based on the observed degree of isotropy of ultra high energy cosmic rays (UHECR, Sigl et al. 2003). Carretti et al. (2023) measured the magnetic field of filaments with LOFAR, and inferred an IGMF of 0.04–0.11 nG on Mpc scales. Many of these methods measure the magnetic field only in filaments, thus we have limited constraints on the low density Universe. Fast radio bursts (FRB) are a promising, unique tool for measuring the IGMF as they account for every ionized baryon along a line of sight (Akahori et al. 2016, Zheng et al. 2014).

FRBs are millisecond radio transients; some are one-off sources and some are confirmed repeaters. Since the first discovery by Lorimer et al. (2007), an increasing number of FRBs have been observed; for example, there are 118 unique FRB sources listed in the FRB catalogue by Petroff et al. (2016)[1], and the Canadian Hydrogen Intensity Mapping Experiment (CHIME) observed over 400 one-off FRBs (CHIME/FRB Collaboration et al. 2021). The Five-hundred-meter Aperture Spherical radio Telescope (FAST) observed 1652 bursts by one repeating FRB, FRB121102 alone (Li et al. 2021, Spitler et al. 2016).The most

[1] http://www.frbcat.org

complete catalogue is the Transient Name Server (Yaron et al. 2020).

FRBs experience propagation effects due to the intervening material they pass through, causing a dispersion in the observed pulse (Cordes & Chatterjee 2019), which is characterized by the dispersion measure (DM, see below for more details). Some FRBs are linearly polarized (~20 known to date), and thus also undergo Faraday rotation (Masui et al. 2015), which causes the angle of polarization to change upon passing through a magneto-ionic medium. This is characterized by the rotation measure (RM, see below for more details). The observed DM of FRBs (100 – 2600 pc cm^{-3}, based on the FRB catalogue, Petroff et al. 2016) are larger than expected due to the Milky Way material alone, suggesting they are extragalactic (Thornton et al. 2013). Recently, more and more FRBs have been localized to distant galaxies (see e.g. Chatterjee et al. 2017, Bannister et al. 2019, and Marcote et al. 2022). The |RM| of FRBs have a wide range from 1.5 to 10^5 rad m^{-2} (Petroff et al. 2019, Michilli et al. 2018). Unfortunately, many early FRB detections did not record polarization data, resulting in only a small sample of FRBs (~20) with measured RMs. In the future many surveys will also analyze the polarized signals of their detections (e.g. CHIME, Mckinven et al. 2021). Due to their extragalactic origin and high event rate (predicted to be $10^3 - 10^4$ per day over the whole sky above a fluence of ~2 Jy ms, Bhandari et al. 2018), FRBs can be used as cosmological probes. They can detect the baryonic content along the line-of-sight (LOS) into the distant Universe, and are a powerful tool of cosmic magnetism (e.g. IGMF, Akahori et al. 2016, Zheng et al. 2014), because they provide information on both DM and RM simultaneously. Furthermore, they provide a unique tool for the study of the missing baryons (McQuinn 2014), cosmological parameters (Macquart et al. 2015, Gao et al. 2014, Zhou et al. 2014), Hubble constant (H_0) measurements (James et al. 2022), the intergalactic medium (IGM), and the interstellar medium (ISM) of our or other galaxies (e.g. Mannings et al. 2022).

The DM is the integral of the free electron density (n_e [cm^{-3}]) along the LOS (l [pc]) from a source to the position of an observer:

$$\mathrm{DM} = \int_{\mathrm{source}}^{\mathrm{observer}} n_e \mathrm{d}l. \tag{1}$$

Because DM is an integral along the entire LOS, there are multiple contributors to the observed DM of FRBs ($\mathrm{DM_{obs}}$): the immediate source environment ($\mathrm{DM_{source}}$), the host galaxy ($\mathrm{DM_{host}}$), the IGM ($\mathrm{DM_{IGM}}$), and the Milky Way ($\mathrm{DM_{MW}}$). Thus the observed DM of a source at redshift z_{host} (i.e. $z_{\mathrm{source}} = z_{\mathrm{host}}$) can be described in the following way:

$$\mathrm{DM_{obs}} = \frac{\mathrm{DM_{source,rf}}}{(1+z_{\mathrm{host}})} + \frac{\mathrm{DM_{host,rf}}}{(1+z_{\mathrm{host}})} + \mathrm{DM_{IGM}} + \mathrm{DM_{MW}}, \tag{2}$$

where $\mathrm{DM_{source,rf}}$ and $\mathrm{DM_{host,rf}}$ are in the rest-frame, and can be converted to the observer's frame by the standard correction of $1/(1+z_{\mathrm{host}})$, because of the cosmological time dilation and the frequency shift. Below, we discuss the magnitude of the different components' DM contributions. There are many different FRB progenitor models, but the majority assume a connection to neutron stars (Platts et al. 2019).In the case of a young neutron star progenitor, the local environment of an FRB can be a supernova remnant (SNR), which theoretical models predict can result in a wide range of DMs (0.1 – 1000 pc cm^{-3}, Piro & Gaensler 2018). In the case of a magnetar, its near wind zone would only contribute 10^{-6} pc cm^{-3} to $\mathrm{DM_{source}}$ (Lyutikov 2022). $\mathrm{DM_{MW}}$ has contributions of the Milky Way and its dark matter halo. The DM from the Milky Way can be estimated from models based on Galactic pulsar measurements (e.g. NE2001: Cordes & Lazio 2002, YMW: Yao et al. 2017) and is usually below ~ 200 pc cm^{-3} at Galactic longitudes $|l| > 120°$, but can reach ~ 1700pc cm^{-3} at $|l| < 60°$. However, these lack the virialized dark matter halo with a hot gaseous atmosphere, which would give an additional contribution to the DM. Dolag et al. (2015) estimate this to be 30 pc cm^{-3}, but Keating & Pen (2020) suggest it could be as small as 10 pc cm^{-3}. The contribution of the host galaxy can vary from ~10 pc cm^{-3} to a few thousand pc cm^{-3} and depends on the galaxy type and FRB location (see e.g. Zhou et al. 2014, Walker et al. 2020, and Zhang et al. 2020). $\mathrm{DM_{IGM}}$ increases with redshift (Macquart et al. 2020), and Akahori et al. (2016) shows it can reach ~ 1000 pc cm^{-3} at z=1, and a few thousand pc cm^{-3} at z=5. However, its exact value can be different if the LOS goes through a dense region, e.g. a cluster or a filament.

Once we can isolate the DM contribution of the IGM, it can be an excellent tracer for the ionized cosmic baryon density (Akahori et al. 2016, Macquart et al. 2020). The majority of the baryonic content of the Universe is in a diffuse state, which is difficult to directly observe (Cen & Ostriker 1999, Kovács et al. 2019). Various techniques have been used previously to detect this component of baryonic matter: absorption studies of quasars (Nicastro et al. 2018), the Sunyaev-Zel'dovich effect (de Graaff et al. 2019) and direct X-ray observation of filaments (Eckert et al. 2015). Recently, Anderson et al. (2021) showed RM grid studies can also trace these baryons. However, absorption studies are more sensitive to lower temperature gas ($<10^5$ K), while X-ray measurements only detect hot ionized plasma (10^7 K), and the Sunyaev-Zel'dovich method can only study the gas in filaments, missing some of the baryons. On the other hand, FRBs are a powerful cosmological probe that considers every ionized baryon, both in the cold and hot (but not relativistic) media, as the DM of FRBs provides us with information about the electron column density along the full line-of-sight (McQuinn 2014; Macquart et al. 2020).

The RM of a source is defined similarly to DM, but the integral is weighted by the LOS component of the magnetic field ($B_\parallel$ [μG], parallel to the LOS):

$$\mathrm{RM} = k \int_{\mathrm{source}}^{\mathrm{observer}} B_\parallel n_e \mathrm{d}l, \tag{3}$$

where $k = 0.81\ \mu\mathrm{G}^{-1}$.

Similar to DM, the observed RM of a source at redshift z_{host} also consists of the components from the source ($\mathrm{RM_{source}}$), host ($\mathrm{RM_{host}}$), IGM ($\mathrm{RM_{IGM}}$), and the Milky Way ($\mathrm{RM_{MW}}$):

$$\mathrm{RM_{obs}} = \frac{\mathrm{RM_{source,rf}}}{(1+z_{\mathrm{host}})^2} + \frac{\mathrm{RM_{host,rf}}}{(1+z_{\mathrm{host}})^2} + \mathrm{RM_{IGM}} + \mathrm{RM_{MW}}. \tag{4}$$

where $\mathrm{RM_{source,rf}}$ and $\mathrm{RM_{host,rf}}$ are in the rest-frame, and can be converted to the observer's frame by the standard correction of $1/(1+z_{\mathrm{host}})^2$. $|\mathrm{RM_{source}}|$, considering again a neutron star progenitor, could be between 10^{-2} and 10^6 rad m^{-2} (Piro & Gaensler 2018). The near wind zone of magnetars can produce large RMs (magnitude of 10^5 rad m^{-2}, Lyutikov 2022), and the RM can vary greatly, even changing sign with time. The RM contribution of the MW can be estimated from all-sky Galactic RM maps (e.g. Oppermann et al. 2012; Hutschenreuter et al. 2022). $|\mathrm{RM_{MW}}|$ is below 150 rad m^{-2} in a large fraction of the sky, but can exceed 3000 rad m^{-2} towards the inner disk ($l \in (270°, 90°)$). The RM contribution of the host galaxy can vary widely depending on

the type of the host galaxy: Hackstein et al. (2019) showed the different $|RM_{host}|$ contributions from galaxy models of a Milky Way-like galaxy and a starburst dwarf galaxy, which can range from 10^{-4} to 10^{4} rad m^{-2}, and Hackstein et al. (2020) found an $|RM_{host}|$ contribution of ≤ 1000 rad m^{-2} using galaxy models from Rodrigues et al. (2019). Both Hackstein et al. (2019) and Akahori et al. (2016) show that $|RM_{IGM}|$ increases towards higher redshift, predicting it to be ≤ 10 rad m^{-2}. If we can isolate the contribution of the IGM from the other contributions in the observed RM, we can study the IGMF.

To be able to study the cosmic baryon density and the IGMF using the DM and RM measurements of FRBs, we need to constrain the other components, as they can all contribute significantly to the observed DM and RM mentioned above. In this paper, we focus on constraining the contribution of host galaxies. To do this, we calculated the DM and RM contribution of galaxies selected from the TNG50 simulation of the IllustrisTNG project (Pillepich et al. 2018, Nelson et al. 2019b), a state-of-the-art cosmological magnetohydrodynamic simulation, which contains thousands of galaxies at every redshift, of different types of galaxies, with relatively high resolution (70-140 pc), allowing us to provide good DM and RM estimates. We used 16.5 million sightlines to construct DM and RM Probability Density Functions (PDF) for different galaxy types to account for a large variety of possible FRB host galaxies.

This paper is organized as follows: in Section 2, we describe the simulation we used, our galaxy selection, and our DM and RM calculation methods. In Section 3, we show how the DM and RM distributions depend on different galaxy properties, for example, redshift, stellar mass, and inclination. In Section 4, we discuss the possible reasons behind the trends we show in Section 3 and compare our results to previous works. In Section 5, we investigate how the observed DM and RM of hosts changes with redshift, and its implications on measuring the RM of the IGM. In Section 6, we show an example of how we can estimate the host contribution of a localized FRB (using FRB190608). In Section 7, we summarize our findings.

2. Methods

In this section we summarize the TNG50 simulation of the IllustrisTNG project, we describe the selection process for our sample galaxies, and how we place FRBs within these galaxies. Finally, we show how we calculate the rest frame DM and RM host contributions of the galaxies.

2.1. TNG50

We have used IllustrisTNG, a state-of-the-art cosmological magnetohydrodynamical (MHD) simulation (Pillepich et al. 2018, Nelson et al. 2019b) to estimate the distribution of the DM and RM contribution of FRB host galaxies. The TNG project consists of three different simulation cubic volumes: TNG300, TNG100, and TNG50 with side lengtha of approximately 300, 100, and 50 Mpc, respectively. We chose TNG50-1 because it has the highest physical resolution compared to the TNG300 and TNG100, and the other subruns of TNG50: TNG50-2 etc. (Pillepich et al. 2019, Nelson et al. 2019a).

In these simulations, the physical resolution depends on the gas density, which results in higher resolutions and larger numbers of cells in high-density regions (e.g. galaxies), and lower resolutions and numbers of cells in the IGM. Since the DM and RM of FRBs are calculated as a LOS integral, passing through the galaxy as a pencil beam, we need the highest physical resolution possible for our study, as in reality both n_e and $B_{\parallel}$ can change on small scales (a few 10s of pcs) due to turbulence (Haverkorn et al. 2008). We want to calculate a DM and RM from n_e and $B_{\parallel}$ that are realistic on all scales, down to as small of a scale as possible. In the simulation volume of TNG50, the magnetic fields are also modeled with the highest physical resolution in cosmological MHD simulations at the moment: the average cell size is 70 – 140 pc in the star-forming regions of galaxies. In comparison, the mean cell size of star-forming cells is 355 pc in TNG100, and 715 pc in TNG300 (Nelson et al. 2019b), and 370 pc in zoom-in simulations of the Auriga galaxies (Grand et al. 2017). The magnetic field information in TNG50 was saved in 20 snapshots by the TNG team, and the redshifts of these snapshots that we used in our study are listed in Table 1.

Table 1. The number of galaxies selected at each redshift. All galaxies have a stellar mass ($\log(M_*/M_\odot)$) between 9 and 12.

z	$N_{\rm halos}$
0.0	1849
0.1	1834
0.2	1813
0.3	1752
0.4	1707
0.5	1695
0.7	1658
1.0	1607
1.5	1389
2.0	1208
3.0	676
4.0	301
5.0	105

2.2. Galaxy selection

The TNG50 simulation includes a large number of galaxies (also called 'subhalos'[2]) at various redshifts, from $z = 0$ to $z = 12$. These include a wide variety of galaxies, for example spiral galaxies and early-type galaxies. To be able to provide DM and RM contribution estimates for different possible FRB host galaxies, we assume that different types of galaxies with different properties could be a host to an FRB. How DM and RM depend on these properties is described in Sections 3 and 4. Due to computational limitations, we do not analyze every galaxy in the TNG50 simulation, but restrict our study to a subset of galaxies, which we describe below.

Of the 18 currently known FRB-hosts, 15 have $9 < \log(M_*/M_\odot) < 11$ (Heintz et al. 2020)[3]. We include galaxies with a stellar mass (M_*) in the range $\log(M_*/M_\odot) = 9 - 12$, so we not only can study normal spiral galaxies as possible hosts, but we can also account for possible future hosts with high masses, such as large elliptical galaxies.

The capabilities of current and near-future surveys are expected to be sensitive to FRBs up to a high redshift. For example the Parkes radio telescope and CHIME will detect FRBs up to a redshift of $z = 2$, while the Australian Square Kilometre Array Pathfinder (ASKAP) can detect FRBs up to $z = 1$ (predicted by Hackstein et al. 2020 using FRBPOPPY Gardenier 2019), and

[2] The friends-of-friends algorithm organizes the dark matter particles into halos, and the subfind algorithm separates the halos into subhalos.
[3] https://github.com/FRBs/FRBhostpage

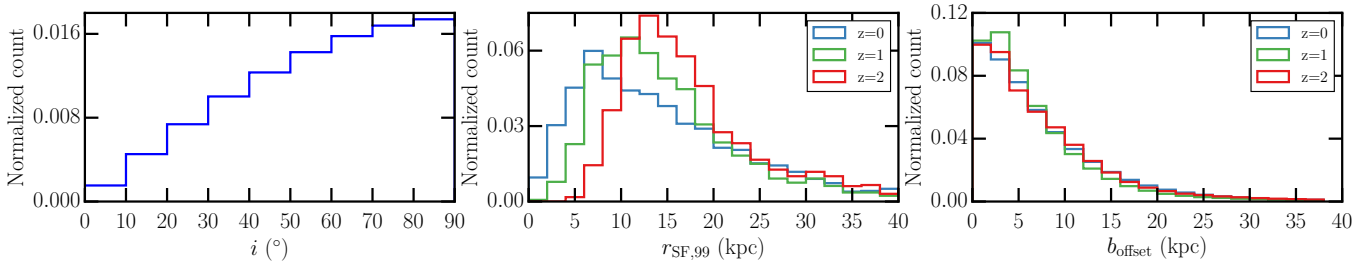

Fig. 1. Left: The inclination distribution of the galaxies, which is the same at every redshift. We define the inclination as the angle between the total angular momentum vector of the galaxy's stars and the LOS. **Middle:** The distribution of galaxy radii at different redshifts. This changes slightly with redshift, with larger radii at higher redshift. **Right:** The distribution of the projected offsets ($b_{\rm offset}$) of the FRBs with respect to the center of their host galaxy. There are more FRBs in the center of galaxies, and the distribution does not change significantly with redshift.

SKA-mid will also detect high redshift FRBs (Macquart et al. 2015). To date, the highest measured FRB host galaxy redshift is only $z = 0.66$ (Ravi et al. 2019). For FRBs without identified host galaxies we can only estimate the redshift based on their DM, however, this method is less certain, since the measured DM can have a significant contribution from the source environment and the host galaxy. Walker et al. (2020) constrained the redshift of unlocalised FRBs (from the FRB catalogue in 2020), accounting for uncertainties due to different potential host galaxies and progenitor scenarios, finding that in all cases the most probable redshifts are $z \leq 1.6$, except for one FRB for which it was $z \sim 2.5$. Therefore based on present and future observational capacities, we decided to constrain our sample to galaxies at $z \leq 2$.

In addition to these observational constraints, our choice of $z = 2$ as our upper redshift range is also due to the rapid falloff of the number of galaxies in the simulation beyond $z = 2$. This is as expected, because of hierarchical structure formation there are fewer massive galaxies at higher redshifts. We note that recent results from the *James Webb Space Telescope* might challenge this view. Ferreira et al. (2022) and Labbé et al. (2023) show the presence of massive galaxies and a higher rate of galaxy disks at earlier cosmological times than expected from the lambda cold dark matter (ΛCDM) model, which IllustrisTNG is based on. Our results at $z < 2$ should not be significantly affected, but at higher redshifts DM and RM might be higher in reality than our results from the simulation. At $z \leq 2$ there are more than 1000 galaxies per redshift with stellar mass $\log(M_*/{\rm M}_\odot) = 9 - 12$, vs. 676, 301, 105 at $z = 3, 4, 5$, respectively. We briefly investigate the overall redshift dependence of galaxies at these redshifts in Section 3, but do not include them in the statistical studies where we divide the galaxies/sightlines into groups.

We excluded satellite galaxies, which are defined as the galaxies that are not the most massive subhalos of their parent halo. Subhalos which are flagged by the simulation as unsuitable for most analysis were also left out from our study, as they are not of cosmological origin. These are defined as satellite galaxies that form within the virial radius of their parent halo, and their ratio of dark matter mass to total subhalo mass is less than 0.8 (Nelson et al. 2019b). Furthermore, we also excluded galaxies labeled with star formation rate (SFR) = 0 in the simulation output. These galaxies have an SFR below the SFR resolution limit of TNG50, 10^{-5} ${\rm M}_*$/yr. Other galaxy types that may be of interest to study are satellite galaxies and dwarf galaxies ($\log(M_*/{\rm M}_\odot)$<9), but these are not included in this paper.

In summary, we select galaxies from $z = 0$ out to $z = 2$, with $\log(M_*/{\rm M}_\odot)$ in the range of 9 – 12, resulting in a total of 16 500 galaxies (Table 1).

2.3. Positions of FRBs

Although there are many different possible progenitors of FRBs, recent evidence suggests some progenitors are likely young magnetars (Wang et al. 2020, CHIME/FRB Collaboration et al. 2020, Zanazzi & Lai 2020), which are typically found in star-forming regions (Bochenek et al. 2021).

We therefore place FRBs in our selected galaxies according to this paradigm, as follows. We define a radius for each galaxy that encloses 99% of the star-forming gas of the subhalo ($r_{\rm SF,99}$). Fig. 1 (middle) shows the distribution of $r_{\rm SF,99}$ at different redshifts are, with slightly larger radii at higher redshifts, where the star-forming gas is not yet confined to the inner parts of the galaxies. We then randomly select 1000 gas cells inside this radius, which we adopt as the positions of our FRBs. As the physical resolution of the simulations is adaptive, this means we have more FRBs in denser regions of the galaxies, closer to regions where magnetars could be found, and most FRBs are in the disk. In Fig. 1 (right) we show the distribution of the projected offset of FRBs from the center of their host galaxies ($b_{\rm offset}$), and we show three example illustrations of $b_{\rm offset}$ in galaxies with different inclinations in Fig. 2. These distributions do not change significantly with redshift. We point out that among the current sample of FRBs that have been observationally localized, the FRB with the smallest $b_{\rm offset}$ is at 0.6 ± 0.3 kpc (Heintz et al. 2020) and the FRB with the largest $b_{\rm offset}$ is at 27.2 ± 22.6 kpc (Bhandari et al. 2022) away from the center of their host galaxies (where the errors are due to the uncertainties of the localization of the FRBs). This is consistent with our resulting range of $b_{\rm offset}$. We note that different progenitors could have different spatial distribution in galaxies (see e.g. Walker et al. 2020; Mo et al. 2023).

2.4. Inclination of galaxies

We assume that galaxies are randomly oriented with respect to the line of sight. To ensure this, first we rotate each galaxy to face-on view, by rotating the total angular momentum vector of its stars ($\boldsymbol{L}$, which is perpendicular to the plane of the galaxy) to point to the observer. Then for each galaxy, we generate 1000 random rotation matrices using Fast Random Rotation Matrices (Arvo 1992), so that for each FRB position, the same galaxy has a unique orientation. After the rotations, the total angular momentum vectors are uniformly distributed on a sphere. We define the inclination as the angle between the total angular momentum vector and the line-of-sight, and we show three example illustrations of different inclinations in Fig. 2. Multiple orientations can result in the same inclination. An example of the distribution of the inclinations is shown in Fig. 1 (left). The magnetic field

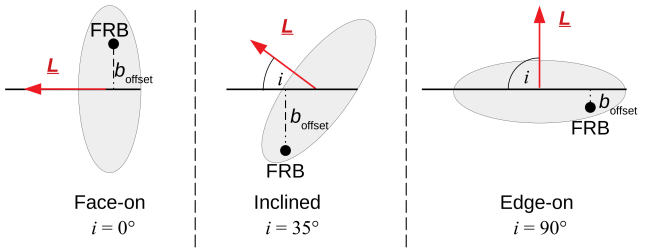

Fig. 2. Illustration of the inclinations of host galaxies and the projected distance of FRBs from the center of the host galaxy ($b_{\rm offset}$), showed for face-on, inclined, and edge-on galaxies. The observer is on the left side. The total angular momentum vector of the host galaxy ($\boldsymbol{L}$) is perpendicular to the plane of its disk. The inclination is the angle between the line of sight and $\boldsymbol{L}$. The filled circles indicate the positions of the FRBs.

vectors and the position vectors of the cells of the galaxies are rotated by the same matrices.

2.5. Conversion of the simulation units

Following the recommended procedures for the TNG data (Nelson et al. 2019b), we convert from comoving units (coordinates of cells, gas density, magnetic field strength, masses) to physical units using the scale factor (a) and the Hubble parameter (h). We can obtain kpc from comoving kpc (ckpc) via:

$$1\mathrm{kpc} = 1\mathrm{ckpc}/h \cdot a. \tag{5}$$

After this, the density and magnetic field are converted to CGS units from the physical units in the simulation:

$$\rho[\mathrm{g\,cm^{-3}}] = 6.8 \cdot 10^{-22} \rho_{\rm sim}[10^{10} M_\odot\,\mathrm{kpc^{-3}}], \tag{6}$$

and

$$B[\mu\mathrm{G}] = 2.6 \cdot B_{\rm sim}[(10^{10}\mathrm{M_\odot/kpc})^{1/2} \cdot (\mathrm{km/s})/\mathrm{kpc}]. \tag{7}$$

2.6. Calculating n_e

The ionisation in the simulation that sets n_e is computed as the equilibrium state given radiative cooling and heating from the UV background and nearby AGN. The electron density (n_e) must be calculated differently for star-forming and non star-forming cells (where SFR = 0 $\mathrm{M_\odot/yr}$, i.e. below the SFR resolution of the simulation). For non star-forming cells, it can simply be computed from the electron abundance ($e_{\rm ab}$, the fractional electron number density with respect to the total hydrogen number density) and the hydrogen number density ($n_{\rm H}$):

$$n_e[\mathrm{cm^{-3}}] = e_{\rm ab} \cdot n_{\rm H}. \tag{8}$$

$e_{\rm ab}$ is available in the IllustrisTNG particle data. However, $n_{\rm H}$ has to be calculated using the total gas density of the cells (ρ):

$$n_{\rm H}[\mathrm{cm^{-3}}] = \rho \cdot X_{\rm H}/m_{\rm p+}, \tag{9}$$

where we assume the fraction of hydrogen to be $X_{\rm H} = 0.76$ (based on the initial conditions of TNG, Pillepich et al. 2018), and $m_{\rm p+}$ is the mass of a proton.

For star-forming cells, we must consider the sub-grid model for star formation and the multi-phase interstellar medium used by the simulation (Springel & Hernquist 2003). Following Springel & Hernquist (2003) (see also e.g. Pakmor et al. 2018, Zhang et al. 2020) we calculate n_e assuming each cell's interstellar medium consists of volume-filling hot ionized gas ($T \sim 10^7$ K) and small neutral cold clouds ($T \sim 10^3$ K), that our sightlines do not cross the cold clouds, and the temperature in the warm phase is hot enough to fully ionize hydrogen and helium.

Then by finding the mass fraction of the warm gas ($x_{\rm warm}$), and assuming it is 100% ionized:

$$n_e[\mathrm{cm^{-3}}] = x_{\rm warm} \cdot [X_{\rm H} + (Y_{\rm He}/4 \cdot 2)] \cdot \rho/m_{\rm p+}, \tag{10}$$

where $Y_{\rm He}$ (the fraction of helium) is 0.23. We note that the n_e calculated using this subgrid model might be uncertain by a factor of 2–3, but a better estimate would require resolving the ISM. Pellegrini et al. (2020) presented a new method of postprocessing galaxies from MHD simulation to obtain better estimates on the small-scale ISM properties by including stellar clusters and their impact on the ISM. Comparing their radial and vertical profiles of $n_{\rm e}$ with a single galaxy from the Auriga simulations, they found that n_e can vary by a factor of 2 lower or higher in different parts of the galaxy compared to when computed using Eq. 10. We argue that because for most sightlines we integrate across a large part of the galaxies, these differences would average out, and our DMs and RMs are not affected significantly.

2.7. Calculating DM and RM

The DM is the line-of-sight integral of the electron density (n_e). For a given sightline in the simulation, we compute this by replacing the integral with a discrete sum between the FRB position in the inclined galaxy and $r_{\rm SF,99}$ of the galaxy. We use N steps of dl=20 pc stepsize, and the integration takes the closest cell to the position on the sightline in every step:

$$\mathrm{DM} = \sum_{i=0}^{N} n_{e,i}\mathrm{d}l, \tag{11}$$

where i is the index for the N steps and $n_{e,i}$ is the electron density at each step. We also assume that the origin of the FRB is a point source, and its emission originates from scales smaller than 20 pc. For a discussion on the effect of different parameter choices (integral length, integral stepsize, number of rotations), see Appendix B.

The RM is calculated similarly as DM:

$$\mathrm{RM} = k \sum_{i=0}^{N} B_{\parallel,i} n_{e,i}\mathrm{d}l, \tag{12}$$

where $B_{\parallel,i}$ is the line of sight magnetic field at each step. The same parameter tests were performed as during DM calculations (see Appendix B).

2.8. Pipeline summary

In summary, we selected 16 500 galaxies, rotated each to a random inclination 1000 times and randomly chose 1000 FRB positions in each galaxy. Then we calculated the DM and RM contribution by the host galaxy for each FRB sightline.

For each sightline we save the galaxy ID, the position of the FRB, the n_e of that cell, the calculated DM and RM, and the used rotation matrix. For each galaxy we save the stellar mass, star formation rate, $r_{\rm SF,99}$, the properties of its magnetic field (average total magnetic field of the disk, and the average of its components – azimuthal, radial and vertical), and the radial and vertical profile for the magnetic field and its components (for details see Appendix D). We also calculate these profiles for n_e and ρ.

3. Results

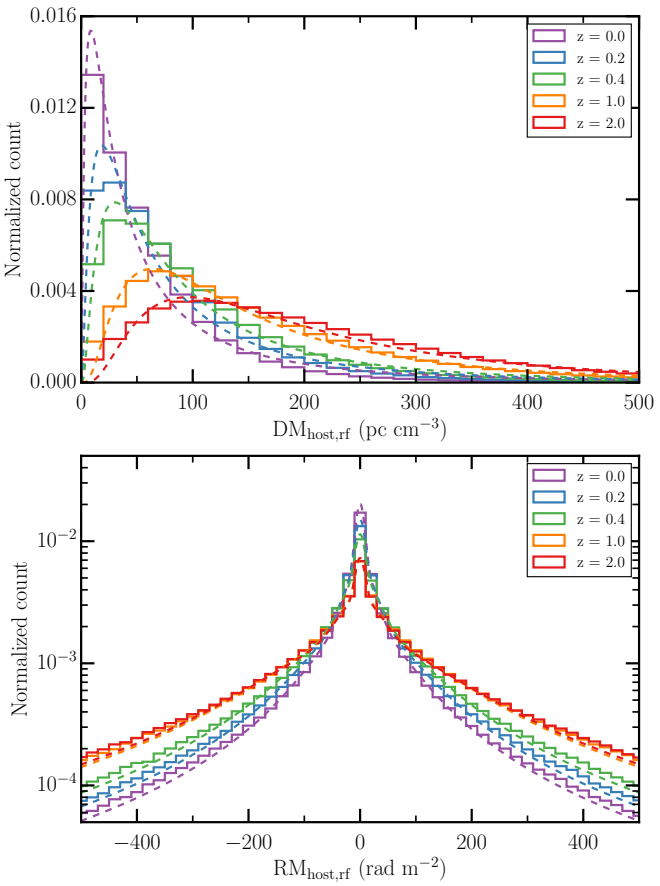

Fig. 3. Top: The PDF of the rest frame DM contribution of host galaxies, using FRBs at different redshifts. The distributions are lognormal, with a long positive tail. The fits are shown by the dashed lines, and the colors correspond to the different redshifts. The PDFs become broader at higher redshifts, with larger possible DM values. **Bottom:** The PDF of the rest frame RM contribution of host galaxies, using FRBs at different redshifts. The distributions are symmetric with a sharp peak at 0 rad m^{-2}, similar to a Lorentzian. The fits are shown by the dashed lines, and the colors correspond to the different redshifts. The PDFs become broader at higher redshifts up to $z = 1$, with larger RMs. After $z = 1$, the distributions do not change significantly.

In this section, we calculate the DM$_{\rm host,rf}$ and RM$_{\rm host,rf}$ PDFs[4] for different subsets of galaxies, and investigate how the properties of these distributions change with redshift. First we show the redshift dependence of the full sample, then the differences between star-forming and red galaxies (i.e. 'quenched'), and how the distributions change with stellar mass. Assuming we also have information about the inclination of observed host galaxies, or the $b_{\rm offset}$ of the FRB from the center of the galaxy, we also provide PDFs for different inclinations and offsets. Finally, we also investigate if the overall redshift evolution of DM$_{\rm host,rf}$ and RM$_{\rm host,rf}$ up to z=5 is well described by our fits for hosts below z=2. We discuss the possible reasons behind these trends in Section 4.

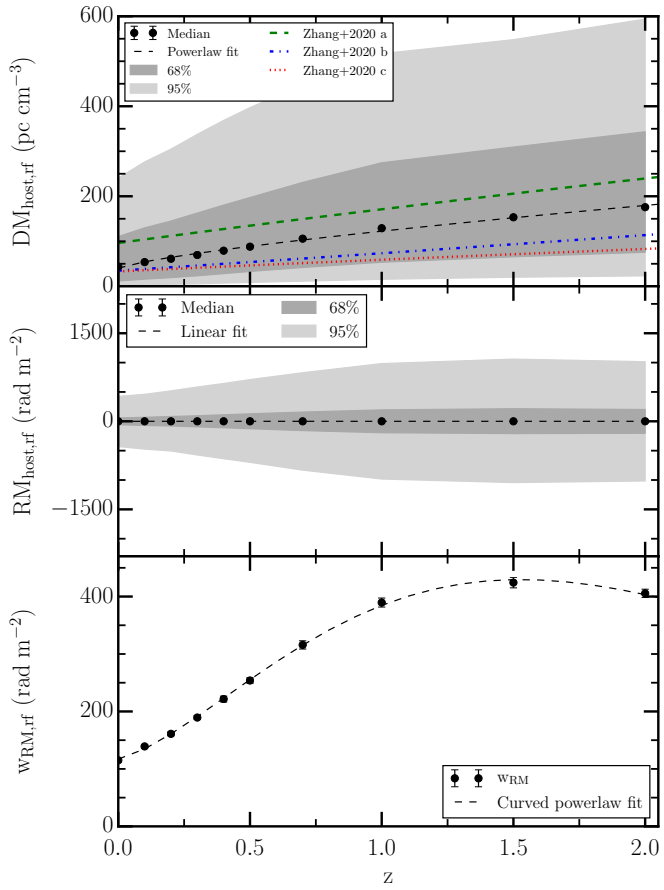

Fig. 4. Top: The median of DM$_{\rm host,rf}$ increases at larger redshifts. The shaded regions correspond to the 1σ and 2σ width of the distributions. This relation can be fitted by a power law. For comparison we also plotted the results from Zhang et al. (2020), in the case of host galaxies like the host of FRB180916 (a), galaxies similar to the hosts of non repeating FRBs (b) - hosts known at the time of Zhang et al. (2020)'s paper, and galaxies similar to the host of the repeating FRB121102 (c). For further details on the comparison see Section 4.3.1. **Middle:** The median of RM$_{\rm host,rf}$ stays the same at all redshifts. The shaded regions correspond to the 1σ and 2σ width of the distributions, which increases until $z = 1$. **Bottom:** The 1σ width of the distributions of RM$_{\rm host,rf}$ increases at larger redshifts, but it stays the same after $z = 1$. This relation can be fitted by a curved power law (black dashed line). The errors are from the bootstrap method.

3.1. Redshift evolution of DM$_{\rm host,rf}$ and RM$_{\rm host,rf}$

We show the PDFs of DM$_{\rm host,rf}$ and RM$_{\rm host,rf}$ individually for each redshift, explore their functional forms and investigate how their parameters change across redshift. We provide these functional forms in the paper for easier application. The PDFs for redshifts 0.0, 0.2, 0.4, 1.0, and 2.0 are shown in Fig. 3. We only show the PDFs for half of the snapshots in our analysis to make the plot clearer, but we will show below that the parameters of the distributions change smoothly with redshift. We calculate the PDFs individually for each redshift, and for each PDF we take into account the DM and RM of every FRB at the given redshift.

We found that the PDF of DM$_{\rm host,rf}$ can be described by a lognormal distribution:

$$f_{\rm DM,host}(x) = \frac{1}{\sqrt{2\pi}x\sigma} \exp(-(\ln(x) - \mu)^2/(2\sigma^2)), \quad (13)$$

[4] All histograms presented in this work have been normalized to unit area.

parametrized with μ and σ, which are the mean and standard deviation of the DM's natural logarithm, and not the DM itself.

We find broader distributions at higher redshifts. We note that other distributions that can be fitted to the data include the gamma function, however this overestimates the 16th percentile by a factor of 4. The median of DM also increases with redshift, following a power law:

$$\text{median DM}_{\text{host,rf}}(z) = a \cdot z^b + c, \tag{14}$$

with fitting parameters (a, b, c, see in Table A.1). The difference between the median of the actual PDF and the median from the lognormal fit ($\exp(\mu)$) is below 10 pc cm^{-3} at all redshifts. We define the 1σ width of the distribution as the difference between the 84th and 16th percentile ($w_{\text{DM,rest}}$). The $w_{\text{DM,rest}}$ also increases with redshift, and its redshift evolution can also be fitted by Eq. 14, with fitting parameters listed in Table A.1. We note that the tail of the distribution is slightly overestimated by the lognormal fit The μ and σ parameters of the fitted PDFs also change with redshift, we find they are better described by an exponential function:

$$\mu(z) = A_{\text{DM},\mu} \exp(-B_{\text{DM},\mu} z) + C_{\text{DM},\mu}, \tag{15}$$

$$\sigma(z) = A_{\text{DM},\sigma} \exp(-B_{\text{DM},\sigma} z) + C_{\text{DM},\sigma}, \tag{16}$$

where A_{DM}, B_{DM} and C_{DM} are the parameters of the fit (see Table A.2). We note that the difference of best fit function form (exponential instead of power law) is due to the fact that μ and σ are related to the variable's natural logarithm.

We find that the PDF of $\text{RM}_{\text{host,rf}}$ (shown in Fig. 3 bottom) is symmetric, with both peak and median at RM = 0.00 ± 0.03 rad m^{-2} at every redshift. It can be fitted by the sum of one Lorentzian and two Gaussian functions, similar to the results of Basu et al. (2018) (for more details see Section 4):

$$f_{\text{RM,host}}(x) = a_1 \cdot \left[\frac{\gamma^2}{\pi\gamma(\gamma^2 + x^2)}\right] + a_2 \exp\left[-\frac{1}{2}\left(\frac{x}{\sigma_1}\right)^2\right] + a_3 \exp\left[-\frac{1}{2}\left(\frac{x}{\sigma_2}\right)^2\right], \tag{17}$$

where a_1, a_2 and a_3 are normalization fractions, γ is the parameter of the Lorentzian function, and σ_1 and σ_2 are parameters of the Gaussian functions. We note that the exact definition of the function is different from that of Basu et al. (2018), for example we did not define a variable for the mean, but assumed it to be 0 rad m^{-2}. We also experimented with a purely Lorentzian fit, and different combinations of Gaussian and Lorentzian fits, but the combination from Basu et al. (2018) captured the long tails and peak of the distribution best.

We find that the RM distribution becomes broader with redshift, up to $z = 1$, where it flattens, and turns over at $z = 2$. The 1σ width of the distributions ($w_{\text{RM,rest}}$, containing 68% of the data) as a function of redshift can be fitted by a curved power law:

$$w_{\text{RM,rf}}(z) = A_{\text{RM}} \cdot z^{D_{\text{RM}} + B_{\text{RM}} \cdot z} + C_{\text{RM}}, \tag{18}$$

and the fitted parameters (A_{RM}, B_{RM}, C_{RM} and D_{RM}) are in Table A.1. We estimate the uncertainty of $w_{\text{RM,rf}}$ with the bootstrapping method. $w_{\text{RM,rf}}$ can also be fitted by a broken power law, but the curved power law has the advantage of the fit changing more smoothly, without a sharp peak. We use the curved power law for the remainder of the paper.

We find that the parameters of the fitted RM PDFs (a_1, a_2, a_3, γ, σ_1, and σ_2) also change as curved power laws. Apart from the normalization parameters of the Gaussian components (a_1 and a_2), all parameters increase towards higher redshift. We list the results of the fits in Table A.3. The 1σ width of the fitted PDFs differs from that of the real PDFs by less than 20 rad m^{-2}.

If the redshift of an FRB is known, the relations above can be used to derive the possible $\text{DM}_{\text{host,rf}}$ and $\text{RM}_{\text{host,rf}}$ contribution.

3.2. $\text{DM}_{\text{host,rf}}$ and $\text{RM}_{\text{host,rf}}$ in star-forming and red galaxies

The structure and properties (e.g. SFR, stellar mass) of star-forming spiral and red elliptical galaxies are different (see e.g. Conselice 2014 for a review), and their electron densities and magnetic field strength and structure can also differ: ellipticals might have weaker large-scale fields because they lack a differentially rotating disk (Beck 2012). Considering this, we would expect the DM and RM contribution of these galaxies to also be different. It is relatively easy to separate them observationally based on their color–magnitude diagram (Bell et al. 2004), which means FRB host galaxies could easily be divided based on this property in the future.

To separate them in the simulation we adapt a method from Donnari et al. (2019), who derived the Main Sequence (MS) of galaxies in TNG100. We describe this in Appendix C. The MS is a tight relation between the stellar mass and SFR of star-forming galaxies based on observations (e.g. Noeske et al. 2007), and this relation also scales with redshift.

We separated the galaxies based on the MS, and in Fig. F.2 we show the DM and RM distributions of quenched and star-forming galaxies at z=0.5. In the top panels of Fig. 5 and Fig. 6, we show how the median DM and the RM distribution width ($w_{\text{RM,rf}}$) changes with redshift, respectively. We fit the former with a power law and the latter with a curved power law. At high redshifts ($z \geq 1.5$), we have fewer than ten quenched galaxies in a redshift bin. Because of this, the trends at high redshift for quenched galaxies can not be seen clearly.

We find that quenched galaxies have a lower median DM and RM contribution on average, compared to star-forming galaxies. Star-forming galaxies have a wider DM and RM distribution, and a larger median DM. The same trend can be seen at all redshifts.

Both the DM and RM PDFs of star-forming galaxies closely follow the DM and RM PDF of all galaxies, as most of the sampled galaxies are star-forming (97% in total, with 95% at z=0 and 99% at z=2). To test if the different distribution shape is caused by the small sample size of the quenched galaxies, we randomly selected the same number of galaxies from the star-forming sample as there are in the quenched sample. The resulting DM and RM PDFs also closely resemble the PDFs of all star-forming galaxies, suggesting the quenched galaxies have a different PDF unrelated to the sample size.

3.3. $\text{DM}_{\text{host,rf}}$ and $\text{RM}_{\text{host,rf}}$ in different stellar mass bins

We investigate how the properties of the DM and RM PDFs change if we separate the sightlines by the stellar mass of the host galaxies. We divided the galaxies into five stellar mass bins at each redshift (the bins are listed in Table A.1) and constructed PDFs for each group.

We show an example of these DM and RM PDFs for galaxies at z=0.5 in Fig. F.1. The shapes of the distributions are the same as the ones for the full sample; the DM distributions are log-normal, and the RM distributions are Lorentzian-like. While the

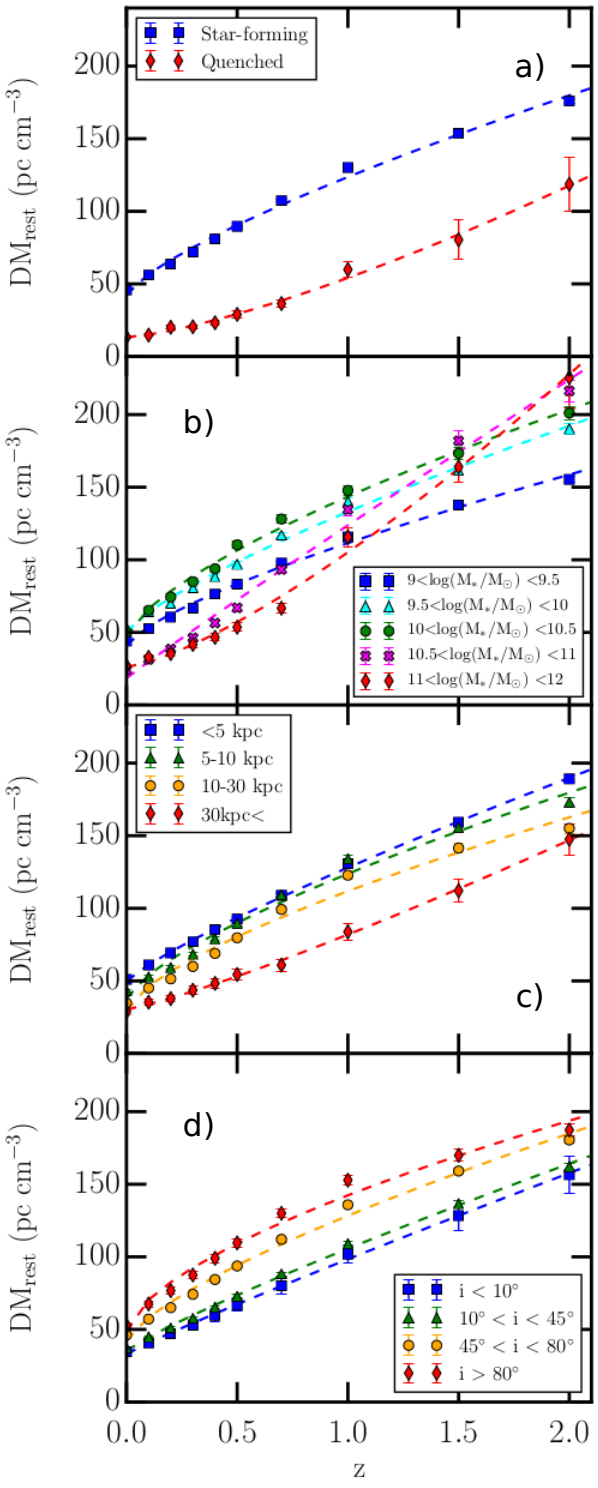

Fig. 5. The redshift evolution of median $DM_{host,rf}$ of different subsets of galaxies. A power law can be fitted to each group. The error bars are from bootstrapping. **a**: Quenched and star-forming galaxies. **b**: Different stellar mass bins. **c:** Sightlines with different inclinations. **d**: Sightlines with different b_{offset}.

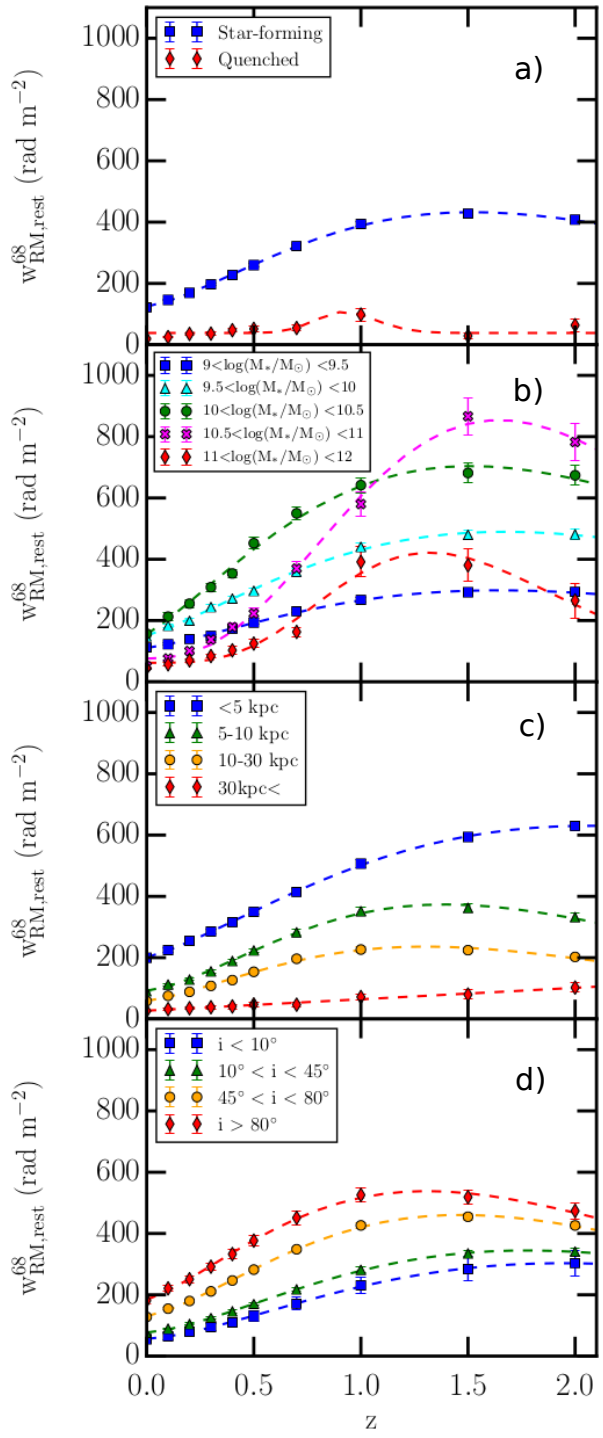

Fig. 6. The redshift evolution of the width of the rest frame RM distribution ($w_{RM,rest}$) of different subsets of galaxies. A curved power law can be fitted to each group. The error bars are from bootstrapping. **a**: Quenched and star-forming galaxies. At high z we only have a few (<10) quenched galaxies, which makes it difficult to obtain a good fit. **b**: Different stellar mass bins. **c:** Different inclinations. **d:** Sightlines with different b_{offset}.

shape of the PDFs remains the same, the parameters of the PDFs change with stellar mass. We show these changes in Fig. 7 a) and d). The median of DM increases linearly with stellar mass, up to very high mass galaxies ($\log(M_*/M_\odot) > 10.6$). But for galaxies with very large stellar masses the PDF becomes narrower, the median DM drops significantly, and the RM distribution width ($w_{RM,rf}$) also follows the same trend. This can be seen at every redshift, but for $z > 1$ the drop occurs at a larger stellar mass $\log(M_*/M_\odot) > 11$). The $w_{RM,rf}$ decreases linearly after the drop at every redshift. The median DM does not always follow this trend.

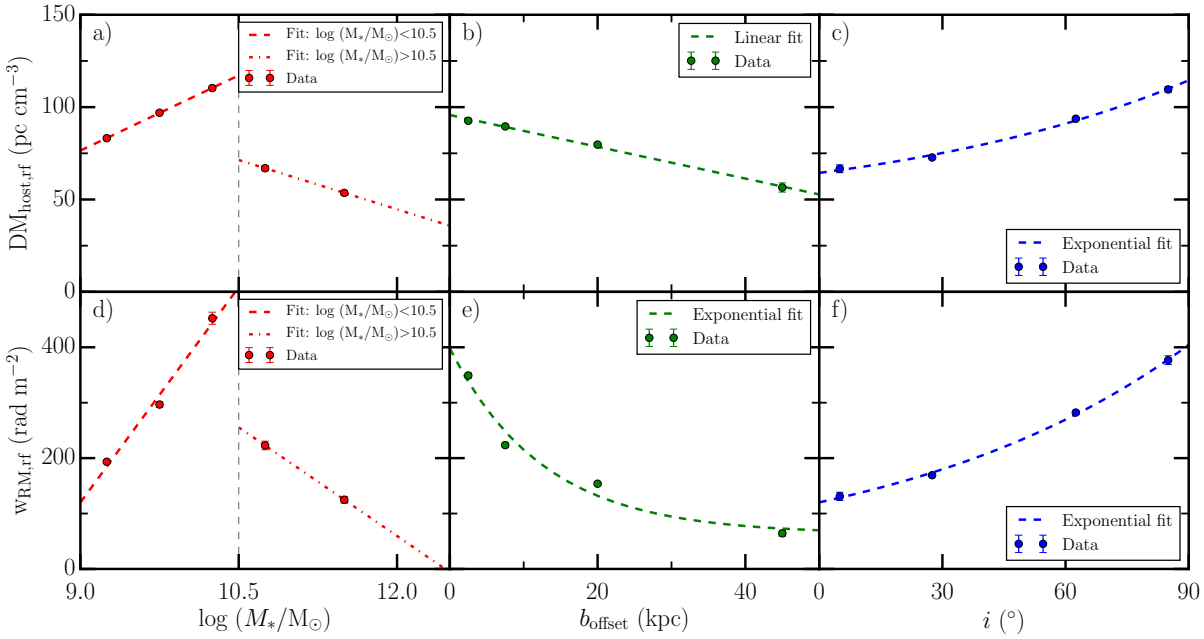

Fig. 7. The top row shows how the median $DM_{host,rf}$ changes as a function of stellar mass, b_{offset} and galaxy inclination. The bottom row shows the same for the $RM_{host,rf}$ distribution width ($w_{RM,rf}$). This figure shows these trends for galaxies at z=0.5. **Left column:** The median $DM_{host,rf}$ and $w_{RM,rf}$ linearly increases with stellar mass, but suddenly drops for galaxies with very high stellar masses ($\log(M_*/M_\odot) > 10.5$), and after that linearly decreases with increasing stellar mass. **Middle column:** The median $DM_{host,rf}$ decreases linearly, and the $w_{RM,rf}$ decreases exponentially with b_{offset}. **Right column:** The median $DM_{host,rf}$ and $w_{RM,rf}$ increases exponentially with host galaxy inclination.

In panel b) of Figs. 5 and 6 we show that the median DM and $w_{RM,rf}$ of the different stellar mass bins as a function of redshift can be fitted by a power law and a curved power law, respectively. The fit parameters for the different stellar mass bins can be found in Table A.1. The difference between the fits are more visible in the case of RM. For galaxies below $\log(M_*/M_\odot) = 10.5$, the exponents are similar, but the scaling parameters are higher at higher stellar mass. For massive galaxies, the exponents are also different. At low redshifts (z<0.2), the galaxies with lower stellar mass have a higher median DM and $w_{RM,rf}$ than galaxies with larger masses.

3.4. $DM_{host,rf}$ and $RM_{host,rf}$ at different inclinations

We expect $DM_{host,rf}$ and $RM_{host,rf}$ contributions to differ for face-on vs. edge-on hosts. For edge-on galaxies, we expect sightlines to propagate through more ISM, resulting in higher DMs and affected RMs. In real observations, if a host galaxy is identified and assumed to be a circular disk galaxy, its inclination can be measured by the ratio of its major and minor axis. For our TNG50 galaxy sample, we define the inclination angle as the angle between the total angular momentum vector of the galaxy's stars and the line of sight (see Section 2).

We divide the galaxies into four inclination bins, which are listed in Table A.1, and their DM and RM distributions at z=0.5 are shown in Fig. F.3. The distributions for galaxies at other redshifts can be found in Appendix G.

We find that the median DM increases exponentially with inclination, shown in Fig. 7 c): face-on galaxies ($i < 10°$) have a smaller median DM than galaxies with larger inclinations ($10° < i < 80°$), while edge-on galaxies ($i > 80°$) have the highest DM range (larger by a factor of ~ 2 compared to face-on galaxies). The same trends are found at all other redshifts (see Appendix G).

In Fig. 7 f) we also see the RM distribution width ($w_{RM,rf}$) increasing exponentially with galaxy inclination: edge-on host galaxies have an $w_{RM,rf}$ a factor of ~ 4 larger compared to face-on galaxies. The increase with inclination can be seen at every redshift (see Appendix G), but at $z \geq 1.5$, the increase is only linear in contrast to the exponential increase at $z < 1.5$.

The median DM and $w_{RM,rf}$ from each inclination group can be fitted by a power law and a curved power law, respectively, as a function of redshift. The fits can be found in Figs. 5 and 6, and the fitted parameters are listed in Table A.1.

3.5. $DM_{host,rf}$ and $RM_{host,rf}$ at different FRB b_{offset}

We expect both n_e and B field to change as a function of distance from the center of the galaxy (see e.g. Beck 2007 regarding how the energy densities of magnetic fields and ionized gas decrease with radius in NGC6946). As a result, the DM and RM distributions can also be affected. We define the projected offset (b_{offset}) as the projected distance of the FRB position from the center of the galaxy, which should be readily available for well-localized observed FRBs. Therefore, we investigate how $DM_{host,rf}$ and $RM_{host,rf}$ distributions are affected by b_{offset}.

In Fig. F.4 we show the distributions of $DM_{host,rf}$ and $RM_{host,rf}$ with different FRB offsets for galaxies at $z = 0.5$. We find that the median $DM_{host,rf}$ and the RM distribution width ($w_{RM,rf}$) decrease with larger FRB offsets. In Fig. 7 b), we show that the median of DM decreases linearly, and in Fig. 7 e) we see how $w_{RM,rf}$ decreases exponentially. The magnitude of the change from $b_{offset} = 0$ kpc to $b_{offset} = 50$ kpc is more significant in the case of $w_{RM,rf}$ (decrease by a factor of ~8), compared to the median $DM_{host,rf}$ (factor of ~2).

The median $DM_{host,rf}$ and $w_{RM,rf}$ of the sightlines in the different offset bins may also be fitted by a power law and broken power law as a function of redshift, as shown in Figs. 5 and 6 (d). The fitted parameters are listed in Table A.1. The exponents

stay similar for all offset bins, but the scaling changes more significantly from the smallest to the largest offset bin: a factor of ∼1.5 in the case of DM, and ∼7 in the case of RM.

3.6. $DM_{host,rf}$ and $RM_{host,rf}$ above z=2

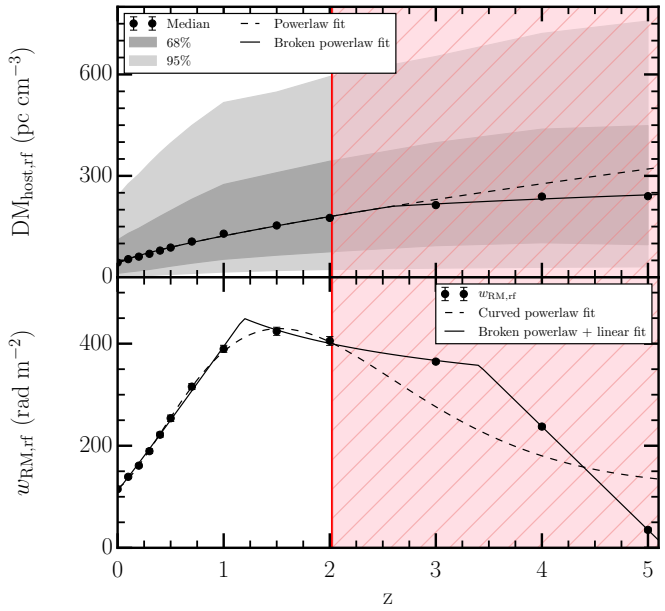

Fig. 8. Top: The median $DM_{host,rf}$ as a function of redshift, including FRBs at $3 \leq z \leq 5$. These high redshift sightlines are not included in the further analysis, indicated by the red hashed pattern. $DM_{host,rf}$ at $z \geq 3$ changes differently compared to our fit based on sightlines in galaxies at $z \leq 2$ (black dashed line). It increases more slowly, and can be fitted by a broken power law (black solid line). **Right:** The $RM_{host,rf}$ distribution width ($w_{RM,rf}$) as a function of redshift, including FRBs at $3 \leq z \leq 5$. These high redshift sightlines are not included in the further analysis, indicated by the red hashed pattern. The $w_{RM,rf}$ changes differently than our fits based on $z \leq 2$ (black dashed lined) predicted, and drops significantly after $z = 3$. It can be fitted by the combination of a broken power law and a linear decrease after $z = 3.3$, indicated by the black solid line.

As we might observe FRBs at higher redshifts in the future with the SKA (Hashimoto et al. 2020), we investigate how the $DM_{host,rf}$ and $RM_{host,rf}$ trends evolve over redshift above z=2, and whether it follows the functions we found based on galaxies at $z \leq 2$. However, these snapshots contain significantly fewer galaxies than the ones discussed in the previous sections (see Table 1), hence it is harder to split them into subgroups. Therefore, we only discuss their overall redshift evolution.

We calculated $DM_{host,rf}$ and $RM_{host,rf}$ at redshifts of 3, 4, and 5. We show the evolution of median DM as a function of redshift in Fig. 8 (right) and find that the DM does not increase as much as we would expect based on the fit from DMs at lower redshift. Between z=4 and z=5 median $DM_{host,rf}$ has only a few pc cm^{-3} difference. The redshift evolution of the median $DM_{host,rf}$ as a function of redshift can be fitted by a broken power law:

$$DM_{host,rf}(z) = \begin{cases} 82.2 \pm 5.3 \cdot z^{0.8\pm0.1} + 40.2 \pm 4.2, \\ \qquad\qquad \text{if } z < 2.6 \pm 0.3; \\ 130.7 \pm 15.9 \cdot z^{0.3\pm0.1} + 40.2 \pm 4.2, \\ \qquad\qquad \text{if } z \geq 2.6 \pm 0.3, \end{cases} \quad (19)$$

with a break at z=2.4, and the power law below this redshift is the same as the one we found before using $z \leq 2$ galaxies.

We previously found that the RM distribution width ($w_{RM,rf}$) turns over for $z > 1.5$ (see Section 3.1). In Fig. 8 (right) we see that it continues to slowly decrease until z=3, and at z=4 it drops significantly (by about 50%), and continues to quickly decrease. At z=5, it becomes even lower than it is at z=0. Our fit to $w_{RM,rf}$ below $z \leq 2$ can not predict $w_{RM,rf}$ at $z \geq 2$, and we find that the redshift evolution could be described by a broken power law (with a break at z=1.2) and a linear fit after z=3.4:

$$w_{RM,rf}(z) = \begin{cases} 282.3 \pm 6.6 \cdot z^{1.0\pm0.05} + 112.2 \pm 4.9, \\ \qquad\qquad \text{if } z < 1.2 \pm 0.03; \\ 357.8 \pm 7.2 \cdot z^{-0.3\pm0.04} + 112.2 \pm 4.9, \\ \qquad\qquad \text{if } 1.2 \pm 0.03 \leq z < 3.4 \pm 0.06; \\ 1048.6 \pm 33.5 - 202.5 \pm 8.0 \cdot z, \\ \qquad\qquad \text{if } z \geq 3.4 \pm 0.06. \end{cases} \quad (20)$$

4. Discussion

In this section, we discuss the possible physical reasons behind the trends of $DM_{host,rf}$ and $RM_{host,rf}$ we described in Section 3. To be able to interpret the role of n_e and B in the resulting DM and RM, we calculated the electron density, gas density, and magnetic field radial and vertical profiles, and other properties of the magnetic field. To calculate the magnetic field properties we followed the methods in Pakmor et al. (2017) and Pakmor et al. (2018), who studied Milky-Way-like galaxies from the Auriga simulations. The range of magnetic field strengths are in agreement with what we have found in the examined galaxies (see Appendix D). Finally, we compare our results to previous works.

4.1. Interpretations of $DM_{host,rf}$ trends

As DM is calculated by Eq. 11, it depends on the electron density and path length, and any changes we see in DM should be caused by one or both of these quantities.

4.1.1. $DM_{host,rf}$ changes versus redshift – the role of n_e

The median and 1σ width of the DM distribution increases with redshift (see Fig. 3), with both the lower and upper bound increasing at higher redshifts. We see that the median DM increases by a factor of ∼4 from z=0 to z=2, and the 1 sigma width of the distribution changes by a factor of ∼2.5.

We also find that from $z = 0$ to $z = 2$, the median n_e of the locations of FRBs ($n_{e,FRBpos}$) increases by a factor of ∼4, and the range of values increases by a factor of ∼3 (shown in panel a of Fig. 9). As the 1000 positions for each galaxy were randomly selected, their properties can tell us about the general environment in these galaxies. In summary, we find that $n_{e,FRBpos}$ significantly increases with redshift, which can cause a significant increase in DM.

Another cause of larger DMs at higher redshifts may be a longer integral path length through the host galaxy. We find that the median of path lengths increase by a factor of 1.15−1.3 at z>1 (shown in panel d of Fig. 9) with respect to $z < 1$, but at lower redshifts it only changes by a few %. The reason behind larger path lengths can be due to the radius of the galaxies. Since we calculate the integral until the $r_{SF,99}$ radius, a larger radius can cause larger path lengths, thus larger DMs. We find that indeed,

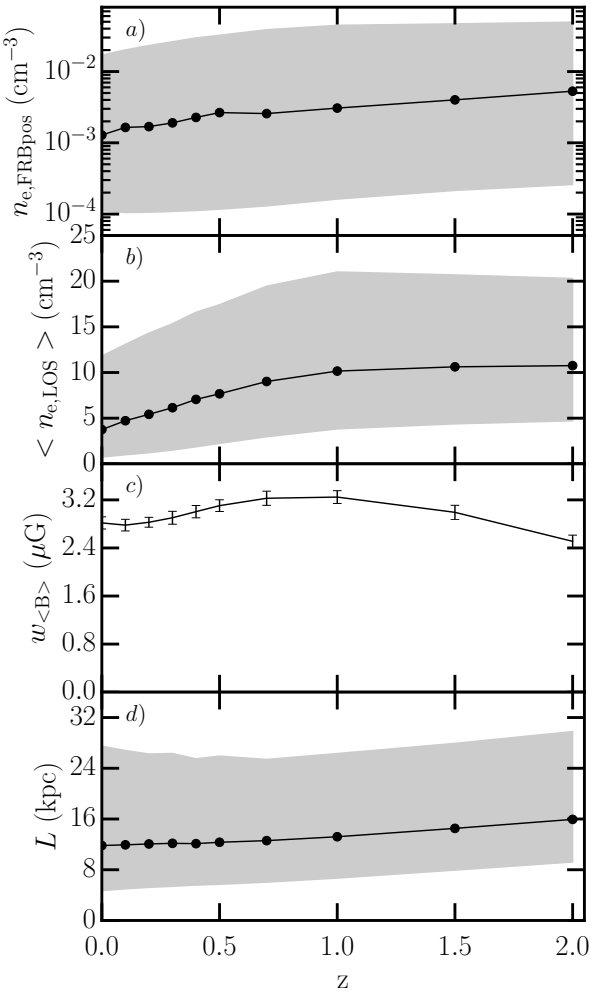

Fig. 9. We show how different properties change with redshift, in order to help to understand what drives the DM and RM trends. **a:** The median of the n_e of the starting position of the FRBs across redshift, and the ranges of values between the 16th and 84th percentile. It increases by a factor of ∼4, and the range of values increases by a factor of ∼3. **b:** The median of $\langle n_{e,LOS} \rangle$ increases with redshift up to $z = 2$ by a factor of 2.9, but between $z = 1$ and $z = 2$ only increases by a few %. **c:** The distribution width of $\langle B_{||LOS} \rangle$ increases until $z = 1$ by a factor of 1.15. From $z = 1$ to $z = 2$ it decreases by 20%, becoming smaller than at $z = 0$. **d:** The median of path lengths increase by a factor of 1.15−1.3 at higher redshifts ($z > 1$) with respect to $z < 1$, but at lower redshifts it only changes by a few %.

the median of the $r_{SF,99}$ increases by 10−25% at redshifts above $z = 1$ with respect to $z < 1$, and it only changes by a few % at $z < 1$, which can cause a small increase in path lengths and thus DM.

We also note that we can calculate the average electron density along an FRB sightline as we know the path length (L), if we rearrange Eq. 11: $\langle n_{e,LOS} \rangle = \frac{DM}{L}$ cm^{-3}. We find that this increases with redshift up to $z = 2$ by a factor of 2.9, but between $z = 1$ and $z = 2$ only increases by a few % (shown in panel b of Fig. 9). We previously saw that at $z > 1$ the path length increases, which could explain why DM keeps increasing despite $\langle n_{e,LOS} \rangle$ only increasing slightly. This could mean that at higher redshifts the galaxies have star-forming gas out to a larger distance compared to lower redshifts, but n_e is low in the outskirts of galaxies, causing us to measure a lower $\langle n_{e,LOS} \rangle$ than expected from DM. This idea is supported by the fact that the difference between the radius containing 95% and 99% of the star-forming gas in galaxies are larger at higher redshifts. At $z = 2$, the difference is 40% of $r_{SF,99}$ on average, while it is only 20% at $z = 0$.

We performed a simple test to see if the increase in electron density plays the major part in the increase in the median DM: we select a galaxy at z=0 (ID = 1004, $\log(M_*/M_\odot) = 9.8$, SFR=0.5 $M_\odot$/yr) with a DM_{median} = 49 pc cm^{-3} close to the median DM of the whole sample at z=0 (43 pc cm^{-3}). This galaxy was selected to have average properties of the sample. As there might be a more complicated relation between n_e and DM (e.g. n_e changes with radius), we conducted three tests: 1) scaling up the n_e of each cell by a factor of 4, 2) increasing the integration limit by a factor of 1.25, and 3) and increasing both. As expected, the median DM increases by 3.9, 1.3, and 4.1, respectively. Thus we conclude that the increasing trend of median DM with increasing redshift can be mainly explained by higher electron densities, but an increase in path lengths can also contribute to a lesser degree.

The higher electron densities are possibly caused by higher star formation rates at higher redshifts. In the sub grid star formation model from Springel & Hernquist (2003) the star forming process converts matter in the cold cloud phase to stars if the density exceeds a certain limit, and by the feedback of supernovae heats up the warm phase of the ISM. This depletes the cold gas that is used in star formation, which causes a decrease in SFR and electron densities as a function of time. This is why we see larger SFR and electron densities at higher redshifts, when there is still a large amount of star-forming gas available in these galaxies. This interpretation is supported by how the median SFR of the selected galaxies is also larger by a factor of ∼9 at $z = 2$ compared to $z = 0$, similarly to observed galaxies (see Fig. E.1). The 1σ width of the SFR distribution increases by a factor of ∼10 from $z = 0$ to $z = 2$, which could contribute to the increasing $w_{DM,rest}$ towards higher redshift. The fraction of star-forming cells in each galaxy also increases from a few % at z=0 to ∼ 20 % at z=2. Furthermore, we find the number of quenched galaxies decreases towards higher redshift, which is in agreement with observations: at high redshifts most galaxies are star-forming, and the fraction of red galaxies increases towards lower redshift. If the fraction of quenched galaxies is larger, the fraction of low DM values is also higher, resulting in a lower median DM.

There is also observational evidence of a connection between the SFR and the n_e of galaxies. Based on optical spectroscopic observations of galaxies at z=2.5, Shimakawa et al. (2015) found that n_e is correlated with the surface density of SFR, and found that highly star-forming galaxies have higher n_e. Kaasinen et al. (2017) compared galaxies at z=1.5 to local ones, and found that the n_e for the former is a factor of 5 greater than that of the latter. They found that n_e for galaxies with similar SFRs was the same, independently of their redshift. A high SFR density increases the number of young massive stars, which in turn, by stellar winds and shocks will have a larger energy input to HII regions, and the diffuse ionized gas, increasing the electron density of galaxies.

4.1.2. $DM_{host,rf}$ changes versus star formation activity – the role of n_e

In galaxies that we classified as star-forming, the median DM and $w_{DM,rf}$ is larger than in the case of quenched galaxies by a factor of ∼ 3 (see Fig. 5). In spite of this, we find that the path length in quenched galaxies is usually two times larger on average. However, this is not surprising, as the quenched galaxies have large stellar masses (∼ 10 times larger than average SF

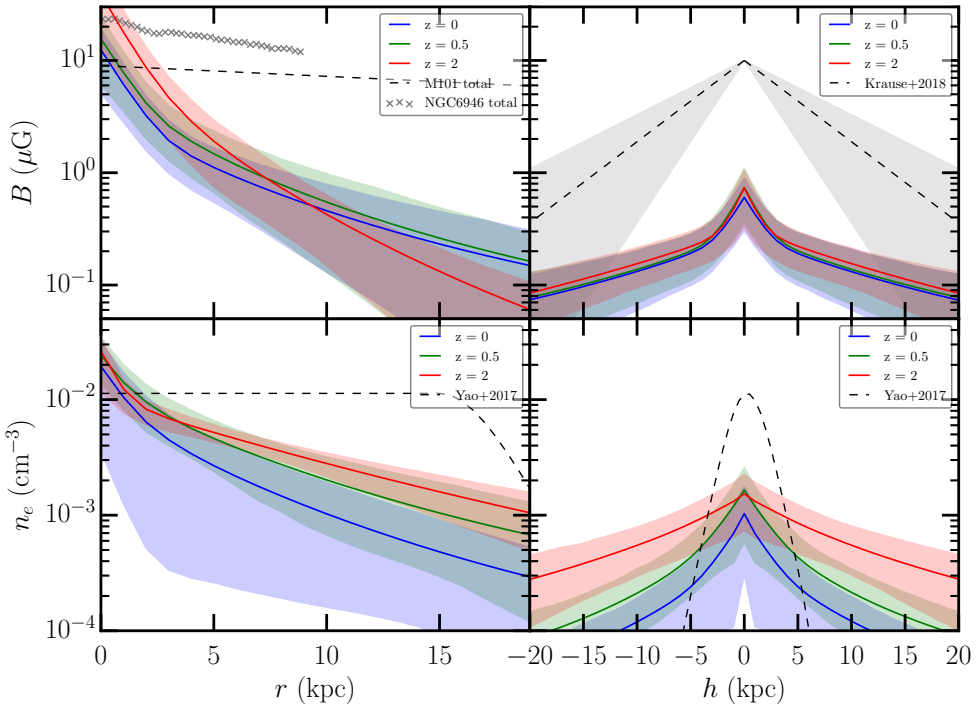

Fig. 10. Top row: The averaged radial and vertical profile of B of galaxies at various redshifts, and their 1σ width. In the top left panel, we show the total magnetic strength profile of NGC6946 (Beck 2007) and M101 (Berkhuijsen et al. 2016). In the top right panel, we show the average vertical B profiles of CHANG-ES galaxies (Krause et al. 2018) with a scale-height of 6 ± 3 kpc. **Bottom row**: The averaged radial and vertical profile of n_e of galaxies at various redshifts, and their 1σ width. We overplotted the n_e profiles of the thick disk from Yao et al. (2017).

galaxies) and galaxy sizes (∼ 3 times larger), similar to large ellipticals. Only a few quenched galaxies (∼ 15%) have radii below 5 kpc, and we found that 95% of these galaxies have log ($M_*/M_\odot$) < 10.5. The average radial profile of n_e of red galaxies is 1.5–3 times lower at all radii, and the average vertical profile is 2 times lower than that of SF galaxies. We also find that the average $n_{e,FRBpos}$ is 4 times larger in star-forming galaxies than in quenched galaxies. The $\langle n_{e,LOS}\rangle$ is 5 times smaller for quenched galaxies. So in summary while the path lengths are larger, the electron densities are lower in red galaxies, which causes their smaller DM contributions.

The red galaxies have already started or gone through quenching, their cold star-forming gas is depleted and the electron densities decreased. As we already described in the previous subsection, there is a connection between the SFR and the n_e of galaxies based on observations (see Section 4.1.1), We also find that in galaxies with similar SFR at different redshifts, the median of DM is almost the same (the difference is a few pc cm^{-3}).

4.1.3. $DM_{host,rf}$ changes versus stellar mass – the role of n_e

The increase in median DM and width with stellar mass (see Fig. 7) can be explained by the MS relation between stellar mass and SFR, as SFR increases with stellar mass, thus the electron densities do too. This increase in median DM continues up to very high mass galaxies (log($M_*/M_\odot$)=10.5), where it suddenly drops to half of its value. Here we investigate what causes this sudden drop.

We find that the magnitude of the radial and vertical n_e profiles of galaxies with log($M_*/M_\odot$)>10.5 is half of that of galaxies with lower stellar masses, and $\langle n_{e,LOS}\rangle$ also decreases by a factor of 2. Although the path length increases as a function of stellar mass, the n_e decrease is more prominent, producing low DMs in very massive galaxies.

These massive galaxies are analogous to large ellipticals with low electron densities and star formation rates. The supermassive blackhole (SMBH) feedback mechanism in the simulation (described in Weinberger et al. 2017, Weinberger et al. 2018) becomes very efficient at larger black hole masses (∼ $10^8 M_\odot$). At lower black hole masses (found in galaxies with lower stellar masses), kinetic energy is injected in pulses, and it is proportional to the surrounding density. The change in the feedback mechanism occurs in galaxies with a stellar mass of around log($M_*/M_\odot$) ∼ 10.5: then thermal energy is continuously injected, subsequently lowering the gas densities, electron densities and SFR. The feedback mechanism at large black hole masses is consistent with X-ray observations that show strong outflows are possible from AGNs (Tombesi et al. 2010), which could cause the expulsion of gas from their host galaxies and the suppression of star formation (Combes 2017).

We investigated if the massive galaxies in our sample are truly undergoing quenching. We find that 70% to 90% (corresponding to different redshifts) of galaxies we classified as quenched have a stellar mass above log($M_*/M_\odot$) ∼ 10.5. However only <30% of log($M_*/M_\odot$) > 10.5 galaxies are classified as quenched. This is because we only consider galaxies red if they are 1 dex below the MS. So while for galaxies with smaller stellar masses we find an average SFR close to the SFR of the main sequence, for massive galaxies we find SFRs that lie below the MS. These galaxies might have already started the quenching process. The fraction of quenched galaxies decreases at higher redshift, and more massive galaxies are classified as star-forming. We also note that <4% of star-forming galaxies are massive and very active in star formation: with log($M_*/M_\odot$) > 11 and a mean SFR ∼ 10 $M_\odot$/yr. As we showed

in Section 4.1.2, n_e is correlated with SFR, and a lower SFR can explain lower DMs.

4.1.4. $DM_{host,rf}$ changes versus inclination – the role of n_e

Galaxies viewed at larger inclinations have larger average DM contributions: the median DM is higher by a factor of ~ 1.5 for edge-on galaxies compared to face-on galaxies (see Fig. 7). This is because those sightlines have a longer path through the dense ISM inside the galaxy's disk, compared to the case of face-on galaxies, where the sightline only passes through a short path in the disk. We divided the sightlines, consisting of 1000 sightlines with different inclinations for each galaxy, into four inclination bins at each redshift, resulting in each bin having the same galaxy property (e.g stellar mass, SFR) distribution. This also means there are no differences in the radial and vertical profiles of n_e and B field strength of galaxies in these bins. And, as we select the FRB positions randomly, $n_{e,FRBpos}$ only fluctuates by 4% for the different inclination bins. Thus we conclude that the trend with inclination is a geometric effect, and is independent of the physical properties of individual galaxies.

We find the $\langle n_{e,LOS} \rangle$ is larger by a factor of $\sim$ 1.5-2 for edge-on compared to face-on galaxies, which is due to larger n_e in galaxy disks. The median path length decreases slightly with inclination, but the mean path length stays the same. This could be explained by how in edge-on view, both small and long path lengths are possible depending on the line of sight. As our FRB sources are mostly found in a disk, an FRB from a source at the edge of the disk can go through the whole disk and the halo of the galaxy, or only the halo, depending on whether the source is on the near-side or the far-side of the disk with respect to the observer. In face-on view the path lengths are closer to each other, as all sightlines go through the halo.

4.1.5. $DM_{host,rf}$ changes versus b_{offset} – the role of n_e

Sightlines with large b_{offset} have smaller DM on average (see Fig. 7), than sightlines with small offsets, and the median DM decreases linearly with increasing b_{offset}. The reason behind this is that at the center of galaxies in the simulation the electron density is higher, and it decreases by a double exponential as a function of radius and distance from the midplane (see the profiles in Fig. 10). We find that the path lengths increase with b_{offset}, along with galaxy radius, because galaxies with larger radii have a higher chance of having an FRB with larger offset.

We find that the fitted radial profiles of n_e averaged by redshift (shown in Fig. 10, and see Section 2) show that in the outskirts of galaxies (outside of the inner 5 kpc) n_e is higher at higher redshifts. At a radial distance of 20 kpc, n_e at z=2 is higher than at z=0 by factor of $\sim$2, but in the center of galaxies it decreases by $\sim$20%. The 1σ width changes only by a factor of $\sim$1.2. The vertical profile of n_e shows a similar behaviour, with a slight decrease in the center ($\sim$20%), but larger n_e beyond 2.5 kpc at higher redshifts. At a vertical distance of 15 kpc from the midplane of the galaxy, the n_e is $\sim$2.3 times larger at z=2 compared to galaxies at z=0, and the 1σ range of values changes by a factor of ~ 1.7.

4.2. Interpretation of $RM_{host,rf}$ trends

As RM is calculated using Eq. 12, in addition to the electron density and path length, it also depends on the strength and direction of the line-of-sight magnetic field, and any change we see in RM should be caused by these quantities. However, considering the large number of galaxies with different field directions, we will see that the magnetic field direction of large-scale fields without reversals will not have an effect on the PDFs. Changes in the direction of the magnetic field in the LOS (due to random fields and field reversals) can cancel out along the LOS thus can lower RM. The way the magnetic field properties were calculated can be found in Appendix D. Here we investigate the reasons behind the changes in the width of $RM_{host,rf}$ ($w_{RM,rf}$) with different parameters.

4.2.1. $w_{RM,rf}$ changes versus redshift – the role of B fields

One main question is whether the change in RM is dominated by changes in n_e or $\boldsymbol{B}_{\parallel}$. Similarly to DM, the width of the RM distribution ($w_{RM,rf}$) also increases as a function of redshift for $z < 1.5$ (see Fig. 7), by a factor of ~ 3.5. The $w_{RM,rf}$ increase below $z = 1$ can be partly attributed to increasing electron densities, but for $1 < z < 1.5$ the $w_{RM,rf}$ does not increase as rapidly as before. For $z > 1.5$ it starts decreasing, and for $z > 3$, it drops even further (see right panel of Fig. 8). The average of the total magnetic field strength in the disk (calculated from the thin projections of the magnetic field strength, details in Appendix D) increases by a factor of 1.2 up to $z = 1$, and at $z = 2$ it drops to the same value as at $z = 0$ (Fig. E.1). Although this is only a small factor, we also need to consider the factor of 4 increase we see in DM. Until $z = 1$, both n_e and the average B field strength increase, so $w_{RM,rf}$ also increases. For $z > 1$ only n_e increases and the average B field strength decreases, which is partly the reason why the $w_{RM,rf}$ stops its steep increase.

In Fig. 10 we show the radial profiles of B field strength (calculated from the thin projections of the magnetic field strength, described in Appendix D). We find that below z=1, the radial profiles do not show significant changes. However at $z = 2$, the magnetic field strength is 1.5–3 times higher than at lower redshifts within radial distances of less than 7 kpc. At larger radial distances the magnetic field strength is only half of what we see in low redshift galaxies. In the case of the vertical profiles, we find a slight increase of a factor of 1.15 at z=2 compared to z=0. We note that the magnetic field strength profiles are lower in magnitude than those from the observations of NGC6946 (Beck 2007), M101 (Berkhuijsen et al. 2016) and the CHANG-ES galaxies (Krause et al. 2018). This can be due to the limited resolution of IllustrisTNG, causing a missing turbulent field (similar to the Auriga simulations Pakmor et al. 2017).

Assuming a constant magnetic field with no field reversals, we can estimate the average line-of-sight magnetic field strength (a lower limit of the actual magnetic field strength), if both DM and RM are measured for the same FRB sightline: $\langle B_{\parallel,LOS} \rangle = 1.23 \frac{RM}{DM} \mu G$. The distribution width of $\langle B_{\parallel,LOS} \rangle$ increases until $z = 1$ by a factor of 1.15, and then decreases by 20% from $z = 1$ to $z = 2$, becoming smaller than at $z = 0$ (shown in panel c of Fig. 9). This is in agreement with the $w_{RM,rf}$ increase mainly caused by the increase in n_e below $z = 1$, and at higher redshifts the magnetic field properties of the galaxies change. Since we estimated $\langle B_{\parallel,LOS} \rangle$ with the assumption of no field reversals, one possible explanation for the decrease in $\langle B_{\parallel,LOS} \rangle$ is the presence of more reversals or random field at $z > 1$ compared to $z < 1$.

Furthermore, we find that the strength of the different magnetic field components changes with redshift. In the top panel of Fig. 11 we show that the relative strength of the azimuthal field increases with time. At higher redshift, the azimuthal and radial components of the magnetic field have similar relative strengths,

and are only twice as strong as the vertical field strength. As we go towards lower redshift, the relative strength of the azimuthal field increases, becoming 5-6 times larger than the other two components. The increase in the azimuthal field strength is caused by the ordering of the field by the differential rotation of the galaxy disks (Arshakian et al. 2009; Beck 2013). The total magnetic field is already amplified at higher redshifts to saturation, but the ordering of the field only happens at redshifts of $z = 1 - 2$ (similar to Pakmor et al. 2017). The presence of a strong large-scale ordered field can cause high |RM| values, which would increase $w_{\rm RM,rf}$. However, the mean-field dynamo would cause an increase in all magnetic field strength components (see e.g. Shukurov & Subramanian 2021, Section 13.5), in contradiction to the results from TNG50, suggesting the simulation does not contain the mean-field dynamo, which can be due to its limited physical resolution. Nevertheless, purely differential rotation would not cause a decrease in the radial and vertical magnetic field strength with time either, and these would stay constant. The decrease we see in these components could be explained by other processes, such as outflows (Chamandy & Taylor 2015), accretion (Moss et al. 2000), dissipation or reconnection.

Lastly, we use the magnetic field maps where we preserved the sign of the field (thin projections of the magnetic field components centered on the mid-plane) for each magnetic field component, to investigate the presence of 1) large-scale B fields, and 2) B field reversals or random fields in the galaxies. By calculating the average magnetic field strength of the face-on maps with preserved field signs (from here on called signed magnetic field strength), we can separate the two cases. If its absolute value is a few μG the galaxy has a large-scale field without reversal, and if this value is close to 0 μG the field is random or has a field reversal. The distribution of these signed magnetic field strengths is symmetric about 0 μG. In the case of the radial and vertical field, the width of this distribution is low (< 1) and does not change with redshift. This is due to their lower field strength compared to the azimuthal component, and that they are more likely to have random field. We find that the number of galaxies with reversals in the azimuthal field or with azimuthal fields dominated by random fields increases towards higher redshift. At $z = 0$ we find 26% (53%) of galaxies have a mean azimuthal field larger than 2 μG (1 μG), and at $z = 2$ we find 6% (22%) of galaxies have a mean azimuthal field larger than 2 μG (1 μG). In the bottom plot of Fig.11 we show how the width of the signed azimuthal magnetic field strength distribution ($w_{\rm B,signed}$) changes with redshift. At $z \geq 0.7$ it quickly decreases. As the changes in field direction along the line of sight can cancel each other, more field reversals and random fields can also cause lower $w_{\rm RM,rf}$.

4.2.2. $w_{\rm RM,rf}$ changes versus star formation activity – the role of B fields

The width of the RM distribution ($w_{\rm RM,rf}$) of quenched galaxies is six times lower than that of star-forming galaxies (see Fig. 6). This is mainly caused by the decrease in n_e, but we find that the width of the distribution of $\langle B_{\parallel,\rm LOS}\rangle$ along the line of sight in star-forming galaxies is 1.5 times larger than that of red galaxies. This suggests a difference in the magnetic field properties of quenched and star-forming galaxies, in addition to the differences in n_e. Marinacci et al. (2018) investigated the magnetic fields of galaxies in IllustrisTNG100 and IllustrisTNG300, and found that the highest values of field strength are at the highest density peaks. They found that early-type galaxies have an irregular gas distribution (due to the interaction of AGN feedback with the surrounding gas). The magnetic field traces the gas density closely and is therefore also irregular. We also see similar trends in our sample: quenched galaxies are often not well described by a double exponential radial magnetic field strength profile, with a maximum B field strength at larger radii instead of at the center of the galaxy. Their central magnetic field strengths are lower than those for star-forming galaxies. They also exhibit "wiggles" (magnetic field strength fluctuating with radius) in the radial profiles. Similar features can be seen in the gas density profiles, but the n_e profiles can still be described by double exponentials. This irregularity in the magnetic field can cause lower $w_{\rm RM,rf}$.

4.2.3. $w_{\rm RM,rf}$ changes versus stellar mass – the role of B fields

We find that the width of the RM distribution ($w_{\rm RM,rf}$) changes with stellar mass. For galaxies below $\log(M_*/{\rm M}_\odot) \sim 10.5$ $w_{\rm RM,rf}$ increases, and for galaxies above that stellar mass, $w_{\rm RM,rf}$ drops and decreases (see Fig. 7). As the quenching process usually starts at $\log(M_*/{\rm M}_\odot) \sim 10.5$ in the simulation (Weinberger et al. 2018), the galaxies start to have a different radial B field profile, with lower magnetic field strength at the center and a more irregular magnetic field. This, in combination with lower electron densities, causes a lower $w_{\rm RM,rf}$.

4.2.4. $w_{\rm RM,rf}$ changes versus galaxy inclination – the role of B fields

Galaxies with larger inclinations have a larger RM distribution width ($w_{\rm RM,rf}$, see Fig. 7) because the sightlines pass through more interstellar medium inside the galaxy, than in the case of face-on galaxies. Another reason is the azimuthal field dominating over the two other magnetic field components (at most redshifts, see Section 4.2.1); in the case of an edge-on galaxy, the azimuthal field can be parallel to the line of sight, causing a higher possible RM if there is no field reversal. In the case of a face-on galaxy, the vertical field (which is weaker than the azimuthal field) will contribute the most to the line-of-sight magnetic field, resulting in lower RMs. We note this contribution can be close to 0 in the case of symmetric vertical fields. We can see that at $z \geq 1$, $w_{\rm RM,rf}$ does not increase as much with inclination, compared to lower redshifts. This is because the field was less ordered at higher redshift (see Section 4.2.1 and Fig. 11), and the azimuthal field does not dominate over the other components, causing a weaker inclination dependence.

4.2.5. $w_{\rm RM,rf}$ changes versus projected FRB offset – the role of B fields

Sightlines with larger $b_{\rm offset}$ have smaller RM distribution width ($w_{\rm RM,rf}$), on average, than sightlines with smaller $b_{\rm offset}$ (see Fig. 7). At the center of galaxies the magnetic field is the strongest (apart from quenched galaxies), and the radial profile often can be fitted by a decreasing double exponential (see Appendix D). RM decreases more rapidly than DM, because both n_e and B exponentially decrease with radius.

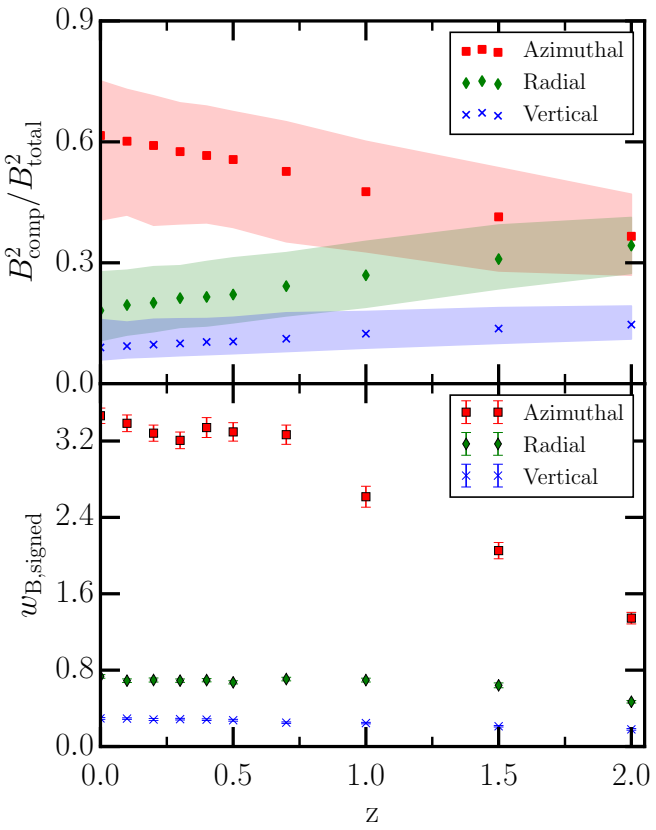

Fig. 11. Top: The median of the different magnetic field components' ratios to the total magnetic field ($B^2_{\rm component}/B^2_{\rm total}$, where the components are azimuthal, radial, and vertical). The median ratio of azimuthal field increases with time, while the ratio of radial and vertical field decreases. This shows how the differential rotation orders the field, converting other magnetic field components to azimuthal field. **Bottom:** The distribution width of the average of the signed magnetic field strength maps. The distribution width of the azimuthal B field decreases with increasing redshift, showing that there are more reversals and random field at high redshift. The distribution widths of the radial and vertical B field are small at all redshift.

4.3. Comparison to previous works

4.3.1. DM

There have been multiple previous works in the past years that have estimated $\rm DM_{host}$. Here we compare our results to most of them.

Hackstein et al. (2019) investigated $\rm DM_{host}$ in a spiral similar to the MW (using the NE2001 electron density model of the Milky Way, Cordes & Lazio 2002). They found an observed mean DM contribution of ∼110 pc cm^{-3} at z=0, double our result, and this is also the case if we select galaxies with MW mass (10.69<log(M_*/M$_\odot$)<10.86, Licquia & Newman 2015). The differences could be due to the differences in the n_e profiles: NE2001 has a thick disk profile, where $n_e > 10^{-2}$ cm^{-3} out to 15 kpc, whereas we have a double exponential decline that reaches n_e of $\sim 10^{-2}$ cm^{-3} at ∼ 12 kpc on average. As Hackstein et al. (2019) did not take into account increasing n_e at higher redshift, they found that the observed DM decreases with increasing z to ∼35 pc cm^{-3} at z=2 (compared to ∼50 pc cm^{-3} from our results).

Xu & Han (2015) investigated the galaxy disk inclination dependence of the DM of FRB hosts, also using the NE2001 model. They find a similar exponential DM decrease with increasing inclination, similar to our result, but with a larger magnitude decrease. We find larger DMs for face-on galaxies by a factor of two and lower DMs for edge-on galaxies by a factor of two than Xu & Han (2015). This can be again explained by different n_e profiles: while the radial n_e profiles of our galaxies are lower on average than the one from NE2001, our vertical profiles have larger n_e out to larger vertical heights. In face-on view, the majority of the sightline passes through the halo providing us with a larger DM compared to Xu & Han (2015), and in edge-on view the sightline passes through the disk causing us to have a smaller DM.

Walker et al. (2020) calculated DM for a spiral and an elliptical galaxy n_e model with different starting positions corresponding to different progenitors (OB stars, young and old pulsars, millisecond pulsars). The DM of sources following stellar distributions in spiral galaxies have similar lognormal shaped DM distributions, with medians of 68 – 98 pc cm^{-3}, which is slightly higher than ours. They found DM can potentially be higher than 700 pc cm^{-3}, while our sample can produce DMs of several 1000 pc cm^{-3}. In summary, their results are consistent with ours.

Hackstein et al. (2020) used galaxy models from Lacey et al. (2016) produced by GALFORM, a semi-analytic galaxy formation model (SAM), to calculate DM. GALFORM includes effects of gas cooling, angular momentum conservation, star formation, and AGN as well as stellar feedback. The model provides the evolution of the global properties of galaxies, from which n_e can be calculated. Hackstein et al. (2020) give the likelihood function of observed host DMs for the full sample considering redshift distributions based on the capabilities of ASKAP, CHIME and Parkes radio telescope: possible values range from approximately 0.1 to 450 pc cm^{-3}. To compare, we also use our sightlines from every redshift, and convert them to the observer's frame. Considering 3 σ (99.7% of data points), DM ranges from 10^{-4} to 490 rad m^{-2}, which has a similar range. It is not surprising that in general the range of values are consistent, as previous works show that SAMs and hydrodynamical simulations are generally in good agreement, although there are differences due to the dissimilarity in the evolution of gas properties (see e.g. Mitchell et al. 2018's comparison between EAGLE and GALFORM).

As we showed in Fig. 3, Zhang et al. (2020) calculated the DM contribution of host galaxies using IllustrisTNG100-1, considering redshifts up to z=1.5. They selected (a) 200 galaxies similar to the host of FRB180916, (b) 200 similar to the hosts of non-repeating FRBs known at the time of Zhang et al. (2020)'s paper and (c) 1000 similar to the host of the repeating FRB121102. For each subhalo they selected 500 starting positions, and for each position they consider 10 random direction. Their $\rm DM_{median}$ results agree within the 1 σ width of our result from Section 3 (using every galaxy below z=2), despite the physical resolution of TNG100 being three times worse than TNG50's[5]. Based on the galaxy selection criteria, our selection should be similar to cases (a) and (b), as both have a similar stellar mass range: 9<log(M_*/M$_\odot$)<11 and 9<log(M_*/M$_\odot$)<11.5, respectively. Case (c) has galaxies with log(M_*/M$_\odot$) < 8, which our selection does not include. Zhang et al. (2020) reports that the difference between the (a) and (b) cases are due to the different FRB positions, as in case (b) the FRBs are at the edges of the galaxies. This is in agreement with the decreasing $\rm DM_{host,rf}$ trend we have found as a function of $b_{\rm offset}$. However, it does not

[5] The TNG model has systematics with resolution: galaxies with the same halo masses have larger stellar masses with increasing resolution. This can have an effect on the black hole masses, and on the gas fractions, thus n_e(Pillepich et al. 2018)

explain why the median $DM_{host,rf}$ in case (a) is larger than in our sample. One possible explanation is the difference in resolution between the two simulations. Alternatively, it may also be due to the longer integral path lengths they used to calculate DM, which can be larger than ours by a factor of ~ 10, due to how they defined the integral to extend to each cell that is assigned to a subhalo.

We note that another key difference between the two cases is the SFR of the selected galaxies: (a) contains galaxies with $0.01<SFR(M_\odot/yr)<10$, and (b) has ones with $0<SFR(M_\odot/yr)<2$, meaning that group has a lower SFR on average. As we showed in Section 4.1.2, star formation increases with the electron densities, thus it is also connected to DM_{host}, which could explain why DM is generally larger in case (a) than in case (b). Since we consider all galaxies with SFRs above 0, our result can be found in between the two cases from Zhang et al. (2020). Additionally, we also include galaxies with even larger stellar masses, which have lower DM on average, further lowering the median DM.

Jaroszyński (2020) used IllustrisTNG100-3 and IllustrisTNG100-1 subboxes to calculate the host galaxy contributions to DM, using galaxies with $7.5<\log(M_*/M_\odot)<11$ at $0 \leq z \leq 3$. They stack galaxies to determine n_e as a function of distance from the galaxy center out to 10 Mpc, and the free parameters for their DM calculation are the FRB distance from the host center and the angle between the ray and the direction to the center. They find that n_e and DM increase with stellar mass, up to $\log(M_*/M_\odot)<10.5$, and both are lower for massive galaxies with $\log(M_*/M_\odot)>10.5$, similarly to what we found. However, this changes after z=2, where $\log(M_*/M_\odot)>10.5$ galaxies have larger DMs than galaxies with lower stellar mass. For us this change already happens at z=1.5. This can be due to resolution affecting the black hole masses, which would cause the quenching mechanism to turn on earlier in TNG50. They also find that DM decreases with the distance of the line of sight from the center of the galaxy (so equivalent to our b_{offset}). While qualitatively the trends are similar to what we found, the host DM values are significantly higher than what we calculated, and even higher than the results of Zhang et al. (2020). At $z \leq 2$ their DMs can be a factor of 2 – 3 higher than ours, and at z=2 these becomes 6 times higher. We noticed that the difference is larger for galaxies with stellar masses above $\log(M_*/M_\odot)>10$, for less massive galaxies our results are in a better agreement. The large magnitude in DM difference is probably due to differences in how Jaroszyński (2020) define the end of the integral (the galaxy's radius). They integrate up to $\sim$ 600 kpc as their n_e profiles fall to 0 cm^{-3} at that radius, while most of our galaxies have a radius of $\sim$ 20 kpc. Another reason for differences could be that they calculated the n_e profiles statistically from galaxies in IllustrisTNG100-3 and IllustrisTNG100-1 subboxes which have lower resolution. In contrast, we used TNG50 with higher resolution and directly integrated n_e in many sightlines. Jaroszyński (2020) also calculated the DM contribution of FRB190608, which we investigate in Section 6. We found the observed $DM_{host,median}$ to be 90 – 130 pc cm^{-3}, and they derived 144 ± 30 pc cm^{-3}, which are in agreement with each other within 1σ. The DM difference is not large for this case because of the galaxy's low redshift.

Using FRBs that have been localized to host galaxies, Macquart et al. (2020) fitted their DM_{excess} versus redshift relation, and found that the host DM contributions are best described by a lognormal distribution with median 100 pc cm^{-3} and σ =1. Our DM host distribution medians at $z = 0$ are half of that (but they reach 100 pc cm^{-3} at $z = 0.7$), and our σ is slightly larger ($\sim$1.3). However, the parameters of the lognormal from Macquart et al. (2020) and our results are on the same order of magnitude.

Walker et al. 2023 (in prep) have investigated the contribution of the Cosmic Web to the DM of FRBs based on TNG300, including intervening galaxies in the LOS. They found a similar trend of increasing restframe DM with increasing intervening galaxy redshift, but this increase is suppressed when the DM is converted to the observer's frame. The median of their DM distributions is on an order of 1 pc cm^{-3}, which is significantly lower than ours, but this is expected as the sightlines can go through at impact parameters of 100s or 1000s of kpc in the intervening galaxies (Walker et al. 2023, in prep).

4.3.2. RM

We compare our results to two studies about the RM contribution of FRB host galaxies, and also to a work about intervening galaxies in front of background quasars.

Basu et al. (2018) investigated the RM distribution of disk galaxies, using galaxies with a large-scale axisymmetric spiral magnetic field and a radially decreasing electron density (while neither the B field geometry nor n_e changes with distance from the midplane). They studied the RM of background sources, thus their sightlines go through the entire galaxy, unlike in our case. In spite of these differences, they found a similar distribution shape as we did for the RM of FRBs in Section 3: they modelled these distribution as the sum of a Lorenztian and two Gaussians, and found that the width of the Lorentzian was proportional to the mean axisymmetric field strength. Our distributions can also be fitted by the same function. The width of their Lorentzian ranges from 15 – 60 rad m^{-2} for different B field strengths. We find that at z=0 the width of the Lorentzian for our sample is 60 rad m^{-2}, which is close to their results. However, the width of our Lorentzian increases with redshift with the largest value of 150 rad m^{-2} at z=1.5, more than two times larger than Basu et al. (2018)'s results, while the total magnetic field strengths of our sample does not increase with redshift. The increase in width is probably caused by the increase in n_e. Nevertheless, there is a number of differences between the two experiments: in Basu et al. (2018) there is only a large-scale magnetic field, with no vertical magnetic field component, and the sightlines go through the whole galaxy. In our simulation, while the total magnetic field strength does not change with redshift, the strength of the different magnetic field components do, and we also find more reversals as redshift increases.

Hackstein et al. (2019) calculated the RM contribution of a possible MW-like spiral host galaxy (using NE2001 and a model of the MW galactic-scale magnetic field – Jansson & Farrar 2012), and found the mean |RM| is $\sim$ 65 rad m^{-2} at z=0. To compare our results, we also calculate the mean |RM| at z=0, and we derive $\sim$ 100 rad m^{-2}, which is almost twice as large. Since the n_e and B models they used were for the Milky Way, we selected galaxies at $z = 0$ with similar stellar masses as the Milky Way ($10.69<\log(M_*/M_\odot)<10.86$, Licquia & Newman 2015), and recalculated |RM|. We found it to be 63 rad m^{-2}, which is very close to what Hackstein et al. (2019) found. This is surprising as the DM distributions we find are different compared to the NE2001 model, but might show that for MW-like galaxies, their model gives the same result as TNG50. As Hackstein et al. (2019) did not consider that n_e or B change with redshift, they predicted that the observed RM would fall to |RM| $\sim$ 7 rad m^{-2} at z=2. We find the observed |RM| would be $\sim$ 50 rad m^{-2} at $z = 2$ from our sample: it would still be smaller compared to z=0, but by only a factor of two.

Hackstein et al. (2020) used galaxy models from Rodrigues et al. (2019), who studied the evolution of magnetic fields of galaxies from Lacey et al. (2016) produced by GALFORM, a semi-analytic galaxy formation model, by using the MAGNETIZER code on them (Rodrigues & Chamandy 2020). This code numerically solves the non-linear turbulent mean-field dynamo equation, which provides them with the radial profiles of the strength of the radial and toroidal components of the coherent magnetic field, and both the B field strength and the density declines exponentially with the distance from the plane. When calculating RM they do not include the small-scale field. They use a few million galaxies with stellar masses of $7<\log(M_*/M_\odot)<12$, including spiral, lenticular and elliptical galaxies, but do not include irregular galaxies. A large fraction of this galaxy sample have a very weak B field strength (<0.05 μG). They give the likelihood function of observed host |RM|s for the full sample (the same way as for DM): possible values range approximately from 0.01 to 320 rad m^{-2}. To compare our results to theirs, we also use all of our sightlines from every redshift, and convert them to the observer's frame and use the absolute values of RM. Considering 2 σ (95% of our data), we get a range of 0.2 to 490 rad m^{-2}, which shows slightly larger possible |RM|s than those from Hackstein et al. (2020) but is consistent with their results. As the magnetic fields in Hackstein et al. (2020) are based on the mean-field dynamo theory and only includes large-scale field, it surprising their results agree so well with our RMs from the TNG50 MHD simulation, where we do not see the amplification from the mean-field dynamo. However, if we consider 3 σ (99.7%), we get a range of 10^{-8} to 2650 rad m^{-2}, which includes significantly higher |RM| values. This could be because the magnetic field of many galaxies in their sample are very weak, and they only include the large-scale coherent magnetic field and not the small-scale or random field. Rodrigues et al. (2019) found that only 40% of galaxies with $\log(M_*/M_\odot)=9$ have significant B field, and they found a clear bimodality in the distribution of B field strengths, one of the parameters they used to characterize B field is the maximum B field strength in the radial profile. We find a small bimodality in the distribution of the B field strengths at the center of galaxies (for us the maximum magnetic field strength is usually at the center of the galaxy), but only ∼15% of our galaxies are in the group of weak magnetic fields.

Overall, we found that our results are consistent with previous results, even though they were derived with different methods. This can be due to the fact that all of these methods mainly resolve the large-scale magnetic field of galaxies. We might find differences if we can resolve the small-scale field, for example if we use a simulation with even higher spatial resolution than IllustrisTNG50.

5. Implication on future studies of the magnetic field of the IGM

5.1. DM_{host} and RM_{host} in the observer's frame

Zhou et al. (2014) has pointed out that if $DM_{host,rf}$ does not increase as fast as the $1+z$ factor from the redshift dilution decreases it, FRBs can be easily used as cosmological probes without much contamination from the host galaxy DMs. Because of this, we investigate how the DM and RM contributions of the host galaxies change with redshift in the observer's frame ($DM_{host,obs}$ and $RM_{host,obs}$). We calculated $DM_{host,obs}$ and $RM_{host,obs}$ by correcting $DM_{host,rf}$ and $RM_{host,rf}$ calculated from the simulation with the redshift of the galaxies:

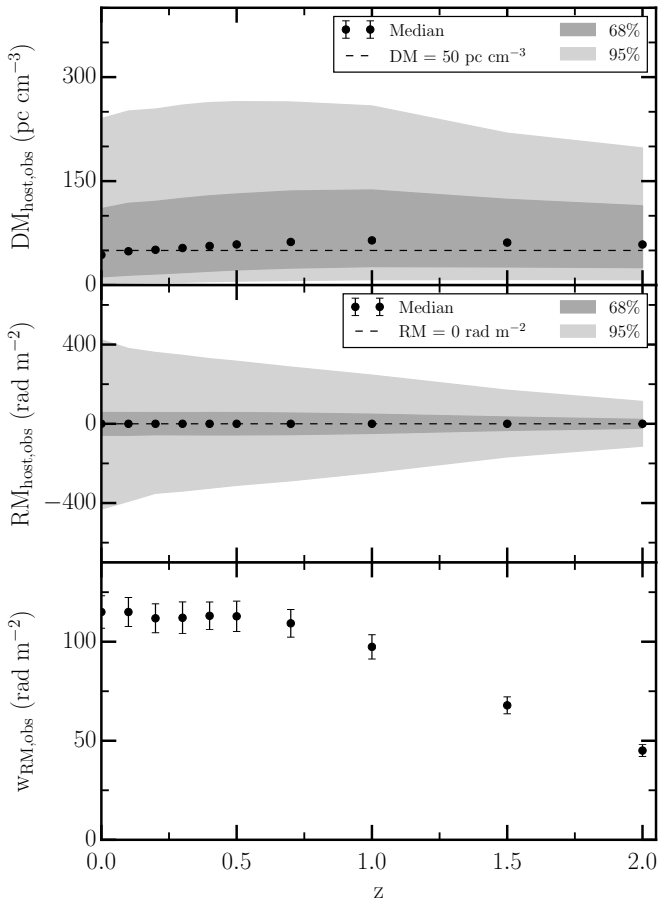

Fig. 12. Top: The possible observed DM contribution of host galaxies based on 68% and 95% of our sightlines. The black points are the medians of DM at each redshift. The contribution decreases slightly at higher redshifts. **Middle:** The same as top, but for the possible observed RM contribution of host galaxies. This contribution decreases significantly with redshift. **Bottom:** The width of the observed RM distribution as a function of redshift. It decreases significantly as a function of redshift.

$$\mathrm{DM_{host,obs}} = \frac{\mathrm{DM_{host,rf}}}{(z_{\mathrm{host}}+1)} \tag{21}$$

and

$$\mathrm{RM_{host,obs}} = \frac{\mathrm{RM_{host,rf}}}{(z_{\mathrm{host}}+1)^2}. \tag{22}$$

In Fig. 12, we show the 68% and 95% of DM and RM for each redshift. Considering all sightlines at all redshifts 95% of $DM_{host,obs}$ is between 4 and 250 pc cm^{-3}, and 95% of $|RM_{host,obs}|$ is less than 310 rad m^{-2}. These ranges decrease at higher redshift: only slightly in the case of $DM_{host,obs}$, but significantly in the case of $RM_{host,obs}$.

The differences in the $DM_{host,obs}$ at different redshifts is smaller than what we have seen in the rest frame DMs. The median of $DM_{host,obs}$ is between 46 and 69 pc cm^{-3}, it first increases slightly, then decreases after $z = 1$. Thus, the median $DM_{host,obs}$ is similar at every redshift. The $w_{DM,obs}$ also does not change significantly (1σ width: 92−115 pc cm^{-3}, and 2σ width: 202−278 pc cm^{-3}). This means if we have no information about the host galaxy, we can subtract the same host DM contribution from each FRB's total observed DM, independently from the host's

redshift. This is in contrast to the results of Jaroszyński (2020), who found even the observed DM increases with redshift (probably due to their longer integral path lengths).

We show in the middle panel of Fig. 12 that the median of $RM_{host,obs}$ is 0 rad m^{-2} at every redshift. The 2 σ width of the $RM_{host,obs}$ distribution linearly decreases with redshift: it drops from 800 rad m^{-2} at $z = 0$ to 200 rad m^{-2} at $z = 2$. In the bottom panel of 12 we show the changes of $w_{RM,obs}$: at $z \leq 0.5$ it does not change significantly ($w_{RM,obs} = 111 - 119$ rad m^{-2}), but it starts to decrease after $z = 0.7$.

We find that the increase in $DM_{host,rf}$ and $RM_{host,rf}$ with increasing redshift is weaker, than the decrease due to redshift dilution. As both DM_{IGM} and RM_{IGM} should increase towards higher redshift, if we observe FRBs at high redshift, we can get better constraints on cosmological parameters and the IGMF.

5.2. Number of FRBs needed for IGM studies

FRBs can be used as a promising probe of the IGMF (Zheng et al. 2014; Akahori et al. 2016). However, since the RMs measured towards a sample of FRBs contains contribution from the FRB host galaxy and the IGMF, we investigate the minimum number of polarized FRBs required to statistically infer the IGMF. We note that in the past most surveys have not recorded the polarization data of FRBs, however, the current and future surveys are going to also observe polarization, which will result in an increase in the number of FRBs with measured RMs.

We perform a two-sample Kolmogorov-Smirnov (KS) test on the distributions of RM, with and without the contribution from IGMF, in order to estimate the number of polarized FRBs needed to constrain the IGMF. We assume that the RM contributed by the Milky Way has been robustly subtracted, the RM contributed by the FRB host galaxies at a particular redshift follows the distribution shown in the bottom panel of Fig. 3, and the RM from the local environment is negligible. We model the statistical distribution of RM arising in the IGMF (RM_{IGM}) as Gaussian distribution with mean zero, and standard deviation $\sigma_{RM,IGM}$.

For the purpose of this work, we consider $\sigma_{RM,IGM} = 2$, 10, 20, and 40 rad m^{-2}, following the findings of Akahori et al. 2016. They found that $\sigma_{RM,IGM}$ increases from $z = 2$ to $z = 7$, from 16 to 45 rad m^{-2} considering all IGM (including hot gas in clusters), and from 1.3 to 9 rad m^{-2} for only filaments. In order to estimate the statistical difference in the distributions of RM for N_{FRB} FRBs, with and without the contribution of IGMF, we randomly draw N_{FRB} values of $RM_{host,obs} + RM_{IGM}$ and $RM_{host,obs}$, and determine the p-value by applying KS test. We performed 1000 Monte-Carlo simulations for a given N_{FRB}, where N_{FRB} ranges between 10 and 10^6. For a given $\sigma_{RM,IGM}$, the N_{FRB}, for which at least 95% of the Monte-Carlo samples has $p < 0.05$, is considered as the minimum number of FRBs needed to discern the contribution of IGMF at 95% confidence level. We did these tests for sightlines at $z = 0.5$ and $z = 2$.

In Fig. 13 we show how many FRBs we need to detect an IGMF with a given $\sigma_{RM,IGM}$ at these redshifts. To detect a $\sigma_{RM,IGM}$ of 40 rad m^{-2}, we need at least 350 FRBs at $z = 0.5$ or 150 FRBs at $z = 2$. For a small $\sigma_{RM,IGM}$ of 2 rad m^{-2} we need at least 95 000 FRBs at $z = 0.5$ or 9 500 FRBs at $z = 2$. We need fewer high redshift FRBs than low redshift FRBs to detect the same $\sigma_{RM,IGM}$ due to the width of the distribution of the observed RM_{host} decreasing with redshift. We find that N_{FRB} as a function of $\sigma_{RM,IGM}$ can be fitted by a function in the following form:

Table 2. The parameters of the fit (Eq. 23) for N_{FRB} as a function of $\sigma_{RM,IGM}$ at $z = 0.5$ and $z = 2$.

z	a_{IGM}	b_{IGM}	c_{IGM}
0.5	3706.0 ± 413.6	-7.0 ± 0.2	-4118.0 ± 547.7
2.0	1759.0 ± 202.9	-4.0 ± 0.2	-1825.0 ± 227.4

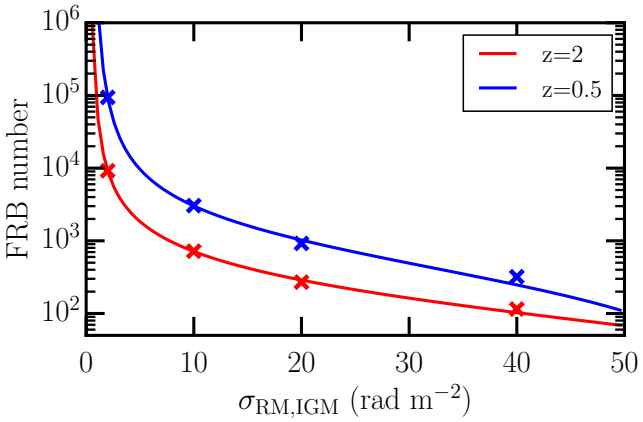

Fig. 13. The number of FRBs needed to detect a given $\sigma_{RM,IGM}$ at two redshifts ($z = 0.5$ and $z = 2$). We consider the IGMF possible to detect if the KS test returns a p-value below 0.05 for 95% of Monte Carlo tests (for details see Section 5.2). The data points show the FRB number needed for significant detection for a given $\sigma_{RM,IGM}$, and the solid line is the reciprocal exponential fit.

$$N_{FRB} = a_{IGM} \exp(-b_{IGM}/\sigma_{RM,IGM}) + c_{IGM}, \quad (23)$$

where the a_{IGM}, b_{IGM} and c_{IGM} parameters are listed in 2 for $z = 0.5$ and $z = 2$.

We also investigate how adding measurement uncertainty to the observed RM would affect the number of FRBs needed. We added a Gaussian noise with $\sigma = 1$, 5, 10, 20, and 50 rad m^{-2} to our RMs. We found that the number of FRBs needed to detect the IGMF exponentially increases with the error of RM. An error of 1 to 10 rad m^{-2} would increase the number of FRBs by 1.5 to 5 times (depending on σ_{IGM}). In the case of σ_{IGM}> 10 rad m^{-2} higher errors also increase the required number of FRBs by a similar magnitude. For $\sigma_{IGM} = 2$ rad m^{-2}, an $RM_{error} = 20$ rad m^{-2} and $RM_{error} = 50$ rad m^{-2} increases the required number of FRBs by 20 and 300 times, respectively. This additional uncertainty can also be considered the contribution of the immediate environment if it is on an order of 1 – 50 rad m^{-2}. Thus the increase in the required number of FRBs is true as well as in the case of RM from the source environment.

We conclude that in the case of a $\sigma_{RM,IGM} = 40$ rad m^{-2} we will be able to constrain the IGMF with a few hundred - thousand FRBs (even if we take into account the measurement error of RM), which will be realistically achieved in the next years. In the case of $\sigma_{RM,IGM} = 2$ rad m^{-2}, we will need significantly more FRBs.

6. Application to localized FRBs: FRB190608 as a case study

In this section, we show how we can constrain the $DM_{host,rf}$ and $RM_{host,rf}$ contribution of localized FRBs with identified host galaxies (with detailed information about the galaxy properties

Table 3. The median and 1σ range of FRB190806's $DM_{host,rf}$ and $RM_{host,rf}$ from different sightlines.

Subset of sightlines	N_{sl}	median $DM_{host,rf}$ (pc cm^{-3})	1σ DM (pc cm^{-3})	median $RM_{host,rf}$ (rad m^{-2})	1σ RM (rad m^{-2})
Spec. loc.	3000	118	60 – 190	+7	−74 – +99
DB. all	3000	103	47 – 207	+3	−192 – +231
DB. b_{offset}	257	107	49 – 207	+3	−222 – +226
DB. i	61	87	50 – 146	−17	−186 – +89
DB. b_{offset}+i	7	93	75 – 144	+24	−143 – +262

Notes: First line lists the results from placing the FRBs at the minor axis of the host galaxy analogs, and the rest of the table shows the results using our 'database' of sightlines from Section 3.1. We show the results using all sightlines from the analog galaxies in the database, sightlines selected based on their galaxy inclination, b_{offset}, and both. We show how the number of appropriate sightlines decreases when we apply stricter selection rules.

and the FRB position within the host) using TNG50 of the IllustrisTNG simulation. First, we calculate $DM_{host,rf}$ and $RM_{host,rf}$ by placing FRBs in galaxies with similar properties to the host at specific locations. Then we use our sightlines calculated in Section 3 (referred to as 'database' from here on), and select sightlines that match the host galaxy properties, i and b_{offset}. We compare these methods to see how well our database of sightlines can be used. We also show that our estimates are consistent with observations.

The host galaxy of FRB190608 is well known, thus it provides numerous constraints on both the selection of analog galaxies from the simulation and the location of the FRBs in them. The FRB was detected by Macquart et al. (2020) with the ASKAP-ICS. The host is a spiral galaxy at $z = 0.12$ with $\log(M_*/M_\odot) = 10.06^{+0.09}_{-0.12}$ and an SFR of $0.69 \pm 0.21\, M_\odot\,yr^{-1}$ (Heintz et al. 2020). It has an inclination of 43° and a position angle (PA) of 54° based on the HST NIR image of the host galaxy, and the FRB is along the minor axis of the galaxy at a projected offset of 6.52 ± 0.82 kpc from the center, in a spiral arm (Mannings et al. 2021). The DM and RM of the FRB were measured as well: $DM_{obs} = 338.7 \pm 0.5$ pc cm^{-3} (Macquart et al. 2020) and $RM_{obs} = +353 \pm 2$ rad m^{-2} (Day et al. 2020). These contain all the different components along the line of sight; the immediate source environment, the host galaxy, the IGM and the Milky Way.

We select analogs of the host galaxy of FRB190608 from the TNG50 simulation based on their stellar mass, SFR and $r_{SF,99}$ from the snapshot at $z = 0.1$. We found three galaxies that had the same stellar mass as the host within the error of the stellar mass, the same SFR_{MS}-SFR difference, and an $r_{SF,99}$ larger than the offset of the FRB. We calculate the host's difference from the MS of star-forming galaxies using the relation from Zahid et al. (2012), then we use the same difference from the simulation derived MS to constrain the SFR of the host galaxy analogs. The halo IDs are 554, 637 and 694, and all of the selected galaxies are the first (most massive) subhalos of their parent halo. We rotate the galaxies to the same inclination as the one measured for the host galaxy. Considering the PA of the host and the position of the FRB in the HST image, we place the FRBs along the minor axis of the galaxy. We then calculate the DM and RM in the same way as we calculated for the other FRBs in this paper (see Section 2).

The DM distributions of the three host galaxy analogs of FRB190608 are shown in Fig. 14. The median of the DM distributions for each galaxy is between 101 and 146 pc cm^{-3} (118 pc cm^{-3} for all sightlines), and the 1σ range of possible values is 60 – 190 pc cm^{-3}. We convert this to the observed DM: median $DM_{host,obs}$ = 83 – 121 pc cm^{-3}, and the range of values is 50 – 157 pc cm^{-3}. This is consistent with the observation, as it is smaller than the observed DM of the FRB. Even if we consider the 2 sigma range of possible values, we get 286 pc cm^{-3} as the upper bound. If we subtract the DM contributed by MW (DM_{MW} = 38 pc cm^{-3} along this sightline Cordes & Lazio 2002) from the observed DM we derive 300.7 pc cm^{-3}, which is still above our upper limit.

Chittidi et al. (2021) derived the host DM from the Hα emission measure: the DM of the host ISM is 94 ± 38 pc cm^{-3} (range of 56 – 132 pc cm^{-3}) and the DM of the host halo is 55 ± 25 pc cm^{-3} (range of 30 – 80 pc cm^{-3}). Including both the ISM and the halo of the host they derived a range of 100 – 190 pc cm^{-3}. Their range of host ISM DM is very close to the host DMs we derived, although in our case larger values are also possible, which could mean we have some DM contribution from the halos of the galaxies. Thus we conclude that our results are consistent with observations.

We constrain the IGM's DM contribution by subtracting our host contribution estimate and the contribution of the Milky Way from the observed DM, including the ISM and the halo – the latter is 39 pc cm^{-3} according to Prochaska & Zheng 2019. We obtain a residual DM_{res} = 105 – 212 pc cm^{-3}. This DM can arise from the IGM and the immediate source environment, making this estimate an upper limit on DM_{IGM}. In comparison, Simha et al. 2020 derived a DM_{IGM} (also including intervening halos) of 98 – 154 pc cm^{-3} using the Monte Carlo Physarum Machine (Elek et al. 2022), which has a very similar range to our result. We may have some larger possible DM values because we did not take into account the immediate environment of the source.

We calculate a median $RM_{host,rf}$ of +7 rad m^{-2} with 1σ range of −74 – +99 rad m^{-2}. If we convert this to the observer's frame, we derive a median $RM_{host,obs}$ = +5.6 rad m^{-2} and a 1σ range of −59 – +79 rad m^{-2}. We note that median $RM_{host,rf}$ might be further from 0 rad m^{-2} as we have multiple restrictions on the position of the FRB, which can skew the distribution. Based on the all-sky RM map of Hutschenreuter et al. (2022), the contribution of the Milky Way towards FRB190608 is $RM_{MW} = -24 \pm 13$ rad m^{-2}. If we subtract these contributions, we derive a range of residual RM_{res} = +283 – +451 rad m^{-2}, which includes the contributions of the IGM and the immediate source environment. In the case of RM, the contributions along the line of sight can be negative or positive, hence it is difficult to determine if RM_{IGM} is lower or higher than this estimate.

We can also provide DM and RM estimates using our database of 16.5 million sightlines calculated in Section 3, however, there will be fewer sightlines that fulfill all the placing criteria we used above. In table 3, we show the median and 1σ ranges of DM and RM of all sightlines that belong to the three analog galaxies regardless of inclination and b_{offset}, of sightlines that have $b_{offset} = 6.52 \pm 0.82$, of sightlines with $42.27 < i < 43.95$,

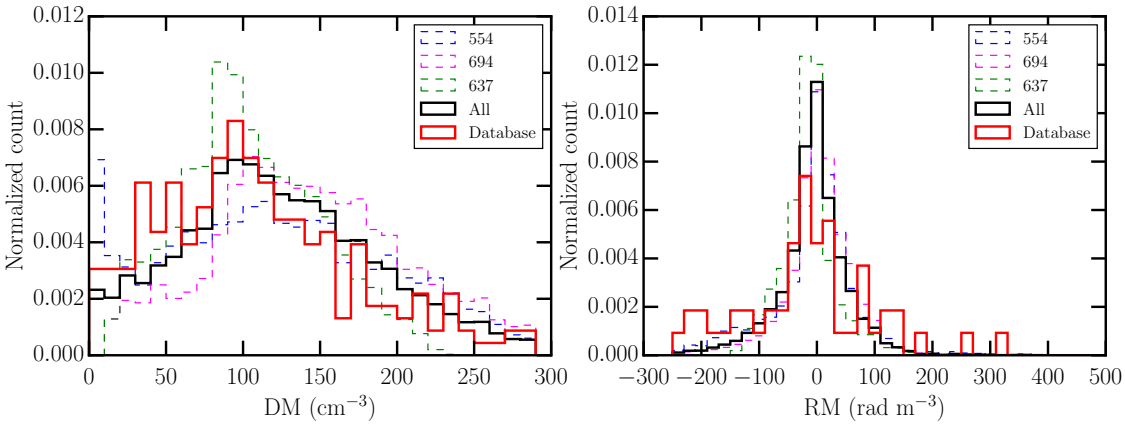

Fig. 14. Left: The $DM_{host,rf}$ distribution of FRBs placed in the analogs of the host galaxy of FRB190608. Right: The $RM_{host,rf}$ distribution of FRBs placed in the in the analogs of the host galaxy of FRB190608.

and of sightlines that fulfill both the b_{offset} and i criteria. The medians and ranges of the different sightline selections are of the same magnitude. We find that constraining the inclination of selected sightlines had a bigger effect on the ranges of DM and RM than constraining b_{offset} (which gives almost the same DM and RM range compared to the full sample of sightlines). We find this to be the case even if we increase the uncertainty of the inclination ($32.27 < i < 53.95$), so it is not only caused by the lower relative uncertainty of the inclination compared to that of the offset.

We can see that in the case of host DM we get a similar range of values from our database of sightlines (even without strict selection criteria) and from placing FRBs at a more specified location, but for host RM the possible range is much larger in the case of sightlines from our database. This could be because RM is more sensitive to the exact place in the galaxy, as in our previous test we placed FRBs specifically on the minor axis. The DM histogram of the offset-selected sightlines, and the inclination-selected RM sightlines match the histogram of our previous test the most. Therefore we suggest, if possible, selecting sightlines based on their inclination when one wants to constrain the RM contribution of a host galaxy from our database of sightlines.

In summary, we showed that IllustrisTNG gives reasonable estimates on the DM and RM of host galaxies as they are consistent with observations. We demonstrated that our database of sightlines can be used to constrain the DM and RM contributions of host galaxies.

7. Conclusions

We have calculated the DM and RM contribution of FRB host galaxies ($DM_{host,rf}$ and $RM_{host,rf}$) using the state-of-the-art MHD simulation TNG50 of IllustrisTNG project for a large sample of galaxies (~16 500). We investigated how the median $DM_{host,rf}$ and the width of the $RM_{host,rf}$ distribution ($w_{RM,rf}$) change with redshift, stellar mass, inclination, and FRB projected offsets from the center of galaxies (b_{offset}).

Our main findings are:

- The distributions of $DM_{host,rf}$ can be fitted by a lognormal function, and the shape of the distributions of $RM_{host,rf}$ can be fitted by a combination of one Lorentzian and two Gaussian functions. The shape of the distributions does not change with the host galaxy's redshift, stellar mass, star formation, inclination, or b_{offset}. However, we find that the parameters of these distributions change with the properties listed above (see Tables A.1 and A.3).
- We find that the median of $DM_{host,rf}$ increases as a function of redshift. This can be explained by galaxies at higher redshifts having higher SFRs and therefore higher electron densities. This can be seen as an increase in the electron density profiles of galaxies in the simulation at higher redshifts.
- The median of $RM_{host,rf}$ is always 0 rad m^{-2}, and $w_{RM,rf}$ increases with redshift up to $z = 1.5$. After that, it quickly decreases. This is caused by a change in the magnetic field properties: the average of the total magnetic field strength in the disk increases by a factor of 1.2 up to z = 1, and at z=2 it drops to the same value as at z=0. At $z = 2$ the azimuthal and radial components have similar relative strengths, but at $z = 0$ the relative strength of the azimuthal field is 5-6 times larger than the other two components. We also find the presence of more azimuthal reversals or random fields at $z > 1$ compared to $z < 1$, showing the B field becomes ordered as redshift decreases.
- The median of $DM_{host,rf}$ increases with stellar mass, up to $\log(M_*/M_\odot)$>10.5), beyond which it drops. The same trend can be seen for $w_{RM,rf}$. This is caused by the increase in n_e due to increasing SFR with stellar mass, and the quenching process beginning in galaxies with $\log(M_*/M_\odot) \sim 10.5$, which also causes B fields with irregularities and lower central B field.
- We show that the median $DM_{host,obs}$ of our entire sample of galaxies from the simulation does not change significantly with redshift, remaining between 46 and 69 pc cm^{-3}, in spite of $DM_{host,rf}$ increasing with redshift. This can be useful in cases where we do not know the redshift of the FRB's galaxy, as we can assume the same range of $DM_{host,obs}$ at all redshifts.
- We find that $w_{RM,rf}$ is decreasing with redshift, which means we can constrain the host's contribution more precisely at high redshift. We find that we would need more than 95 000 polarized FRBs at $z = 0.5$ to measure an $\sigma_{RM,IGM}$ ~2 rad m^{-2} with a confidence level of 95%, but we would only need 9 500 FRBs at $z = 2$ for the same precision. As more surveys are carried out recording polarization data of FRBs, the number of FRBs with measured RM is expected to increase significantly.
- The fitted DM and RM PDFs can be used in the frameworks of Walker et al. (2020) and Hackstein et al. (2020) to estimate the redshift of FRBs and to constrain the IGMF, providing additional choices for the host galaxy DM and RM PDFs.

– We apply our method to estimate the host DM and RM contribution for the well localized FRB190806. We found our DM and RM estimates are consistent with observations, thus our database of sightlines can be used to constrain the DM and RM contributions of host galaxies.

We note that the TNG50 model probably does not model the action of the mean-field dynamo, due to the limited spatial resolution. A future (improved) MHD simulation may be able to include the mean-field dynamo, which might affect our RM results. However, observations show that the large-scale field is generally weaker than the field at small scales (Beck et al. 2019), so these effects might be low but would warrant further investigations.

We provide an estimate of the host galaxies' DM and RM contribution which will allow future studies to separate the DM and RM of the IGM from the observed DM and RM of the FRBs. These results will help studies of the magnetic field of the IGM and the cosmic baryon density. We will publish the list of 16.5 million DM and RM values, together with the galaxy IDs in TNG50, positions of the FRBs and galaxy inclinations on github and provide a python package that can be used to get the PDFs fitted in this work. This will allow future works to use their own subset of FRBs, with different assumptions on host galaxy properties (stellar mass and star formation rate) and FRB redshift distributions to fit their own distributions.

Acknowledgements. We thank Rainer Beck for his valuable suggestions and comments. The IllustrisTNG simulations were undertaken with compute time awarded by the Gauss Centre for Supercomputing (GCS) under GCS Large-Scale Projects GCS-ILLU and GCS-DWAR on the GCS share of the supercomputer Hazel Hen at the High Performance Computing Center Stuttgart (HLRS), as well as on the machines of the Max Planck Computing and Data Facility (MPCDF) in Garching, Germany. Computations in this paper were performed on the HPC system Raven at the MPCDF. This research has made use of NASA's Astrophysics Data System Bibliographic Services.

References

Akahori, T., Ryu, D., & Gaensler, B. M. 2016, ApJ, 824, 105
Anderson, C. S., Heald, G. H., Eilek, J. A., et al. 2021, PASA, 38, e020
Arshakian, T. G., Beck, R., Krause, M., & Sokoloff, D. 2009, A&A, 494, 21
Arvo, J. 1992, in Graphics Gems III (IBM Version), ed. D. KIRK (San Francisco: Morgan Kaufmann), 117–120
Bannister, K. W., Deller, A. T., Phillips, C., et al. 2019, Science, 365, 565
Basu, A., Mao, S. A., Fletcher, A., et al. 2018, MNRAS, 477, 2528
Baym, G., Bödeker, D., & McLerran, L. 1996, Phys. Rev. D, 53, 662
Beck, R. 2007, A&A, 470, 539
Beck, R. 2012, Space Sci. Rev., 166, 215
Beck, R. 2013, in Large-Scale Magnetic Fields in the Universe, ed. R. Beck, A. Balogh, A. Bykov, R. A. Treumann, & L. Widrow, Vol. 39, 215–230
Beck, R., Chamandy, L., Elson, E., & Blackman, E. G. 2019, Galaxies, 8, 4
Bell, E. F., Wolf, C., Meisenheimer, K., et al. 2004, ApJ, 608, 752
Berkhuijsen, E. M., Urbanik, M., Beck, R., & Han, J. L. 2016, A&A, 588, A114
Bhandari, S., Heintz, K. E., Aggarwal, K., et al. 2022, AJ, 163, 69
Bhandari, S., Keane, E. F., Barr, E. D., et al. 2018, MNRAS, 475, 1427
Bochenek, C. D., Ravi, V., & Dong, D. 2021, ApJ, 907, L31
Brandenburg, A. & Subramanian, K. 2005, Phys. Rep., 417, 1
Carretti, E., O'Sullivan, S. P., Vacca, V., et al. 2023, MNRAS, 518, 2273
Cen, R. & Ostriker, J. P. 1999, ApJ, 514, 1
Chamandy, L. & Taylor, A. R. 2015, ApJ, 808, 28
Chatterjee, S., Law, C. J., Wharton, R. S., et al. 2017, Nature, 541, 58
CHIME/FRB Collaboration, Amiri, M., Andersen, B. C., et al. 2021, ApJS, 257, 59
CHIME/FRB Collaboration, Andersen, B. C., Bandura, K. M., et al. 2020, Nature, 587, 54
Chittidi, J. S., Simha, S., Mannings, A., et al. 2021, ApJ, 922, 173
Combes, F. 2017, Frontiers in Astronomy and Space Sciences, 4, 10
Conselice, C. J. 2014, ARA&A, 52, 291
Cordes, J. M. & Chatterjee, S. 2019, ARA&A, 57, 417
Cordes, J. M. & Lazio, T. J. W. 2002, arXiv e-prints, astro
Day, C. K., Deller, A. T., Shannon, R. M., et al. 2020, MNRAS, 497, 3335
de Graaff, A., Cai, Y.-C., Heymans, C., & Peacock, J. A. 2019, A&A, 624, A48
Dolag, K., Gaensler, B. M., Beck, A. M., & Beck, M. C. 2015, MNRAS, 451, 4277
Donnari, M., Pillepich, A., Nelson, D., et al. 2019, MNRAS, 485, 4817
Eckert, D., Jauzac, M., Shan, H., et al. 2015, Nature, 528, 105
Elek, O., Burchett, J. N., Prochaska, J. X., & Forbes, A. G. 2022, arXiv e-prints, arXiv:2204.01256
Ferreira, L., Adams, N., Conselice, C. J., et al. 2022, ApJ, 938, L2
Ferreira, R. J. Z., Jain, R. K., & Sloth, M. S. 2013, J. Cosmology Astropart. Phys., 2013, 004
Gao, H., Li, Z., & Zhang, B. 2014, ApJ, 788, 189
Gardenier, D. W. 2019, frbpoppy: Fast radio burst population synthesis in Python, Astrophysics Source Code Library, record ascl:1911.009
Grand, R. J. J., Gómez, F. A., Marinacci, F., et al. 2017, MNRAS, 467, 179
Hackstein, S., Brüggen, M., Vazza, F., Gaensler, B. M., & Heesen, V. 2019, MNRAS, 488, 4220
Hackstein, S., Brüggen, M., Vazza, F., & Rodrigues, L. F. S. 2020, MNRAS, 498, 4811
Hackstein, S., Vazza, F., Brüggen, M., Sigl, G., & Dundovic, A. 2016, MNRAS, 462, 3660
Hashimoto, T., Goto, T., On, A. Y. L., et al. 2020, MNRAS, 497, 4107
Haverkorn, M., Brown, J. C., Gaensler, B. M., & McClure-Griffiths, N. M. 2008, ApJ, 680, 362
Heintz, K. E., Prochaska, J. X., Simha, S., et al. 2020, ApJ, 903, 152
Hutschenreuter, S., Anderson, C. S., Betti, S., et al. 2022, A&A, 657, A43
James, C. W., Ghosh, E. M., Prochaska, J. X., et al. 2022, MNRAS, 516, 4862
Jansson, R. & Farrar, G. R. 2012, ApJ, 757, 14
Jaroszyński, M. 2020, Acta Astron., 70, 87
Kaasinen, M., Bian, F., Groves, B., Kewley, L. J., & Gupta, A. 2017, MNRAS, 465, 3220
Kahniashvili, T., Brandenburg, A., Campanelli, L., Ratra, B., & Tevzadze, A. G. 2012, Phys. Rev. D, 86, 103005
Kahniashvili, T., Tevzadze, A. G., Brandenburg, A., & Neronov, A. 2013, Phys. Rev. D, 87, 083007
Keating, L. C. & Pen, U.-L. 2020, MNRAS, 496, L106
Kovács, O. E., Bogdán, Á., Smith, R. K., Kraft, R. P., & Forman, W. R. 2019, ApJ, 872, 83
Krause, M., Irwin, J., Wiegert, T., et al. 2018, A&A, 611, A72
Labbé, I., van Dokkum, P., Nelson, E., et al. 2023, Nature, 616, 266
Lacey, C. G., Baugh, C. M., Frenk, C. S., et al. 2016, MNRAS, 462, 3854
Li, D., Wang, P., Zhu, W. W., et al. 2021, Nature, 598, 267
Licquia, T. C. & Newman, J. A. 2015, ApJ, 806, 96
Lorimer, D. R., Bailes, M., McLaughlin, M. A., Narkevic, D. J., & Crawford, F. 2007, Science, 318, 777
Lyutikov, M. 2022, ApJ, 933, L6
Macquart, J. P., Keane, E., Grainge, K., et al. 2015, in Advancing Astrophysics with the Square Kilometre Array (AASKA14), 55
Macquart, J. P., Prochaska, J. X., McQuinn, M., et al. 2020, Nature, 581, 391
Mannings, A. G., Fong, W.-f., Simha, S., et al. 2021, ApJ, 917, 75
Mannings, A. G., Pakmor, R., Prochaska, J. X., et al. 2022, arXiv e-prints, arXiv:2209.15113
Marcote, B., Kirsten, F., Hessels, J., et al. 2022, in European VLBI Network Mini-Symposium and Users' Meeting 2021, Vol. 2021, 35
Marinacci, F., Vogelsberger, M., Pakmor, R., et al. 2018, MNRAS, 480, 5113
Masui, K., Lin, H.-H., Sievers, J., et al. 2015, Nature, 528, 523
Mckinven, R., Michilli, D., Masui, K., et al. 2021, ApJ, 920, 138
McQuinn, M. 2014, ApJ, 780, L33
Michilli, D., Seymour, A., Hessels, J. W. T., et al. 2018, Nature, 553, 182
Mitchell, P. D., Lacey, C. G., Lagos, C. D. P., et al. 2018, MNRAS, 474, 492
Mo, J.-F., Zhu, W., Wang, Y., Tang, L., & Feng, L.-L. 2023, MNRAS, 518, 539
Moss, D., Shukurov, A., & Sokoloff, D. 2000, A&A, 358, 1142
Nelson, D., Pillepich, A., Springel, V., et al. 2019a, MNRAS, 490, 3234
Nelson, D., Springel, V., Pillepich, A., et al. 2019b, Computational Astrophysics and Cosmology, 6, 2
Nicastro, F., Kaastra, J., Krongold, Y., et al. 2018, Nature, 558, 406
Noeske, K. G., Weiner, B. J., Faber, S. M., et al. 2007, ApJ, 660, L43
Oppermann, N., Junklewitz, H., Robbers, G., et al. 2012, A&A, 542, A93
O'Sullivan, S. P., Brüggen, M., Vazza, F., et al. 2020, MNRAS, 495, 2607
Pakmor, R., Gómez, F. A., Grand, R. J. J., et al. 2017, MNRAS, 469, 3185
Pakmor, R., Guillet, T., Pfrommer, C., et al. 2018, MNRAS, 481, 4410
Pellegrini, E. W., Reissl, S., Rahner, D., et al. 2020, MNRAS, 498, 3193
Petroff, E., Barr, E. D., Jameson, A., et al. 2016, PASA, 33, e045
Petroff, E., Hessels, J. W. T., & Lorimer, D. R. 2019, A&A Rev., 27, 4
Pillepich, A., Nelson, D., Springel, V., et al. 2019, MNRAS, 490, 3196
Pillepich, A., Springel, V., Nelson, D., et al. 2018, MNRAS, 473, 4077
Piro, A. L. & Gaensler, B. M. 2018, ApJ, 861, 150
Planck Collaboration, Ade, P. A. R., Aghanim, N., et al. 2016, A&A, 594, A19
Platts, E., Weltman, A., Walters, A., et al. 2019, Phys. Rep., 821, 1
Prochaska, J. X. & Zheng, Y. 2019, MNRAS, 485, 648
Ravi, V., Catha, M., D'Addario, L., et al. 2019, Nature, 572, 352

Rodrigues, L. F. S. & Chamandy, L. 2020, Magnetizer: Computing magnetic fields of evolving galaxies, Astrophysics Source Code Library, record ascl:2008.011
Rodrigues, L. F. S., Chamandy, L., Shukurov, A., Baugh, C. M., & Taylor, A. R. 2019, MNRAS, 483, 2424
Shimakawa, R., Kodama, T., Steidel, C. C., et al. 2015, MNRAS, 451, 1284
Shukurov, A. & Subramanian, K. 2021, Astrophysical Magnetic Fields: From Galaxies to the Early Universe, Cambridge Astrophysics (Cambridge University Press)
Sigl, G., Miniati, F., & Ensslin, T. A. 2003, Phys. Rev. D, 68, 043002
Simha, S., Burchett, J. N., Prochaska, J. X., et al. 2020, ApJ, 901, 134
Spitler, L. G., Scholz, P., Hessels, J. W. T., et al. 2016, Nature, 531, 202
Springel, V. & Hernquist, L. 2003, MNRAS, 339, 289
Thornton, D., Stappers, B., Bailes, M., et al. 2013, Science, 341, 53
Tombesi, F., Cappi, M., Reeves, J. N., et al. 2010, A&A, 521, A57
Vazza, F., Locatelli, N., Rajpurohit, K., et al. 2021, Galaxies, 9, 109
Walker, C. R. H., Ma, Y.-Z., & Breton, R. P. 2020, A&A, 638, A37
Wang, X.-G., Li, L., Yang, Y.-P., et al. 2020, ApJ, 894, L22
Weinberger, R., Springel, V., Hernquist, L., et al. 2017, MNRAS, 465, 3291
Weinberger, R., Springel, V., Pakmor, R., et al. 2018, MNRAS, 479, 4056
Xu, J. & Han, J. L. 2015, Research in Astronomy and Astrophysics, 15, 1629
Yao, J. M., Manchester, R. N., & Wang, N. 2017, ApJ, 835, 29
Yaron, O., Ofek, E., Gal-Yam, A., & Sass, A. 2020, Transient Name Server AstroNote, 70, 1
Zahid, H. J., Dima, G. I., Kewley, L. J., Erb, D. K., & Davé, R. 2012, ApJ, 757, 54
Zanazzi, J. J. & Lai, D. 2020, ApJ, 892, L15
Zhang, G. Q., Yu, H., He, J. H., & Wang, F. Y. 2020, ApJ, 900, 170
Zheng, Z., Ofek, E. O., Kulkarni, S. R., Neill, J. D., & Juric, M. 2014, ApJ, 797, 71
Zhou, B., Li, X., Wang, T., Fan, Y.-Z., & Wei, D.-M. 2014, Phys. Rev. D, 89, 107303

Appendix A: Fit parameter tables

In Table A.1 we list the fitted parameters of the redshift evolutions of the median $DM_{host,rf}$, $w_{DM,rf}$ and $w_{RM,rf}$ (which are derived from the actual distributions of DM and RM host contributions) from Eq. 14 and 18. In Tables A.2 and A.3, we also list the parameters (A_{DM}, B_{DM} and C_{DM} for DM from Eq. 16, and A_{RM}, B_{RM}, C_{RM} and D_{RM} for RM from Eq. 18) of the redshift evolution of the parameters of the fitted PDFs: lognormal function for DM (Eq. 13, σ and μ) and the sum of two Gaussian and a Lorentzian for RM (Eq. 17, a_1, a_2, a_3, γ, σ_1 and σ_2).

Table A.1. The fitted parameters of the power law relation of the median and 1σ width ($w_{\rm DM,rf}$) of the actual restframe $\rm DM_{host}$ distributions (without fitting) as a function of redshift, and the fitted parameters of the curved power law relation of the 1σ width ($w_{\rm RM,rf}$) of the actual restframe $\rm RM_{host}$ distributions (without fitting) as a function of redshift.

	median $\rm DM_{host,rf}$ fit			$w_{\rm DM,rf}$ fit			$w_{\rm RM,rf}$ fit			
	a	b	c	a	b	c	$A_{\rm RM}$	$D_{\rm RM}$	$B_{\rm RM}$	$C_{\rm RM}$
All galaxies	82 ± 4	0.8 ± 0.1	40 ± 3	241 ± 40	0.6 ± 0.1	93 ± 34	267 ± 4	1.24 ± 0.04	-0.57 ± 0.03	117 ± 3
Star-forming	81 ± 4	0.8 ± 0.1	43 ± 3	113 ± 8	0.7 ± 0.1	94 ± 7	264 ± 4	1.24 ± 0.04	-0.57 ± 0.03	125 ± 3
Red	41 ± 3	1.4 ± 0.1	13 ± 2	82 ± 7	1.3 ± 0.1	33 ± 4	60 ± 17	20.41 ± 304.02	-24.0 ± 433.73	38 ± 7
9 <$\log(M_*/\rm M_\odot)$< 9.5	70 ± 3	0.74 ± 0.05	41 ± 3	95 ± 6	0.7 ± 0.1	87 ± 5	155 ± 4	1.16 ± 0.07	-0.47 ± 0.05	111 ± 3
9.5 <$\log(M_*/\rm M_\odot)$< 10	83 ± 4	0.78 ± 0.05	50 ± 3	107 ± 8	0.7 ± 0.1	105 ± 7	280 ± 8	1.1 ± 0.07	-0.44 ± 0.05	151 ± 6
10 <$\log(M_*/\rm M_\odot)$< 10.5	97 ± 5	0.7 ± 0.05	47 ± 4	121 ± 8	0.6 ± 0.1	121 ± 6	484 ± 20	1.04 ± 0.1	-0.49 ± 0.07	155 ± 17
10.5 <$\log(M_*/\rm M_\odot)$< 11	105 ± 8	0.97 ± 0.08	18 ± 6	188 ± 15	0.7 ± 0.1	56 ± 12	530 ± 20	2.32 ± 0.19	-0.94 ± 0.1	76 ± 12
$\log(M_*/\rm M_\odot) > 11$	79 ± 6	1.35 ± 0.09	26 ± 4	168 ± 18	1.2 ± 0.1	52 ± 12	293 ± 27	3.4 ± 0.65	-2.02 ± 0.41	62 ± 15
$i < 10°$	65 ± 2	0.93 ± 0.03	33 ± 1	94 ± 5	0.9 ± 0.1	62 ± 4	171 ± 3	1.38 ± 0.05	-0.43 ± 0.03	56 ± 2
$10° < i < 45°$	70 ± 2	0.87 ± 0.04	35 ± 2	98 ± 5	0.9 ± 0.1	67 ± 4	202 ± 2	1.35 ± 0.03	-0.48 ± 0.02	77 ± 2
$45° < i < 80°$	86 ± 5	0.73 ± 0.05	42 ± 4	117 ± 8	0.7 ± 0.1	95 ± 7	291 ± 4	1.22 ± 0.04	-0.6 ± 0.03	130 ± 4
$80° < i$	94 ± 7	0.63 ± 0.07	48 ± 6	124 ± 15	0.4 ± 0.1	142 ± 14	333 ± 8	1.11 ± 0.07	-0.67 ± 0.05	184 ± 7
$b_{\rm offset} < 5$ kpc	78 ± 2	0.84 ± 0.02	50 ± 1	96 ± 5	0.67 ± 0.05	112 ± 4	301 ± 3	1.16 ± 0.03	-0.33 ± 0.02	201 ± 2
5 kpc < $b_{\rm offset}$ < 10 kpc	86 ± 7	0.72 ± 0.08	38 ± 6	121 ± 10	0.69 ± 0.08	86 ± 9	253 ± 6	1.3 ± 0.07	-0.7 ± 0.05	92 ± 5
10 < $b_{\rm offset}$ < 30 kpc	82 ± 7	0.7 ± 0.08	30 ± 6	135 ± 14	0.64 ± 0.09	68 ± 12	166 ± 6	1.18 ± 0.1	-0.72 ± 0.07	59 ± 5
30 < $b_{\rm offset}$	52 ± 2	1.18 ± 0.05	30 ± 1	136 ± 13	0.88 ± 0.1	55 ± 10	37 ± 5	0.99 ± 0.32	0.0 ± 0.17	27 ± 4

*Notes:*The different lines of the table correspond to using every galaxy, galaxies with different star formation activity, galaxies in different stellar mass bins, galaxies with different inclinations and FRBs with different projected offsets from the center of the host galaxy ($b_{\rm offset}$). We also list the fitted parameters of the curved power law relation between the width of the actual RM distribution (without fitting) and redshift for the same subsets of galaxies.

Table A.2. The exponential fits of the redshift evolution of the parameters of the fitted lognormal DM PDFs (μ and σ).

Galaxies	Parameter	$A_{\rm DM}$	$B_{\rm DM}$	$C_{\rm DM}$
All	μ	-1.48 ± 0.02	1.24 ± 0.05	5.33 ± 0.02
	σ	0.49 ± 0.01	2.15 ± 0.05	0.8 ± 0.003
Star-forming	μ	-1.43 ± 0.02	1.21 ± 0.05	5.332 ± 0.021
	σ	0.44 ± 0.01	2.22 ± 0.08	0.801 ± 0.004
Quenched	μ	-3.05 ± 0.31	0.56 ± 0.12	5.786 ± 0.355
	σ	0.05 ± 0.18	3.21 ± 20.14	1.02 ± 0.048
$9 < \log(M_*/\rm M_\odot) < 9.5$	μ	-1.29 ± 0.02	1.14 ± 0.05	5.22 ± 0.02
	σ	0.6 ± 0.05	3.46 ± 0.36	0.82 ± 0.01
$9.5 < \log(M_*/\rm M_\odot) < 10$	μ	-1.36 ± 0.04	1.12 ± 0.11	5.42 ± 0.05
	σ	0.45 ± 0.02	2.72 ± 0.23	0.77 ± 0.01
$10 < \log(M_*/\rm M_\odot) < 10.5$	μ	-1.43 ± 0.04	1.53 ± 0.12	5.37 ± 0.04
	σ	0.48 ± 0.03	1.65 ± 0.3	0.75 ± 0.03
$10.5 < \log(M_*/\rm M_\odot) < 11$	μ	-2.64 ± 0.09	1.06 ± 0.08	5.79 ± 0.1
	σ	0.87 ± 1.12	0.19 ± 0.29	0.23 ± 1.13
$\log(M_*/\rm M_\odot) > 11$	μ	-4.0 ± 0.99	0.4 ± 0.14	7.3 ± 1.01
	σ	-0.12 ± 0.03	1.65 ± 1.07	1.0 ± 0.03
$i < 10°$	μ	-1.79 ± 0.03	0.95 ± 0.03	5.35 ± 0.03
	σ	0.32 ± 0.01	2.55 ± 0.19	0.75 ± 0.01
$10° < i < 45°$	μ	-1.68 ± 0.03	1.03 ± 0.04	5.33 ± 0.03
	σ	0.35 ± 0.01	2.47 ± 0.15	0.76 ± 0.01
$45° < i < 80°$	μ	-1.42 ± 0.02	1.33 ± 0.05	5.33 ± 0.02
	σ	0.51 ± 0.0	2.25 ± 0.05	0.8 ± 0.0
$80° < i$	μ	-1.22 ± 0.02	1.63 ± 0.08	5.31 ± 0.02
	σ	0.8 ± 0.01	1.87 ± 0.07	0.84 ± 0.01
$b_{\rm offset} < 5$ kpc	μ	-1.38 ± 0.03	0.8 ± 0.04	5.53 ± 0.04
	σ	0.96 ± 0.04	3.8 ± 0.33	0.76 ± 0.02
5 kpc < $b_{\rm offset}$ < 10 kpc	μ	-1.56 ± 0.03	1.36 ± 0.07	5.32 ± 0.03
	σ	0.43 ± 0.02	2.41 ± 0.25	0.83 ± 0.01
10 < $b_{\rm offset}$ < 30 kpc	μ	-1.66 ± 0.04	1.49 ± 0.09	5.18 ± 0.04
	σ	0.07 ± 0.01	2.01 ± 0.8	0.94 ± 0.01
30 < $b_{\rm offset}$	μ	-2.3 ± 0.22	0.58 ± 0.1	5.72 ± 0.24
	σ	-0.21 ± 0.05	5.29 ± 2.65	1.06 ± 0.02

Galaxies	Par.	A_{RM}	B_{RM}	C_{RM}	D_{RM}
All	a_1	0.24 ± 0.01	-0.38 ± 0.05	0.57 ± 0.01	0.68 ± 0.06
	a_2	-0.06 ± 0.0	-0.7 ± 0.09	0.19 ± 0.0	1.24 ± 0.14
	a_3	-0.18 ± 0.02	-0.29 ± 0.06	0.25 ± 0.02	0.5 ± 0.08
	γ	76.45 ± 0.67	-0.59 ± 0.02	72.46 ± 0.51	1.37 ± 0.03
	σ_1	1.11 ± 0.13	-0.38 ± 0.17	6.84 ± 0.1	0.64 ± 0.16
	σ_2	12.25 ± 0.33	-0.52 ± 0.05	20.64 ± 0.26	1.13 ± 0.07
Star-forming	a_1	0.23 ± 0.01	-0.38 ± 0.04	0.59 ± 0.01	0.68 ± 0.05
	a_2	-0.06 ± 0.0	-0.66 ± 0.09	0.2 ± 0.0	1.2 ± 0.13
	a_3	-0.16 ± 0.01	-0.31 ± 0.06	0.23 ± 0.01	0.51 ± 0.07
	γ	75.44 ± 0.77	-0.6 ± 0.02	73.81 ± 0.54	1.37 ± 0.03
	σ_1	1.07 ± 0.12	-0.53 ± 0.2	6.99 ± 0.09	0.65 ± 0.17
	σ_2	12.01 ± 0.31	-0.55 ± 0.05	20.99 ± 0.22	1.14 ± 0.07
Quenched	a_1	0.16 ± 0.1	0.18 ± 0.1	0.35 ± 0.1	0.2 ± 0.2
	a_2	0.06 ± 0.01	-5.55 ± 5.2	0.12 ± 0.0	11.34 ± 10.41
	a_3	-0.26 ± 0.14	0.81 ± 0.58	0.58 ± 0.14	0.27 ± 0.38
	γ	-1.19 ± 28.71	1.39 ± 13.45	44.35 ± 28.84	0.0 ± 22.46
	σ_1	1.58 ± 13.15	-0.97 ± 8.74	1.54 ± 13.06	0.0 ± 1.43
	σ_2	7.52 ± 1.29	-4.69 ± 4.6	14.05 ± 1.16	4.28 ± 3.1
$9 < \log(M_*/\mathrm{M}_\odot) < 9.5$	a_1	0.23 ± 0.02	-0.38 ± 0.09	0.6 ± 0.02	0.66 ± 0.1
	a_2	-0.04 ± 0.01	-0.57 ± 0.36	0.18 ± 0.01	1.05 ± 0.46
	a_3	-0.16 ± 0.02	-0.29 ± 0.09	0.25 ± 0.02	0.44 ± 0.12
	γ	50.1 ± 2.52	-0.7 ± 0.14	65.98 ± 1.58	1.7 ± 0.2
	σ_1	1.97 ± 0.11	-0.85 ± 0.15	6.79 ± 0.08	1.63 ± 0.22
	σ_2	13.12 ± 0.82	-0.96 ± 0.19	20.02 ± 0.4	2.13 ± 0.28
$9.5 < \log(M_*/\mathrm{M}_\odot) < 10$	a_1	0.21 ± 0.01	-0.3 ± 0.09	0.63 ± 0.01	0.5 ± 0.06
	a_2	-0.06 ± 0.01	-0.17 ± 0.16	0.2 ± 0.0	0.54 ± 0.11
	a_3	-0.1 ± 0.01	-0.28 ± 0.12	0.19 ± 0.01	0.29 ± 0.08
	γ	109.63 ± 8.32	-0.72 ± 0.17	82.65 ± 1.92	1.57 ± 0.17
	σ_1	4.92 ± 0.28	-1.16 ± 0.16	7.21 ± 0.09	1.8 ± 0.17
	σ_2	40.45 ± 3.57	-1.27 ± 0.22	22.28 ± 0.45	2.14 ± 0.21
$10 < \log(M_*/\mathrm{M}_\odot) < 10.5$	a_1	0.26 ± 0.01	-0.4 ± 0.08	0.56 ± 0.01	0.62 ± 0.06
	a_2	-0.08 ± 0.01	-0.28 ± 0.15	0.22 ± 0.0	0.62 ± 0.13
	a_3	-0.13 ± 0.01	-0.3 ± 0.11	0.21 ± 0.01	0.35 ± 0.09
	γ	178.25 ± 17.63	-0.83 ± 0.19	98.8 ± 3.3	1.59 ± 0.19
	σ_1	6.17 ± 0.97	-1.66 ± 0.43	7.37 ± 0.2	2.12 ± 0.44
	σ_2	59.5 ± 8.35	-1.69 ± 0.31	24.78 ± 0.69	2.5 ± 0.31
$10.5 < \log(M_*/\mathrm{M}_\odot)) < 11$	a_1	0.31 ± 0.02	-0.43 ± 0.08	0.41 ± 0.01	0.84 ± 0.1
	a_2	-0.04 ± 0.01	-1.43 ± 0.82	0.22 ± 0.01	3.17 ± 1.59
	a_3	-0.29 ± 0.02	-0.28 ± 0.06	0.38 ± 0.02	0.48 ± 0.08
	γ	167.68 ± 11.47	-0.74 ± 0.17	50.79 ± 3.35	1.9 ± 0.23
	σ_1	2.05 ± 0.23	-0.38 ± 0.22	6.71 ± 0.1	1.11 ± 0.25
	σ_2	26.2 ± 2.91	-1.24 ± 0.3	19.52 ± 0.78	2.39 ± 0.42
$\log(M_*/\mathrm{M}_\odot) > 11$	a_1	-0.01 ± 0.06	1.43 ± 2.82	0.62 ± 0.05	0.0 ± 1.84
	a_2	0.03 ± 0.1	0.64 ± 0.39	0.14 ± 0.1	0.47 ± 4.33
	a_3	-1.15 ± 16.54	-0.02 ± 0.32	1.35 ± 16.54	0.04 ± 0.65
	γ	104.54 ± 16.89	-1.07 ± 0.56	34.4 ± 4.12	2.29 ± 0.71
	σ_1	0.75 ± 0.36	-0.4 ± 0.74	6.09 ± 0.31	1.63 ± 1.54
	σ_2	14.03 ± 2.79	-1.27 ± 0.64	15.15 ± 1.8	2.41 ± 0.97
$i < 10°$	a_1	0.19 ± 0.02	-0.44 ± 0.17	0.64 ± 0.02	0.6 ± 0.16
	a_2	-0.05 ± 0.02	-4.64 ± 5.1	0.15 ± 0.01	3.61 ± 3.8
	a_3	-0.26 ± 0.07	-0.26 ± 0.16	0.35 ± 0.07	0.39 ± 0.2
	γ	65.95 ± 2.62	-0.33 ± 0.09	27.86 ± 1.06	1.36 ± 0.11
	σ_1	7.25 ± 1.47	-1.22 ± 0.58	2.57 ± 0.47	1.99 ± 0.69
	σ_2	17.96 ± 1.93	-0.35 ± 0.26	9.77 ± 0.85	1.47 ± 0.35
$10° < i < 45°$	a_1	0.23 ± 0.01	-0.39 ± 0.06	0.6 ± 0.01	0.57 ± 0.05
	a_2	-0.01 ± 0.0	-4.95 ± 3.76	0.14 ± 0.0	5.79 ± 4.57
	a_3	-0.19 ± 0.03	-0.25 ± 0.09	0.29 ± 0.03	0.37 ± 0.1
	γ	73.39 ± 1.04	-0.56 ± 0.04	44.3 ± 0.44	1.61 ± 0.05
	σ_1	2.34 ± 0.18	-0.9 ± 0.22	6.54 ± 0.11	1.88 ± 0.33
	σ_2	18.51 ± 0.51	-1.07 ± 0.09	16.42 ± 0.2	2.41 ± 0.13

Galaxies	Par.	A_{RM}	B_{RM}	C_{RM}	D_{RM}
$45^\circ < i < 80^\circ$	a_1	0.2 ± 0.01	-0.36 ± 0.07	0.6 ± 0.01	0.6 ± 0.07
	a_2	-0.04 ± 0.01	-0.56 ± 0.2	0.19 ± 0.0	1.01 ± 0.27
	a_3	-0.14 ± 0.02	-0.26 ± 0.1	0.23 ± 0.02	0.38 ± 0.1
	γ	100.65 ± 2.96	-0.74 ± 0.07	77.61 ± 1.44	1.5 ± 0.09
	σ_1	2.47 ± 0.15	-0.93 ± 0.16	7.02 ± 0.09	1.73 ± 0.23
	σ_2	24.27 ± 1.14	-1.04 ± 0.13	21.46 ± 0.5	1.92 ± 0.18
$80^\circ < i$	a_1	0.18 ± 0.01	-0.35 ± 0.08	0.59 ± 0.01	0.66 ± 0.08
	a_2	-0.06 ± 0.01	-0.38 ± 0.13	0.21 ± 0.0	0.83 ± 0.18
	a_3	-0.11 ± 0.02	-0.29 ± 0.11	0.2 ± 0.02	0.41 ± 0.12
	γ	107.04 ± 4.11	-0.86 ± 0.1	107.77 ± 2.26	1.43 ± 0.12
	σ_1	2.42 ± 0.21	-1.16 ± 0.27	7.13 ± 0.13	1.99 ± 0.39
	σ_2	25.1 ± 1.59	-0.94 ± 0.17	24.26 ± 0.82	1.56 ± 0.21
$b_{\rm offset} < 5$ kpc	a_1	0.17 ± 0.01	-0.26 ± 0.11	0.65 ± 0.01	0.6 ± 0.06
	a_2	-0.03 ± 0.01	0.16 ± 0.45	0.17 ± 0.0	1.0 ± 0.5
	a_3	–0.09 ± 0.01	-0.41 ± 0.16	0.18 ± 0.01	0.38 ± 0.1
	γ	114.96 ± 5.06	-0.61 ± 0.11	101.19 ± 1.35	1.58 ± 0.11
	σ_1	11.19 ± 0.47	-0.86 ± 0.11	7.07 ± 0.08	2.49 ± 0.14
	σ_2	53.76 ± 3.93	-0.89 ± 0.21	24.94 ± 0.51	2.22 ± 0.2
5 kpc $< b_{\rm offset} <$ 10 kpc	a_1	0.21 ± 0.01	-0.35 ± 0.1	0.6 ± 0.01	0.58 ± 0.07
	a_2	-0.03 ± 0.01	-0.54 ± 0.66	0.18 ± 0.0	1.3 ± 0.72
	a_3	–0.17 ± 0.01	-0.33 ± 0.1	0.25 ± 0.01	0.4 ± 0.09
	γ	93.88 ± 2.61	-0.9 ± 0.07	56.74 ± 0.48	1.7 ± 0.07
	σ_1	3.64 ± 0.27	-1.06 ± 0.2	6.89 ± 0.07	1.85 ± 0.22
	σ_2	27.13 ± 1.85	-1.3 ± 0.19	18.81 ± 0.28	2.32 ± 0.2
10 $< b_{\rm offset} <$ 30 kpc	a_1	0.17 ± 0.04	-0.37 ± 0.15	0.58 ± 0.04	0.49 ± 0.18
	a_2	0.0 ± 0.01	1.09 ± 11.27	0.16 ± 0.01	0.0 ± 0.69
	a_3	–0.18 ± 0.05	-0.32 ± 0.14	0.3 ± 0.05	0.39 ± 0.16
	γ	62.39 ± 2.49	-0.72 ± 0.1	37.06 ± 1.83	1.3 ± 0.13
	σ_1	0.88 ± 0.26	-0.28 ± 0.25	6.44 ± 0.25	0.46 ± 0.27
	σ_2	9.36 ± 0.83	-0.55 ± 0.17	15.2 ± 0.79	1.02 ± 0.23
30 $< b_{\rm offset}$	a_1	-0.17 ± 0.09	-0.79 ± 0.59	0.57 ± 0.09	0.55 ± 0.43
	a_2	0.06 ± 0.02	-1.07 ± 0.48	0.11 ± 0.01	2.64 ± 1.02
	a_3	-0.01 ± 0.28	1.57 ± 9.33	0.41 ± 0.34	0.0 ± 10.36
	γ	56.4 ± 2.44	-0.69 ± 0.11	21.59 ± 1.88	1.39 ± 0.15
	σ_1	0.13 ± 0.15	-2.59 ± 2.34	6.12 ± 0.08	7.25 ± 5.9
	σ_2	5.42 ± 2.52	-0.97 ± 0.95	16.16 ± 2.17	2.08 ± 1.79

Table A.3. The curved power law fits of the redshift evolution of the parameters of the RM PDFs, where the fitted function consists of a Lorentzian and two Gaussian functions. The parameters a_1, a_2 and a_3 are normalization factors. We also list the γ parameter of the Lorentzian function, and the σ_1 and σ_2 parameters of the two Gaussian functions.

Appendix B: Effects of different parameter choices

Appendix B.1: Number of sightlines

Due to computational reasons we do not use 10000 sightlines per galaxy, only 1000 sightlines. Using 10000 sightlines would have taken 30 days for the whole sample. 1000 sightlines is sufficient, as two runs of the pipeline gives the same overall distribution at a given redshift.

Appendix B.2: Integral path length

We performed calculations using different integral path lengths, to see how the choice affects the DM and RM. Using the same galaxies, with the same inclination and FRB positions, we tried integrating out to $r_{SF,99}$, 1.5 x $r_{SF,99}$, 2 x $r_{SF,99}$ and 3 x $r_{SF,99}$. We found a significant difference in the resulting DMs and RMs. In the case of $r_{SF,99}$ and 2 x $r_{SF,99}$, 68% of our sightlines have a DM difference less than 50 pc cm^{-3}, and the maximum DM difference is 7870 pc cm^{-3}. The RM is affected less, 68 % of sightlines have a difference less than 3 rad m^{-2}, but the largest RM difference is 260 000 rad m^{-2}. Since DM does not stop increasing, we define $r_{SF,99}$ as the edge of the galaxy, and we chose the integral path to be 1 x $r_{SF,99}$.

Appendix B.3: Number of rotations per galaxy

We calculated the DM and RM for the same 1200 galaxies four times: using 1, 10, 100 and a 1000 random rotations/galaxy, and investigated if the calculated DM and RM distributions have any significant differences.

Overall distribution: The mean, minimum and maximum of the DM and RM values differ significantly in the different runs (the maximum can be 3.5 times larger, the mean can differ by 30 or 10 pc cm^{-3}), as a result they do not characterize the distributions well. Because of this we looked at the medians and their 3 sigma ranges. The medians of DM and RM differ by less than 0.5 rad m^{-2} and 5 pc cm^{-3}, respectively. The 3 sigma range differs by 3 rad m^{-2} and 3 pc cm^{-3}. (for 1 rotation, there is a 30 difference compared to the others)

We compared the resulting DM and RM distributions for face-on, edge-on and in-between galaxies. If we use one rotation, only around 20 out of 1200 galaxies will be face-on ($i < 10$ °). The DM and RM distributions largely depend on which galaxies get randomly rotated to be face-on. By running the pipeline using only 1 rotation per galaxy, for the same 1200 galaxies, we derived different distributions for face-on galaxies in the two runs. These distributions were not symmetric, showing possible biases. This effect decreases if we use more rotations per galaxy. The median of RM is close to 0 rad m^{-2} in all cases. The difference of the median between RM_{1rot} and $RM_{1000rot}$ is <1 rad m^{-2}, and <0.2 rad m^{-2} between RM_{10rot},RM_{100rot} and $RM_{1000rot}$. The difference of the median between DM_{1rot} and $DM_{1000rot}$ is <40 pc cm^{-3}, and <2.5 pc cm^{-3} between DM_{10rot},DM_{100rot} and $DM_{1000rot}$. While this test shows that using even 10 rotations/galaxy significantly improves the statistics compared to using only one rotation, we saw that there are still slight differences compared to using 1000 rotations, especially in DM. We chose to rotate every galaxy 1000 times, so each FRB sightline has its own inclination.

Appendix B.4: Integral stepsize

The average cellsize in TNG50 is between 70 and 140 pc, however in dense regions the cell size can be even only a few pcs. Because of this, we explored different integral stepsizes: 5, 10, 20, 50 and 200 pc. We calculated the DM and RM for the same starting points in the same galaxies, with the same inclinations. We found that the calculated DM changes by ± 14, ± 6 and ± 3 pc cm^{-3} for the sightlines if we use 50, 20 and 10 pc stepsize, respectively. Nevertheless, the overall shape and properties of the DM distributions remain the same. The differences in the min, max, mean, median, 3 sigma width of the 5, 10 and 20 pc runs are less than 0.2%. In the case of the dl = 50 pc run, the lower range of the 3 sigma width is 2% lower than for dl = 5 pc (3.55 instead 3.62 pc cm^{-3}), otherwise all parameters have a difference of 0.1% or less. After dividing the galaxies into different stellar masses, the resulting DM and RM distributions also do not change significantly between the runs with different stepsizes. This is also the case for different offsets. We chose dl = 20 pc, as the PDF properties do not change significantly with smaller dl.

Appendix C: Main sequence of galaxies

Donnari et al. (2019) investigated the star-forming main sequence (MS) of galaxies in the Illustris TNG100 and TNG300 simulations. Donnari et al. (2019) found that in TNG100, the locus of the MS is lower by about 0.2 – 0.5 dex at z=0.75 – 2 compared to observations (the SFR values in the simulation are lower), but the MS is still qualitatively reproduced in the simulation: the SFR increases with stellar mass and redshift, but decreases for very large stellar masses. Because of this, we separate galaxies using a similar iterative method as they used, opposed to using an MS based on observations. We adapt a linearly extrapolated MS:

$$\log \mathrm{SFR_{MS}}(z) = \alpha(z) \log(\mathrm{M_*/M_\odot}) + \beta(z), \quad \text{(C.1)}$$

where the slope of the MS is determined from galaxies with 9<log($M_*/M_\odot$)<10.5 and is extrapolated to higher stellar masses. To use this method, we also need to take into account galaxies with SFR=0, and assume their SFR is below the reso-

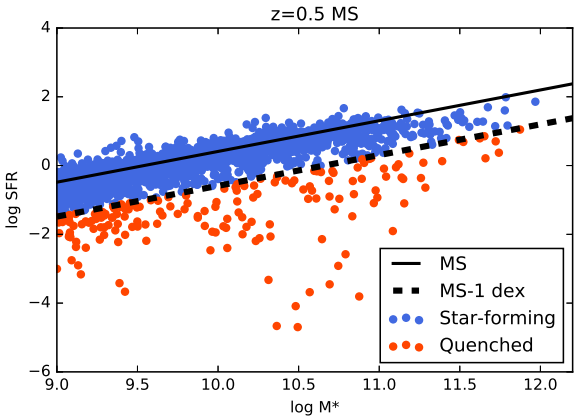

Fig. C.1. We indicate the main sequence of galaxies at z=0.5 with a black line, which was derived using an iterative method from Donnari et al. (2019). We show the the 1 dex difference from the MS with a dotted line: every galaxy below this is classified as quenched, and galaxies above as star-forming.

Table C.1. The fitted parameters of the MS defined by Eq. C.1, based on the iterative method from Donnari et al. (2019). We used this definition of MS to separate the galaxies into star-forming and red galaxies.

z	α	β
3	1.05	-9.15
2	0.98	-8.82
1.5	0.95	-8.63
1	0.94	-8.75
0.7	0.95	-8.99
0.5	0.93	-9.0
0.4	0.84	-8.15
0.3	0.91	-8.94
0.2	1.04	-10.24
0.1	0.96	-9.48
0	0.98	-9.78

lution limit ($SFR_{limit} \sim 10^{-4}$ $M_\odot$) with a random Gaussian distribution.

The fitted parameters α and β are redshift dependent, and are listed in in Table C.1, and in Fig. C.1 we show an example of the fitted main sequence at z=0.5. Galaxies with log SFR below log SFR_{MS} by at least 1 dex are classified as quenched galaxies, and galaxies above this as star-forming galaxies.

Appendix D: Calculation of Magnetic field parameters

The magnetic field properties are calculated similarly to Pakmor et al. (2017) and Pakmor et al. (2018). The equations D.1,D.2 and D.3 were taken from Pakmor et al. (2017).

Appendix D.1: Magnetic field strength - face-on

We calculate the projected absolute magnetic field strength in a face-on view for every galaxy, with two examples shown in the second row of Fig. D.3 and D.4. For this we calculate the line-of-sight integral of the magnetic energy density (B^2) in a $r_{SF,99}$ x $r_{SF,99}$ x $2 \cdot$ h box. We use B^2 because this makes the resulting B strength independent from the sign of the field. For every pixel:

$$B\,(x,y) = \left(\frac{1}{2h}\int_{-h}^{+h} B\,(x,y,z)^2\,\mathrm{dz}\right)^{1/2}, \tag{D.1}$$

where h is chosen to be 1 kpc, which means we integrate from -1 kpc below the disk to +1 kpc above the disk. The size of a pixel is 80pc x 80pc.

We separate the magnetic field into azimuthal, radial, and vertical components. Then we calculate the radial profiles (an example is shown in D.1) for the total B field and the different components:

$$B(r) = \left(\frac{\int_{r-0.5\mathrm{kpc}}^{r+0.5\mathrm{kpc}}\int_{-1\mathrm{kpc}}^{+1\mathrm{kpc}}\int_{0}^{2\pi} B\,(r,\phi,z)^2\,r\,\mathrm{d}\phi\,\mathrm{dz}\,\mathrm{dr}}{\int_{r-0.5\mathrm{kpc}}^{r+0.5\mathrm{kpc}}\int_{-1\mathrm{kpc}}^{+1\mathrm{kpc}}\int_{0}^{2\pi} r\,\mathrm{d}\phi\,\mathrm{dz}\,\mathrm{dr}}\right)^{1/2}. \tag{D.2}$$

We fit a double exponential to the radial profile of the total B field, and the radial profiles of the three B field components:

$$B(r) = \begin{cases} B_{\mathrm{center}} \times e^{[-r/r^B_{\mathrm{inner}}]} & \text{if } r < r^B_0 \\ B_{\mathrm{center}} \times e^{[-r^B_0/r^B_{\mathrm{inner}} - (r-r^B_0)/r^B_{\mathrm{outer}}]} & \text{if } r \geq r^B_0. \end{cases} \tag{D.3}$$

We list the parameters of the fitted radial profiles of the total B field strength in Table D.1 for every redshift.

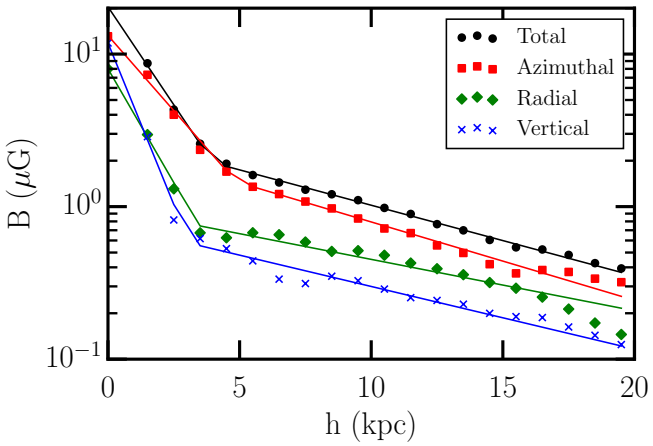

Fig. D.1. The radial profile of the total magnetic field strength and the magnetic field components of an example galaxy (ID487) at $z = 0$, with a double exponential function fitted to each.

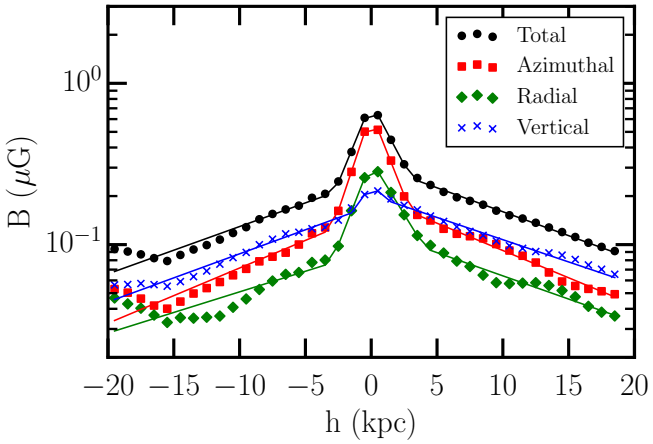

Fig. D.2. The vertical profile of the total magnetic field strength and the magnetic field components of an example galaxy (ID487) at $z = 0$. Two double exponential functions are fitted to each component, with different fit parameters below and above the midplane of the galaxy.

We calculate the average magnetic field strength in the disk by averaging the magnetic field strength of the pixels.

Appendix D.2: Magnetic field strength - edge-on

We also calculate the magnetic field strength in edge-on view (examples shown in the top four panels of Figs. D.3 and D.4), similarly to face-on view. We integrate through $2 \cdot r_{SF,99}$. In Fig. D.2 we show the height profile of the B field strength (total and its components) for one example galaxy, calculated from slices with a 1 kpc width. A double exponential can be fitted to both sides of this profile, and the profiles below and above the disk of the galaxy are not symmetric for every galaxy. The medians of the fitted parameters at each redshift are listed in Table D.2.

Appendix D.3: Magnetic field structure

We also investigated the structure of magnetic fields, by integrating the magnetic field strength of each component ($B_{\mathrm{component}}$, which can be azimuthal, radial, or vertical) separately through the inner 2 kpc of the galaxy (the resulting maps are shown in

Table D.1. The medians of the fitted parameters of the radial profiles of total magnetic field strength at each redshift. The error bars indicate the 1σ range.

z	$B_{\rm center}$ (μG)	r_0^B (kpc)	$r_{\rm inner}^B$ (kpc)	$r_{\rm outer}^B$ (kpc)
0	10^{+9}_{-5}	$2.8^{+1.0}_{-1.4}$	$1.6^{+0.4}_{-0.4}$	$5.3^{+4.7}_{-2.3}$
0.1	10^{+9}_{-5}	$2.8^{+1.1}_{-1.4}$	$1.6^{+0.4}_{-0.4}$	$5.1^{+5.0}_{-2.1}$
0.2	10^{+10}_{-5}	$2.7^{+1.0}_{-1.5}$	$1.6^{+0.4}_{-0.4}$	$4.9^{+4.9}_{-2.0}$
0.3	11^{+11}_{-6}	$2.5^{+1.0}_{-1.2}$	$1.5^{+0.4}_{-0.4}$	$4.7^{+4.4}_{-1.9}$
0.4	11^{+12}_{-6}	$2.4^{+1.1}_{-1.3}$	$1.5^{+0.4}_{-0.3}$	$4.7^{+4.1}_{-1.9}$
0.5	12^{+13}_{-6}	$2.4^{+1.3}_{-1.2}$	$1.5^{+0.4}_{-0.3}$	$4.6^{+3.9}_{-1.9}$
0.7	13^{+15}_{-6}	$2.3^{+1.3}_{-1.1}$	$1.5^{+0.4}_{-0.4}$	$4.2^{+3.1}_{-1.6}$
1	16^{+19}_{-7}	$2.4^{+1.6}_{-1.0}$	$1.5^{+0.4}_{-0.3}$	$4.0^{+2.6}_{-1.5}$
1.5	19^{+32}_{-9}	$2.7^{+1.7}_{-1.2}$	$1.5^{+0.4}_{-0.3}$	$3.7^{+2.3}_{-1.3}$
2	22^{+42}_{-10}	$2.9^{+2.1}_{-1.4}$	$1.4^{+0.4}_{-0.3}$	$3.5^{+2.5}_{-1.2}$

Table D.2. The medians of the fitted parameters of the vertical profiles of total magnetic field strength at each redshift. The error bars indicate the 1σ range.

z	$B_{\rm center}$ (μG)	$h_{0,1}^B$ (kpc)	$h_{\rm inner,1}^B$ (kpc)	$h_{\rm outer,1}^B$ (kpc)	$h_{0,2}^B$ (kpc)	$h_{\rm inner,2}^B$ (kpc)	$h_{\rm outer,2}^B$ (kpc)
0	$0.5^{+0.4}_{-0.2}$	$-3.3^{+1.4}_{-1.5}$	$3.3^{+2.1}_{-1.3}$	$14.6^{+17.2}_{-6.6}$	$3.2^{+1.5}_{-1.3}$	$3.2^{+2.1}_{-1.2}$	$14.8^{+18.2}_{-6.7}$
0.1	$0.5^{+0.4}_{-0.2}$	$-3.2^{+1.3}_{-1.5}$	$3.0^{+1.9}_{-1.1}$	$14.3^{+15.7}_{-6.1}$	$3.3^{+1.4}_{-1.3}$	$3.0^{+2.0}_{-1.1}$	$14.4^{+16.6}_{-6.6}$
0.2	$0.6^{+0.4}_{-0.2}$	$-3.2^{+1.3}_{-1.5}$	$3.0^{+1.8}_{-1.1}$	$14.7^{+16.8}_{-6.5}$	$3.3^{+1.4}_{-1.3}$	$3.0^{+1.7}_{-1.1}$	$14.9^{+19.6}_{-6.9}$
0.3	$0.6^{+0.4}_{-0.2}$	$-3.3^{+1.3}_{-1.5}$	$2.9^{+1.8}_{-1.0}$	$15.3^{+19.3}_{-6.5}$	$3.2^{+1.5}_{-1.3}$	$2.9^{+1.8}_{-1.0}$	$14.7^{+19.5}_{-6.7}$
0.4	$0.6^{+0.4}_{-0.3}$	$-3.3^{+1.3}_{-1.6}$	$2.9^{+1.8}_{-1.0}$	$15.6^{+21.8}_{-7.1}$	$3.3^{+1.6}_{-1.3}$	$2.9^{+1.8}_{-1.0}$	$15.5^{+23.5}_{-7.3}$
0.5	$0.6^{+0.5}_{-0.3}$	$-3.3^{+1.3}_{-1.7}$	$2.9^{+1.7}_{-1.0}$	$15.1^{+21.5}_{-6.9}$	$3.2^{+1.6}_{-1.3}$	$2.9^{+1.7}_{-1.0}$	$14.6^{+21.3}_{-6.7}$
0.7	$0.7^{+0.5}_{-0.3}$	$-3.2^{+1.3}_{-1.5}$	$2.8^{+1.7}_{-0.9}$	$15.1^{+18.9}_{-6.8}$	$3.1^{+1.4}_{-1.3}$	$2.8^{+1.7}_{-1.0}$	$15.4^{+20.2}_{-7.1}$
1	$0.7^{+0.6}_{-0.3}$	$-3.0^{+1.2}_{-1.5}$	$2.8^{+1.7}_{-1.0}$	$15.2^{+18.7}_{-6.5}$	$3.0^{+1.6}_{-1.3}$	$2.7^{+1.8}_{-1.0}$	$15.5^{+18.3}_{-7.0}$
1.5	$0.7^{+0.5}_{-0.3}$	$-2.8^{+1.3}_{-1.6}$	$2.8^{+1.7}_{-1.0}$	$15.1^{+19.2}_{-6.0}$	$2.7^{+1.6}_{-1.3}$	$2.8^{+1.7}_{-1.0}$	$15.3^{+15.8}_{-6.3}$
2	$0.6^{+0.4}_{-0.3}$	$-2.5^{+1.2}_{-1.5}$	$2.8^{+1.8}_{-1.1}$	$15.8^{+14.2}_{-5.8}$	$2.4^{+1.5}_{-1.2}$	$2.8^{+1.7}_{-1.1}$	$15.5^{+14.8}_{-6.0}$

the bottom row of Figs. D.3 and D.4):

$$B\,(x,y) = \frac{1}{2h}\int_{-h}^{+h} B_{\rm component}\,(x,y,z)\,{\rm d}z. \tag{D.4}$$

This preserves their signs, and provides us information about whether the large-scale fields or random fields dominate in a galaxy, and whether there are any field reversals.

We take the average of the magnetic field strength of each map derived this way:

- If it is not 0 μG, it suggests that the B field is large-scale and not random.
- If it is 0 μG, the B field is either random, or it is large-scale but has one or more field reversals in one of the field components: large regions with similar B field strengths but different signs.

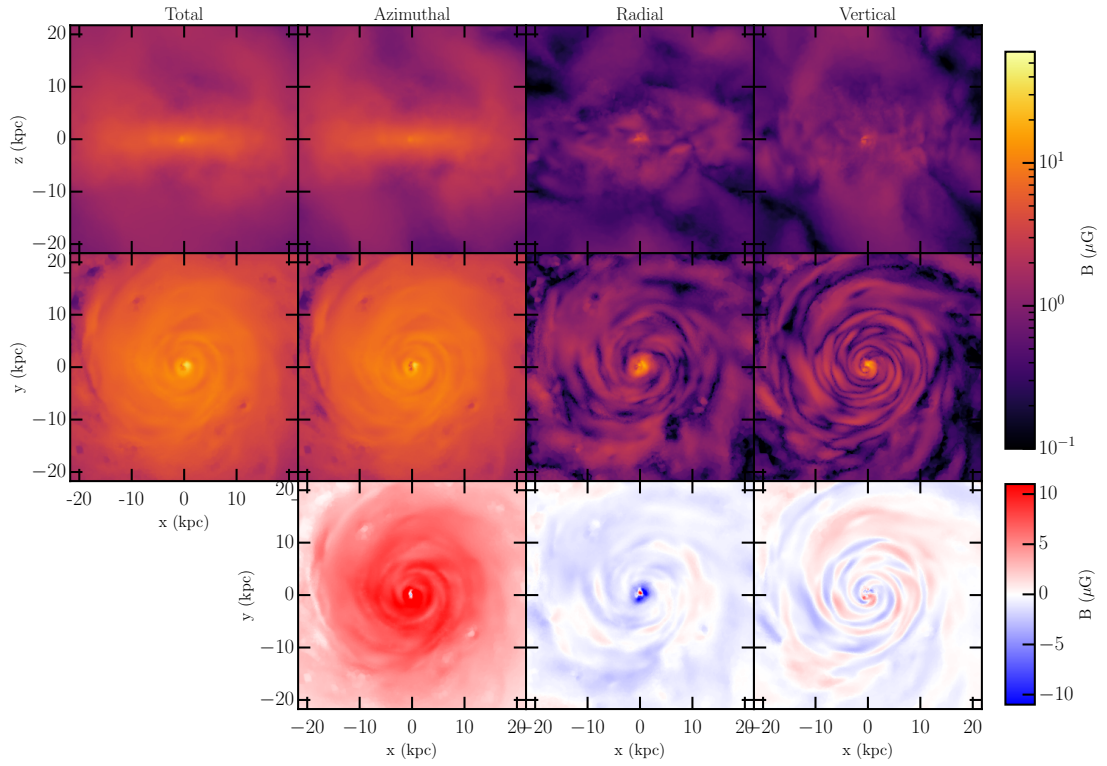

Fig. D.3. We show the magnetic field strength maps (total, and components – azimuthal, radial and vertical) of an example galaxy (ID486) at z=0 with a strong disk field. These maps are calculated for every galaxy. The top row shows the magnetic field strength maps in a edge-on view and the middle row shows them in a face-on view. The bottom row shows the magnetic field strength maps in a face-on view, calculated by keeping the sign of the B field while integrating the magnetic field components. This shows that the azimuthal field's sign remains the same throughout the disk for this galaxy.

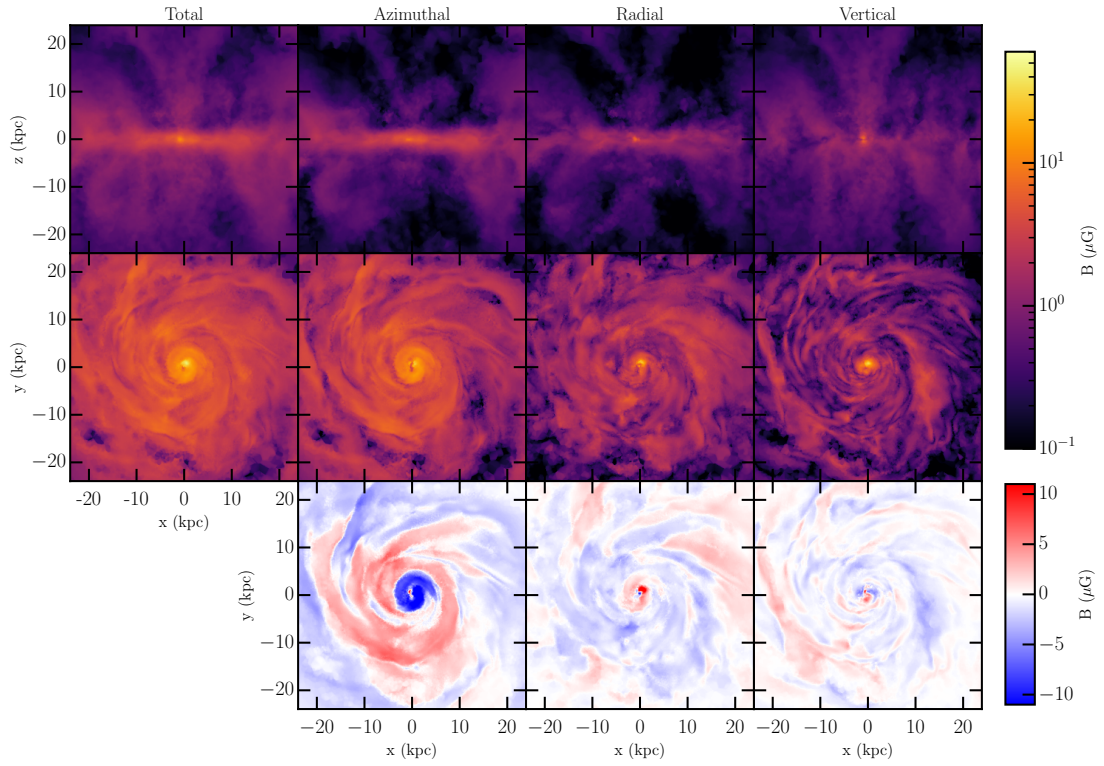

Fig. D.4. Same as Fig. D.3, but for galaxy ID487 at z=0. The azimuthal field strength map in the bottom row reveals reversals in the azimuthal magnetic field of the galaxy.

Appendix E: Galaxy property evolution across redshift

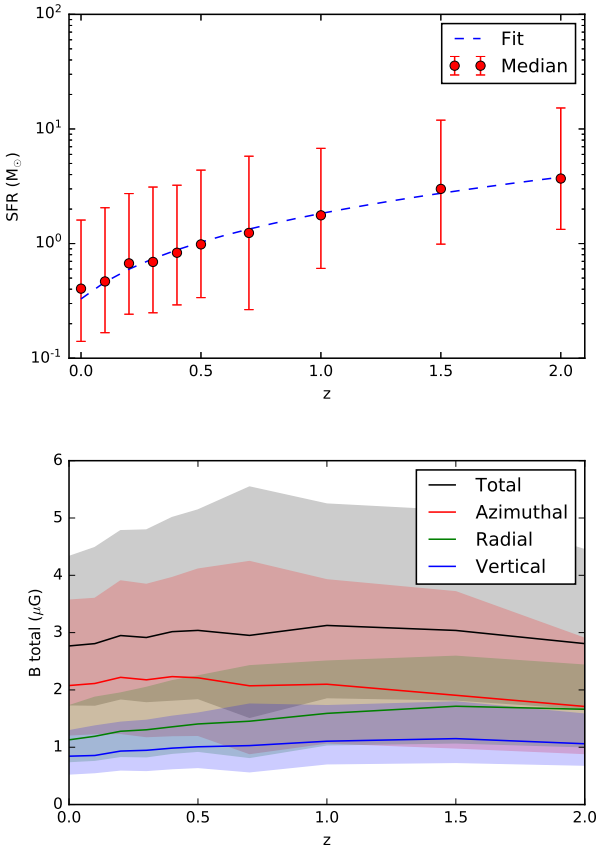

Fig. E.1. Top: The median of the SFR of the selected galaxies across redshift. It continues to increase exponentially towards higher redshift. The error bars correspond to the 16th and 84th percentile. **Bottom:** The average of the total magnetic field strength, and the average of the magnetic field components (azimuthal, radial and vertical) versus redshift. The shaded areas correspond to the 16th and 84th percentiles. These were calculated as described in Appendix D.

In the left panel of Fig. E.1 we show how the SFR of simulated galaxies in our sample evolves with redshift. The SFR increases by a factor of 9 from $z = 0$ to $z = 2$. In the right panel of Fig. E.1 we show the redshift evolution of the total magnetic field strength of galaxies, and also of the different components (azimuthal, radial, vertical). The total magnetic field strength stays around 3 μG at all redshifts as it was already amplified to saturation at $z > 2$. The azimuthal field increases from $z = 2$ to $z = 0$ caused by the ordering of the field by the differential rotation of the disk. In the case of differential rotation the other components would stay constant, however we find that these decrease (possible due to effects of outflows, accretion or dissipation). This is not expected from the mean-field dynamo theory either, from which we would expect an increase in all components, suggesting there is no mean-field dynamo action.

Appendix F: DM and RM histograms at z=0.5

We show the DM and RM histograms of host contributions at $z = 0.5$.

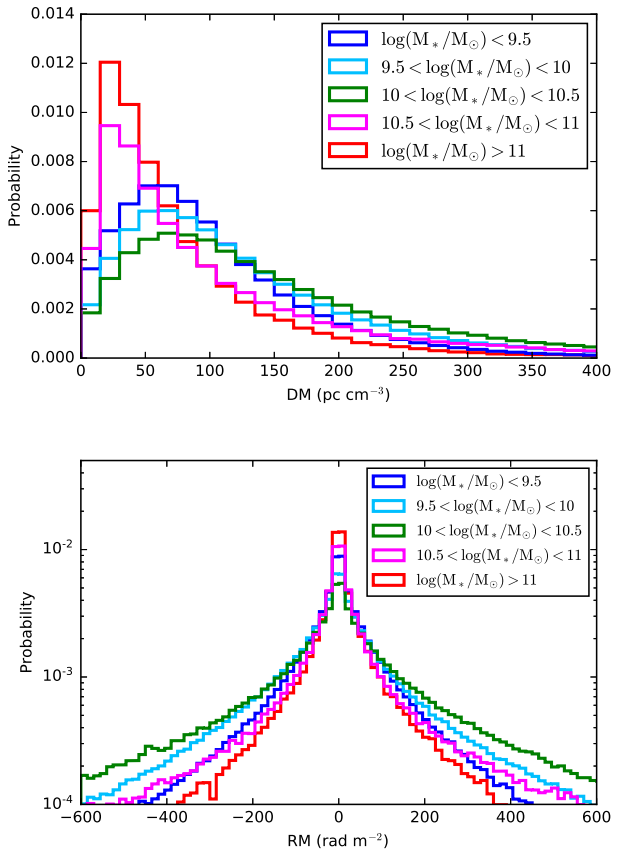

Fig. F.1. Top: The PDF of the rest frame DM contribution of host galaxies at z = 0.5. The PDFs become broader at higher stellar masses, with larger DMs. But for galaxies with log stellar masses above 10.5, the PDF becomes narrower, with lower median DM. **Bottom:** The PDF of the rest frame RM contribution of host galaxies at z=0.5. The PDFs become broader for host galaxies with larger stellar masses (up to log(M$_*$/M$_\odot$) = 10.5), with larger RMs. For galaxies above this mass, the distribution becomes narrower again.

In Fig. F.1 we show the PDFs of different stellar mass bins. The median of DM and $w_{\rm RM}$ increases until $\log(M_*/{\rm M}_\odot) = 10.5$, and at larger stellar masses both decrease.

In Fig. F.2 we show the difference in the DM and RM PDFs of star-forming and quenched galaxies. As the sample size of quenched galaxies is very small compared to star-forming galaxies in our selected sample, we overplotted the PDF of all galaxies and the PDF of randomly chosen (with the same number as the quenched sample) galaxies. As the randomly chosen sample follows the PDF of star-forming galaxies, we conclude that the PDF of quenched galaxies is not only different because of the small sample size, but is due to the properties of the selected galaxies.

In Fig. F.3 we show the DM and RM PDFs for sightlines with different inclinations.

In Fig. F.4 we show the DM and RM PDFs for different $b_{\rm offset}$.

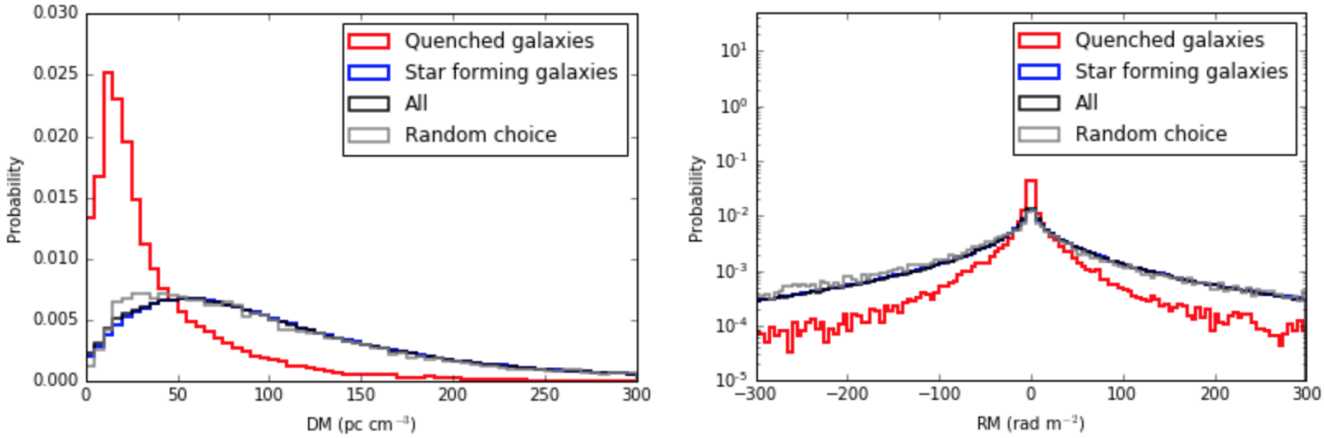

Fig. F.2. Top: The restframe DM distribution of quenched and star-forming galaxies at z=0.5. The DM distribution of all galaxies, and a random selection of the star-forming galaxies (with the same sample size as the quenched galaxies) is also shown, and both follow the same distribution as the full sample of the star-forming galaxies. **Bottom**: The RM distribution of quenched and star-forming galaxies at z=0.5. The distribution of all galaxies, and a random selection of star-forming galaxies is also overlayed.

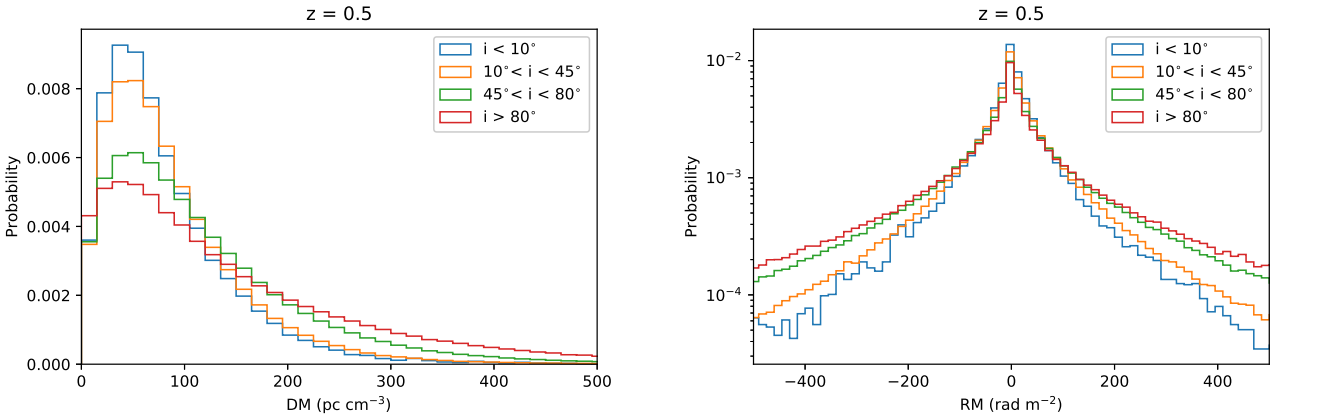

Fig. F.3. Top: The PDF of the rest frame DM contribution of host galaxies at z=0.5, separated based on the inclination of the host galaxies. The PDFs become broader, and the median increases for host galaxies with larger inclinations. **Bottom:** The PDF of the rest frame RM contribution of host galaxies at z=0.5, separated based on the inclination of the host galaxies. The PDFs become broader for host galaxies with larger inclinations.

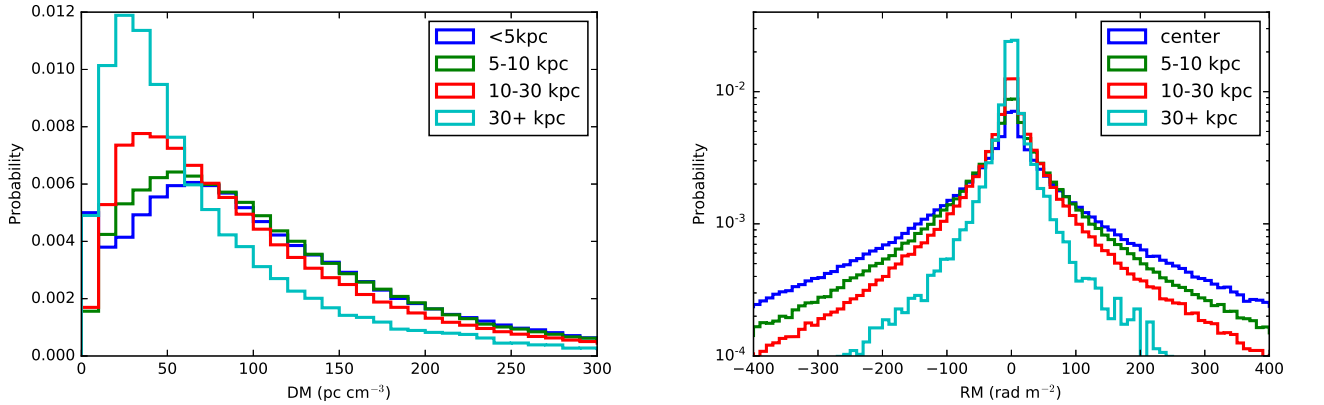

Fig. F.4. Top: The PDF of the rest frame DM contribution of host galaxies at z = 0.5 separated into sightlines with different offsets. The PDFs become narrower at larger offsets, with a smaller DM_{median}. **Bottom:** The PDF of the rest frame RM contribution of host galaxies at z=0.5, separated into sightlines with different offsets. The PDFs become narrower for sightlines with larger offsets parameters.

Appendix G: All DM and RM histograms

Appendix G.1: Inclination

We show the DM and RM PDFs for the different inclination groups at different redshifts (DM: Figs. G.2 and G.3, RM: Figs. G.4 and G.5), and how the DM and RM changes as a function of inclination at each redshift (Fig. G.1).

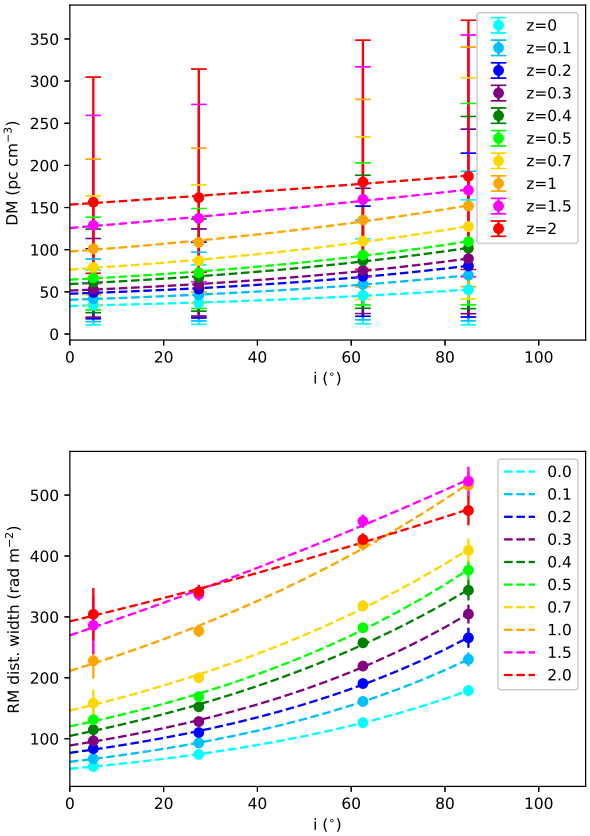

Fig. G.1. Top: The median of DM distribution as a function of inclination for different redshifts. **Bottom:** The width of the RM distribution of galaxies as a function of inclination for different redshifts.

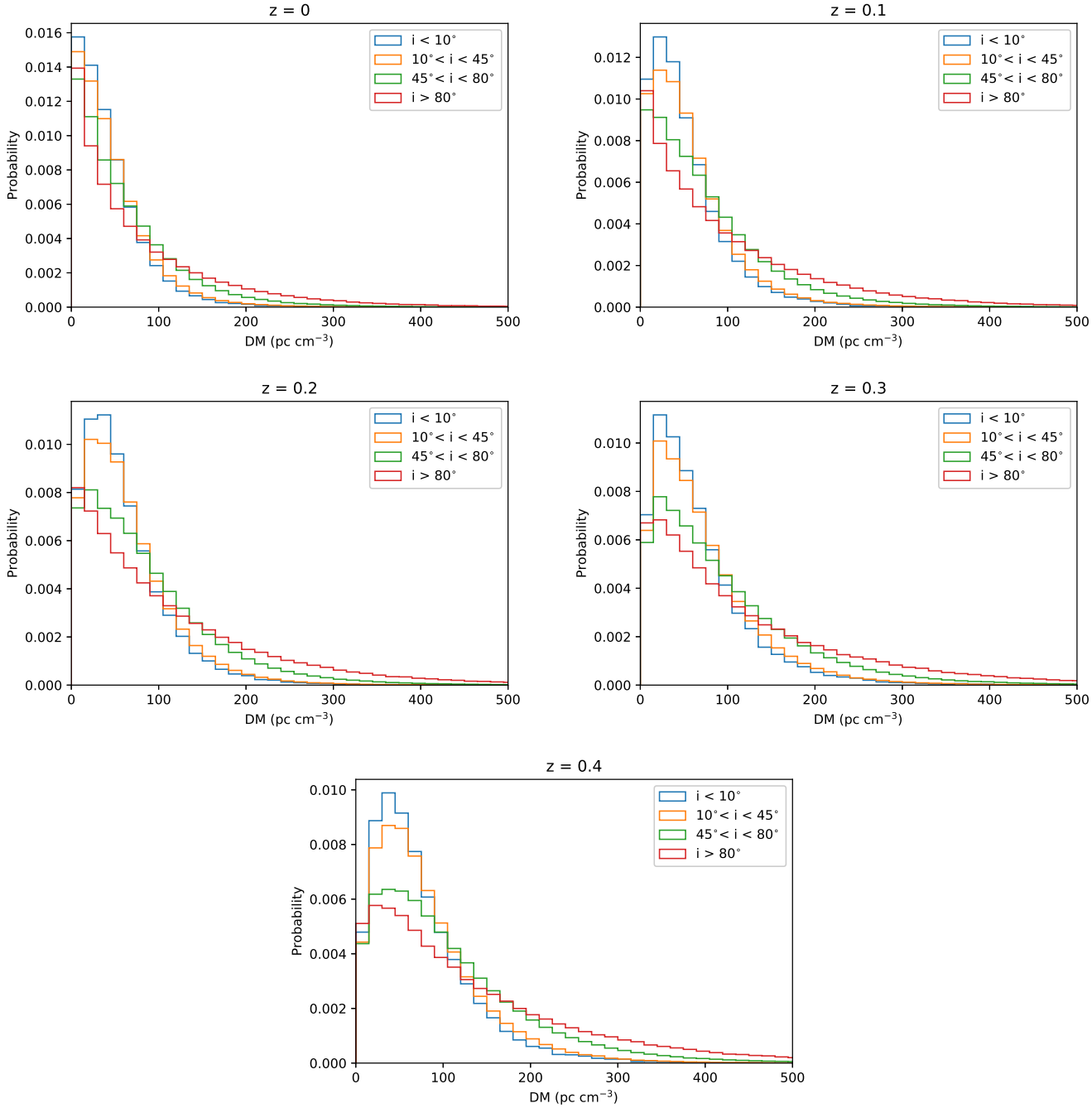

Fig. G.2. Top: The PDF of the rest frame DM contribution of host galaxies at different redshifts, separated based on the inclination of the host galaxies. The PDFs become broader, and their median increases for host galaxies with larger inclinations.

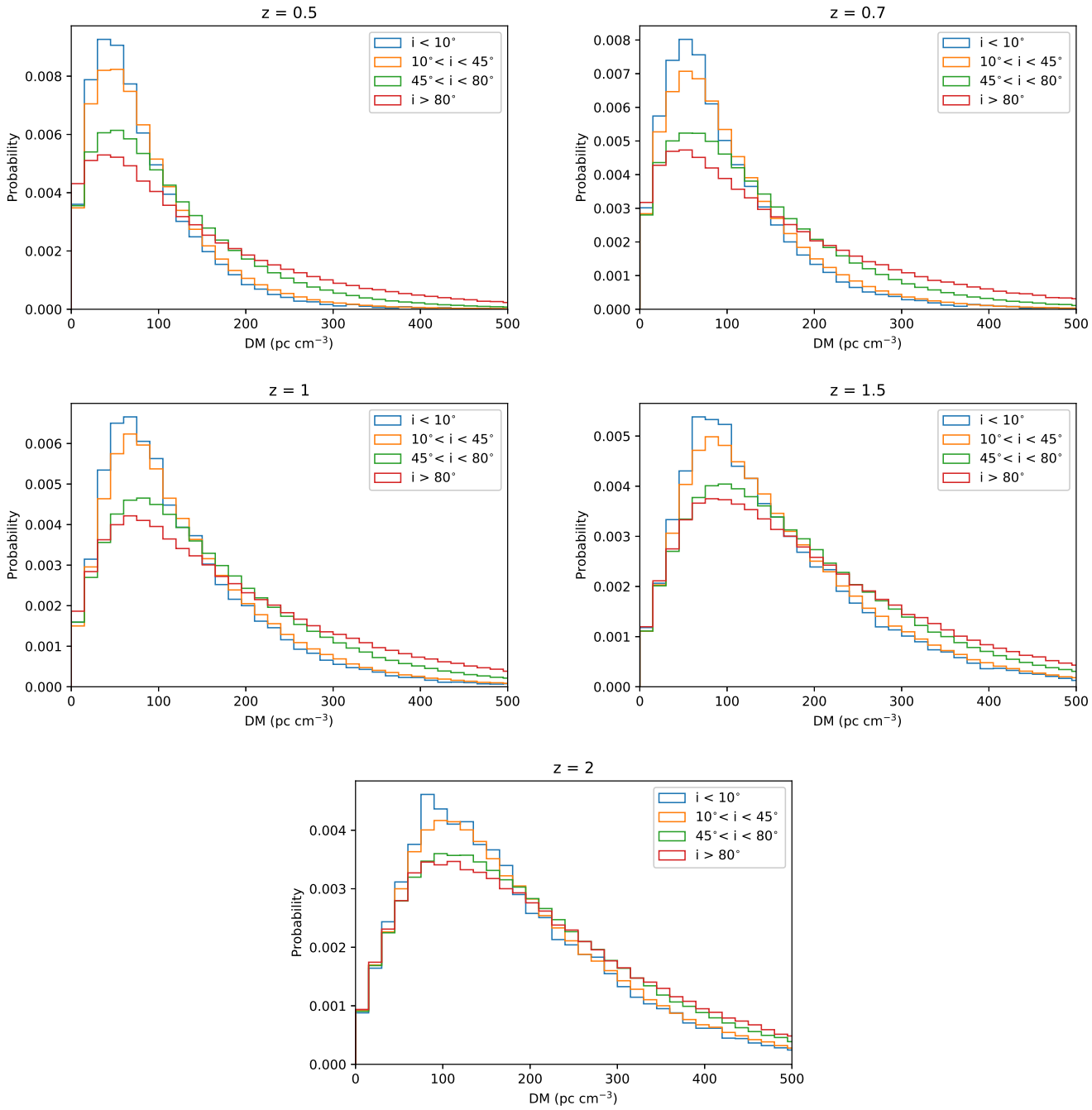

Fig. G.3. The PDF of the rest frame DM contribution of host galaxies at different redshifts, separated based on the inclination of the host galaxies. The PDFs become broader, and their median increases for host galaxies with larger inclinations.

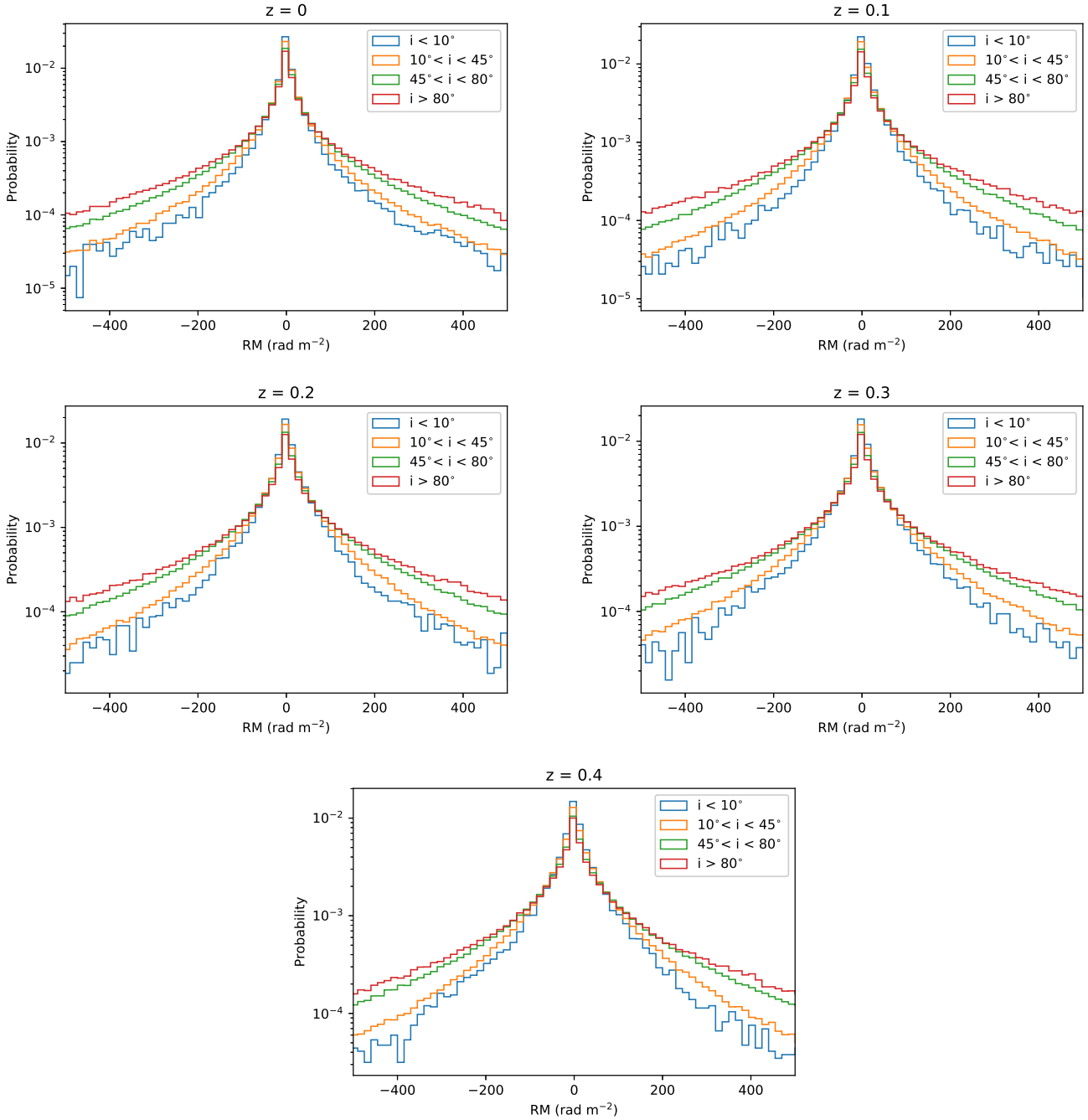

Fig. G.4. Top: The PDF of the rest frame RM contribution of host galaxies at different redshifts, separated based on the inclination of the host galaxies. The PDFs become broader for host galaxies with larger inclinations.

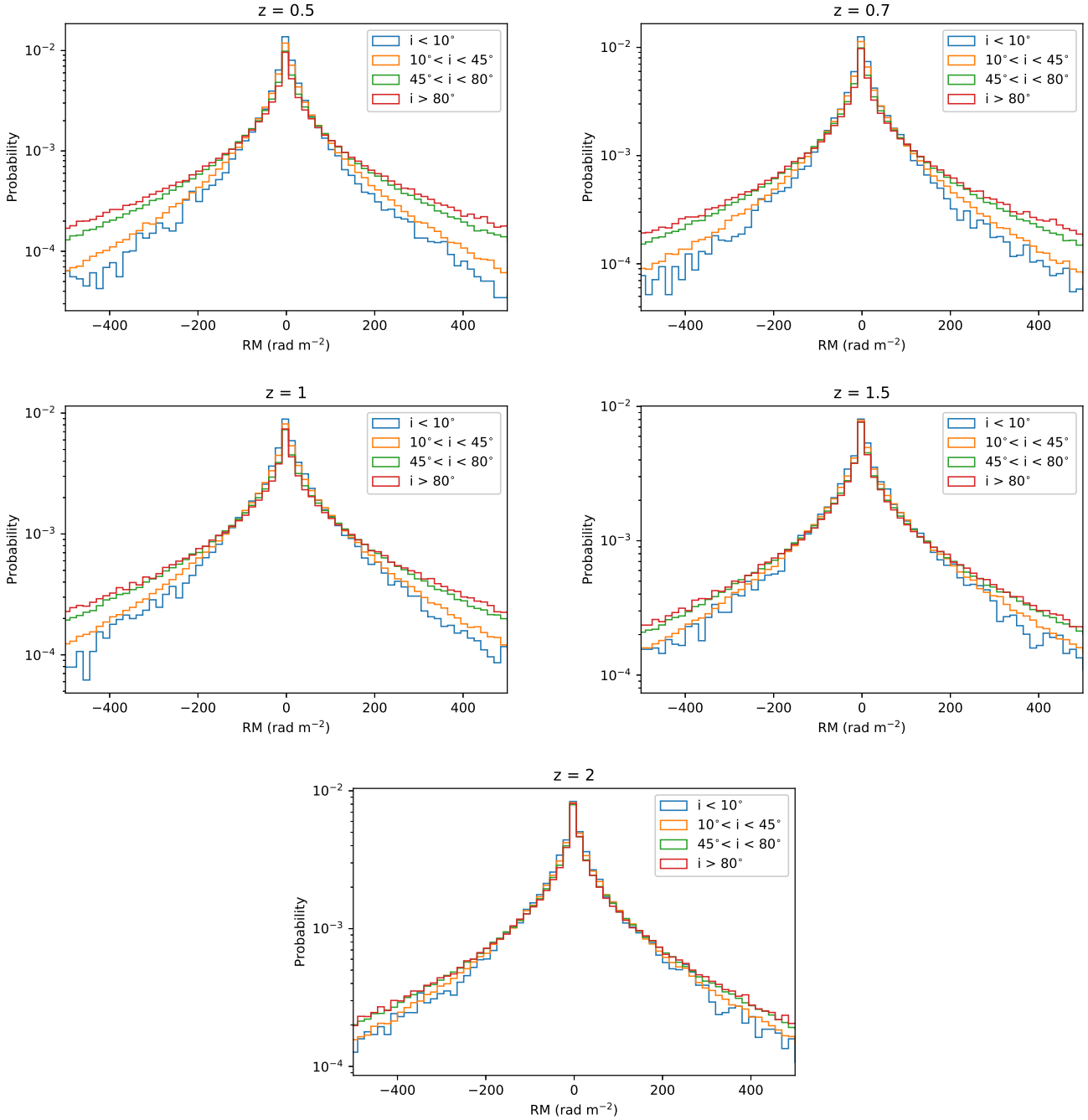

Fig. G.5. The PDF of the rest frame RM contribution of host galaxies at different redshifts, separated based on the inclination of the host galaxies. The PDFs become broader for host galaxies with larger inclinations.

Appendix III. Paper: The dispersion measure and rotation measure from 210 fast radio burst host galaxies based on the IllustrisTNG50 simulation